

Molecular Dynamics Simulation of Bioactive Complexes, Nanoparticles and Polymers

BY

YANXIAO HAN

B. Sc. in Applied Physics, Ludong University, Yantai, 2012

M. Sc. in Atomic and Molecular Physics, Ludong University, Yantai, 2015

THESIS

Submitted as partial fulfillment of the requirements
for the degree of Doctor of Philosophy in Chemistry
in the Graduate College of the
University of Illinois at Chicago, 2021

Chicago, Illinois

Defense Committee:

Prof. Petr Král, Chair and advisor

Prof. Katherine McReynolds, California State University, Sacramento

Prof. Justin Lorieau

Prof. Stephanie Cologna

Prof. Ying Hu

ACKNOWLEDGMENTS

Foremost, I would like to express my sincere gratitude to my advisor, Prof. Petr Král, for his guidance and constant support of my graduate studies and research, for his motivation, research spirit, and immense knowledge. His unwavering enthusiasm for science kept me constantly engaged with my research, and his upright, generous and merciful attitude towards everything helped shape my view of the world. He was always ready to discuss with students and spent enormous amounts of time to teach, motivate and discuss research problems.

My sincere thanks also goes to Prof. Lela Vukovic. Her instruction at my startup of PhD enlightened the first glance of my research. Her guidance and stimulus discussions run through my whole PhD, which have been especially valuable. I would also thank Dr. Soumyo Sen, Dr. Henry Chan, Sanoj Raj, Pavel Rehak, Aayush Gupta, Cong Wang, Daria Galaktionova, Alice Zheng, and Michal Sawczyk for working together with me, for the thoughtful discussions and all the fun we have had over the years. I also want to thank my friends in China and U.S.: Delan Meng, Lihua Yang, Wenhua Zhang, Siling Zhao, Haifeng Li, and the friends from Christian association lead by pastor Peter Qu for all the caring and support.

My appreciation also extends to my collaborators with whom I worked during my graduate studies, Profs. Seungpyo Hong, Rafal Klajn, Francesco Stellacci, Katherine McReynolds, Alexander Spokoyny, Paolo Caliceti, Andrew Whittaker and Wilhelm Huck, for their guidance and support in our joint efforts. The communications and discussions with the collaborators helped me to gain multidimensional knowledge and understanding of the research projects.

I also want to express my thanks to all the faculty members in the Department of Chemistry at UIC, and especially Profs. Preston Snee and Duncan Wardrop for their efforts to advise me in the

ACKNOWLEDGMENTS (Continued)

selection of courses and award application; Dr. George Papadantonakis, Dr. Audrey Hammerich, the late Ms. Rhonda Staudohar, Ms. Silvia Solis, Ms. Jennifer Kazin, and Ms. Gloria Torres, for their effort and support.

I highly acknowledge the supports from Dean's Scholar Fellowship (UIC), Chinese Government Award for Outstanding Self-Financed Students Abroad (China Scholarship Council), Teaching Assistant Appreciation Award (UIC) and Student Presenter Award and Travel Award (UIC). Those awards helped me to accomplish my PhD study.

Last but not the least, I would like to thank my husband, who is my champion and always takes care of all the trifles; my parents and brother, who always support my study, even in hard time; my mom in-law, who spares no effort to help me with the kid and supports me with everything in life; and the little angel who gives me the strength to succeed.

LIST OF ABBREVIATIONS

ACE2	Angiotensin-Converting Enzyme 2
AIMD	Ab-initio Molecular Dynamics
AuNP	Gold Nanoparticle
BO	Born-Oppenheimer
CD	Circular Dichroism
CDn	Cyclodextrin
CHARMM	Chemistry at Harvard Macromolecular Mechanics
CHELPG	Charges from Electrostatic Potentials using a Grid based method
Con A	Concanavalin A
DC-SIGN	Dendritic Cell-Specific Intercellular Adhesion Molecule-3-Grabbing Nonintegrin
DDS	Drug Delivery System
DFT	Density Functional Theory
DM	Dendron-Based Micelle
EM	Electron Microscopy
F-NP	Functionalized Nanoparticle
gB	glycoprotein B
GD	Glycodendrimer
HSPG	Heparan Sulfate Proteoglycans
IEFPCM	Integral Equation Formalism version of Polarizable Continuum Model
LBC	Linear Block Copolymer
LJ	Lennard-Jones
LM	LBC-Based Micelles
MD	Molecular Dynamics
MM	Molecular Mechanism
MMGB-SA	Molecular Mechanics-Generalized Born Surface Area

LIST OF ABBREVIATIONS (Continued)

MP2	2nd order Moller-Plesset Perturbation
MSD	Mean Square Displacement
MUS	Mercapto-Undecane Sulfonic Acid
MV	Viologenterminated Thiol
NAMD	Nanoscale Molecular Dynamics
NP	Nanoparticle
ON	Oligonucleotides
PAMAM	Poly-(amidoamine)
PBC	Periodic Boundary Conditions
PDC	PEGylated Dendron Co-polymer
PEG	PolyEthylene Glycol
PES	Potential Energy Surface
PFPE	Perfluoropolyether
PME	Particle Mesh Ewald
PNP	Polymeric Nanoparticles
QM	Quantum Mechanism
RBD	Receptor Binding Domain
SAPT	Symmetry-Adapted Perturbation Theory
SGD	Sulfated Glycodendrimer
TEM	Transmission Electron Microscopy
vdW	van der Waals
VMD	Visual Molecular Dynamics
WHAM	Weighted Histogram Analysis Method
SB	Sulfobetaine-Based Ligand

SUMMARY

This thesis contains computational modeling research performed during my PhD studies. In close collaborations with several experimental groups, I have studied different types of inhibitors, including functionalized nanoparticles (NPs), cyclodextrins (CDns), and glycodendrimers, against different pathogens, simulated polymer-based drug delivery systems, and interpreted intermolecular interactions by both classical Molecular Dynamics (MD) methods and *ab initio* calculations. Given our experience gained in the inhibition studies of viral systems, including HPV, HSV, and HIV, we have developed a new algorithm combining MD simulations and Monte Carlo (MC) decisions to design peptide inhibitors against the coronavirus causing COVID-19. The thesis is based on 18 original papers [1–3, 5–19] and 1 manuscript [4] which is currently under review. The two projects related to ACE2-based inhibitor-conjugated dendrimers and conformational changes of TRNA aptamers are not included.

The first part of this thesis includes Chapters 1 and 2 and presents a brief introduction into theoretical and computational methods used in the thesis and their applications in biological systems and nanomaterials. Here, we describe the methods, such as MD simulations, forcefield parameter calculations, free energy calculations, and *ab initio* electronic structure calculations.

The second part of this thesis includes Chapters 3, 4, 5 and 6. Here, the coupling between inhibitors and their targets was studied by MD simulations and characterized by analyzing the simulation trajectories to clarify the working mechanisms of antiviral inhibitors. With the gained knowledge, double-faced peptide-based boosters were designed to allow recognition of SARS-CoV-2 by Hepatitis B antibodies. The stability and transport properties of designed drug delivery vehicles were analyzed here through calculations of their binding energies with serum proteins, diffusion con-

SUMMARY (Continued)

stants of sliders, and radii of gyration of polymer tracks, etc. Stretch-healable molecular nanofibers composed of mixed coronene and perfluorocoronene molecular flakes were also designed and studied, where the intermolecular interactions were evaluated by *ab initio* calculations. We have also studied the stabilized ratio of ligands attached on nanoparticles (NPs), the self-assembly of NPs and the supramolecular control of ligands switching on NP surfaces by analyzing the intermolecular interactions.

CONTRIBUTION OF AUTHORS

This thesis is based on 18 published paper and 1 manuscript under review. Although most of the projects were done in collaboration with experimental groups except sections 3.1, 3.2 and 6.1, the computational works done mainly by Yanxiao Han were presented.

In section 3.1, Yanxiao Han contributed to the atomistic MD simulations, computational data analyses for the peptide design, and writing of the manuscript under the guidance of Prof. Petr Král in [1]. Yanxiao Han also collected the mutations on S protein of SARS-CoV-2 and performed initial simulations of mutated RBD with wild type template-2 and wild type RBD with selected mutations of template-2 for [2]. Parth Chaturvedi performed the adaptive evolution related simulations in [2]. Prof. Lela Vukovic accomplished the compiling of algorithm and writing of the manuscript of [2]. Parth Chaturvedi and Yanxiao Han contributed evenly in [2]. Profs. Lela Vukovic and Petr Král both guided the research of adaptive evolution of peptide inhibitors in [2].

In section 3.2, three boosters were computationally designed to trigger the recognition of SARS-CoV- 2 by Hepatitis B antibody [3]. Yanxiao Han performed the design of boosters, tested their binding to antibody and RBD of SARS-CoV-2 by MD simulations, and contributed to the writing of the manuscript under the guidance of Prof. Petr Král. Prof. Katherine McReynolds (California State University, Sacramento) provided biological information about selection of antibody, suggested PEG linkage, and contributed to reviewing and correcting of the manuscript.

In section 3.3, the work was done in collaboration with Prof. Katherine McReynolds (California State University, Sacramento). Glycodendrimers blocking HIV S proteins (gp120) were designed, synthesized and tested *in vitro* in Prof. McReynolds's group. Four glycodendrimers with strong activities in experiments were simulated to check their interactions with gp120. Two top glyco-

CONTRIBUTION OF AUTHORS (Continued)

dendrimers and two hybrid glycodendrimers were further tested by MD simulations to check their binding to the RBD of SARS-COV-2 S protein [4]. All the experimental related results were obtained by Prof. McReynolds’s group, and the manuscript was written by Prof. McReynolds. Yanxiao Han contributed to the MD simulations, analyses of simulation data and writing of the simulation parts under the guidance of Prof. Petr Král. In this section, the focus is only put on the simulation part.

In section 4.1, the work was done in collaboration with Prof. Seungpyo Hong (UW-Madison). Peptide-conjugated dendrimers were designed as cancer immuotherapies [5]. The conformations of peptides on the dendrimer surfaces were examined by MD simulations. The interactions between peptides and dendrimers were quantified by interaction energy calculations. All the experimental related results were obtained and written (manuscript) by Prof. Hong’s group. Yanxiao Han contributed to the MD simulations, MD data analyses and writing of the simulation parts under the guidance of Prof. Petr Král. In this section, the focus is solely on the simulation part.

In section 4.2, the work was done in collaboration with Prof. Francesco Stellacci’s lab (EPFL). In this section, functionalized AuNPs and CDns, synthesized in Prof. Stellacci’s lab, were simulated to examine their working mechanisms in inhibiting viruses. All the experimental related results were obtained and written (manuscript) by Prof. Stellacci’s group. Soumyo Sen performed AuNP related simulations, MD data analyses and writing of simulation parts in [6]. Yanxiao Han performed all the replicas for 5 AuNP systems in [6]. Yanxiao Han performed the CDn related simulations and analyses and contributed to the writing of simulation related parts in [7]. Profs. Petr Král and Lela Vukovic both guided the computational research in [6, 7]. In this section, the focus is solely on the simulation part.

In section 4.3, the work was done in collaboration with Prof. Alexander Spokoyny (UCLA). In this section, various functionalized Boron clusters [8–10], designed in the lab of Prof. Spokoyny, were

CONTRIBUTION OF AUTHORS (Continued)

simulated to check their binding efficiency to their specific proteins. All the experimental related results were obtained and written (manuscript) by Prof. Spokoyny's group. The forcefield of the boron cluster was generated by Pavel Rehak. The atomistic MD simulations, MD data analyses and writing of MD parts (protein with clusters) were performed by Yanxiao Han under the guidance of Prof. Petr Král. In this section, the focus is only on the simulation part.

In section 5.1, the work was done in collaboration with Prof. Paolo Caliceti's group (University of Padova). They synthesized Maltotriose-based cationic polymers, which were used to delivery DNA by forming polymer-DNA polyplexes [11]. All the experimental related results were obtained and written (manuscript) by our collaborators. MD simulations were performed to examine the interactions and morphology of the polymer-DNA polyplexes by Yanxiao Han under the guidance of Prof. Petr Král. Yanxiao Han also contributed to the writing of the simulation related parts. In this section, the focus is solely on the simulations.

In section 5.2, the work was done in collaboration with Prof. Seungpyo Hong (UW-Madison). The dendritic/linear copolymer-based micelles were designed in the lab of Prof. Hong. The coupling of micelles with serum proteins were modeled to study the micelle stability [12]. All the experimental related results were obtained and written (manuscript) by Prof. Hong's group. Yanxiao Han performed the MD simulations and related analyses, and contributed to the writing of simulation parts under the guidance of Prof. Petr Král. In this section, the focus is solely on the simulations.

In section 5.3, the work was done in collaboration with Prof. Andrew Whittaker (The University of Queensland). High F-content perfluoropolyether-based nanoparticles [13–15] were synthesized in the group of Prof. Whittaker. MD simulations were conducted to check the aggregation states and membrane permeability of those nanoparticles. All the experimental related results were obtained and written (manuscript) by our collaborators. Yanxiao Han performed all the MD simulations and

CONTRIBUTION OF AUTHORS (Continued)

related analyses and contributed to the writing of simulation parts under the guidance of Prof. Petr Král. In this section, the focus is only on the simulations.

In section 6.1, stretch-healable molecular nanofibers were designed and modeled by MD simulations [16]. The interaction energies between molecular flakes were calculated by *ab initio* methods. The atomistic MD simulations and data analyses were performed by Yanxiao Han under the guidance of Prof. Petr Král. The quantum calculations and initial MD simulations were performed by Michal Langer. Yanxiao Han and Michal Langer contributed evenly in this work.

In section 6.2, cargo-carrying peptide sliders [17], synthesized in the lab of Prof. Wilhelm Huck (Radboud University Nijmegen), were modeled. MD simulations were conducted to examine the diffusive binding modes of sliders on polymer tracks. All the experimental related results were obtained and written by Prof. Huck's group. Yanxiao Han performed all the MD simulations, free energy calculations, MD data analyses and writing of simulation parts under the guidance of Prof. Petr Král and Prof. Lela Vukovic. Lifei Zheng, Hui Zhao, and Yanxiao Han contributed evenly in this work. In this section, the focus is only on the simulation results.

In section 6.3, AuNPs functionalized with different ligands were synthesized in Prof. Rafal Klajn's lab (Weizmann Institute of Science). All the experimental related results were obtained and written by our collaborators. MD simulations were performed to study the ligand ratio on AuNP surface and self-assembly of AuNPs [18]. The atomistic MD simulations, MD data analyses and writing of the simulation parts were performed by Yanxiao Han under the guidance of Prof. Petr Král. In this section, the focus is only on the simulation part.

In section 6.4, AuNPs functionalized with ligands carrying different functional groups were synthesized in Prof. Rafal Klajn's lab (Weizmann Institute of Science). All the experimental related

CONTRIBUTION OF AUTHORS (Continued)

results were obtained and written by our collaborators. MD simulations were performed to study the effect of background ligands on the switching of azobenzene ligands on NPs [19]. The atomistic MD simulations and data analyses were performed by Yanxiao Han under the guidance of Prof. Petr Král. Yanxiao Han also contributed to the writing of simulation parts. The forcefield parameters of ligands (based on cis/trans azobenzene) were taken from [20]. In this section, the focus is on the MD simulations.

TABLE OF CONTENTS

<u>CHAPTER</u>		<u>PAGE</u>
1	INTRODUCTION	1
1.1	Thesis layout	3
2	METHODS	8
2.1	Theory of <i>ab initio</i> calculations	8
	The Born-Oppenheimer (BO) approximation	9
	The wave function-based methods	10
	The Density Functional Theory (DFT)	14
	The Symmetry-adapted Perturbation theory (SAPT)	15
2.2	Molecular Dynamics (MD) simulations	16
	Equations of motion and algorithms	16
	The forcefield evaluation	19
2.3	The Ergodic hypothesis	27
2.4	Free energy calculations from MD simulations	28
	The weighted histogram analysis method	28
	The MMGB-SA method	29
	The adaptive evolution algorithm	30
3	DESIGN OF INHIBITORS AND BOOSTERS FOR SARS-COV-2 . .	32
3.1	Design of ACE2-based peptide inhibitors of SARS-CoV-2	33
	Introduction	33
	Simulation methods and design of algorithm	35
	Preparation of inhibitors	38
	Adaptive evolution of peptide inhibitors	42
	Conclusion	49
3.2	Retrained generic antibodies can recognize SARS-CoV-2	49
	Introduction	50
	Simulation methods	51
	Booster design	54
	Results and discussion	55
	Conclusion	58

TABLE OF CONTENTS (Continued)

<u>CHAPTER</u>		<u>PAGE</u>
3.3	Glycodendrimer inhibitors of HIV and SARS-CoV-2	58
	Introduction	58
	Experimental results	59
	MD simulations of dendrimers with glycoproteins	59
	Conclusion	74
4	DESIGN OF INHIBITORS AGAINST CANCER AND VARIOUS VIRAL PATHOGENS	76
4.1	Peptide-conjugated dendrimers as cancer immunotherapies	77
	Experimental results	78
	MD simulations of peptide-conjugated dendrimers	78
	Conclusion	81
4.2	Modified nanoparticles and cyclodextrins as broad-spectrum antivirals	81
	Introduction	81
	Modified AuNP antivirals	82
	Modified CDns antivirals	85
	MD simulations of CDns coupled with gB proteins	85
	Conclusion	91
4.3	Nanomolecules inhibiting protein–protein interactions	91
	Introduction	91
	Experimental results	92
	MD simulations of nanomolecules coupled with target proteins	95
	Conclusion	106
5	SIMULATIONS OF POLYMER-BASED DRUG DELIVERY SYSTEMS	108
5.1	Novel oligonucleotide carriers	109
	Introduction	109
	Experimental results	110
	MD simulations of DNA-polymer complexes	113
	Conclusion	116
5.2	Polymeric micelles with dendritic PEG outer shells	116
	Introduction	116
	Experimental results	117
	Simulations of serum proteins coupled with DM/LM	118

TABLE OF CONTENTS (Continued)

<u>CHAPTER</u>		<u>PAGE</u>
	Conclusion	123
5.3	High F-content perfluoropolyether-based nanoparticles	123
	Introduction	123
	Experimental results	124
	MD simulations of polymer-based nanoparticles	125
	Conclusion	132
6	MODELING OF DYNAMICAL NANOSYSTEMS	133
6.1	Stretch-healable molecular nanofibers	133
	Introduction	134
	Methods	134
	Interactions between free flakes	135
	MD simulations of free flakes	140
	MD simulations of linked flakes	146
	Conclusion	151
6.2	Cargo-carrying peptide sliders on polymer tracks	152
	Introduction	152
	Experimental results	153
	MD simulations of sliders with tracks	153
	Conclusion	162
6.3	Intermolecular interactions stabilize ligand ratios on nanoparticles .	164
	Introduction	164
	Experimental results	164
	MD simulations of MV/SB functionalized-nanoparticle	165
	Conclusion	170
6.4	Supramolecular control of azobenzene switching on nanoparticles .	170
	Introduction	170
	Experimental results	171
	MD simulations of azobenzene-functionalized nanoparticles . . .	175
	Conclusion	182
7	CONCLUDING REMARKS	185
7.1	A: Design of inhibitors and boosters for SARS-CoV-2	185
7.2	B: Design of inhibitors against cancer and other viral pathogens .	187
7.3	C: Simulations of polymer-based drug delivery systems	188

TABLE OF CONTENTS (Continued)

<u>CHAPTER</u>		<u>PAGE</u>
7.4	D: Modeling of dynamical nanosystems	189
	CITED LITERATURE	191
	APPENDIX	216

CHAPTER 1

INTRODUCTION

Nowadays, computer simulations are widely used in the modeling of physical, chemical, and biological systems. There is a revolution in computation driven by the development of modern supercomputers, computational methods, as well as the connections across different disciplines [21, 22]. Computer simulations are so developed that they can predict the behavior of realistic systems.

In a decreasing order of precision, one can name *ab-initio* MD (AIMD) [23,24], hybrid QM/MM (quantum mechanics/molecular mechanics), atomistic MD and coarse-grained MD simulation methods. AIMD methods, with forces computed by accurate electronic structure calculations [25], are suitable for systems with a few hundred atoms over rather short (ns) trajectories. Hybrid QM/MM methods combine QM (accuracy) and MM (speed) approaches, but they are also limited by the computing time [24]. MD simulations are particularly useful to describe the motions of atoms and molecules in diverse material systems. Typically, the MD simulations are realized by solving classical Newtonian or Langevin equations with forcefields obtained from quantum calculations (QM). Atomistic MD methods with different classical forcefields are often used for systems with nanometer/nanosecond or microsecond scale, but whole viruses or even cell regions with 10^8 atoms have been modeled as well [26,27]. Coarse-grained MD methods are popular in mesoscale modeling, which map functional groups to corresponding beads [28]. Bead motions simulated with large time steps (10-50 fs) can significantly increase the simulation speeds at the expense of slightly less precise results. With the continuous development of algorithms and computer power, limitations in MD simulations are being diminished.

Although the structure and dynamics of bio-related systems can be examined by advanced experimental methods, refined structural details can be difficult or impossible to obtain experimentally [29,30]. It is even more different to obtain mechanistic insight in the observed phenomena [31]. On the other hand, MD simulations can provide detailed information about molecular interactions and other physical chemical properties of the target systems. Therefore, MD simulation methods can complement experiments and assist them in understanding the structural details, dynamics, and principles of microscopic phenomena, which can be useful in designing of innovative molecular systems.

MD simulations have been used to address a broad range of questions in bio-related systems, such as the structure and dynamics of drug delivery systems (DDS), drug distributions, and DDS-protein interactions [29, 32]. Our group has performed many nanomedicine studies [33] in DNA delivery systems [11, 34], DDS based on dendrimers and polymers [12, 35–37], and nanomedicines for the inhibition of viruses [6, 38, 39].

Over the time, experimentalists gained control of the sizes, shapes and self-assembly of NPs [40]. We have also used MD simulation methods to study the interactions and self-assembly of NPs. The self-assembly of NPs is triggered by the interplay of Coulombic coupling, van der Waals (vdW) interactions and H-bonds. Sometimes, the self-assembly proceeds spontaneously, and in other cases, it is triggered by external perturbations [20, 41–45], properties of ligand functionalized [18, 19], and predefined templates [46]. Although the self-assembly of NPs can be observed by various experimental techniques, it can't be easily explained at the atomistic level without modeling. The atomistic details of ligands distribution around NPs and ligand-ligand interactions can be precisely depicted by MD simulations. The mobility of ligands around NP surfaces can determine the role of intermolecular interactions in the self-assembly of NPs [18, 19].

In my thesis, MD simulations were widely used to study nanomedicines prepared by our collaborators. Peptide-based antiviral inhibitors were also designed computationally and tested by MD simulations. QM calculations were also used in the modeling of NPs and their self-assembly [19].

1.1 Thesis layout

The thesis covers modeling of peptide-based inhibitors and boosters, dendrimer/nanomolecule-based inhibitors, drug delivery systems and nano-material systems. Atomistic MD simulations were mostly used to model those systems where forcefield parameters were calculated by *ab initio* methods for the molecules which were absent in the conventional forcefields. *Ab initio* calculations were also performed to interpret the intermolecular interactions between aromatic molecules.

Design of inhibitors and boosters for SARS-CoV-2

Section 3.1: Computational design of ACE2-based peptide inhibitors of SARS-CoV-2.

In this section, we designed and simulated peptide inhibitors against SARS-CoV-2 which currently causing a worldwide pandemic. The inhibitors are mostly composed of two sequential self-supporting α -helices (bundle) extracted from the protease domain (PD) of angiotensin-converting enzyme 2 (ACE2), which is the cellular receptor of SARS-CoV-2. MD simulations indicated that the α -helix peptides maintain stable secondary structure and provide a highly specific and stable binding to SARS-CoV-2 [34]. The designed inhibitors were expected to block the S protein of SARS-CoV-2, and inhibit the viral entry. In collaboration with Prof. Lela Vukovic (UTEP), a new algorithm was developed to design a series of peptides with mutated sequences against various strains of SARS-CoV-2 [2].

Section 3.2: Retrained generic antibodies can recognize SARS-CoV-2. In this highly innovative study, we have computationally designed double-faced peptide-based boosters to allow

recognition of SARS-CoV-2 by Hepatitis B antibodies. MD simulations revealed that the designed boosters have a highly specific and stable binding both to RBD and the antibody fragment (AF) [3].

Section 3.3: Glycodendrimer inhibitors of HIV and SARS-CoV-2. Glycodendrimers with a high binding affinity against HIV and SARS-CoV-2 were designed in the lab of Prof. Katherine McReynolds (California State University) [4]. The binding modes of different glycodendrimers on HIV S protein (gp120) were simulated. The sulfation level of the glycodendrimers was found to be an important factor influencing the binding. Moreover, two promising glycodendrimers were selected to bind to SARS-CoV-2. Our simulations showed that those glycodendrimers could block both the receptor binding region and the basic region of the S protein of SARS-CoV-2.

Section 4.1: Peptide-conjugated dendrimers as cancer immunotherapies. This work was done in collaboration with Prof. Seungpyo Hong (UW-Madison). The dendrimers provided a platform for the attachment of peptides which could increase the binding affinity to the target cells by multivalent binding modes [5]. The peptides were extracted from the programmed death-1 (PD-1) protein. The conformations of peptides on the dendrimer surfaces were sampled by MD simulations. The interactions between peptides and dendrimers were quantified by interaction energy calculations.

Section 4.2: Modified nanoparticles and cyclodextrins as broad-spectrum antivirals. This work was done in collaboration with Prof. Francesco Stellacci (EPFL, Switzerland). Coupling of predesigned NPs (mimicking heparan sulfate molecules) with HPV viral proteins was simulated. Interactions between similarly modified CDns and HSV viral proteins were also examined by MD simulations. The activities of certain NPs and CDns were interpreted based on free energy calculations and contact amino acids analyses [7].

Section 4.3: Nanomolecules inhibiting protein–protein interactions. This work was performed in collaboration with Prof. Alexander Spokoiny (UCLA). Various B_{12} nanomolecules interacting with different protein targets were designed and modeled. The multivalent binding of nanomolecules enhanced the binding affinity to their protein targets [8–10].

Simulations of polymer-based drug delivery systems

Section 5.1: Novel oligonucleotide carriers. In collaboration with Prof. Paolo Caliceti (University of Padova, Italy), supramolecular oligocationic structures ($Agm_6 - M - PEG - OCH_3$) were designed as delivery vehicles of therapeutic oligonucleotides (ONs). The conformations of the single $Agm_6 - M - PEG - OCH_3$ and complex of $Agm_6 - M - PEG - OCH_3$ /DNA were examined with MD simulations [11].

Section 5.2: Polymeric micelles with dendritic PEG outer shells. In collaboration with Prof. Seungpyo Hong (UW-Madison), polymeric micelles, including dendritic micelles and linear micelles, were designed as drug delivery vehicles. MD simulations revealed that the dendritic PEG outer shells prevented the penetration of serum proteins into the core of dendritic micelles, which make them more stable than linear micelles in the presence of serum proteins [12].

Section 5.3: High F-content perfluoropolyether-based nanoparticles. In collaboration with Prof. Andrew Whittaker (The University of Queensland, Australia), the aggregation of polymers with different number of fluorinated moieties was studied by MD simulations. The fluorinated moieties were found to facilitate the aggregation of polymers and increase the uptake of NPs by living cells, which could enhance cell permeability [13–15].

Modeling of dynamical nanosystems

Section 6.1: Stretch-healable molecular nanofibers. Ultrastretchable nanofibers analogous to spider silk proteins were designed from covalently-linked molecular flakes. MD simulations were performed to study their stretching and healing under different forces applied (performed by Yanxiao Han). The interactions between flakes were examined by both quantum calculations and MD simulations, which were conducted by Michal Langer [16].

Section 6.2: Cargo-carrying peptide sliders on polymer tracks. In collaboration with Prof. Wilhelm Huck (Radboud University, Netherlands), the transport of oligoanionic molecular sliders on polycationic tracks were studied. MD simulations captured the jumping and hopping modes of sliders along polymer tracks in atomistic details. The mechanisms for the enhanced reaction rates in the presence of tracks were explained by dramatically increased rates of reactants meeting on 1D polymers as compared to bulk solutions. [17].

Section 6.3: Intermolecular interactions stabilize ligand ratios on nanoparticles. In collaboration with Prof. Rafal Klajn (Weizmann Institute of Science), we studied how intermolecular interactions control the ligands ratio on NPs and the self-assembly of NPs. The ratio of the two thiol related ligands on the NP surfaces reached saturation by increasing their concentration in the solution. The mechanisms for reaching the stabilized ratio and the self-assembly of NPs were explained in MD simulations [18].

Section 6.4: Supramolecular control of azobenzene switching on nanoparticles. In collaboration with Prof. Rafal Klajn (Weizmann Institute of Science), models of NPs with different background ligands and azobenzene ligands were built and simulated to check their interactions.

The length and type of functional groups both influenced the kinetics of azobenzene switching on NP surfaces [19].

CHAPTER 2

METHODS

In this chapter, the *ab initio* electronic structure calculations and MD simulations are introduced. The *ab initio* calculations are used to develop and optimize the forcefield parameters for MD simulations and to interpret detailed intermolecular interactions between coronene/perfluorocoronene molecules.

2.1 Theory of *ab initio* calculations

Ab initio means "from first principles" or "from the beginning", which implies that the only inputs into the calculations are fundamental physical constants. *Ab initio* quantum chemistry methods attempt to solve the electronic Schrödinger equation based on the positions of the nuclei and the number of electrons. Solving Schrödinger equation yields electronic densities, energies and other properties of the systems. The time-dependent Schrödinger equation is

$$i\hbar \frac{\partial \psi(\vec{R}, \vec{r}, t)}{\partial t} = \hat{H} \psi(\vec{R}, \vec{r}, t), \quad (2.1)$$

where \hbar is the reduced Planck constant, \hat{H} is the Hamiltonian of the system. The nuclear and electronic coordinates are \vec{R} and \vec{r} , respectively. If the potential energy is time independent, then solutions of Equation 2.1 can be separated, i.e., written as a product of two functions (time and space coordinates). Then, the time-independent Schrödinger equation is,

$$\hat{H} \psi_n(\vec{R}, \vec{r}) = E_n \psi_n(\vec{R}, \vec{r}), \quad (2.2)$$

where $\psi_n(\vec{R}, \vec{r})$ is a set of eigenfunctions of Equation 2.2 with the eigenenergies E_n [47].

The Born-Oppenheimer (BO) approximation

The BO approximation assumes that nuclear and electronic motions in a molecule can be treated separately (frozen nuclei), due to the fact that the nuclei are much heavier and move much slower than the electrons. Then, the total molecular wave function solving the time independent Equation 2.2 can be written as a product of nuclear and electronic wave functions,

$$\psi(\vec{R}, \vec{r}) = \psi_N(\vec{R})\psi_{el}(\vec{r}, \vec{R}). \quad (2.3)$$

In the BO approximation with frozen nuclei, the electronic Hamiltonian can be written as,

$$\hat{H} = \hat{H}_{el} + V_{NN}. \quad (2.4)$$

The Schrödinger equation of electrons in the potential of frozen nuclei can be written as,

$$(\hat{H}_{el} + V_{NN})\psi_{el}(\vec{r}, \vec{R}) = U_s(\vec{R})\psi_{el,s}(\vec{r}, \vec{R}), \quad (2.5)$$

where $U_s(\vec{R}) = E_{el,s}(\vec{R}) + V_{NN}(\vec{R})$ is the s -th electronic potential energy surface (PES). After solving the electronic Schrödinger equation (Equation 2.5), the nuclear Schrödinger equation can be solved,

$$\begin{aligned} \hat{H}_N(\vec{R})\psi_N(\vec{R}) &= E\psi_N(\vec{R}), \\ \hat{H}_N(\vec{R}) &= \sum_{n=1}^M \hat{T}_n + U_s(\vec{R}), \end{aligned} \quad (2.6)$$

where $\hat{H}_N(\vec{R})$ is the Hamiltonian for nuclei, \hat{T}_n is a kinetic energy operator of a nucleus, $U_s(\vec{R})$ is the s -th electronic PES, calculated by solving Equation 2.5 and E is the total energy of the molecule.

To calculate the ground state wave function ($\psi_{el,s=0}(\vec{r}, \vec{R})$) and its energy ($E_{el,s=0}$), Equation 2.5 needs to be solved. The exact solution of Equation 2.5 can be expressed as a linear combination of Slater determinants (SDs), forming a complete basis set of the l -electron problem,

$$\psi_{exact}(\vec{r}, \vec{R}) = \sum_{s1,s2,\dots,sl} c_{s1,s2,\dots,sl} \begin{vmatrix} \phi_{s1}(\vec{r}1, \vec{R}) & \phi_{s2}(\vec{r}1, \vec{R}) & \dots & \phi_{sl}(\vec{r}1, \vec{R}) \\ \phi_{s1}(\vec{r}2, \vec{R}) & \phi_{s2}(\vec{r}2, \vec{R}) & \dots & \phi_{sl}(\vec{r}2, \vec{R}) \\ \dots & \dots & \dots & \dots \\ \phi_{s1}(\vec{r}l, \vec{R}) & \phi_{s2}(\vec{r}l, \vec{R}) & \dots & \phi_{sl}(\vec{r}l, \vec{R}) \end{vmatrix}, \quad (2.7)$$

where each $\phi_{si}(ri)$ is taken from a complete basis set of one-electron spin orbitals [48]. However, it is impossible to solve the exact multi-electron wave function due to an infinite number of basis set functions in the complete basis set of a l -electron problem. Some approximations are needed [47].

The wave function-based methods

The HF method

In the HF approximation, the wave function of a multi-electron system can be approximated by a single Slater determinant (SD). The HF method assumes that each electron separately interacts with an averaged potential generated by the nuclei and the other electrons (mean-field approach). This fictive electron separation into non-interacting electrons (single SD) omits the correlations of electrons. The electron indistinguishability (Pauli principle) prevents two identical electrons in the same quantum states from being at the same place. At the same time, electrons can not be very

close to each other due to their Coulomb repulsion. This brings additional correlations between the electrons.

The wave function chosen to represent each electron in a molecule (molecular orbital) is often based on the hydrogen atom solutions (atomic orbitals). Although, the HF method involves optimization of a single SD, it is limited because it neglects the electron correlations. Among the many wave function-based approaches which include electronic correlations, three of them are often used [49]: (1) the second-order Møller–Plesset perturbation theory (MP2); (2) coupled-cluster methods (construct multi-electron wave functions by using the exponential cluster operator); (3) multi-reference perturbation methods, such as CASPT2 (complete active space with second-order perturbation theory). Different approaches have different computational scaling. In our projects, the HF and MP2 methods were used for electronic structure calculations.

The N-electron wave function in the HF method can be expressed by SD with correct symmetry properties,

$$\psi_{HF}(\vec{r}_1, \vec{r}_2, \dots, \vec{r}_N) = \frac{1}{\sqrt{N!}} \begin{vmatrix} \phi_1(\vec{r}_1) & \phi_2(\vec{r}_1) & \dots & \phi_N(\vec{r}_1) \\ \phi_1(\vec{r}_2) & \phi_2(\vec{r}_2) & \dots & \phi_N(\vec{r}_2) \\ \dots & \dots & \dots & \dots \\ \phi_1(\vec{r}_N) & \phi_2(\vec{r}_N) & \dots & \phi_N(\vec{r}_N) \end{vmatrix}. \quad (2.8)$$

In this way, a set of i equations can be solved for a set of one-electron wave functions,

$$\left[-\sum_i \frac{\nabla_i^2}{2m} - \sum_{A,i} \frac{Z_A}{r_{Ai}} + \nu_{HF}(i) \right] \phi_i(\vec{r}_i) = \epsilon_{ij} \phi_i(\vec{r}_i), \quad (2.9)$$

where $\nu_{HF}(i) = \sum_j [2\hat{J}_j - \hat{K}_j]$, \hat{J} is the Coulomb operator, \hat{K} is the exchange operator, $\phi_i(\vec{r}_i)$ is one of the functions in the SD of Equation 2.8, and the sum is over all the other j electrons.

The expressions for \hat{J} and \hat{K} are:

$$\hat{J}_j = \int \phi_j(\vec{r}_j)^* \frac{1}{r_{i,j}} \phi_j(\vec{r}_j) dr, \quad (2.10)$$

$$\hat{K}_j \phi_i(\vec{r}_i) = \left[\int \phi_j(\vec{r}_j)^* \frac{1}{r_{i,j}} \phi_i(\vec{r}_i) dr \right] \phi_j(\vec{r}_j). \quad (2.11)$$

The first two terms in Equation 2.9 are often considered as the core terms as they are the kinetic and potential energies for an isolated system such as the hydrogen atom. Therefore they are referred to as \hat{H}^{CORE} . Putting this all together we obtain the HF equation

$$\left(\hat{H}^{CORE} + \sum_j \left[2\hat{J}_j - \hat{K}_j \right] \right) \phi_i(\vec{r}_i) = \sum_j \epsilon_{ij} \phi_i(\vec{r}_i)$$

or simply

$$\hat{f}_i \phi_i(\vec{r}_i) = \epsilon_i \phi_i(\vec{r}_i), \quad (2.12)$$

where \hat{f}_i is a set of Fock operators.

These one-electron wave functions ϕ_i in Equation 2.8 and Equation 2.12 are delocalized over the whole molecule (molecular orbital theory), where the atomic orbitals centered at each atom can be used as the basis for delocalized molecular orbitals. To optimize these atomic orbitals, a linear combination of atomic orbitals (LCAO) $\phi_i(\vec{r}_i) = \sum_\mu c_\mu \alpha_\mu(\vec{r}_i)$ is often used, where the constants c_μ are optimized to minimize the energy in Equation 2.12 (variational method). The wave functions can be improved systematically by a self-consistent-field (SCF) method that is based on variational method [48].

Slater-type orbitals

The Slater-type orbitals (STO) can be written as $\phi^{SLA}(\mathbf{r}) = (\zeta^3/\pi)^{1/2} e^{-\zeta r}$. STOs are the exact solutions for the hydrogen atom. However using them in the calculations of the integrals in Equation 2.10 and Equation 2.11 is expensive as there is no analytical solution for the Coulombic integrals. One possible way is to approximate the STOs using a sum of contracted Gaussian functions (CGF). There are simple analytical expressions for the integrals between two CGFs, so this can save a lot of computing time. For example, three CGFs can be used to approximate STO of a 1s orbital. $\phi_{STO-3G}^{CGF}(\vec{r}) = \sum_n^3 d_n \phi_n^{GF}(\alpha)$, where $\phi^{GF}(\alpha) = (2\alpha/\pi)^{3/4} \exp(-\alpha r^2)$. As the number of CGFs is increasing, the function will describe STOs better.

The MP2 theory

The Møller-Plesset perturbation theory is widely used for relatively precise evaluation of the correlation energies (caused by electron interactions). In general, the second order Møller-Plesset perturbation theory (MP2) is considered as one of the most useful and simplest levels of theory in the post-HF methods, which can be introduced as follows. The HF wave function ψ_0 and energy E_0 (from Equation 2.8 and Equation 2.12) are approximate solutions to the exact Hamiltonian eigenvalue problem or Schrödinger's electronic wave equation, Equation 2.5. However, the HF wave function and energy are exact solutions of the HF Hamiltonian and eigenvalue problem (Equation 2.12). If we assume that the Hartree-Fock wave function ψ_0 and energy E_0 lie near the exact wave function ψ and energy E (from Equation 2.5), we can use a perturbation theory to improve it. We can write the exact Hamiltonian operator for Equation 2.5 as $H = H_0 + \lambda V$, where H_0 is the sum of one-electron Fock operators, V is the small perturbation including the correction functions and λ is a dimensionless parameter. Expanding the exact wave function and energy in terms of the HF wave functions and energies yields $E = E^{(0)} + \lambda E^{(1)} + \lambda^2 E^{(2)} + \lambda^3 E^{(3)} + \dots$, and $\psi = \psi_0 + \lambda \psi^{(1)} + \lambda^2 \psi^{(2)} + \lambda^3 \psi^{(3)} + \dots$.

Substituting these expansions into Equation 2.5 and collecting terms according to powers of λ , we can get the expression for the nth-order(MPn) energy as follows:

$$E^{(0)} = \langle \psi_0 | H_0 | \psi_0 \rangle, \quad (2.13)$$

$$E^{(1)} = \langle \psi_0 | V | \psi_0 \rangle, \quad (2.14)$$

$$E_0^{(2)} = \sum_{s \neq 0} \frac{|\langle \psi_s^{(0)} | \hat{V} | \psi_0 \rangle|^2}{E_0^{(0)} - E_s^{(0)}}, \quad (2.15)$$

where $\psi_s^{(0)}$ can be singly, doubly or higher order excited states. Only the doubly excited $\psi_s^{(0)}$ can have non-zero integration in $\langle \psi_s^{(0)} | \hat{V} | \psi_0 \rangle$ [47]. Thus, the Hartree-Fock energy is simply the sum of the zeroth and first order energies: $E_0 = E^{(0)} + E^{(1)}$; the correlation energy can then be written as $E_{corr} = E_0^{(2)} + E_0^{(3)} + E_0^{(4)} + \dots$. The MP2 energy correction term is $E_0^{(2)}$ [47].

The Density Functional Theory (DFT)

DFT follows the Hohenberg–Kohn theorem, which expresses the total energy of the system as a functional of a single-electron density (one-electron reduced density operator) [50]. The single-electron density depends only on three coordinates (compared to the 3N coordinates of N electrons), which can reduce the computational effort required to solve the equations. "However, the correct functional of the energy is unknown and has to be constructed by heuristic approximations" [51]. Two principal classes of functionals, including gradient-corrected [52] and hybrid functionals [53], have been extensively deployed and tested in both large-scale applications and small molecule benchmarks. "Gradient-corrected functionals begin with the local-density approximation but add terms involving the gradient of the electron density. Hybrid functionals also incorporate gradient corrections but

add an empirically fitted admixture of the exact HF exchange” [51]. For all these reasons, good wave-function-based methods are usually more precise.

The Symmetry-adapted Perturbation theory (SAPT)

For the π -conjugated systems in the designed stretch-healable molecular nanofibers, our collaborators performed SAPT calculations to capture the precise dispersion interaction energies. SAPT can be used to directly calculate the interaction energy between two molecules by partitioning the Hamiltonian of a dimer (A and B) into contributions from each monomer and their interaction, $H = F_A + W_A + F_B + W_B + V$. Here, $F_{A,B}$, are the monomer Fock operators, $W_{A,B}$ are the fluctuation potentials (intramolecular correlation operators) of each monomer and V is the interaction potential. The monomer Fock operators, $F_A + F_B$, are treated as the zeroth-order Hamiltonian. The interaction energy, which is the higher order energy correction terms arising from the perturbation terms V and W , was truncated at the SAPT2+ level, which define the interaction energy as:

$$\begin{aligned}
 E_{SAPT2+} &= E_{SAPT2} + E_{disp}^{(21)} + E_{disp}^{(22)}, \\
 E_{SAPT2} &= E_{SAPT0} + E_{elst,resp}^{(12)} + E_{exch}^{(11)} + E_{exch}^{(12)} + E_{ind}^{(22)} + E_{exch-ind}^{(22)}, \\
 E_{SAPT0} &= E_{elst}^{(10)} + E_{exch}^{(10)} + E_{ind,resp}^{(20)} + E_{exch-ind,resp}^{(20)} + E_{disp}^{(20)} + E_{exch-disp}^{(20)} + \delta_{HF}^{(2)}.
 \end{aligned} \tag{2.16}$$

In this notation, E^{vw} defines the order in V and in $W_A + W_B$; the subscript, *resp*, indicates that orbital relaxation effects are included. E_{elst} is electrostatics energy, which simply represents the electrostatic (Coulombic) interaction of the charged monomers’ distributions, while the induction energy, E_{ind} , includes the mutual polarization of the monomers by the static electric fields of unperturbed partners. E_{exch} is the exchange energy resulting from tunneling of electrons between interacting systems, and E_{disp} is the dispersion energy which include dynamic multipole polarization of monomers. $E_{exch-ind}$

and $E_{exch-disp}$ are exchange energies arising from the anti-symmetrization of the induction and dispersion functions. The δ_{HF}^2 terms take into account higher-order induction effects [54–56].

2.2 Molecular Dynamics (MD) simulations

Classical MD methods are widely used in simulating relatively large systems without reactions (unless reactive forcefields are used), where forces are calculated from classical forcefields and the motions of atoms are solved by the classical Newton or Langevin equations of motion. Classical MD methods can describe the fluctuations and conformational changes of the simulated systems. We used them to investigate material systems (nanoparticles, polymers, and micelles) and biological systems (proteins and nucleic acids). Biological systems exhibit some specific processes which need a wide range of time scales to sample. Local motions, including atomic fluctuations, sidechain motions and loop motions, need a time scale of 10^{-15} to 10^{-1} s. Rigid body motions (helix motions, domain motions and subunit motions), need a time scale of 10^{-9} to 1s. The large-scale motions, which includes helix coil transitions, dissociation/association, folding and unfolding, need 10^{-7} to 10^4 s to evaluate [57].

Equations of motion and algorithms

The MD simulation methods are based on Newton’s (or Langevin) equations of motion,

$$m_{\alpha}\ddot{\vec{r}}_{\alpha} = -\frac{\partial}{\partial\vec{r}_{\alpha}}U_{total}(\vec{r}_1, \vec{r}_2, ..., \vec{r}_N), \alpha = 1, 2...N, \quad (2.17)$$

where m_{α} is the mass of the α th atom, \vec{r}_{α} is the position, and U_{total} is the total potential energy, which is obtained from forcefields. Due to the complexity of the potential energy in Equation 2.17, the equations of motion can only be solved numerically. Different numerical algorithms have been developed and used for integrating the equations of motion. A good algorithm should keep the

energies and momenta of the systems conserved, be computationally efficient and permit a relatively long-time steps for integration (typically 1-2 fs) [58].

Typically, thermodynamical systems in equilibrium can be described by a microcanonical (NVE), canonical (NVT) or isothermal–isobaric (NPT) ensemble. The NVE ensemble can describe a closed system with a specified total energy (E), volume (V) and number of particles (N). The NVT ensemble can describe systems which can exchange energy with a heat bath, but otherwise have a fixed number of particles and volume. The NPT ensemble maintains constant number of particles, temperature (T), and pressure (P). Different ensembles require different algorithms. In each of these ensembles, we work with microstates of the actual macroscopic systems and their distributions associated with the chosen ensembles. Typically, microstates of the same energies are equally likely present in the ensembles, but microstates of different energies have Boltzmann weight factors of $e^{(-E/k_{\beta}T)}$.

In NVE ensembles, a Velocity-Verlet method is often used to solve the Newtonian equations in NAMD [59].

$$\begin{aligned}
 \nu_{n+1/2} &= \nu_n + M^{-1}F_n\Delta t/2, \\
 r_{n+1} &= r_n + \nu_{n+1/2}\Delta t, \\
 F_{n+1} &= F(r_{n+1}), \\
 \nu_{n+1} &= \nu_{n+1/2} + M^{-1}F_{n+1}\Delta t/2,
 \end{aligned}
 \tag{2.18}$$

where M is the mass, F is the force, ν is the velocity and r is the position. The Velocity-Verlet method can obtain the position and velocity of the current step from the previous step based on the computed forces from the potentials. Only one force evaluation is needed for each time step. However, a temperature-related problem arises with the NVE ensemble due to the small number of atoms simulated. The temperature of the system is not well controlled, especially when the target molecules bind to others or experience exothermic conformational change [57].

In NVT ensembles, the systems should be coupled to a reservoir to maintain a constant temperature and to generate correct ensemble distributions. The Langevin equations combined with a Nosé-Hoover thermostat are used to generate the Boltzmann distribution. The generic Langevin equation is:

$$M\dot{\vec{v}} = F(\vec{r}) - \gamma\vec{v} - \sqrt{\frac{2\gamma k_{\beta}T}{M}}R(t). \quad (2.19)$$

In this equation, M is the mass of an atom, v is the velocity, F is the force, r is the position, γ is the friction coefficient, k_{β} is the Boltzmann constant, T is the temperature, and $R(t)$ is a Gaussian random process. Coupling to the reservoir is modeled by adding fluctuating ($\sqrt{\frac{2\gamma k_{\beta}T}{M}}R(t)$) and dissipative ($\gamma\vec{v}$) forces to the Newtonian equations in Equation 2.17. To integrate the Langevin equation, the Brünger-Brooks-Karplus (BBK) method is used in NAMD, which is a natural extension of the Verlet method (Equation 2.18). The BBK equation, which shows the position recurrence relation can be stated as:

$$x_{n+1} = x_n + \frac{1 - \gamma\Delta t/2}{1 + \gamma\Delta t/2}(x_n - x_{n-1}) + \frac{1}{1 + \gamma\Delta t/2}\Delta t^2 \left[M^{-1}F(x_n) + \sqrt{\frac{2\gamma k_{\beta}T}{\Delta M}}Z^n \right], \quad (2.20)$$

where z^n is a series of Gaussian random variables.

In NPT ensembles, NAMD uses the modified Nosé-Hoover thermostat, where Langevin dynamics is used to control fluctuations in the barostat [57]. The Langevin piston Nosé-Hoover method was described by Martyna and co-workers [60,61]. The equations of motion are as follows:

$$\begin{aligned}
r' &= p/m + e'r, \\
p' &= F - e'p - \gamma p + R, \\
V' &= 3Ve', \\
e'' &= \frac{3V}{W(P - P_0)} - \gamma_e e' + \frac{R_e}{W}, \\
W &= 3N\tau^2 k_\beta T, \\
\langle R^2 \rangle &= \frac{2m\gamma kT}{h}, \\
\langle R_e^2 \rangle &= \frac{2W\gamma_e kT}{h},
\end{aligned} \tag{2.21}$$

where W is the mass of piston, R is the noise on atoms, τ is the oscillation period while R_e is the noise on the piston.

The forcefield evaluation

The potential energy functions used in the equations of motion are the forcefield components. The form of potential energy functions is as follows:

$$\begin{aligned}
V &= \sum_{bonds} k_b(b - b_0)^2 + \sum_{angles} k_\theta(\theta - \theta_0)^2 + \sum_{dihedrals} k_\phi[1 + \cos(n\phi - \delta)] \\
&+ \sum_{impropers} k_\omega(\omega - \omega_0)^2 + \sum_{Urey-Bradley} k_u(u - u_0)^2 \\
&+ \sum_{nonbonded} \epsilon \left[\left(\frac{R_{minij}}{r_{ij}} \right)^{12} - \left(\frac{R_{minij}}{r_{ij}} \right)^6 \right] + \frac{q_i q_j}{\epsilon r_{ij}}.
\end{aligned} \tag{2.22}$$

The first term is the bond energy, where k_b is the bond force constant and $b - b_0$ is the distance from equilibrium. The second term is the angle energy, k_θ and $\theta - \theta_0$ are the angle force constant and angle difference from equilibrium, respectively. The third term is the dihedral energy, where k_ϕ is the dihedral force constant, n is the multiplicity of the function, ϕ is the dihedral angle, and δ is the phase shift. The fourth term is the improper energy, which is out of plane bending, where k_ω is the force constant and $\omega - \omega_0$ is the out of plane angle. The fifth term is the Urey-Bradley component which is the cross-term accounting for angle bending using 1,3 nonbonded interactions, where k_u is the respective force constant and u is the distance between the 1,3 atoms in the harmonic potential. The last two terms are nonbonded interactions between pairs of atoms (i, j) . The nonbonded forces are calculated for atom pairs separated by at least three bonds. The van der Waals (vdW) energy is calculated by a standard 12-6 Lennard-Jones potential, while the electrostatic energy is described by the Coulombic potential. In the Lennard-Jones potential, ϵ is the depth of the potential well; R_{minij} should be the distance at which the potential reaches its minimum, but the number is taken from the location where inter-particle potential is zero [57].

In NAMD, vdW interactions are always truncated at the cutoff distance. A switching parameter can be used to truncate the vdW potential energy smoothly at the cutoff distance. The handling of electrostatics is slightly more complicated. There are three options: 1. calculate full electrostatics; 2. truncate the electrostatics at the cutoff distance and ignore the electrostatic interactions beyond a specified distance; 3. calculate the electrostatics every timestep within a distance and periodically calculate the other electrostatics beyond the distance [58]. To increase the efficiency and accuracy, Particle Mesh Ewald (PME) [62] method is used to calculate the long-range electrostatic interactions beyond the cutoff distance. The mesh-based Ewald sums are calculated in the reciprocal space of

periodic system by fast Fourier transforms. Periodic boundary conditions are needed for application of PME during simulations.

CHARMM forcefields have been used for systems having proteins, lipids and nucleic acids [63–70]. New forcefield parameters can be obtained by *ab initio* calculations. The parameters need to be further calibrated and validated by experimental data (heat of vaporization or free energy of solvation).

Fitting of atomic charges

In order to calculate the Coulombic energy in Equation 2.22, the atomic charges need to be calculated and validated. Electrostatic potential (ESP) fitting has proven to be very effective to determine atomic charges [71]. The fitting process is carried out by minimizing the difference between the electrostatic potentials of electrons in the molecules obtained by MP2/6-31g(d) and the potentials generated by point charges representing partly charged atoms forming multipoles. The goal is to solve the least-square minimization problem as

$$\min[\int (V(Q(\vec{r}_a), \vec{r}) - V_{QM}(\vec{r}))^2 d\vec{r}], \quad (2.23)$$

where $V(Q(\vec{r}_a))$ is the potential generated by the multipoles $Q(\vec{r}_a)$, and $V_{QM}(\vec{r})$ is the QM potential.

The object function for minimization is defined as

$$\int W(\vec{r})(V(Q(\vec{r}_a), \vec{r}) - V_{QM}(\vec{r}))^2 d\vec{r} + \lambda(q_{total} - \sum_{j=1}^N q_j) = 0, \quad (2.24)$$

where $W(\vec{r})$ is a weighting function, and q_j is the point charge on each atom.

To evaluate the quality of fitting, a random probe charge can be placed around a molecule to compare the electrostatic energies calculated with electron densities ($E_{ele,i}$) and with ESP charges $E_{ESP,i}$. The criterion is defined as

$$E_{RRMSD} = \sqrt{\frac{\sum_{i=1}^N \left(\frac{E_{ele,i} - E_{ESP,i}}{E_{ESP,i}} \right)^2}{N}}, \quad (2.25)$$

where N is the number of trials to place the probe charges. E_{RRMSD} , relative-root-mean-square-deviation, can measure the quality of the electrostatic interactions computed with ESP fitting [71].

Optimization of forcefield parameters

We used the forcefield toolkit (ffTK) embedded in VMD to parameterize new molecules [72, 73]. ffTK is a plugin protocol designed specifically to develop CHARMM-compatible parameters for small molecules which follows the established parameterization methods of CGenFF. First, we need to build the new molecule by Gaussian view, then we generate psf and pdb files. Notably, the formats of the psf and pdb files that we generate are not accessible by the ffTK plugin. We need to manually format the files according to the ffTK tutorial examples, or use the Molefacture plugin of VMD to construct the molecule. To yield a complete set of parameters, the steps of the parameterization workflow in ffTK need to be followed. 1. Find missing parameters; 2. Geometry optimization (QM); 3. Calculate water interaction energy (QM); 4. Charge optimization; 5. Hessian calculation (QM); 6. Bond and angle optimization; 7. Torsion scan (QM); 8. Dihedral optimization.

The missing parameters can be found automatically by the ffTK plugin (first step of parameterization workflow). The initial parameter values of the new molecule will be assigned based on analogous parameters of similar chemical species available in CGenFF. It is very important to obtain the best possible guess for each parameter, as this maximizes the possibility for adequate param-

ters. Using good initial guess will decreases the iteration times required. Once initial guesses are assigned to the new parameters, we need to test if optimization is required. This validation is based on performing the MM calculations and comparing the results with the QM data. In most cases, only a small number of torsion parameters, associated with only non-hydrogen atoms, need to be optimized [68].

QM calculations are needed in geometry optimization. Theory of QM calculations was introduced in the first part of Chapter 2. Here, only the procedures associated with fTK are described. Bond, angle, Urey-Bradley equilibrium terms, "dihedral phase and multiplicity are based on geometries optimized at the MP2/6-31g(d) (MP2/6-31+g(d) in the case of anions) level. This level of theory has been shown to yield satisfactory agreements with experimental geometries for complex systems such as nucleic acid bases and sugars, while being computationally accessible" [68].

Bond, angle, Urey-Bradley, and improper force constants in Equation 2.22 are based on "MP2/6-31g(d) vibrational spectra calculations. Emphasis is placed on reproduction of both the frequencies and the potential energy distribution (PED) [74]. As the lower frequency modes generally represent larger deviations in the molecule's geometry during MD simulations, it is important to reproduce those modes more accurately. Also, in order to facilitate conformational sampling during MD simulations, it is preferable to produce vibrational frequencies that are slightly lower than the target values, thereby making the molecule flexible" [68].

The dihedral force constants in Equation 2.22 can be optimized by using the MP2/6-31g(d) potential energy surfaces (PES). Usually, the force constants for torsions comprised of only non-hydrogen atoms are optimized. This level of theory has been shown to yield energy surfaces consistent with distributions of dihedrals in oligonucleotides [68, 75].

Optimization of the nonbonded parameters for CGenFF is typically limited to partial atomic charges, though in special cases LJ parameters need to be optimized as well. "Initial estimates for the partial atomic charges may be made by analogy. Optimization of the charges is based on the QM data for model compounds interacting with water molecules in different orientations. For all hydrogen bond donors or acceptors, a complex is built containing an idealized hydrogen bond interaction between the model compound in the MP2/6-31g(d) optimized geometry and a water molecule in the TIP3P geometry [76]" [68]. Electrostatic potential-based charge fitting method can be used for calculating charges [71]. "In the rare cases where the optimization of LJ parameters is necessary, we need to obtain experimental thermodynamic data (eg. pure solvent densities and heats of vaporization) as the target data. Obtaining sufficiently accurate dispersion interactions at QM level requires high levels of theory (ideally CCSD(T) or better) and large basis sets, which carry a substantial computational cost" [68].

During the optimization of bond and angle parameters, both the force constants and equilibrium values are simultaneously optimized to target the QM-optimized geometry. Each objective function evaluation requires a full MM energy minimization of the compound using the trial parameters. The objective function is [72]:

$$\Phi_{bond,angle} = \sum_{bonds,angles} \left(\frac{r^{QM} - r^{MM}}{r_{scale}} \right)^2 + w(E_{distort}^{QM} - E_{distort}^{MM})^2, \quad (2.26)$$

where r is the minimized value of each bond or angle, r_{scale} is 0.03 Å for bonds and 3° for angles, w is the relative weight for the energy component, and E_{scale} is implicitly taken to be 1 kcal/mol.

For the evaluation of dihedrals, the objective function is:

$$\Phi_{dihedral} = \sum_i w_i (E_i^{QM} - E_i^{MM} + c)^2, \quad (2.27)$$

where c is a normalization constant to make $\frac{\partial \Phi_{dihedral}}{\partial c} = 0$ ($c = \bar{E}^M M - \bar{E}^Q M$). W_i is a weight factor [77]. The sum is taken over those discrete conformations determined in the QM scans, with energies recomputed using MM methods. During optimization, only the force constants are varied continuously. The multiplicity n can only have value between 1 and 6, while phase shift δ can be 0 or 180° [72].

Vibrational frequency calculations

Vibrational frequency calculations are used to derive the forcefield parameters of the bonded terms in Equation 2.22. For a simple harmonic motion, the vibrational frequency can be written as: $\bar{\nu} = \frac{1}{2c\pi} \sqrt{\frac{k}{\mu}}$, where k is the force constant and μ is the reduced mass. For a molecule, the force constants are obtained by diagonalization of the mass-weighted Hessian matrix, which is the second derivatives of the energy with respect to geometry. The Hessian is very sensitive to geometry, and need to be evaluated at stationary points. The elements of Hessian are defined as: $H_{i,j} = \frac{\partial^2 E}{\partial x_i \partial x_j}$. Diagonalization of the matrix yields eigenvalues, which represents the quantity $\sqrt{k/\mu}$, where force constants k can be obtained.

External forces

In some cases, we need to add external forces to the systems. For example, a bulk vdW force is applied to NPs [18, 20], which is absent in the conventional forcefields. Usually, the shapes of the

NPs and their medium determine the form of bulk vdW force. Here, the force is derived from the Hamaker potential [78],

$$V_d = -\frac{C}{12} \left[\frac{R}{d(1 + \frac{d}{4R})} + \frac{1}{1 + \frac{d}{R} + \frac{d^2}{4R^2}} + 2 \ln \frac{d(1 + \frac{d}{4R})}{R(1 + \frac{d}{R} + \frac{d^2}{4R^2})} \right], \quad (2.28)$$

where C is the Hamaker constant (1.95 eV), R is the radius of NP, and d is the distance between the centers of NPs.

External forces can also be applied to ligands. To maintain the ligands on a spherical surface but still mobile, a conditional force can be applied. The following is a sample force script used in the project [19]:

```
foreach atom select atoms
set k 0.05
set r0 29
set r [veclength c(atom)]
set force [vecscale [expr - k * (r - r0)/r] c(atom)]
addforce atom force
```

where k is a force constant, $r0$ is the radius of the surface for ligands attachment, r is the distance between ligands and surface, and $force$ is the radial force applied to maintain the ligands around the surface without affecting the motions of ligands on the surface.

In most cases, it's not necessary to recalculate the force values at each time step. Depending on the situation, one may be able to recalculate every 1000 steps, saving a lot of computational effort and therefore increasing the speed of the simulation. By setting the "forcesRecalcFreq", we can change the recalculation interval.

2.3 The Ergodic hypothesis

MD simulations provide information about fluctuations and conformational changes of systems at the microscopic level defined by atomic positions and velocities. However, to compare simulation results with experimental observations, the microscopic information needs to be converted to macroscopic observables such as pressure, energy, heat capacities, etc. Statistical mechanics is needed to connect the results obtained for trajectories formed by individual microstates or averaged over ensembles. In statistical mechanics, ensemble averaging is matching experimental observables. An ensemble average is obtained by large number of replicas of systems in different microstates [79],

$$\langle A \rangle_{ensemble} = \int \int dp^N dr^N A(p^N, r^N) \rho(p^N, r^N), \quad (2.29)$$

where A is an observable, p and r are functions of the momenta and positions of the system, respectively. ρ is the probability density of the ensemble. However, it is extremely hard to calculate the integral in Equation 2.29 because of the numerous possible microstates of the system. Alternatively, one can calculate a time average of A :

$$\langle A \rangle_{time} = \lim_{\tau \rightarrow \infty} \frac{1}{\tau} \int_{t=0}^{\tau} A(p^N(t), r^N(t)) dt \approx \frac{1}{M} \sum_{t=1}^M A(p^N, r^N), \quad (2.30)$$

where t is the simulation time, M is the number of time steps in the simulation and A is the time-dependent value. Both the ensemble average and time average over a trajectory are used in our simulations.

The Ergodic hypothesis states that:

$$\langle A \rangle_{ensemble} = \langle A \rangle_{time} \quad (2.31)$$

The system will eventually sample through all the possible microstates with proper probability when simulation time is indefinite. The goal of a MD simulation is to sample through long simulation times to generate enough representative conformations with proper likelihood of appearance in the equilibrium.

2.4 Free energy calculations from MD simulations

To calculate the free energy of binding, we use the umbrella sampling (US) methods [80]. First, the reaction coordinate (ξ) needs to be defined, e.g. the center to center distance between two objects. Then, the reaction coordinate pathway needs to be partitioned into certain number of windows, where restrain potentials can be introduced in the form of harmonic restraints [81]. Each US window should be run for certain simulation time to make sure that the sampling sufficiently covers the configuration space at that biased conditions. After sorting the resulting trajectories into the specified windows, we use the weighted histogram analysis method (WHAM) [82, 83] to reconstruct the potential of mean force.

The weighted histogram analysis method

In the US method, the Hamiltonian $\hat{H}_0(x)$ which is the potentials in the forcefields is replaced by a modified potential $\hat{H}_{\{\lambda\}}$ including the restrain potentials $\hat{V}(x)$,

$$\hat{H}_{\{\lambda\}} = \hat{H}_0(x) + \sum_{i=1}^L \lambda_i \hat{V}_i(x) = \sum_{i=0}^L \lambda_i \hat{V}_i(x), \quad (2.32)$$

where $\lambda_0 = 1$, $\hat{V}_0(x)$ is identical to \hat{H}_0 , x denotes the coordinates of the atoms and $\{\lambda\}$ denotes a set of values of $\{\lambda\}_i$ ($i = 1, 2, \dots, L$). The restrain potentials are chosen to maintain the sampling distributions along a reaction coordinate. Separate simulations with different coupling parameters $\{\lambda\}$ are carried out to sample different windows of the reaction path.

If R simulations are carried out with the i th simulation having coupling parameter $\{\lambda\}_i$ in Equation 2.32. We can set the number of snapshots taken from the i th simulation (at i window) to be n_i . Then the probability histogram $P_{\{\lambda\},\beta}(\{V\},\xi)$ can be given by

$$P_{\{\lambda\},\beta}(\{V\},\xi) = \frac{\sum_{k=1}^R N_k(\{V\},\xi) \exp(-\beta \sum_{j=0}^L \lambda_i V_i)}{\sum_{m=1}^R n_m \exp(f_m - \beta \sum_{j=0}^L \lambda_j V_j)} \quad (2.33)$$

and

$$\exp(-f_j) = \sum_{\{V\},\xi} P_{\{\lambda\}_j,\beta}(\{V\},\xi) \quad (2.34)$$

where $N_i(\{V\},\xi)$ is the number of counts at $\{V\}$ and ξ during the i th simulation, $\beta = 1/k_B T$ and f_j is the free energy of the system described by Equation 2.32 with coupling parameters $\{\lambda\}_j$.

Equation 2.33 and Equation 2.34 are coupled which can only be solved self-consistently [83, 84]. Once the probability $P_{\{\lambda\},\beta}(\{V\},\xi)$ is calculated, the free energy can be estimated. The number of simulations (windows) on the reaction coordinate should be adequate to allow strong overlapping among the histograms (biased probability distributions) of the windows.

The MMGB-SA method

"For a quick estimation, the MMGB-SA (Molecular mechanics generalized Born - surface area) method [85, 86] can be also used to calculate the relative binding free energy. First the MD simulations should be performed for the system under investigation. Then, corresponding configurations should be extracted from the trajectories. The MMGB-SA free energies of the extracted configurations (from MD trajectories) of the systems are calculated as

$$G_{tot} = E_{MM} + G_{solv-p} + G_{solv-np} - T\Delta S_{conf} ,$$

where E_{MM} , G_{solv-p} , $G_{solv-np}$, and ΔS_{conf} are the sum of bonded and non-bonded energy terms, the polar contribution to the solvation energy, the nonpolar contribution, and the conformational entropy, respectively. The E_{MM} , G_{solv-p} and $G_{solv-np}$ terms can be calculated using the NAMD package [58] generalized Born implicit solvent model [87], with a dielectric constant of the solvent of 78.5. The $G_{solv-np}$ term for each system configuration can be calculated in NAMD as a linear function of the solvent-accessible surface area (SASA), determined using a probe radius of 1.4 Å, as $G_{solv-np} = \gamma SASA$, where $\gamma = 0.00542 \text{ kcal/mol}\text{\AA}^2$ is the surface tension. The ΔS_{conf} term is the entropic contribution [88,89]. The approximate binding free energies of the studied complexes were calculated as $\langle \Delta G_{MMGB-SA} \rangle = \langle G_{tot}(binder - target) - G_{tot}(target) - G_{tot}(binder) \rangle$, where the averaging is performed over configurations within the calculated trajectories” [2].

The adaptive evolution algorithm

”The Adaptive mutation/selection algorithm is developed and used to iteratively increase the affinity of binding between ligands and their targets. The algorithm involves sequences of steps combining MD simulations and Monte Carlo (MC) decisions using the Metropolis criterion [90,91], which results in MC sampling of the peptide sequence space. First, the interaction between ligands and their targets should be equilibrated for certain simulation time. Then, the MMGB-SA free energy of binding for the complex, $\Delta G_{MMGB-SA}^{before}$, is evaluated. Next, a random mutation is introduced at a random position in the ligand, followed by a short equilibration in MD simulations of the complex, and evaluation of the $\Delta G_{MMGB-SA}^{after}$ free energy of binding of the complex. Finally, the mutation is accepted if $\Delta G_{MMGB-SA}^{after} < \Delta G_{MMGB-SA}^{before}$ or if the Metropolis criterion is satisfied,

$$\exp[-(\Delta G_{MMGB-SA}^{after} - \Delta G_{MMGB-SA}^{before})/k_B T] > r,$$

where r is a random number in the $(0, 1)$ interval. If the mutation is accepted, then the new ligand becomes the new reference ligand and its $\Delta G_{MMGB-SA}$ becomes the reference value $\Delta G_{MMGB-SA}^{before}$ for the next attempted mutation. In each run of the algorithm, 100–200 mutations can be attempted on templates” [2].

CHAPTER 3

DESIGN OF INHIBITORS AND BOOSTERS FOR SARS-COV-2

(Previously published as Han, Y., Král, P. Computational Design of ACE2-Based Peptide Inhibitors of SARS-CoV-2. *ACS Nano* **14**, 5143 (2020); Chaturvedi, P., Han, Y., Král, P., Vukovic, L. Adaptive Evolution of Peptide Inhibitors for Mutating SARS-CoV-2. *Advanced Theory and Simulations* **3**, 2000156 (2020); Han, Y., McReynolds, K., Kral, P. Retrained Generic Antibodies Can Recognize SARS-CoV-2. *The Journal of Physical Chemistry Letters* **submitted**, (2020); Wells, L., Vierra, C., Hardman, J., Han, Y., Dimas, D., Gwarada, L., Blackeye, R., Eggers, D. K., LaBranche, C. C., Král, P., McReynolds, K. D. Sulfoglycodendrimer Therapeutics for HIV-1 and SARS-CoV-2. *Advanced Therapeutics* **submitted**, (2020).)

In this chapter, different ways for blocking SARS-CoV-2 are introduced. Using computational modeling methods, ACE2-based peptide inhibitors of SARS-CoV-2 were designed. The inhibitors were further optimized for binding better to the S protein and for treating different strains of SARS-CoV-2. To trigger the immune response to new viruses, double-faced boosters were also designed to allow recognition of SARS-CoV-2 by Hepatitis B antibodies. Those ideas were tested by MD simulations, where the binding modes and dynamics of inhibitors/boosters were analyzed. In collaboration with Prof. Katherine McReynolds (California State University, Sacramento), several glycodendrimer inhibitors, which have promising *in vitro* anti-HIV activity, were also simulated to examine their working mechanism. Two top glycodendrimers were further tested by MD simulations to check their binding to the receptor binding domain (RBD) of SARS-COV-2 S protein.

3.1 Design of ACE2-based peptide inhibitors of SARS-CoV-2

Adapted from Ref. [1, 2] (*ACS Nano* 2020, 6. DOI: doi.org/10.1021/acsnano.0c02857; *Adv. Theory and Simul.* 2020. DOI: doi.org/10.1002/adts.202000156) with the permissions from ACS and Wiley Publishing Groups.

Introduction

Severe acute respiratory syndrome coronavirus 2 (SARS-CoV-2), previously known by 2019 novel coronavirus (2019-nCoV) [92], is the cause of the ongoing pandemic of coronavirus disease 2019 (COVID-19) [93,94]. It is contagious in humans and has caused 18,589 deaths with 416,686 confirmed cases globally according to the World Health organization (WHO) on March 26.

The SARS-CoV-2 virion is approximately 50-200 nanometers in diameter with four structural proteins, known as the S (spike), E (envelope), M (membrane), and N (nucleocapsid) proteins. [93] The S protein which has been imaged at the atomic level using cryogenic electron microscopy (Cryo-EM) [95], is the protein responsible for the host attachment and fusion of the viral membrane with the host-cell membrane. [96,97] This process is triggered when the S1 subunit of S protein binds to a host-cell receptor. To engage a host-cell receptor, the receptor-binding domain (RBD) of S1 undergoes transient hinge-like conformational movements (receptor-accessible or receptor-inaccessible states) [98]. Angiotensin-converting enzyme 2 (ACE2) is found to be the cellular receptor for SARS-CoV-2 with a higher affinity than SARS-CoV [95]. The protease domain (PD) of ACE2 mainly engages the $\alpha 1$ helix in the recognition of the RBD with minor contribution from the $\alpha 2$ helix and the linker between $\beta 3$ and $\beta 4$ (bundle). [98,99]

The therapies that act on the coronavirus can be divided into several categories: (1) preventing the virus RNA syntheses and replication; (2) blocking virus from binding to human cell receptor; (3)

restore host's innate immunity; (4) blocking host's specific receptors or enzymes. [100] However, there are no confirmed effective treatments specifically for COVID-19 to date. Computational methods has been used to analyze the therapeutic targets for SARS- CoV-2 and discovery of potential drugs [101]. As for the virtual screening of potential drugs against S protein (corresponding to category 2), some small molecule compounds showed high binding affinity, unfortunately, most of the compounds were not predicted to bind with the binding interface of RBD-ACE2 complex. Hesperidin is the only compound which was predicted to lie on the surface of RBD, but it shows deficiency to cover the whole interface. [100] Instead of small molecules, designed proteins with specific binding domains to RBD could be a promising direction, given the fact that protein therapies show highly specificity, less interference with biological processes, good tolerance to human organisms, and relative faster FDA approval time [102].

In this work, we designed several inhibitors against SARS-CoV-2 which include the components from virus binding domains of ACE2 based on the recently released crystal structure (PDB code: 2AJF [99]). The designed inhibitors are structural stable and highly specific with relative lower molecular weight. The current study could generate testable hypotheses and provide potential guidance to the study of antigen recognition, structure-based antibody designs for higher affinity or desired modifications. A promising application may lie in the design of inhaled protein therapeutics [103] for topical lung delivery providing an efficient way to combat the virus in lung.

"SARS-CoV-2 is mutating and further adjusting to the human environment, like other novel viral pathogens. Many strains of SARS-CoV-2 have already been detected [104, 105]. Some mutations, such as D614G on the S protein, lead to rapid and enhanced viral transmission [106], causing this strain to locally dominate. The mutating SARS-CoV-2 coronavirus could also adapt to new hosts, such as domestic animals [107]. Therefore, to mitigate the large spreading and effects of SARS-CoV-

2, it is important to identify classes of therapeutics that could be rapidly developed to act against multiple coronavirus strains.

Here, we address this problem by introducing libraries of adaptive peptide therapeutics that could block different S protein strains from interacting with ACE2. With the use of advanced computational methods, we show that adaptive evolution of suitable peptide templates can provide multiple inhibitors for competitive binding to different S protein variants. Using libraries of peptides adapted to different S protein variants could prevent their mutational escape, analogous to using cocktails of S protein antibodies [108]. Our algorithm can evolve peptide inhibitors that competitively bind to (block) a set of desired targets, such as different S protein variants, S proteins with glycan shielded sites [109–111], and other related systems [112]” [2].

Simulation methods and design of algorithm

Simulations for designed peptides based on various templates

The inhibitors and RBD of the virus were simulated by NAMD [58] and the CHARMM36 protein forcefield [64]. The PME method was used for the evaluation of long-range Coulombic interactions [62]. The time step was set to 2 fs. The simulations were performed in the NPT ensemble ($p = 1$ bar and $T = 310$ K), using the Langevin dynamics with a damping constant of 1 ps^{-1} . After 2,000 steps of minimization, ions and water molecules were equilibrated for 2 ns around proteins, which were restrained using harmonic forces with a spring constant of $2 \text{ kcal}/(\text{mol } \text{\AA}^2)$. The last frames of restrained equilibration were used to start simulations of free inhibitors and partially constrained PD of ACE2 (two residues on the bottom). The simulations last for 120 - 300 ns due to different atom numbers in different systems and different computer power used.

Calculation of RMSD: The time-dependent RMSD for the critical amino acids and the whole inhibitors were calculated from

$$RMSD_{\alpha}(t_j) = \sqrt{\frac{\sum_{\alpha=1}^{N_{\alpha}} (\vec{r}_{\alpha}(t_j) - \vec{r}_{\alpha}(t_0))^2}{N_{\alpha}}}, \quad (3.1)$$

where N_{α} is the number of atoms whose positions are being compared, $\vec{r}_{\alpha}(t_j)$ is the position of atom α at time t_j and $\vec{r}_{\alpha}(t_0)$ is the initial coordinate. The selection of coordinates contains all the atoms in the inhibitors or critical amino acids, excluding hydrogens.

The time-dependent RMSD was averaged over the last 50 ns of simulation time, which corresponds to the last 50 frames of each trajectory as shown in Figure 2f. The standard deviations were shown by the error bars.

Calculation of Binding Energy: The interacting residues from inhibitors and RBD of SARS-CoV-2 were first selected with a 3 Å cutoff distance. The electrostatic and vdW energy contributions between the interacting residues are calculated by the NAMD energy plugin. The electrostatic contribution and Lennard-Jones (LJ) 6 – 12 potential are given by the corresponding terms in Equation 2.22. The dielectric constant of the solvent is set to 1. To increase the efficiency of the simulations, pairwise interaction calculations are not performed beyond a cut-off distance. Long range electrostatic interactions are calculated by the PME method [62].

The time evolution of the interaction energy is shown in [1] and the time averaged interaction energy over the last 50 ns (50 frame) is shown in Figure 2g with standard deviation shown by error bar.

Methods for adaptively evolved peptide inhibitors

The simulated peptide template-1 (amino acids 21 – 43 of ACE2) and template-2 (amino acids 19 – 83 of ACE2) were separately bound to the S protein RBD. All structures were directly based on the crystal structure of the human ACE2 protein bound to the SARS-CoV-2 S protein RBD (pdbID: 6LZG) [113]. The mutations in peptides and RBD were introduced using the *psfgen* plugin in VMD [73].

The systems were simulated using NAMD2.13 [58] and the CHARMM36 protein forcefield [63]. The simulations were conducted with the Langevin dynamics ($\gamma_{Lang} = 1 \text{ ps}^{-1}$) in the NPT ensemble, at temperature of $T = 310 \text{ K}$ and pressure of $p = 1 \text{ bar}$. The PME method was used to evaluate Coulomb coupling, with periodic boundary conditions applied [114]. The time step was set to 2 fs. The long range Coulombic coupling were evaluated every 2 time steps. After 2,000 steps of minimization, the solvent molecules were equilibrated for 1 ns, while the complexes were restrained using harmonic forces with a spring constant of $1 \text{ kcal}/(\text{mol } \text{\AA}^2)$. Next, the systems were equilibrated in 100 ns production MD runs with no restraints.

The free energies were estimated from separate MMGB-SA calculations (Chapter 2) for three systems (peptide/ACE2, RBD, and the whole complex) in configurations extracted from the MD trajectories of the whole complex in the explicit solvent.

Adaptive evolution algorithm: A mutation/selection algorithm was developed and used to iteratively increase the affinity of binding between peptide templates and the S protein RBD. The algorithm involves sequences of steps combining MD simulations and MC decisions using the Metropolis criterion [90,91], which results in MC sampling of the peptide sequence space. Initially, the selected peptide template (directly extracted from ACE2) complexed with RBD is equilibrated for 100 ns. Then, the free energy of binding of the peptide:RBD complex, $\Delta G_{MMGB-SA}^{before}$, is evaluated. Next, a random mutation is introduced at a random position in the peptide, followed by a short 1 – 10 ns

equilibration in MD simulations of the complex, and evaluation of the $\Delta G_{MMGB-SA}^{after}$ free energy of binding of the complex. Finally, the mutation is accepted if $\Delta G_{MMGB-SA}^{after} < \Delta G_{MMGB-SA}^{before}$ or if the Metropolis criterion is satisfied,

$$\exp[-(\Delta G_{MMGB-SA}^{after} - \Delta G_{MMGB-SA}^{before})/k_B T] > r,$$

where r is a random number in the $(0, 1)$ interval. If the mutation is accepted, then the new peptide becomes the new reference peptide and its $\Delta G_{MMGB-SA}$ becomes the reference value $\Delta G_{MMGB-SA}^{before}$ for the next attempted mutation. In each run of the algorithm, 100 – 200 mutations were attempted on peptide templates, as stated in the results.

Preparation of inhibitors

In the structure of ACE2 and RBD of SARS-CoV-2 (PDB: 6m17 [99]), we first analyzed the interacting amino acids at the ACE2 and RBD interface. In total, 15 residues from ACE2 interact with the RBD: residues 24(Q), 27(T), 30(D), 31(K), 34(H), 35(E), 37(E), 38(D), 41(Y), and 42(Q) are in α_1 , one residue (residue 82 M) comes from α_2 , residues 353(K), 354(G), 355(D) and 357(R) come from the linker between β_3 and β_4 . Therefore, the 15 amino acids can be labeled as critical amino acids and α_1 , α_2 , β_3 and β_4 as critical binding components.

Since most of the interacting residues are from α_1 , we picked as **inhibitor 1** the α_1 helix alone. In particular, the 21 - 55 residues, shown in Figure 1a, were selected. Realizing that α_1 (alone) might not be even stable, we next picked as **inhibitor 2** both α_1 and α_2 helices (residues 21 to 88), and the residues 349 to 357 (residues between β_3 and β_4 shown in orange in Figure 1b). This selection included all the 15 interacting residues from the structure 6M17 [99]. Since the two α helices are closely joined on one side (Figure 1b), they stabilize each other. To connect the two helices (red)

with the β sheets with residues 349 to 357 (orange), as shown in Figure 1b, residues 45 (LEU) and 351 (LEU) were linked together by a side chain with a carbon-carbon bond, as shown in Figure 1b.

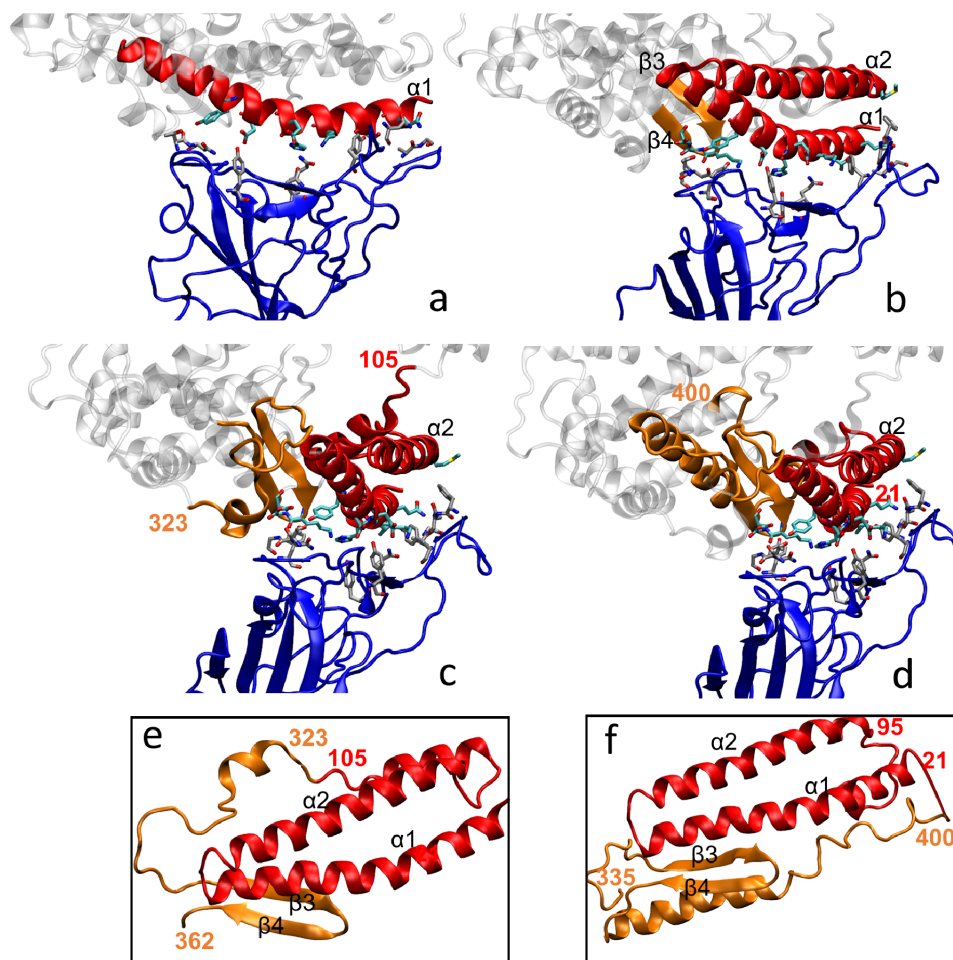


Figure 1: Structural components of the inhibitors designed: (a) **inhibitor 1** is composed of α_1 (residues 21 to 55), (b) **inhibitor 2** is composed of α_1 , α_2 , and a loose chain between β_3 and β_4 connected by a C-C bond between residues 45 and 351 (residues 21 to 88 and 349 to 357); (c) **inhibitor 3** is composed of α_1 , α_2 , and β_3 , β_4 (residues 21 to 105 and 323 to 362) (d) **inhibitor 4** has the same composition as **inhibitor 3** but a different linkage (residues 21 to 95 and 335 to 400); (e) details of **inhibitor 3** (c), reorganized with residue 323 connecting residue 105; (f) details of **inhibitor 3** (d), reorganized with residue 21 connecting residue 400. In (e-f), the conformation of the α helices and β sheets were maintained with the rest adapting to the connection. Coloring scheme: Red - α helices; orange - β sheets or other linker components; blue - RBD of SARS-CoV-2; grey - other parts of ACE2; licorice - the initial contacting residues in the RBD-ACE2 interface.

We also designed other inhibitors that are closer to the ACE2 protein, whose parts are connected by peptide bonds, and which contain all 15 residues that initially bind to RBD in the 6m17 structure

[99]. Figure 1c (detail Figure 1e) shows **inhibitor 3**, where residues 323 to 362 (orange) include the two β sheets and a random coil (residues 323 to 348), while residues 21 to 105 (red) include the two α helices with another random coil (residues 89 to 105). The two sequences are joined together by a peptide bond between residues 105 and 323, and the two pieces of random coils were moved close to each other. Finally, Figure 1d (detail Figure 1f) shows **inhibitor 4**, where two sequences including residues 21 to 95 (red) and residues 335 to 500 (orange) were selected. An extra peptide bonds was made between residue 21 and residue 400 by adjusting the position of the corresponding sequences.

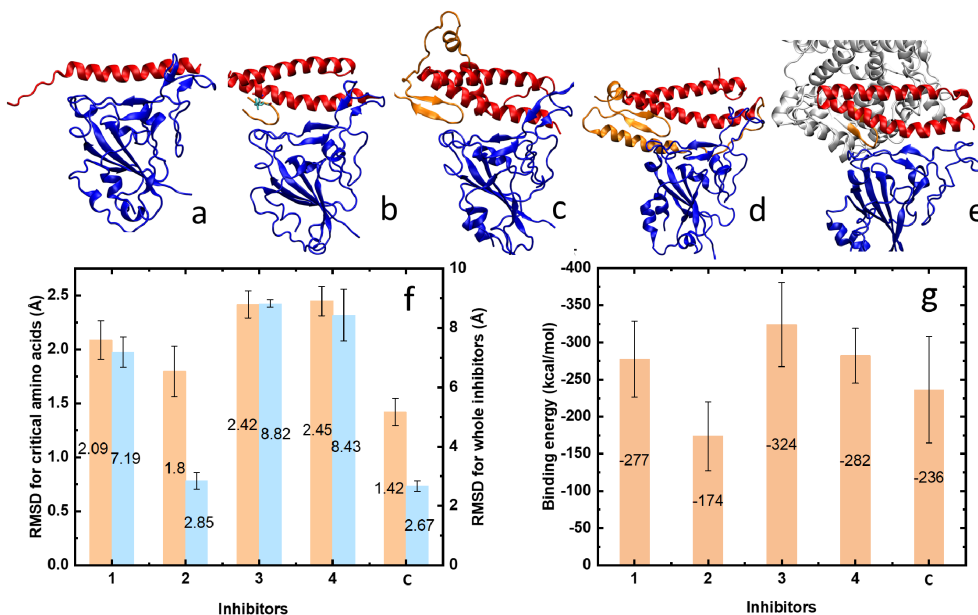


Figure 2: (a-e) Final conformations of **inhibitors 1, 2, 3, 4** and **control**. (f) Averaged RMSD for the critical amino acids (orange bar) in each inhibitor and for the whole inhibitors (blue bar) when binding with the RBD of SARS-CoV-2. Numbering scale: 1-4 - inhibitors 1-4 with the RBD; C - control system of PD from ACE2 and the RBD of SARS-CoV-2. (g) The average interaction energies between the contact residues of inhibitors 1-4 (or ACE2) and the RBD of SARS-CoV-2.

To examine how these potential inhibitors bind to RBD of SARS-CoV-2, we have prepared these systems in the initial position known from the structure(PDB:6M17), and simulated them in physiological solution (Methods), as shown in Figure 2a-d. As a control, the PD of ACE2 (residues 19 to 615) and RBD of SARS-CoV-2 were also simulated (Figure 2e).

Binding conformations: In Figure 2a, 200 ns long simulations showed that the helical structure of **inhibitor 1** deformed from the left side - loose end unfolding, although it still binds to the RBD of SARS-CoV-2. In Figure 2b-d, 120 – 300 ns long simulations revealed that **inhibitors 2-4** bind in a stable way to the RBD of SARS-CoV-2, without α_1 losing its structure. Due to different linkages among the critical binding components, the overall conformations of **inhibitors 2-4** vary. Specifically, the α_1 helix, which mostly contributes to the complementary sequence and conformational matching to the RBD, is maintained in **inhibitors 2-4** with different degrees of bending. The β sheets in **inhibitors 3-4** structures are also preserved. Overall, the critical binding components in **inhibitors 2-4** bind to the RBD in a very similar manner to the crystal structure. The simulated stable conformation of **inhibitors 2, 3, and 4** correspond to their energy minima of folding, which would drive the folding process towards the stable direction.

RMSD and interaction energies: To further quantify the binding of these inhibitors to RBD, we calculated RMSD (root mean square deviation) for the 15 critical amino acids in each inhibitor and for the whole inhibitors. Figure 2f shows the average RMSD at the end of our simulations. **Inhibitor 1** has a larger RMSD for the critical amino acids than the control and the largest fluctuations both for the critical amino acids and the overall RMSD. This can be attributed to the unfolding of α_1 , shown in Figure 2 a. The highly promising **inhibitor 2** has RMSD of the critical amino acids and the overall RMSD similar to those in the control (lowest). **Inhibitor 3** has higher RMSD of the critical amino acids and the overall RMSD than the control and **inhibitors 1-2**. However, **inhibitor 3** has a very smooth overall RMSD at later times. This may be due to a poor adaption of their added connections at early times. **Inhibitor 4** shows slightly bigger fluctuations for the overall RMSD but steady RMSD for the critical amino acids at later time, which indicates the fluctuations shown in the overall structure come from non-essential connection parts.

The interaction energies have van der Waals (vdW) and electrostatic components, calculated by the NAMD energy plugin. The total energies are shown in Figure 2 g. The residues which contribute to the interaction energies between inhibitors and SARS-CoV-2 are selected with a cutoff of 3 Å. The selections are updated in every frame. **Inhibitors 1, 4** show similar interaction energies as the control with **inhibitor 3** having slightly stronger binding than the control, while **inhibitor 2** show a slightly lower interaction energies than the control. The larger interaction energy in **inhibitor 1** might be due to non-specific interactions caused by the deformed helix. The lower interaction energy in **inhibitor 2** could be attributed to the total number of residues which is less than for **inhibitors 3-4**.

Adaptive evolution of peptide inhibitors

S proteins variants: Over the time and geographical regions, SARS-CoV-2 virus has so far evolved into more than 10^4 mutated strains, shown in the mutation tree of publicly available unique genome sequences (through June 2020) in Figure 3a [115]. Out of these mutations, so far (June 2020) 25 have been recognized in the S protein RBD, as summarized in Figure 3b. Five of these mutations include amino acids that form a part of the ACE2-binding surface (A475V, G476S, S477I, V483A, and V503F), as highlighted in Figure 3c.

In Figure 3d, we present the RBD-ACE2 host-receptor binding free energies, $\Delta G_{MMGB-SA}$, obtained in the presence of these 5 mutations. The 5 RBD:ACE2 complexes were simulated for 30 ns, and their average binding energies were obtained in the last 15 ns. The originally reported RBD and the S477I RBD have the strongest binding to the human ACE2, $\Delta G_{MMGB-SA} \approx -50$ kcal/mol, while the other systems bind with $\Delta G_{MMGB-SA} \approx -(40 - 50)$ kcal/mol. In order to block all of these RBD variants, the peptide inhibitors should have comparable or lower $\Delta G_{MMGB-SA}$ values.

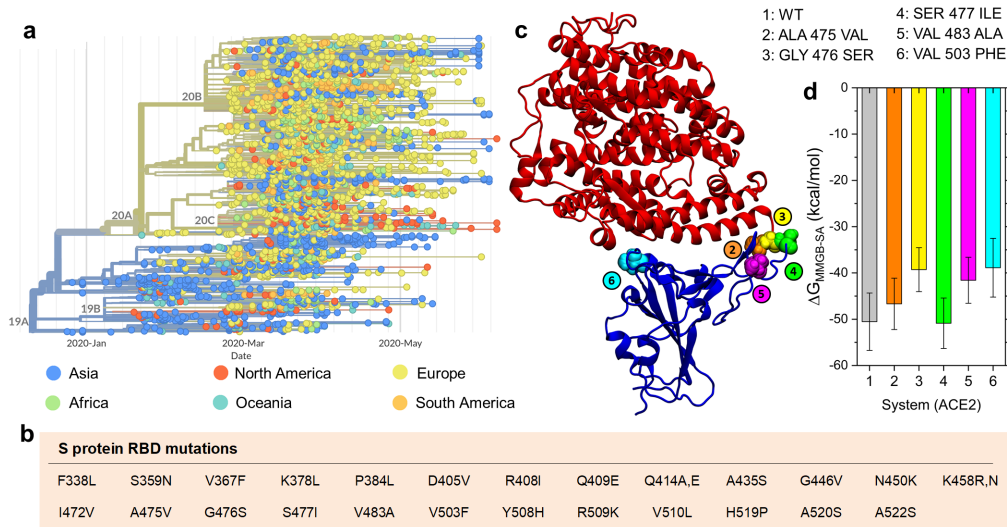


Figure 3: Mutations of SARS-CoV-2. a) Time-dependent mutation tree of SARS-CoV-2 colored according to geographical regions of origin (through June 2020) [115]. b) 25 single mutations identified in RBD of the S protein. c) 5 amino acid mutations on RBD in contact with the ACE2 receptor. d) Binding free energies are evaluated with the MMGB-SA method for the ACE2-RBD complexes, including the originally reported RBD (wild type, labeled as WT) and the five mutant RBDs listed in panel c.

Adaptation of peptides by single mutations: Figure 4a shows locations of five S protein mutations examined in the present work marked by blue spheres. Amino acid residues changed in singly mutated peptides are marked by yellow spheres. In Figure 4c, the sequence of the optimized peptide was obtained after 100 mutation attempts, with 10 ns long MD simulation after each mutation. The final peptide with the optimized sequence was further relaxed in a 175 ns MD simulation. The initial peptide is shown as a red helix, with amino acids that were subsequently mutated shown in thin faded yellow licorice. The optimized peptide is shown as an orange helix, with mutated amino acids shown in thick yellow licorice. In Figure 4d, the plot shows the binding free energies, $\Delta G_{MMGB-SA}$, between the peptide and the original RBD, presented as a function of the performed mutation, where the peptide:RBD complexes are relaxed for 10 ns after each mutation attempt. Figure 4e shows the time evolution of $\Delta G_{MMGB-SA}$ between the final optimized peptide and the original RBD. The av-

erage value, obtained from the last 75 ns of the trajectory (gray), is $\Delta G_{MMGB-SA} = -57$ kcal/mol. The faded green line shows the data points calculated every 0.1 ns, and the dark green line shows the running average. Figure 4f shows the initial and optimized sequences of template-1 peptides. The final peptides were optimized for binding to the original and mutant RBDs, with peptide-RBD complexes relaxed in 10 ns MD simulations after each attempted mutation. Two ACE2-based peptide structures, shown in Figure 4a, were selected as templates for the first generation peptide inhibitors of the S protein [1]. The smaller **template-1** includes single truncated α_1 helix of ACE2 (amino acids 21 – 43), and the larger **template-2** includes two $\alpha_1\alpha_2$ helices of ACE2 (amino acids 19 – 83). In the adaptive evolution search for optimized therapeutics, the selected ACE2-extracted peptide templates should be gradually mutated to increase their binding strength to RBD.

In recent mutagenesis experiments, the whole ACE2 with single mutations in regions directly contacting RBD were examined for their binding to the original S protein [116]. To perform preliminary testing of our adaptive evolution search of peptide therapeutics, we first selected the most fit mutants from these experiments, and implemented their mutations in our **templates-1,2**. We simulated 22 peptides, i.e., the original templates and their 10 single mutants, complexed with the original S protein RBD. Their free energies of binding, $\Delta G_{MMGB-SA}$, were evaluated in 100 ns simulations and presented in Figure 4b. **Template-1** binds to RBD with $\Delta G_{MMGB-SA} \approx -19$ kcal/mol, while its mutants have higher affinities giving $\Delta G_{MMGB-SA} \approx -(24 - 35)$ kcal/mol. In all cases, **template-1** significantly changes its conformation in the bound configuration, as the helix loses the curvature observed when within ACE2, and the hydrogen bonding between Glu35 (**template-1**) and Gln493 (RBD), enabled by the helix curvature, is broken.

In contrast, **template-2** has more direct contacts with RBD than the shorter **template-1** variants, so it binds to it more strongly, $\Delta G_{MMGB-SA} \approx -36$ kcal/mol. However, only two **template-**

2 mutants (H34A and K31W) have higher affinities to RBD than the original template-2, having $\Delta G_{MMGB-SA} \approx -45$ kcal/mol. These simulations also revealed that peptides with a stronger binding covered larger RBD sections, and reduced the RBD exposure to other potential binding partners. These results show that the experimental results obtained for mutated ACE2 [116] can provide a good guidance in the mutation of **template-1**, but the same mutations are less effective in the larger **template-2**.

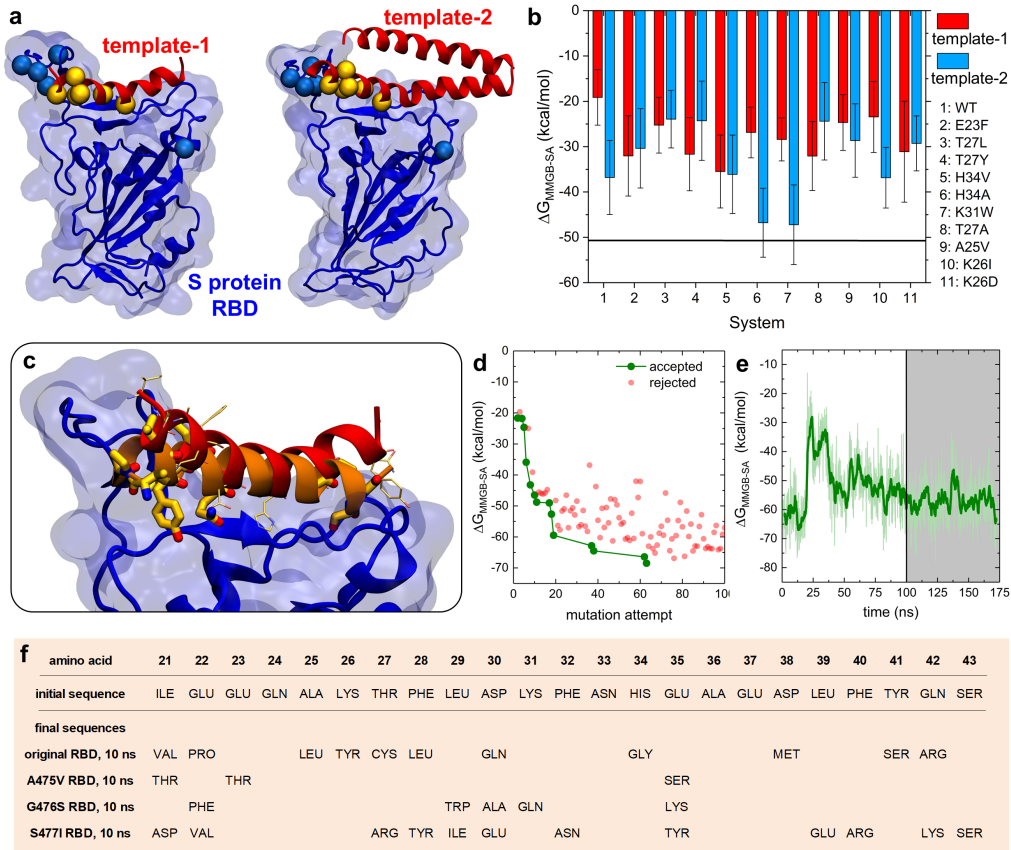


Figure 4: Modeling of peptide-RBD complexes. a) Complexes of S protein RBD (blue) and two peptide templates (red). b) Free energies of binding, $\Delta G_{MMGB-SA}$, between the originally reported S protein RBD and the wild type or singly mutated ACE2-based peptides. Locations of mutated peptide amino acids are highlighted in panel a. c) Snapshots of initial and optimized template-1 peptides binding to the original RBD. d) Adaptive evolution of template-1. e) Free energy of binding over time for template-1. f) Amino acid sequences of the initial and final peptides.

Adaptive evolution of peptide inhibitors: The above results have clearly demonstrated that suitable peptide templates with appropriate mutations can acquire a strong binding to specific

targets. To optimize such peptides against specific viral strains, we have developed combined mutation/selection (evolution) computational algorithms which can guide a multi-step adaptive evolution of the peptides: 1) Random mutations are introduced into random positions of the peptide templates. 2) Short MD simulation trajectories of the mutated-peptide:RBD complex are run and followed by a selection or rejection of the mutation via Monte Carlo (MC) sampling using a Metropolis criterion applied to the change of the free energy of peptide-RBD binding, $\Delta G_{MMGB-SA}$ (Methods). 3) The mutation/selection process is iteratively repeated until the binding affinity of peptides to the target S protein RBD is satisfactory (Methods). 4) Additional evolution of the molecules might be considered after the MC decisions to allow for a better internal relaxation of the molecules. Due to a partly stochastic nature of MD simulations, the randomness in mutations, and the MC selection, different peptides can be obtained in separate trajectories that correspond to separate local minima of the free energy surface. These peptides form a pool (ensemble) of potential therapeutics evolved for a selected viral strain, which can be further enriched by considering multiple viral strains.

In Figure 4c-e, S3, and Table S1 [2], coupling of **template-1** to the RBD was optimized in the adaptive evolution, where 10 ns MD simulation trajectories were generated after each trial mutation of **template-1**. Of the 100 mutations attempted, 13 mutations were accepted, and 11 amino acids were changed (individual residues can be mutated more than once). Figure 4d reveals the progression of binding free energies with the mutations of **template-1**, starting from $\Delta G_{MMGB-SA} = -19$ kcal/mol. As detailed in Figure 4c, during the adaptive evolution, the mutating helical peptide lost its bending (this change is independent of mutations) and multiple initial contacts with the RBD. At the same time, it shifted with respect to its initial position and formed many new contacts. Peptide residue E37 formed a salt bridge with the original RBD, while residues Q24, Y26 (mutated), Q30 (mutated), S41 (mutated) and R42 (mutated) formed hydro-

gen bonds of varying stability with the original RBD. The resulting peptide bound to RBD with $\Delta G_{MMGB-SA} = -70$ kcal/mol at the end of thirteen 10 ns-long trajectories (associated with individual accepted mutations).

As shown in Figure 4e, additional 175 ns relaxation of this peptide resulted in a slightly less favorable $\Delta G_{MMGB-SA} \approx -57$ kcal/mol. Therefore, adaptive evolution requires sufficiently long relaxation times for a good stabilization of the whole system. Short relaxation times may result in incomplete peptide adjustments and free energies that can be misleadingly favorable. Moreover, a faster MC convergence could be achieved by considering the whole free energy changes rather than the peptide-RBD binding free energies. However, internal reorganizations of molecules inevitably take part in long trajectories, so the difference in binding energies alone might be sufficient for the MC decision, as long as additional relaxation is allowed between individual MC steps (point 4 in the method).

Next, we adaptively evolved **template-1** coupled to 3 separate singly-mutated RBDs, chosen from Figure 3d. For simplicity, 100 mutations were attempted, followed by 10 ns simulations after each attempt. The adaptive evolution gave peptides with $\Delta G_{MMGB-SA} \approx -(45 - 70)$ kcal/mol, as summarized in Figure 5a-c and Figure 4f. Peptides targeting A475V and G476S RBDs each had 5 accepted mutations, respectively, while peptides targeting S477I RBD had 19 accepted mutations. In the A475V RBD case, one of the early accepted mutations lead to breaking of the helix secondary structure, and thus to a different peptide-RBD binding mode. This shows that individual alpha helices without additional stabilization, such as by side branching [117], might be too simplistic for therapeutic development.

In Figure 5d, the adaptive evolution was performed with a more stable **template-2** ($\alpha_1\alpha_2$), but random mutations were only introduced into the α_1 helix, which was in direct contact with the

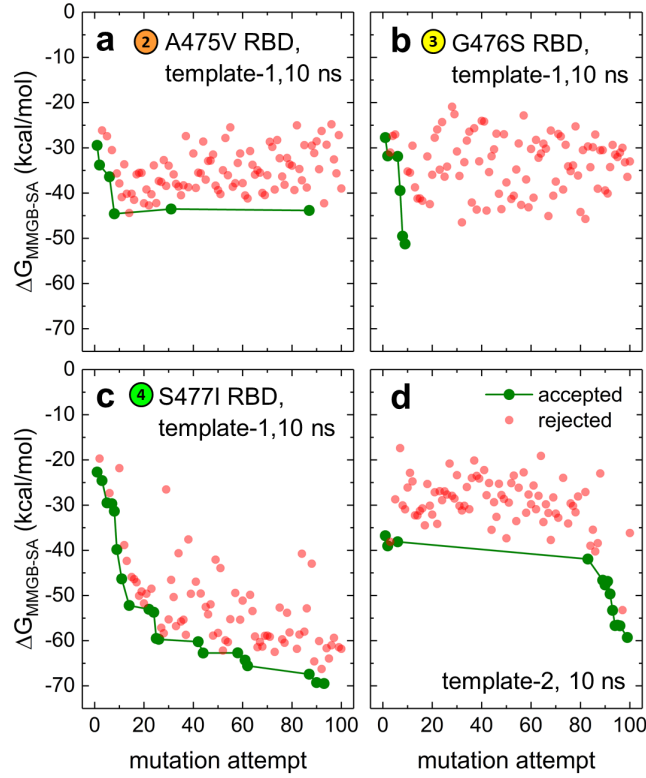


Figure 5: (a-c) Adaptive evolution of template-1 coupled with singly-mutated RBDs. (d) Adaptive evolution of template-2 coupled with the original RBD. After attempted mutations, peptide:RBD complexes were relaxed in 10 ns simulation steps.

original RBD. After 12 accepted mutations and 10 changed amino acids (listed in Table S2) [2], the binding strength increased from $\Delta G_{MMGB-SA} = -36$ kcal/mol to -60 kcal/mol. Therefore, the adaptively evolved **template-2** can compete with the whole ACE2, having $\Delta G_{MMGB-SA} \approx -50$ kcal/mol (Figure 3c). Both the initial and optimized **template-2** preserve the curvature of the α_1 helix, despite the mutation of E35 (to Y35), which is observed to interact with Q493 (RBD). This feature preserves the binding pattern observed in ACE2:S protein RBD complex [118]. However, the salt bridge between D30 (initial peptide) and K417 (RBD) is lost in the peptide optimized with 10 ns simulations after mutations.

Conclusion

In summary, using classical molecular dynamics simulations, we have shown that peptide inhibitors extracted from ACE2 provide highly promising trials for SARS-CoV-2 blocking. The single α 1-helix used in **inhibitor 1** is less stable, whereas the α 1,2-helices used in **inhibitors 2–4** support each other and retain their bent shape, which provides a conformational matching to the RBD of SARS-CoV-2 and a full covering of the RBD surface. Precise conformational matching between the designed peptides and the virus provides room for improving the binding affinity, which should be considered in future inhibitor design protocols. Suitable inhibitors should have a selective binding with lower RMSD for critical amino acids and relatively high binding energies. The binding affinity could be further enhanced by a multivalent binding of multiple peptides attached to surfaces of nanoparticles, dendrimers, or clusters.

”ACE2-based peptide templates can be adaptively evolved by computation using mutation/selection processes to form optimized inhibitors for a strong and competitive S protein RBD binding. The developed approach can be used to design peptide inhibitors based on templates extracted from different ACE2 polymorphs, including those from other species [119], and other proteins binding to viral pathogens. The optimized inhibitors obtained in different evolution runs can be collected to form libraries of suitable therapeutics for different RBD variants. Cocktails (ensembles) of peptide therapeutics could be delivered by different means to provide a broad-spectrum protection against different SARS-CoV-2 strains” [2].

3.2 Retrained generic antibodies can recognize SARS-CoV-2

Adapted from Ref. [3] (*ChemRxiv* 2020. DOI: 10.26434/chemrxiv.13249559.v1)

Introduction

In the last decades, zoonotic pathogens have represented a major public health problem around the world [120]. The spread of a zoonotic disease in the human population is always very fast with short resolution period. The severe acute respiratory syndrome coronavirus 2 (SARS-CoV-2) is a novel pathogen that has rapidly caused a devastating pandemic of coronavirus disease 2019 (COVID-19) with huge fatalities, wide-ranging socioeconomic disruptions, and losses. There are several possible ways to treat the disease including, but not limiting to, development of vaccines, antibody therapies, and antiviral drugs [121].

There are always pros and cons associated with each method. Although many COVID-19 vaccines are under development worldwide, there are still uncertainties about vaccine safety, long-term protection, and protection of older people [122,123]. Rather than wait for vaccines to coax the body to make its own antibodies, some researchers are focused on monoclonal antibodies which are generally more expensive [124]. The antibodies are difficult to reproduce and limited to injection only [123]. One investigational drug, Remdesivir, has been authorized by FDA for emergency use in the clinic, but most of the antiviral drugs have uncertain effectiveness [125,126]. Given the urgency of the pandemic, some easier and cheaper ways are needed to combat COVID-19. Nanomedicine, including functionalized cyclodextrins, gold nanoparticles, nanorods and quantum dots, offers numerous opportunities against a broad spectrum of viruses and coronaviral infections [6,7,127]. However, it is still highly challenging to safely translate NPs from laboratory innovation to the clinic [127]. Computational approaches have been used to search potential drugs against SARS-CoV-2 protease and the S protein, but most of the drugs are not promising or have unknown effectiveness [128]. Computational designed peptide or small protein inhibitors against the S protein exhibit potential advantages over antibodies as potential therapeutics [1,2,129]. The synthetic protein inhibitors

show comparable and even better blocking of SARS-CoV-2 infection than monoclonal antibodies. The designed inhibitors are also conformationally stable, easier to produce and store [129]. The fatal disadvantage of the synthetic inhibitors could be the limitation in promoting rapid clearing of the virus, while the natural antibody does a better job in both blockage and cleaning of recognized viruses [130]. An innovative method is needed to address the problem inherited with synthetic inhibitors.

In this work, we design an interfacial booster with one face blocking the virus and the other catching the preexisting antibody in the human body. The designed double-faced boosters combine the new viruses and the old antibodies, which are preexisting due to the previous immunity or vaccination, as if the old antibodies are redesigned and adapted to recognize the new viruses. The booster is composed of the previously designed ACE2-based inhibitor and a piece of the Hepatitis B antigen. The hepatitis B antibody could recognize the SARS-CoV-2 through the designed booster which is composed of hepatitis B antigen and ACE2-mimic. The clearing of virus can be triggered by the preexisting antibody. This study could provide a potential guidance in design generic therapeutics against any new emerging pathogens with the combined advantages of small protein therapy and antibody therapy.

Simulation methods

The two faces of boosters were separately bound to RBD and antibody fragment (AF). All structures were directly based on the crystal structure of the human ACE2 protein bound to RBD of SARS-CoV-2 (pdbID: 6LZG) [113] and Hepatitis B antigen bound to AF [131]. Snapshots were taken by VMD [73].

The systems were simulated using NAMD2 [58], the CHARMM36 protein forcefield [63] and the CHARMM36 general forcefield. The simulations were conducted with the Langevin dynamics ($\gamma_{Lang} = 1 \text{ ps}^{-1}$) in the NPT ensemble, at temperature of $T = 310 \text{ K}$ and pressure of $p = 1 \text{ bar}$. The PME method was used to evaluate Coulomb coupling, with periodic boundary conditions applied [114]. The time step was set to 2 fs. The long range van der Waals and Coulombic coupling were evaluated every 1 and 2 time steps, respectively. After 2,000 steps of minimization, the solvent molecules were equilibrated for 3 ns, while the complexes were restrained using harmonic forces with a spring constant of 1 kcal/(mol Å). Next, the systems were equilibrated in 100 ns production MD runs with restraints on the top part of AF.

Calculation of RMSD: The time-dependent RMSD for Face 1 and Face 2 were calculated from

$$RMSD_{\alpha}(t_j) = \sqrt{\frac{\sum_{\alpha=1}^{N_{\alpha}} (\vec{r}_{\alpha}(t_j) - \vec{r}_{\alpha}(t_0))^2}{N_{\alpha}}}, \quad (3.2)$$

where N_{α} is the number of atoms whose positions are being compared, $\vec{r}_{\alpha}(t_j)$ is the position of atom α at time t_j and $\vec{r}_{\alpha}(t_0)$ is the initial coordinate. The selection of coordinates contains all the atoms in Face 1 or Face 2, excluding hydrogens. The time-dependent RMSD was averaged over the last 50 ns of simulation time, which corresponds to the last 500 frames of each trajectory as shown in Figure 7d. The standard deviations were shown by the error bars.

MMGB-SA Calculations: We used the Molecular Mechanics Generalized Born - Surface Area (MMGB-SA) method [85,86] to estimate the relative binding free energies between booster faces and their binders (RBD or AF). The free energies were estimated from separate MMGB-SA calculations for three systems related to the face and its binder (the face, the binder of the face, and the complex of the face and its binder) in configurations extracted from the MD trajectories of the whole complex

in the explicit solvent. The MMGB-SA free energies of the extracted configurations of the three systems were calculated as

$$G_{tot} = E_{MM} + G_{solv-p} + G_{solv-np} - T\Delta S_{conf} ,$$

where E_{MM} , G_{solv-p} , $G_{solv-np}$, and ΔS_{conf} are the sum of bonded and Lennard-Jones energy terms, the polar contribution to the solvation energy, the nonpolar contribution, and the conformational entropy, respectively. The E_{MM} , G_{solv-p} and $G_{solv-np}$ terms were calculated using the NAMD 2 package [58] generalized Born implicit solvent model [87], with a solvent dielectric constant of $\epsilon = 78.5$. The $G_{solv-np}$ term for each system configuration was calculated in NAMD as a linear function of the solvent-accessible surface area (SASA), determined using a probe radius of 1.4 Å, as $G_{solv-np} = SASA \gamma$, where $\gamma = 0.00542$ kcal/(mol Å²) is the surface tension. The ΔS_{conf} term was neglected, as the entropy term is often calculated with a large computational cost and low prediction accuracy, which is likely to be similar for the studied systems with difference in the connecting part of the two faces. [88,89]. Since the G_{tot} values are obtained for configurations extracted from the trajectories of complexes, G_{tot} doesn't include the free energies of faces reorganization; the correct free energies of binding should consider configurations of separately relaxed systems. The approximate binding free energies of the studied complexes were calculated as $\langle \Delta G_{MMGB-SA} \rangle = \langle G_{tot}(face - binder) - G_{tot}(face) - G_{tot}(binder) \rangle$, where face-binder represents the complex of face with its binder, and the \langle averaging \rangle is performed over configurations within the second half of the calculated trajectories.

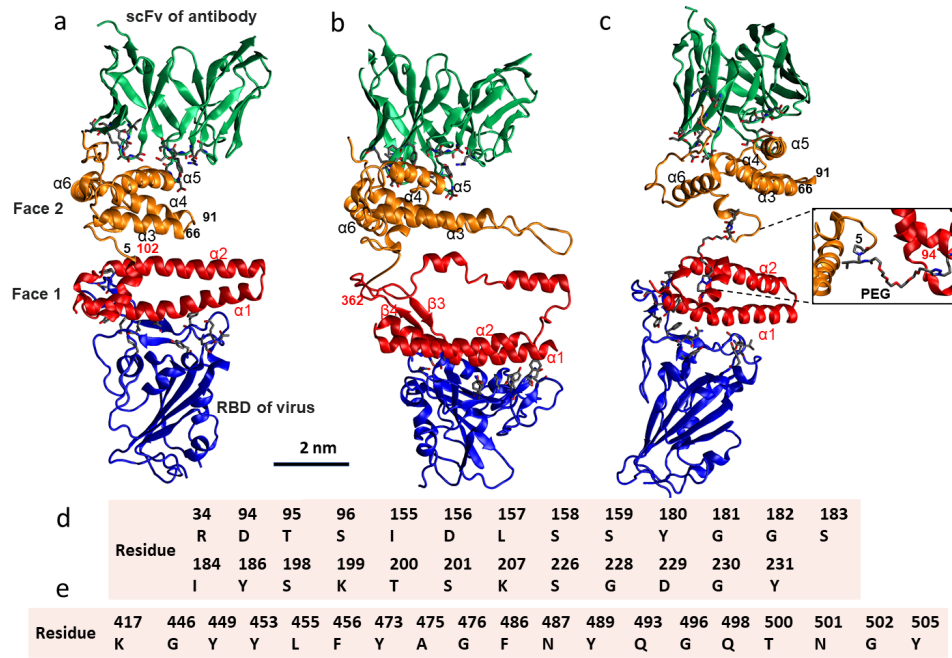


Figure 6: The structure of double-faced boosters bound to the S RBD and AF. (a) Booster 1 is composed of Face 1 (ACE2-mimic, 19 – 102 amino acids [113]) and the Hepatitis B antigen (without residues between 66 – 91 [131]); (b) Booster 2 is composed of inhibitor 3 from the previous work [1] as Face 1 and the Hepatitis B antigen [131] as Face 2; (c) Booster 3 is composed of the same faces as Booster 1 but with a PEG linker in between (inset); (d) the initial amino acids of the antibody which interact with Face 2; (e) the initial amino acids of the RBD which interact with Face 1. Color scale: green-antibody, orange-antigen, red-ACE2-mimic, blue-RBD, gray-C atom, red-O atom, blue-N atom. ACE2: Angiotensin-converting enzyme 2, which is the cellular receptor of SARS-CoV-2.

Booster design

Figure 6a-c present the designed boosters, each having two linked ACE2-mimic (Face 1 - red) and antigen (Face 2 - orange) faces coupled with the RBD (blue) and AF (green), respectively. Face 1 and RBD are based on the crystal structure (pdbID:6LZG) [113]. Face 2 and AF are taken from the crystal structure of the single-chain variable fragment (scFv) of Hepatitis B antibody and the core-antigen of Hepatitis B (pdbID:6CWD [131]), respectively.

Booster 1: Face 1 is composed of the $\alpha_1\alpha_2$ helices of ACE2 (19 – 102 amino acids). Face 2 is the Hepatitis B core-antigen without the 66 – 91 amino acids. The two faces are connected between

position 102 of the ACE2 helices and amino acid 5 of the Hepatitis B core-antigen, as shown in Figure 6a.

Booster 2: Face 1 is the previously-designed SARS-CoV-2 Inhibitor 3 [1]. Face 2 is taken from the 5 – 145 amino acids of the Hepatitis B antigen. The two faces are connected between amino acid 362 of Inhibitor 3 and amino acid 5 of the Hepatitis B core antigen.

Booster 3: The same components were used as in Booster 1, but with an extra linker made of a PEG chain between amino acid 94 of the ACE2 helices and amino acid 5 of the Hepatitis B core-antigen, as shown in the inset of Figure 6c. The amino acids of the RBD and AF which initially contact with the two faces are shown in licorice, with the ID and amino acid names listed in Figure 6d and e, respectively.

Results and discussion

Binding Conformations: In Figure 7a, in 100 ns simulations, we show that both faces of Booster 1 stay tightly bound with the expected partners (RBD and AF), while the 3D peptide structure is largely preserved (insets). In Figures.S1-3 [3], we analyze the binding hot spots on the RBD and AF, which have been contacted more than 250 times during 500 frames (last 50 ns). The hot spots of the AF binding with Face 2 are formed by 14 amino acids, 95T, 96S, **97T**, 156D, 158S, 159S, **161A**, **176T**, **177S**, 201K, **202S**, **205D**, **206G**, and 207Y. The hot spots of the RBD binding with Face 1 are formed by 16 amino acids, 417K, 453Y, 455L, 456F, 473Y, 475A, 476G, 486F, 487N, 489Y, 493Q, **494S**, **495Y**, 498Q, 500T, and 501N. Above, we show in bold the new binding contacts, compared to the initial contacts in Figure 6 d and e.

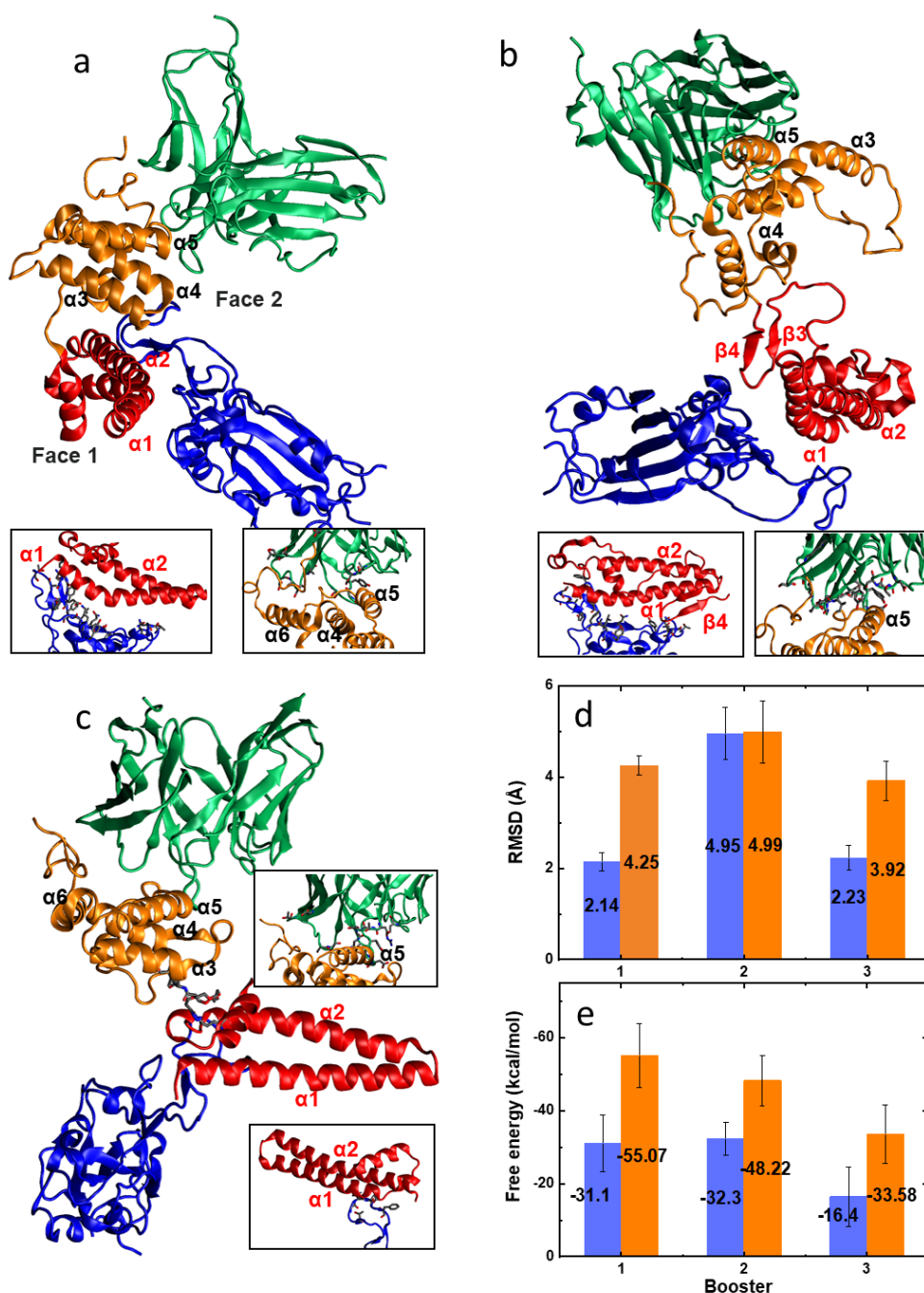


Figure 7: Simulated booster, RBD and AF complexes. (a-c) Final conformations of Booster 1-3 systems at 100 ns. (d) Averaged RMSD for Face 1 (ACE2-mimic, blue bar) and Face 2 (antigen, orange); (e) Averaged free energy of binding of RBD with Face 1 (blue bar) and antibody with Face 2 (orange bar).

Figure 7b shows the binding conformation of Booster 2. The conformations of the α helices and the β hairpin during their binding to the RBD are similar to those present in the crystal structure.

Although Booster 2 has an extra hairpin and coil structure compared to Booster 1, Face 1 of Booster 2 has the same number of hot spots as Face 1 of Booster 1, which include 417K, 453Y, 455L, 456F, 473Y, 475A, 476G, 486F, 487N, 489Y, 493Q, 498Q, 500T, 501N, 502G, and 505Y, with no new contacts forming. The hot spots on AF are composed of 94D, 95T, 96S, 158S, 159S, 180Y, 181G, 182G, 183S, 184I, 186Y, 199K, 201S, **202T**, 226S, 228G, 229D, 230G, and 231Y.

Figure 7c shows that Face 1 of Booster 3 dissociates from the RBD with only a few amino acids contacts including 456F, 475A, **484E**, 486F, 487N, and 489Y, while Face 2 still binds to AF (hot spots: 34R, 94D, 95T, 96S, 157L, 158S, 159S, **175K**, **176T**, **177S**, **178T**, **202S**, **205D**, **206G**).

RMSD and Free Energy of Binding: To further quantify the binding of these boosters to their targets, we calculated the Root-Mean-Square Deviation (RMSD) and the free energy of binding, $\Delta G_{MMGB-SA}$, for each face in each booster. Figure 7d shows the average RMSD at the end of our simulations. Boosters 1 and 3 have similar RMSD, which is slightly smaller in Booster 1. Booster 2 shows a large RMSD due to the additional loop structures present in both Face 1 and Face 2. In Boosters 1 and 3, Face 2 (antigen) always has a larger RMSD than Face 1, due to the extra random coil presented, while Booster 2 has comparable RMSD values in both faces.

Figure 7e shows $\Delta G_{MMGB-SA}$ calculated for each face coupled to its target. Booster 1 has the best overall binding with RBD and AF, while Booster 3 has the weakest binding in both faces. Booster 2 has a similar free energy of binding as Booster 1, but only on Face 1. Notably, Face 1 of Booster 3 dissociated from RBD, which leads to the lowest free energy of binding on that side. This may be caused by the flexibility of the PEG linker between the two faces.

Conclusion

In summary, using classical molecular dynamics simulations, we have shown that the double faced boosters provide highly promising trials for targeting the Hepatitis B antibody and RBD of SARS-CoV-2. Booster 3 is less promising, whereas the Booster 1 shows stable binding to both antibody and RBD. With the bent shape of Face 1 maintained, Booster 1 provides a conformation matching to the RBD of SARS-CoV-2 and a full cover of the RBD surface. The designed boosters aim to bridge the preexisting antibody with the new virus, which could tiger the immune system to recognize the new virus without generating new antibody. This booster concept can be further developed to a generic therapeutic method which could be used to treat any newly emerging pathogens.

3.3 Glycodendrimer inhibitors of HIV and SARS-CoV-2

Adapted from Ref. [4] (submitted)

Introduction

Heparan sulfate proteoglycans (HSPGs) are ubiquitous cellular receptors for various different viruses, including HIV, HPV, HSV and Dengue virus, etc [132]. Designing antivirals mimicking HSPGs is a promising strategy to inhibit viruses [6,6], especially when there are no vaccines and effective medicines available. HIV is one type of virus that has no effective cure and cause long term side effects, or even death. Development of effective anti-HIV medicines would benefit not only the patients but also the whole society.

Heparin, dextran sulfate and various different sugar based molecules were found to have anti-HIV properties [133–137]. Prof. Katherine McReynolds’s group has previously synthesized sulfated sugar based dendrimers which were effective in preventing HIV-1 infection [138]. They suggested that the

dendrimers could bind to and block the regions containing basic amino acids of the HIV S protein (gp120), e.g. V3 loops [139].

The new coronavirus, SARS-CoV-2, were also found to have a HSPG binding site [140] and a trimeric S protein. The similarity between SARS-CoV-2 and HIV S proteins suggest that they might have the similar binding pathway to the host cells [141–143]. We hypothesized that the anti-HIV dendrimers could also be effective anti-SARS-CoV-2 agents.

More potent and non-toxic glycodendrimers against HIV-1 were designed and tested *in vitro* in Prof. McReynolds’s group. Based on the experimental results, four top glycodendrimers from anti-HIV essays were selected and further simulated to check their binding with gp120. Cellobiose and Lactose based glycodendrimers and two hybrid glycodendrimers were simulated to check the binding with the RBD of SARS-CoV-2. The mechanism of the inhibition was further analyzed based on MD simulation results.

Experimental results

The structures of few glycodendrimers (GDs) are shown in Figure 8. Among the 14 GDs, Lactose, Cellobiose, Maltotriose and Melibiose functionalized ones show strong activity with IC_{50} in the range of μ M, as shown in the reference [4]. From the average of the significant responses of the pseudoviruses for each sulfated glycodendrimer (SGD), the order of activity of the SGDs from strongest to weakest was: Lactose(15e), Cellobiose(12e), Maltotriose(17e), Melibiose(18e), Maltose(16e), Gentioibiose (14e) [4].

MD simulations of dendrimers with glycoproteins

In order to check the experimentally observed binding between GDs and gp120 (HIV associated glycoprotein), these systems were modeled by atomistic MD simulations using NAMD [58]. In the

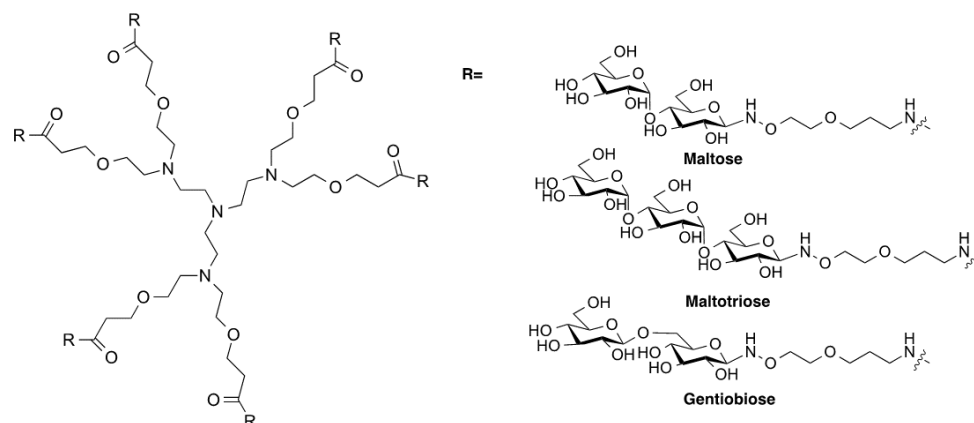


Figure 8: Structures of Oxime-Linked Hexavalent Glycodendrimers

simulations, the gp120 protein complex used was a trimer based on PDB code 5v8m [144]. Its V3 loop, a principle neutralizing domain with amino acids 303-338, is known to bind with a host cell surface via heparan sulfate proteoglycans (HSPG) [138]. Several different GDs were designed and synthesized to inhibit the binding of the V3 loops in gp120 to HSPG. Four oxime-linked hexavalent GDs with a high activity in *in vitro* experiment were selected to simulate the interaction with gp120. Having the same dendritic core, the four GDs differed by their functional groups, which include cellobiose, lactose, melibiose, and maltotriose. The sulfated (SGD) and un-sulfated states (GD) of the four functional groups were also considered, which gave eight simulated systems. The sulfate groups were mostly added to C6 of each sugar unit, according to the average number of sulfates per sugar. Here, the averaged number of sulfates is 1.6/sugar (Cellobiose), 1.8/sugar (Lactose), 1.3/sugar (Melibiose) and 1/sugar (Maltotriose). The four non-sulfated GDs work as negative controls. All the systems were immersed in 150 mM NaCl solutions. Different GDs were named by their sugar functional groups.

Since the new coronavirus, SARS-CoV-2, also has a HSPG binding site [140], we selected Lactose GDs and SGDs (15d and 15e) and Cellobiose GD and SGD (12d and 12e) to test their binding with the receptor binding domain (RBD, PDB:6M17 [99]) of SARS-CoV-2. The four GDs were separately placed around the top and middle part of RBD with two trials for each case. The top region is the binding site of ACE2, which is the cellular receptor of SARS-CoV-2 [99], and the middle part contains the exposed basic regions which is the proposed the binding site for HSPG. In addition, two types of hybrid compounds with an octavalent core functionalized by half SGD and half GD were also designed to examine the binding strength.

All the systems were immersed in 150 mM NaCl solutions. Different GDs were named by their sugar functional groups. The simulations were performed for 100 – 200 ns for gp120 systems and 70 – 100 ns for SARS-CoV-2 systems, with slightly difference due to the computer power and time needed to reach equilibrium.

The gp120 proteins were described by a CHARMM36 forcefield [64], while the GD/SGDs were described by a CHARMM general forcefield [68]. The PME [62] method was used for the evaluation of long-range Coulombic interactions. The time step was set to 2.0 fs. The simulations were performed in the NPT ensemble ($p = 1$ bar and $T = 300$ K), using the Langevin dynamics ($\gamma_{\text{Lang}} = 1 \text{ ps}^{-1}$). After 2,000 steps of minimization, ions and water molecules were equilibrated for 2 ns around protein and GD/SGDs, which were restrained using harmonic forces with a spring constant of 1 kcal/(mol Å²). The last frames of restrained equilibration were used to start simulations of free GD/SGDs and partial constrained protein (the helical part on the bottom). The trajectories and snapshots were visualized by VMD [73]. The free energy of binding between compounds and protein targets were evaluated by NAMD [58] in a generalized Born Implicit Solvent (150 mM). The averaged MMGB-SA free energy was taken from the last 20 ns (500 frames) of each simulation.

Binding of SGDs/GDs to gp120

To better understand how and where specifically the SGDs interact with the HIV-1 gp120 protein, we set out to evaluate the binding interactions of the four most active SGDs based on the inhibition of infectivity results (12e, 15e, 17e, 18e). Figure 9 shows the two most favorable binding configurations of each SGD to the gp120 trimer (HIV S proteins). All these SGDs tend to bind to the gp120 trimer in a multivalent manner, where different chemical groups of SGDs bind to gp120 in a correlated manner by the Coulombic and van der Waals (vdW) coupling [7–10,33]. In this multivalent coupling, different branches of SGDs can simultaneously reach several gp120 monomers, as shown in Figure 9B for the Lactose SGD binding. On the other hand, the neutral GDs (non-sulfated) are less active in their binding with gp120 (Figure 10), which shows the contact times of amino acids of V3 loop interacting with different SGD/GDs.

The contact time is defined as the number of frames out of the last 500 frames (20 ns), where the interaction or contact happens. ARG and ILE present as frequent interacting amino acids, which stand for charged and hydrophobic interactions with SGD/GDs. Then, we divide the interacting amino acids into three categories: positively charged, hydrophobic, and polar (polar uncharged and negatively charged). The percentages of different types of interactions for SGDs are shown in Figure 10E, where we counted the number of interaction times for each type of amino acids over the period of last 20 ns (500 frames), and then divided that number by the overall contact times of all amino acids. The interacting residues were selected either from the V3 loop or from the whole protein, as shown in Figure 10E. As the V3 loop is a basic region on gp120, the amount of charged interaction with the V3 loop is above 32%, which is more than 10 % higher than that with the whole protein. The percentages of hydrophobic interactions are comparable regardless targeting V3 loop

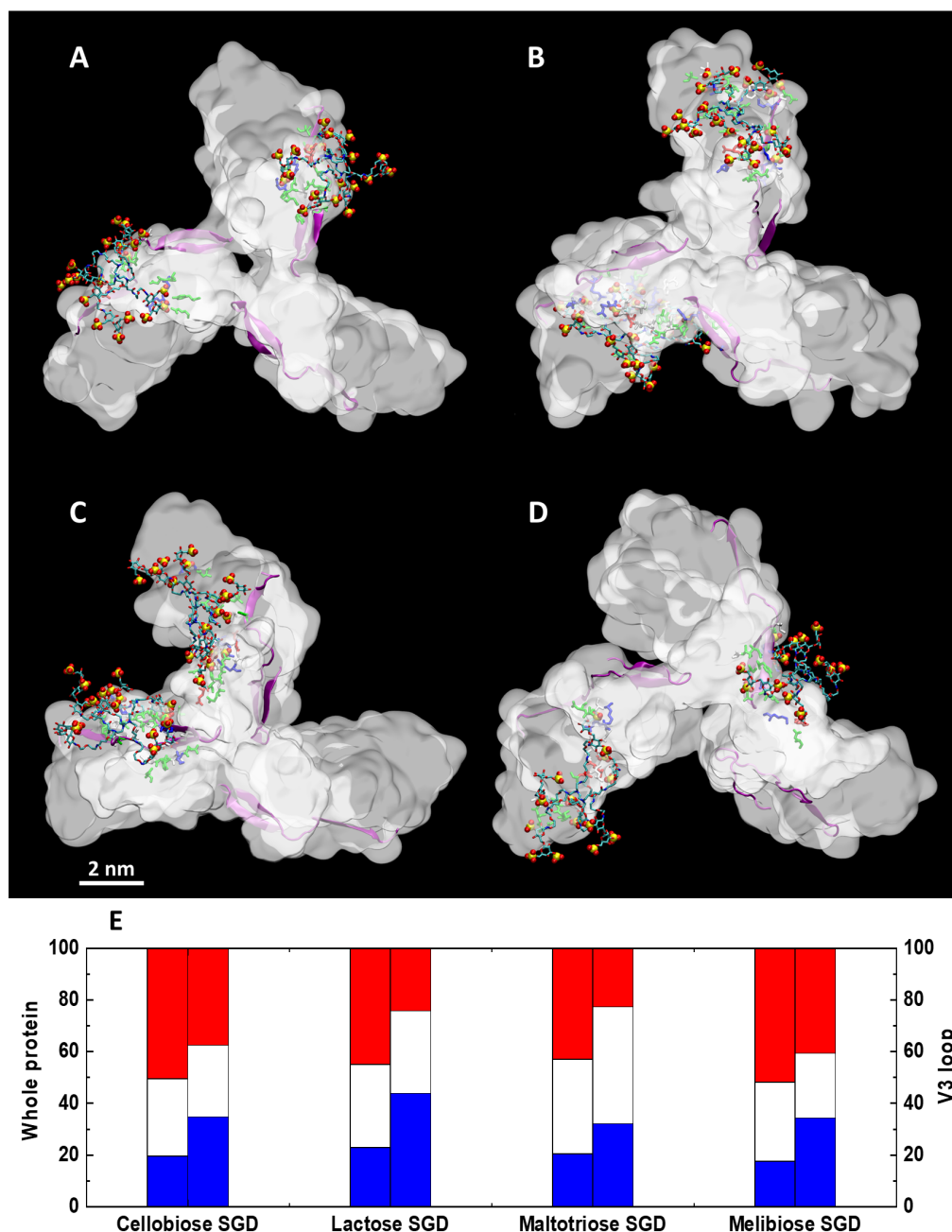


Figure 9: Different SGDs attached to one gp120 trimer: A. Cellobiose SGD (12e); B. Lactose SGD (15e); C. Maltotriose SGD (17e); D. Melibiose SGD (18e). Only two SGDs with the most favorable binding configuration are shown in each case. Proteins are shown as a white surface, SGDs are represented in atomistic details, and the gp120 residues interacting with SGDs (within 3 Å) are shown in licorice. The coloring scheme: V3 loop - purple, C - cyan, O - red, S - yellow, N - blue, H - omitted, basic residue - blue, acidic residue - red, polar residue - green, nonpolar residue - white. Water and ions are omitted for better visualization. E. Percentage of different interactions contributing to the SGD-gp120 binding (left: quantified over the whole protein; right: quantified only with V3 loop. Polar - red: interaction with polar amino acids; hydrophobic - white: interaction with hydrophobic amino acids; charge - blue: interaction with positively charged amino acids.

or the whole protein. The percentage of polar interaction is in complementary to that of charge interaction.

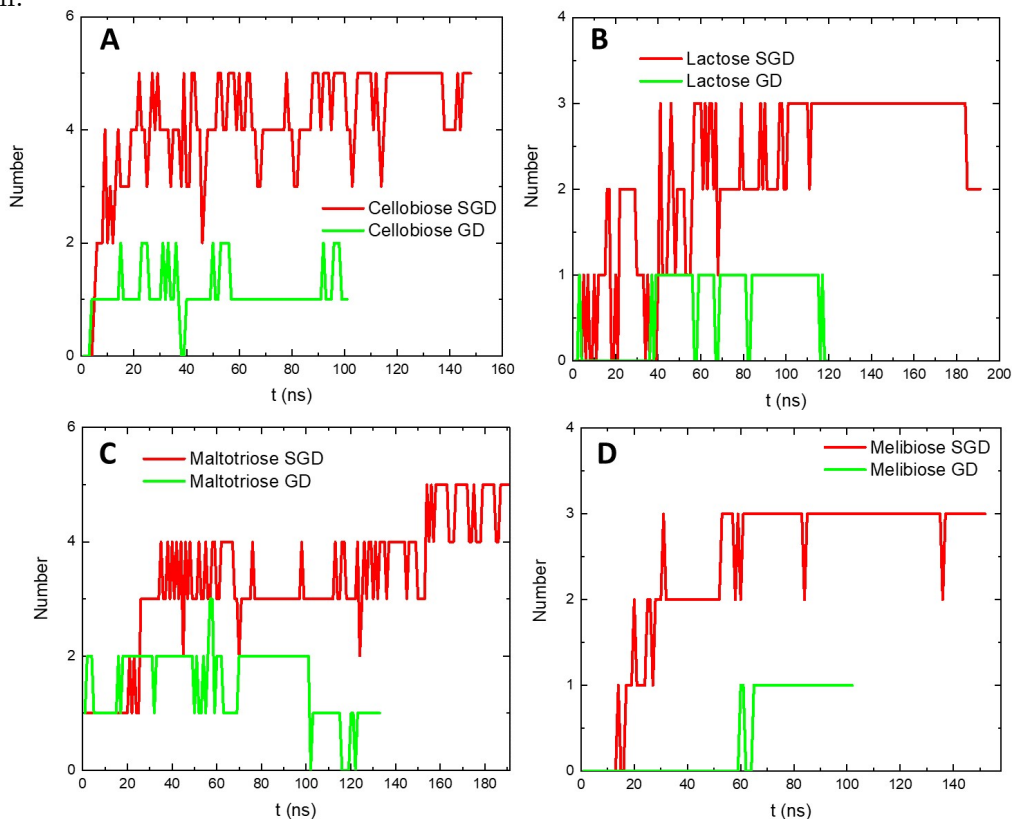


Figure 10: Number of SGD/GDs contacting with the V3 loop. A. Cellobiose 12e; B. Lactose 15e; C. Maltotriose 17e; D. Melibiose 18e. Red: SGDs; green: GDs.

In our earlier studies of sulfonated AuNPs coupled with HPV capsids, we found that the free energy per one charged interaction (-6 kcal/mol) is 12 times larger than that per one typical hydrophobic group (alkyl, -0.5 kcal/mol) [6]. Coulombic coupling should also dominate the binding of SGDs and gp120. Furthermore, the ranking of SGDs sorted by the charged interactions contributing to the overall interaction (Figure 9E, left) matches with that of binding affinities obtained from MST (microscale thermophoresis analysis) experiments: $15e > 17e > 12e > 18e$. However, the ranking of SGDs sorted by sulfation level ($15e > 12e > 17e > 18e$) is slightly different from that of the binding affinity obtained by MST [4]. The spatial orientations of hydroxy groups, number of sugar units and

linkage between sugar units are all contributing in a delicate manner to the overall strength of SGDs and gp120 binding. Lactose with three hydroxy groups on one side of a ring structure and a smooth β -1 \rightarrow 4 glycosidic linkage could provide a more polar face, which leads to stronger binding of 15e to gp120 (Figure 11, Figure 12, Figure 13). The sulfation level, number of sugars, orientations of polar groups and overall arrangement of sugars in SGDs determines the strength of their multivalent interactions with substrates [7–10, 33, 145].

Figure 12 shows the contact times of amino acids of V3 loop interacting with different SGDs. The contact time is defined as the number of frames out of the last 500, where the interaction or contact happens. The two most frequent amino acids in the binding of 12e/17e to V3 loop are ARG and ILE, while in the case of 15e, they are ARG and ALA; in the case of 17e, they are ARG and LYS. The frequently interacting amino acids among the four SGDs are slightly different, but they stand for the two major amino acids categories, basic and hydrophobic. Among the four SGDs, ARG is the common amino acid which contacts for more than half of the counting time (250). The long binding time of amino acids arises from the strong Coulombic interaction between the positively charged amino acids and the sulfate groups of SGDs.

As negative controls, the number of interacting amino acids with GDs were far less than SGDs. The contact times of the amino acids interacting with GDs are less condense than their SGDs partners as shown in Figure 12. As the GDs are neutral, the charged interaction is impaired in the whole interaction, which could significantly weaken the binding strength of GDs to the V3 loops as discussed in the SGD cases.

Figure 13 shows the contact times of atoms in sugar units interacting with the V3 loop averaged over 36 branches in the cases of SGDs. For 12e, the total contacting times are 213 for the second glucose, and 132 for the first glucose. For 15e, there are 117 contacting times for the first sugar ring

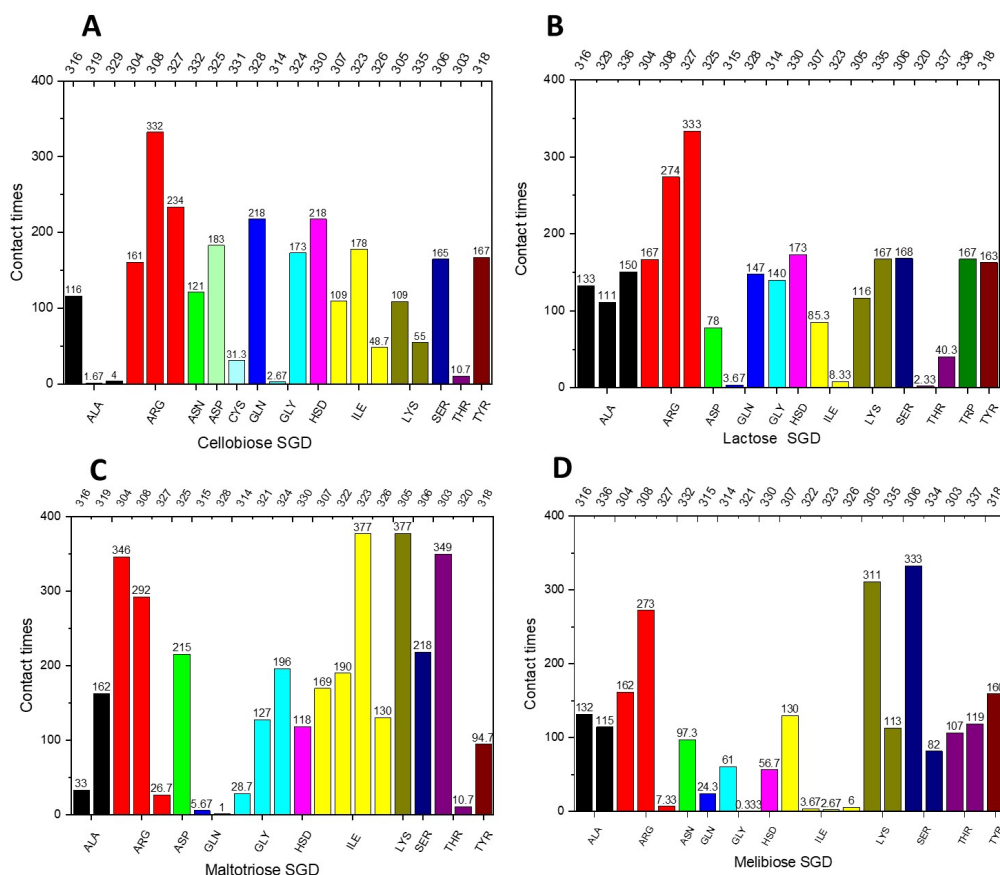


Figure 11: The contact times of amino acids from the V3 loop (per monomer) interacting with SGDs, averaged over the last 500 frames (20 ns). A. Cellobiose 12e; B. Lactose 15e; C. Maltotriose 17e; D. Melibiose 18e.

(glucose), and 113 contacting times for the second sugar ring (galactose). For 18e, there are 139 contacting times for the first sugar ring (glucose) and 84 contacting times for the second sugar ring (galactose). For 17e, there are 180 contacting times for the third glucose, 66 contacting times for the second glucose, and 63 contacting times for the first glucose. Note here, not all of the branches bind to the V3, the numbers obtained above cannot be used directly to compare among different SGDs. We further defined a term, "sugar ring attaching factor" (SRAF), to make the data comparable among different cases. SRAF equals the difference of contacting times between sugar ring 1 and 2 divided by the total contacting time of ring 1 and 2. A smaller value of SRAF corresponds to a higher

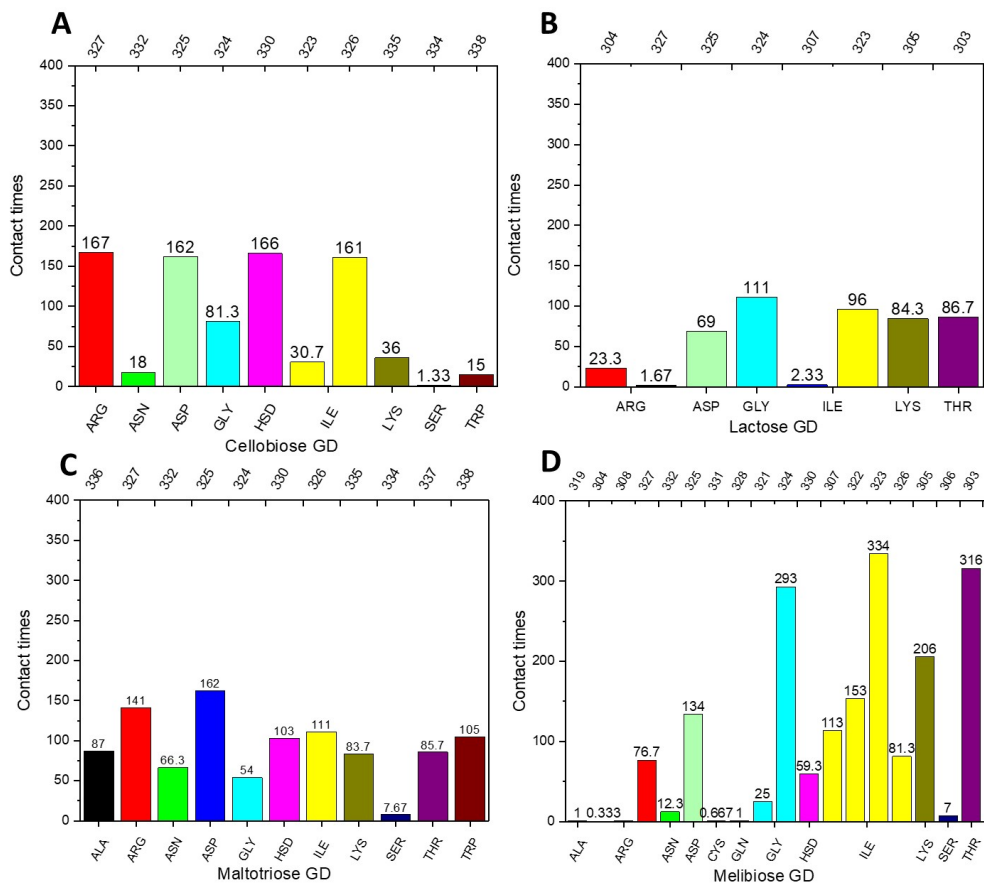


Figure 12: The contact times of amino acids of the V3 loop (per monomer) interacting with GDs, averaged over the last 500 frames (20 ns). A. Cellobiose 12d; B. Lactose 15d; C. Maltotriose 17d; D. Melibiose 18d.

potential for the multivalent binding. For example, the SRAF of 12e equals $(213-132)/(213+132)$, which gives 0.23. Similarly, the SRAF is 0.02 for 15e and 0.25 for 18e. As 17e has three sugar units with the ring 1 and ring 2 presenting very similar contacting times, we consider ring 1 and ring 2 as one unit which contributes 129 contacting times. So, the SRAF of 17e is 0.17.

Collectively, we find 15e shows the best SRAF (0.02) followed by 17e (0.17), 12e (0.23), then, 18e (0.25). Only 15e with the lowest SRAF shows comparable contacting time for both sugar units, which indicates a more ideal multivalent interaction against V3 loop; while the rest of the SGDs favor the terminal sugar binding style which is a sign of weaker multivalency. Given that 15e and

12e are different by the terminal sugars, we propose that galactose (terminal unit of 15e, with three OH groups toward one side of the ring) could provide a more polar side concentrated with more OH groups. The concentrated OH groups in galactose unit of 15e could increase the polar interactions between SGD and V3 loop. As 15e (β 1-4 linkage) and 18e (α 1-6 linkage) have the same sugar units but different linkages and SRAF, we propose that β 1-4 linkage could be the structural origin of the better multivalency. Comparing the 15e and 17e, we find the multivalency is not in proportional to the number of sugar units.

Binding of SGDs to monomeric SARS-CoV-2 spike

Due to the emergence of the COVID-19 pandemic caused by the SARS-CoV-2 virus, and the similarities shared with HIV-1 and coronaviruses in interacting with the ubiquitous cell surface proteoglycan, HSPG [146–148], we selected two of our best performing SGDs, Cellobiose 12e and Lactose 15e, to determine how they interact with the RBD of SARS-CoV-2. Specifically, the type and locations of amino acids contacting with the SGDs were identified. Cellobiose and Lactose GDs (12d and 15d) were selected as controls. As the basic amino acids concentrate in the middle part of RBD on the front side [146–148], and the host cell receptor (ACE2) binding region resides on the top of RBD [99], the four compounds were initially placed near the top and middle regions of RBD, respectively. Two repeating trials were set for each case. Our simulations show that the SGDs 12e and 15e can separately target the top and middle regions of RBD(Figure 14A-B and Figure 15), while the GDs 12d and 15d only target the top part of RBD due to the lack of sulfate groups (Figure 16). Two most favorable binding modes of 15e targeting either the top or middle region of RBD are shown in Figure 14A and B, where the interacting ARG and LYS residues are highlighted. Most of the branches of 15e interact with the basic amino acids near the top of RBD. Branches of

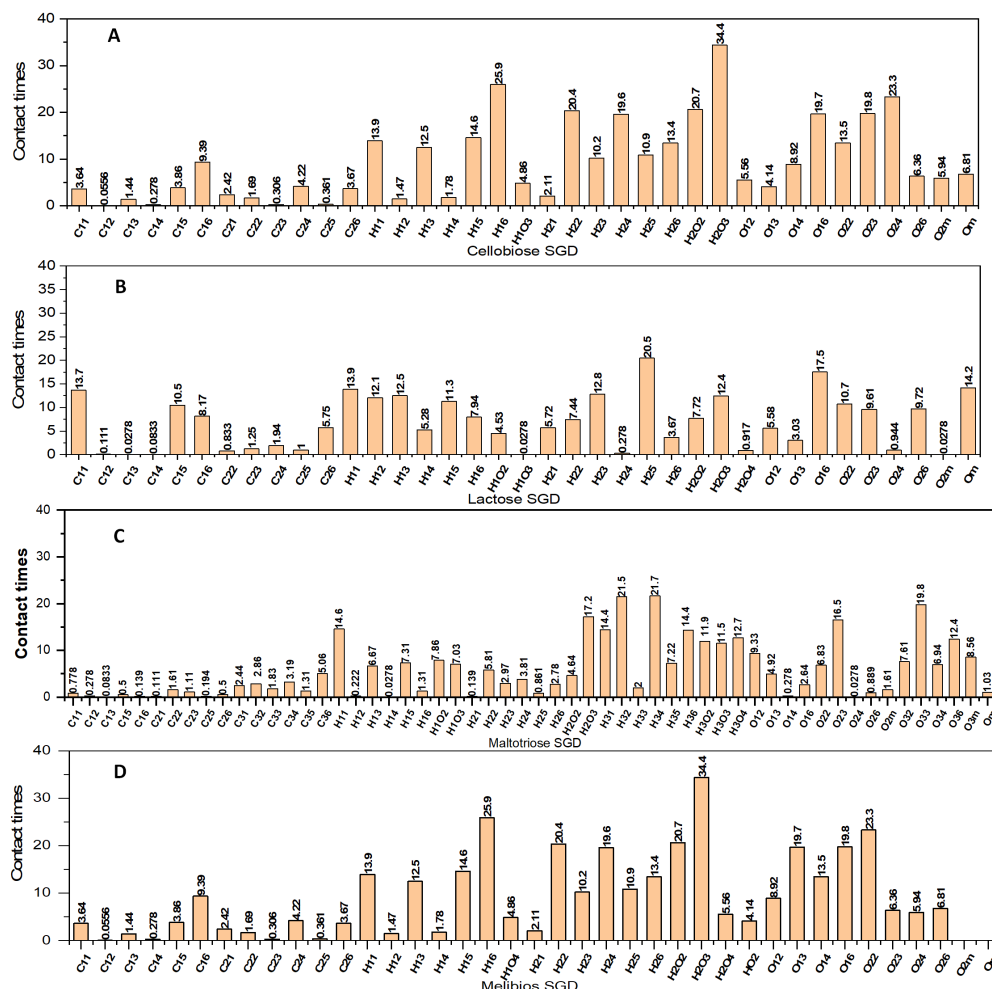


Figure 13: Contact times of sugar groups of SGDs with the V3 loops. A. Cellobiose 12e; B. Lactose 15e; C. Maltotriose 17e; D. Melibiose 18e. Naming rule: the ring close to compound core is named as ring 1, the ring far from compound core is named as ring 2. The atoms are named by the element symbol, followed by the ring name, then normal naming number for ring structure, e.g. C12 means carbon in ring 1 at position 2; C23 means carbon in ring 2 at position 3; H1O3 means hydrogen in ring 1 in hydroxyl group at position 3; H2O2 means hydrogen in ring 2 in hydroxyl group at position 2.

15e could span the top region of RBD, which is facilitated by the charged interaction between sulfate groups and basic amino acids, as shown in the side view of Figure 14A.

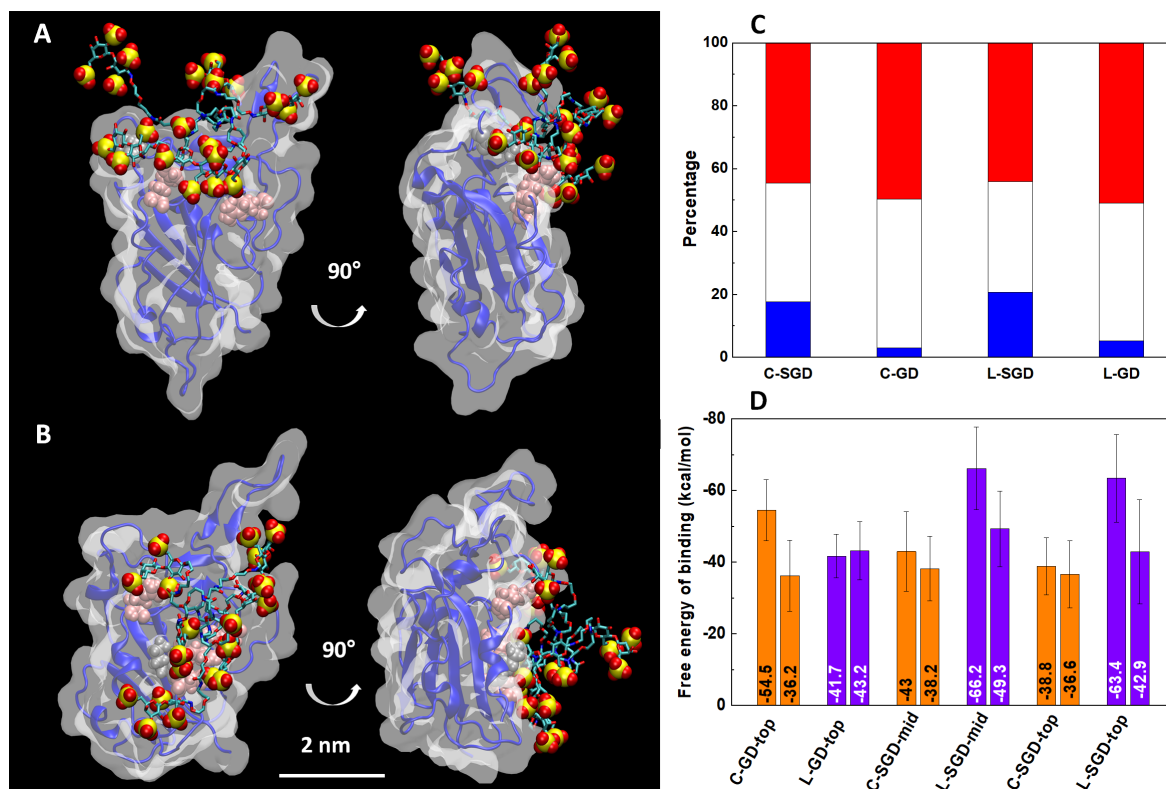


Figure 14: Lactose SGD (15e) binding with RBD of SARS-CoV-2. A. Two views (90 ° rotation) of 15e binding with the ACE2 binding region. B. Two views (90 ° rotation) of 15e binding with the purported HSPG binding region. Coloring scheme: SGD: C-cyan, O-red, S-yellow, N-blue, H-omitted, SARS-CoV-2 interacting amino acids: ARG-pink, LYS-grey. Water and ions are omitted for better visualization. C. Percentage of different interactions contributing to the binding to the RBD of SARS-CoV-2 averaged over all the binding modes. Polar - red: interaction with polar amino acids; hydrophobic - white: interaction with hydrophobic amino acids; charge - blue: interaction with positively charged amino acids. C-cellobiose (12e); L-lactose (15e). D. Free energy of binding for GDs (12d, 15d) and SGDs (12e, 15e) with RBD of SARS-CoV-2 (two trials for each system). Top: refers to the initial placement of the GD/SGD near the ACE2 binding region. Mid: Refers to the initial placement of the GD/SGD near the HSPG binding region.

In analogy to the gp120 systems, multiple ligands in SGDs develop multivalent binding to the RBD. Moreover, 15e exhibits a stronger Coulombic coupling (percentage of charged interaction) and overall affinity to the RBD than 12d, 12e, and 15d. (Figure 14C and D). As in the gp120 systems, charged interactions originating from sulfated groups largely dominate the SGDs' binding to the

RBD, the binding affinity of 15e with the highest sulfation level (3.6/branch) is expected to be larger than the others. Importantly, the SGDs and GDs with multiple binding modes to the RBD are not designed to be specific inhibitors. The flexibility of branches of the dendrimers facilitates multivalent binding to the the RBD, which causes different conformational changes to the the RBD. The SGDs could work as broad-spectrum antivirals against HIV, SARS-CoV-2, and other possible viruses.

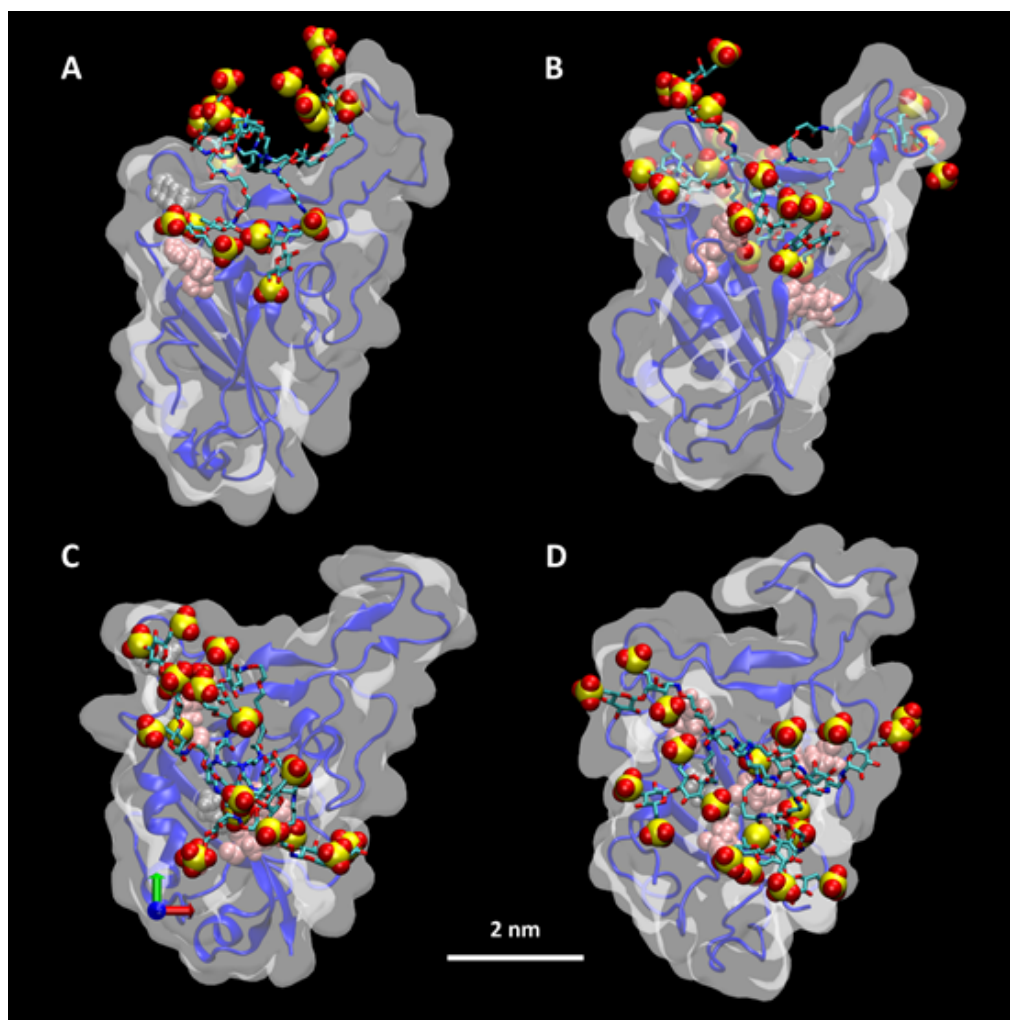


Figure 15: Cellobiose SGD binding with RBD of SARS-CoV-2. The coloring scheme: C - cyan, O - red, S - yellow, N - blue, H - omitted, interacting ARG- pink, LYS- grey. Water and ions are omitted for better visualization (four binding modes A, B, C and D).

In addition to SGD and GD, the hybrid octavalent GDs (HGDs) as conceptional compounds were simulated with both sulfated and un-sulfated ligands, as shown in Figure 17 for Cellobiose HGD

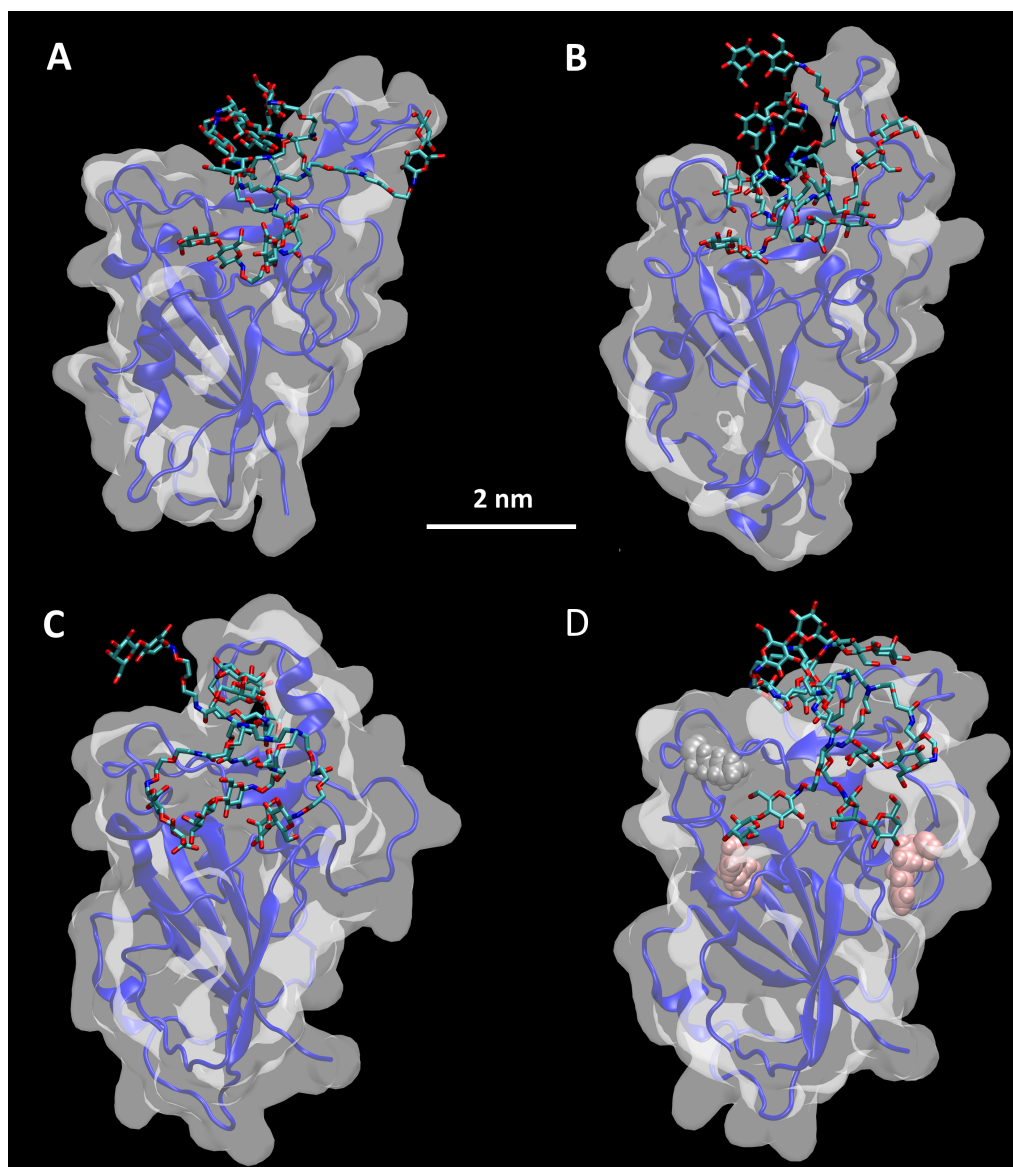


Figure 16: A and B: Cellobiose GD binding with RBD of SARS-CoV-2. C and D: Lactose GD binding with RBD of SARS-CoV-2. The coloring scheme: C - cyan, O - red, S - yellow, N - blue, H - omitted, interacting ARG- pink, LYS- grey. Water and ions are omitted for better visualization.

(C-HGD) and Lactose HGD (L-HGD). The sulfation level is the same in C/L-HGD (3.0/branch). Although the octavalent HGDs have more ligand branches than the hexavalent SGDs, only four of their branches are sulfated, while all six branches are sulfated in SGD. Figure 18 shows that the percentages of charged interactions are comparable in the cases of 15e, C-HGD and L-HGD due to the compensation of non-sulfated ligands in HGDs. As discussed in the gp120 systems, charge interaction dominates the binding, the overall binding affinities of C/L-HGD are expected to be comparable to 15e (Figure 14 and Figure 15). HGDs can target both the top and middle parts of RBD simultaneously, which could be promising inhibitors inhibiting both the specific binding of ACE2 to the top of RBD and non-specific binding of HSPG to the middle of RBD.

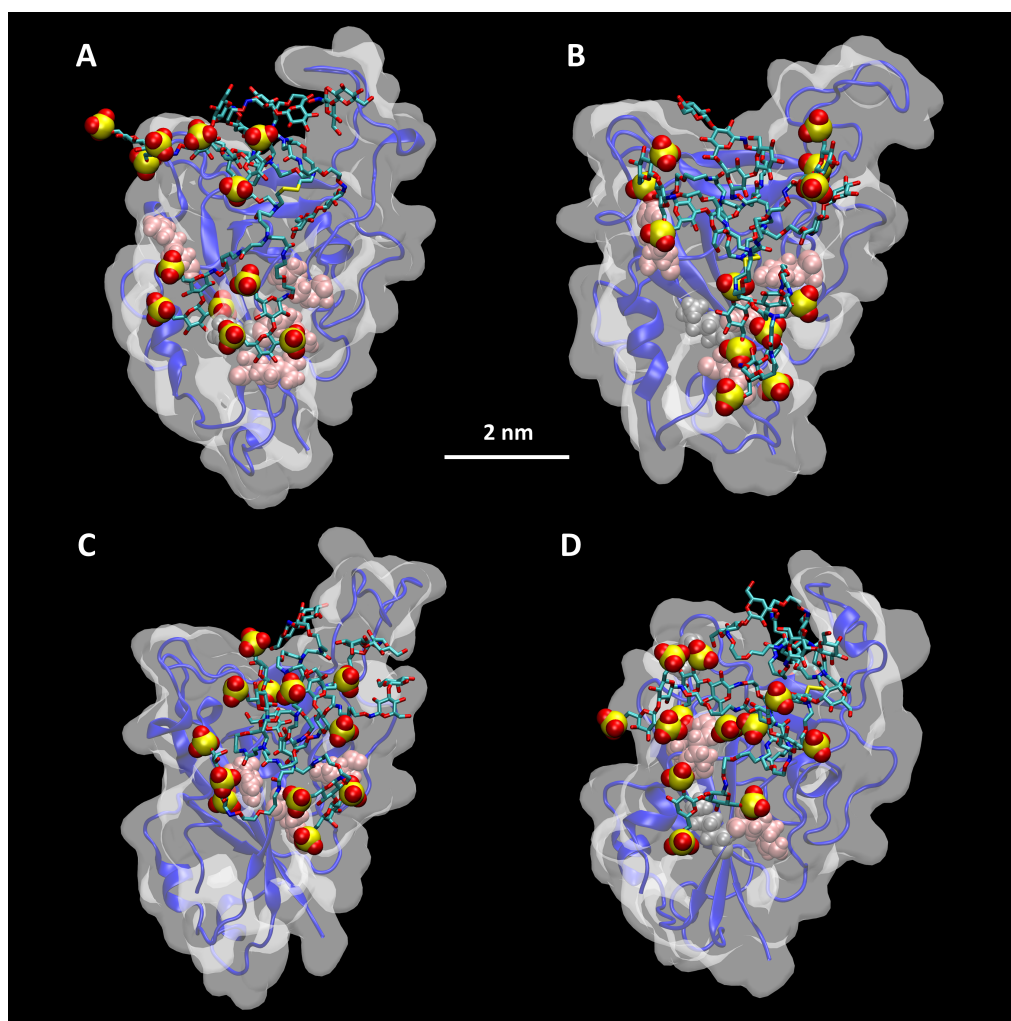


Figure 17: A and B: Cellobiose HGD binding with RBD of SARS-CoV-2. C and D: Lactose HGD binding with RBD of SARS-CoV-2. The coloring scheme: C - cyan, O - red, S - yellow, N - blue, H - omitted, interacting ARG- pink, LYS- grey. Water and ions are omitted for better visualization.

Conclusion

In summary, through MD simulations, we found that different binding affinities (K_d) preserved by different SGDs are not driven by their sulfonation levels. Sulfate groups can increase the binding strength of SGDs towards V3 loop by electrostatic interactions, but they are not the only factor controlling the various efficiency of binding. Multivalency plays important roles in the strengthening of binding between protein-protein or inhibitor-protein interactions [6,8–10]. Here, the oxime-linked

hexavalent scaffold provides the first level multivalency with additional multivalency provided by the disaccharide or trisaccharide terminus. Orientations of hydroxyl groups and linkage between units are delicate factors determining the binding strength of the designed SGDs/GDs. For the inhibiting of HIV-V3 loop, galactose terminus and β 1-4 linkage are found to be the factors causing the higher binding affinities. However, the additional multivalency cannot be improved by just increasing the number of sugar units in the branch of SGDs. An optimization of spatial structure of the SGD terminal groups can be done by adjusting number of sugar units, polar group orientations, and linkage, which is also essential for designing better SGDs.

The best SGD (15e) in binding with gp120 also presents promising binding affinity towards SARS-CoV-2. The binding of SGDs against SARS-CoV-2 is also largely determined by the number of sulfate groups in SGDs as analyzed in the case of gp120. Although HGDs could not provide a significantly higher binding affinity towards RBD than SGDs, they could target both the top and middle part of RBD. The design of the HGDs could be improved by increasing the sulfation level to strengthen the Columbic interaction or increasing the overall valency.

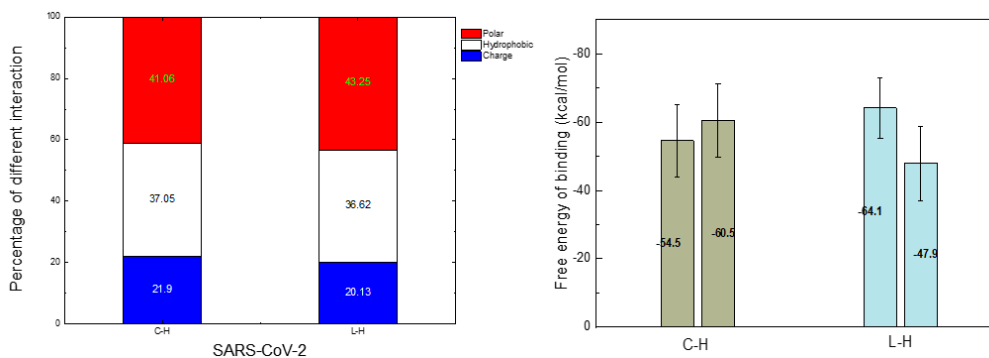


Figure 18: Left: Percentage of different interactions contributing to the binding between HGDs and RBD of SARS-CoV-2. Polar: interaction with polar amino acids; hydrophobic: interaction with hydrophobic amino acids; charge: interaction with positively charged amino acids. Right: The free energy of binding for HGDs targeting RBD of SARS-CoV-2. C - Cellobiose; L - Lactose; H - hybrid (two trials for each case).

CHAPTER 4

DESIGN OF INHIBITORS AGAINST CANCER AND VARIOUS VIRAL PATHOGENS

(Previously published as Jeong, W.-j., Bu, J., Han, Y., Drelich, A. J., Nair, A., Král, P., Hong, S. Nanoparticle Conjugation Stabilizes and Multimerizes β -Hairpin Peptides To Effectively Target PD-1/PD-L1 β -Sheet-Rich Interfaces. *Journal of the American Chemical Society* **142**, 1832 (2020); Cagno, V., Andreozzi, P., D'Alicarnasso, M., Silva, P. J., Mueller, M., et.al. Broad-Spectrum Non-Toxic Antiviral Nanoparticles with a Virucidal Inhibition Mechanism. *Nature Materials* **102**, 195 (2018); Jones, S. T., Cagno, V., Janeček, M., Ortiz, D., Gasilova, et.al. Modified Cyclodextrins as Broad-Spectrum Antivirals. *Science Advances* **6**, eaax9318 (2020); Qian, E. A., Wixtrom, A. I., Axtell, J. C., Saebi, A., Jung, D., et.al. Atomically Precise Organomimetic Cluster Nanomolecules Assembled via Perfluoroaryl-Thiol SNAr Chemistry. *Nature Chemistry* **9**, 333 (2017); Qian, E. A., Han, Y., Messina, M. S., Maynard, H. D., Král, P., Spokoyny, A. M. Multivalent Cluster Nanomolecules for Inhibiting Protein-Protein Interactions. *Bioconjugate Chemistry* **30**, 2594 (2019); Stauber, J. M., Qian, E. A., Han, Y., Rheingold, A. L., Král, P., Fujita, D., Spokoyny, A. M. An Organometallic Strategy for Assembling Atomically Precise Hybrid Nanomaterials. *Journal of the American Chemical Society* **142**, 327 (2020).)

In this chapter, different nanomaterials presenting multivalent binding properties were studied. Peptide-conjugated dendrimers, modified NPs and CDns, functionalized Boron clusters were simulated to clarify their binding modes to specific targets. Working mechanisms of antiviral NPs and CDns were proposed based on MD simulations.

4.1 Peptide-conjugated dendrimers as cancer immunotherapies

Adapted from Ref. [5] (*J.Am.Chem.Soc.* 2020, 142, DOI:10.1021/jacs.9b10160) with the permission from ACS Publishing Groups.

Introduction

PD-1 is an immunoinhibitory receptor which is expressed on activated T cells. PD-L1 is the ligand targeting PD-1 which are often expressed by tumor cells [149,150]. The binding of PD-L1 to PD-1 will disable the anticancer immunity [151]. As the interface for proteins binding is very wide and flat, small molecules are less likely to inhibit the binding of PD-L1 to PD-1 [152]. Most of the anti PD-1/PD-L1 agents are based on monoclonal antibodies which are limited by their low stability and high cost and complexity in manufacturing [153]. Using peptide segments extracted from proteins is a promising method to achieve high affinity and specificity to their targets [154,155]. However, peptides extracted from proteins are usually unstable with deformed secondary structure in solution which hinder their binding capabilities [156]. To further improve the stability of peptides, stapling approach, molecular self-assembly and bio-inorganic hybridization methods were used [157–159].

In this study, a novel PD-1/PD-L1 inhibitor was designed based on the unnatural peptides (extracted from PD-1) optimized by Maute et. al. [160,161]. The PD-1 peptides were conjugated to the surface of dendrimers which provide multivalent binding modes to their targets, PD-L1 proteins on tumor cells. The dendrimer surface also support the secondary structure of the PD-1 peptides, which were analyzed by MD simulations. We proposed that the peptide-conjugated dendrimers could provide competitive binding with PD-L1 as monoclonal antibodies for the recovery of antitumor immunity.

Experimental results

"The Surface Plasmon Resonance (SPR) analysis revealed that G7- β H2_mt showed 5 orders of magnitude higher PD-L1 affinity than β H2_mt (K_D of 2.75×10^{-9} M vs 1.19×10^{-4} M), which is comparable to that of whole α PD-L1 antibody (K_D of 2.09×10^{-9} M), as shown in Figure 19 B, C and D. It is noteworthy that the dissociation rate constant (kd) of G7- β H2_mt was decreased by 180 times, as compared to the free peptide, although there were only 30 peptides per dendrimer. This nonlinear enhancement in binding is characteristic of the multivalent binding effect; that is, a multivalent object has a higher rebinding chance to target molecules than its monovalent counterpart (statistical rebinding mechanism)" [5].

MD simulations of peptide-conjugated dendrimers

Methods

The peptides used in the simulations were described by a CHARMM36 [64] forcefield, while the dendrimers were described by a CHARMM general forcefield [68]. The PME [62] method was used for the evaluation of long-range Coulombic interactions. The time step was set to 2.0 fs. The simulations were performed in the NPT ensemble ($p = 1$ bar and $T = 300$ K), using the Langevin dynamics ($\gamma_{\text{Lang}} = 1 \text{ ps}^{-1}$). After 2,000 steps of minimization, ions and water molecules were equilibrated for 2 ns around peptide conjugated dendrimers, which were restrained using harmonic forces with a spring constant of $1 \text{ kcal}/(\text{mol } \text{\AA}^2)$. The last frames of restrained equilibration were used to start simulations of free peptide conjugated dendrimers.

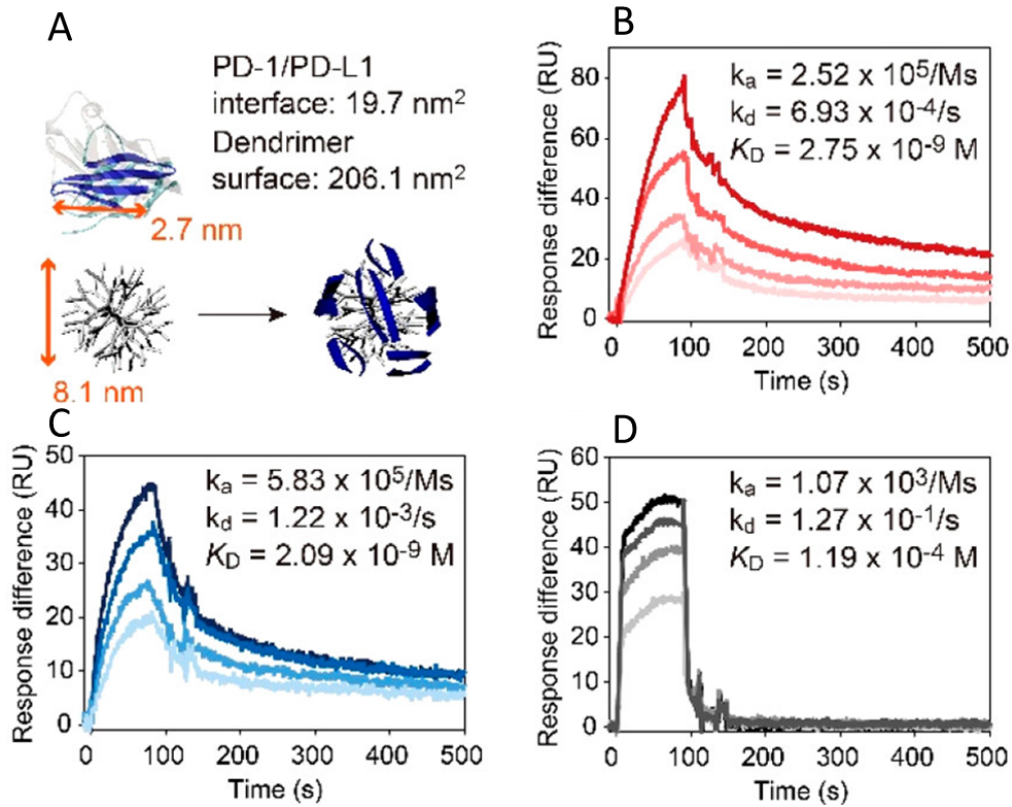


Figure 19: (A) Size comparison among the β H2_mt peptide, G7 poly(amidoamine) (PAMAM) dendrimer, and PD-1/PD-L1 interface, indicating that the dendrimer surface accommodates multiple peptides being separated by enough spatial distance for binding; Concentration-dependent binding kinetics of (B) G7- β H2_mt conjugates (45, 90, 180, 270 nM), (C) α PD-L1 antibodies (25, 50, 100, 200 nM), and (D) free β H2_mt peptides (17, 25, 33, 42 μM) to PD-L1. β H2_mt:HVVWHRESPSGQTDTKAA

Simulations of β H_mt upon conjugation with a G5 PAMAM dendrimer

To support the experimental results about the structure of peptide conjugated dendrimer, we performed molecular dynamics (MD) simulations using a single β H2_mt peptide-generation five (G5) PAMAM dendrimer conjugate. Note that G5 PAMAM dendrimer, instead of larger G7, was used for efficient computing time. The peptide behaviors on the surface of a dendrimer were compared for 500 ns from initially (1) extended and (2) folded β H2_mt (Figure 20A and B). β H2_mt in physiological solution is also illustrated in Figure 20C. In contrast to free β H2_mt exhibiting both folded and

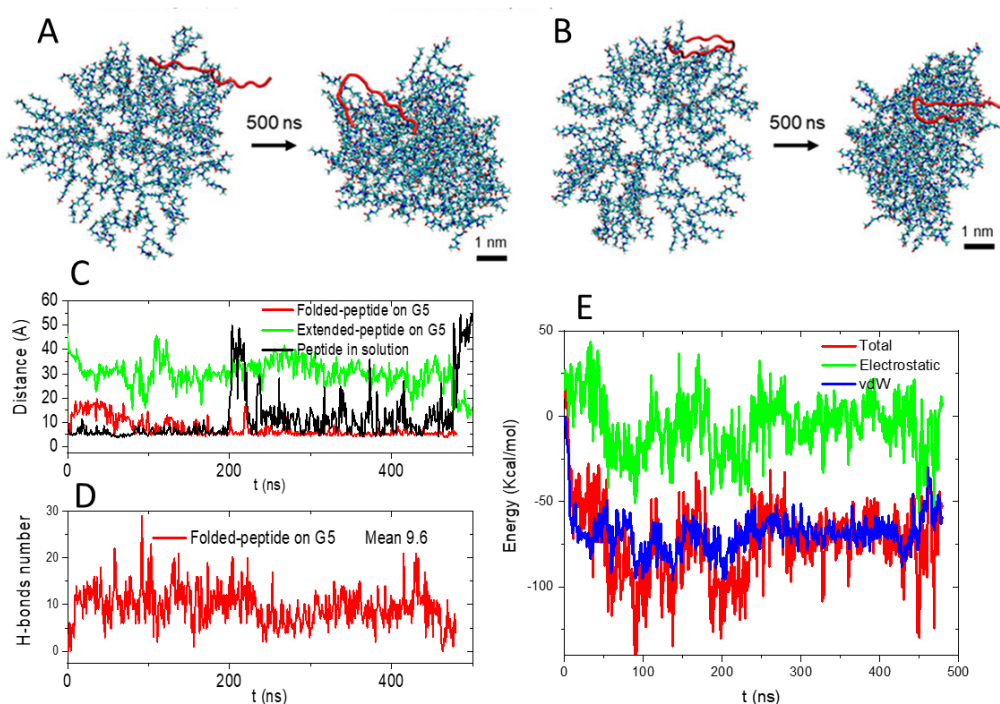


Figure 20: (A) initially extended β H2_mt versus (B) initially folded β H2_mt (β H2_mt in red ribbon; atoms in G5: oxygen in red, carbon in cyan, nitrogen in blue, and hydrogen in white). Molecular dynamics (MD) simulation study. (C) Distance between N- and C-termina of a β H2_mt molecule. (D) The number of hydrogen bonds (H-bonds) between a folded β H2_mt backbone and a G5 PAMAM dendrimer. (E) van der Waals and electrostatic energy between a folded β H2_mt and a G5 PAMAM dendrimer. The dielectric constant was set to one for electrostatic energy measurement to show the trend clearly.

extended conformations in the solution, the initially extended peptide bent to a folded structure, and initially folded β H2_mt stably maintained the folded conformation on the dendrimer surface. Interestingly, the peptide generated various intermolecular forces with the dendrimer surface, including hydrogen bonds, electrostatic interactions, and van der Waals interactions, while maintaining the hairpin structure (Figure 20D and E). In general, formation of such molecular interactions with a surface is known to reduce the structural stability of proteins. However, β H2_mt is an isolated peptide segment that is originally exposed to multiple molecular interactions within the entire PD-1 protein structure. These molecular interactions seem to contribute to the further stabilization of

the peptide molecule in a folded conformation on the dendrimer surface, in addition to the reduced entropy cost.

Conclusion

Experimental results show that the peptide-conjugated dendrimers exhibiting significantly enhanced target affinity (avidity) and a strong PD-1/PD-L1 inhibitory effect comparable to that of PD-L1 antibodies. MD simulations revealed that the dendrimer can stabilize the conformation of peptides by various interactions including: H-bonding, electrostatic and VdW energies. The stable conformation of peptides could provide geometry matching to their targets which improve their specificity. Here, the dendrimer offers a platform accommodating more than one peptide which facilitate the multivalent binding modes. This study provides a newly engineered peptide–dendrimer system for effective regulation of protein interactions which can be used to tackle various diseases, including immune checkpoint blockade for cancer therapy [5].

4.2 Modified nanoparticles and cyclodextrins as broad-spectrum antivirals

Adapted from Ref. [6, 7] (*Nat. Mater.* 2018, 6. DOI: 10.1038/nmat5053; *Sci. Adv.* 2020, 6. DOI: 10.1126/sciadv.aax9318) with the permissions from Nature and Science Publishing Groups.

Introduction

Viruses cause negative effects to our society which can infect food crops and livestock and also cause serve health impacts on human. Effective drugs are needed to inhibit viral invasion and replication, especially when prevention fails. However, most antivirals are limited by the problems of permeability, toxicity, virus specificity [162], and/or reversible (virustatic) effect [163–165]. By

mimicking the cellular receptor HS, broad-spectrum antivirals were developed including heparin or heparin-like materials [166,167]. But the clinical efficacy remains unclear due to the recovery of viral infectivity upon dilution of the drug [163–165]. Here, a non-toxic drug which can disable the virus irreversibly, i.e., a virucidal drug, is needed to provide long lasting antiviral effects [168].

Prof. Stellacci’s group synthesized highly sulfonated gold nanoparticles (AuNPs) which display broad-spectrum virucidal properties *in vitro*, *ex vivo*, and *in vivo* [6]. However, there are concerns about usage of gold nanoparticles due to the unknown clearance mechanism and possible long-term toxicity [169].

Cyclodextrins (CDns) are naturally occurring glucose derivatives, which were used in many commercial applications including drug delivery, air fresheners, cosmetics, and food [170]. Sulfonated CDs were found to be virustatic and specific only to HIV [171–173]. In this work, highly sulfonated chemicals were attached to a U.S. Food and Drug Administration (FDA)–approved CDn scaffold. The functionalized CDns exhibited broad-spectrum antiviral properties and highly efficient virucidal effect *in vitro*, *ex vivo*, and in an animal model. The possible working mechanism is explained by MD simulations.

Modified AuNP antivirals

As the highly sulfonated AuNPs were first found to have broad-spectrum antiviral properties, we briefly present some of the results from [6]. To elucidate the fate of the viruses after NPs binding, a series of transmission electron microscopy (TEM) studies on HSV-2 exposed to modified AuNPs were performed. Figure 21A and B show cryo-TEM images of viruses with and without AuNPs. Figure 21C and D show the percentage of cells infected by HSV-2 and HPV16 with their IC_{50} s.

"To understand how MUS-type (mercapto-undecane sulfonic acid) AuNPs can induce irreversible changes upon interaction with virus, we performed MD simulations of different AuNPs interacting with the capsid of HPV-16, Figure 21E. The simulations were performed in physiological solutions, where NPs were placed close to the solvent exposed HSPG-binding sites (amino acid residues K278, K356, K361, K54 and K59) [174] at the surface of HPV-16 capsid L1 proteins. The simulation results for MUS:OT-NP 2.4nm cores, with two types of ligands (MUS (mercapto-undecane sulfonic acid) and OT (1-octanethiol)) in their ligand shell, 50:50 in composition, are shown in Figure 21E. They demonstrate that selective multivalent binding develops between the negative sulfonate groups of MUS:OT-NP and the positive HSPG binding lysine residues of L1 capsid protein complexes from the HPV-16 capsid. Within 50-80 ns, on average 5-6 local charge interactions form between NP terminal sulfonate groups and L1 HSPG binding sites, which are supported by a similar number of non-local coupling contacts between nonpolar alkyl chains of NP ligands and L1 proteins. Each of the 5-6 sulfonate groups binds to positively charged amine groups of lysine residues with a relatively large Gibbs free energy around 6 kcal/mol, while the non-polar ligand chains acquire on average a non-local total binding energy about 21 kcal/mol.

This multivalent binding can induce large stresses and deformations of the L1 complexes. Given the local nature of binding of the sulfonated groups, we can use this binding to estimate the effective force with which the NPs act on the L1 complexes. By considering the increase of binding energy, during the NP motion on the capsid surface, we can get an effective force that drives the NP binding and capsid deformation process forwards (Figure 21E). By combining the above Coulombic energy change of -28 kcal/mol and considering, at the beginning of simulations, NP interacting with a lysine, with a distance of 10.4 Å over which the MUS:OT-NP moves, while acquiring this binding energy, we obtain an effective force of ~ 189 pN. This force can deform the L1 complexes and even disturb the

relative position of one L1 pentamer with respect to a neighbouring L1 pentamer. This disruption of viral capsids by AuNPs with a multivalent Coulombic binding is analogous to pore formation in neutral membranes by Ca^{2+} ions [175]” [6].

Modified CDns antivirals

To test whether a modified CDn (CD1; Figure 22A) has antiviral activity like its AuNP counterpart [6], Prof. Stellacci's group used sodium MUS to synthesize a modified CDn (CD1) that exposes the sulfonate groups in a similar manner. In addition, two other modified CDns were synthesized. To alter the length of the linker, CD2 was synthesized (Figure 22A), which bears a seven-carbon sulfonated alkyl chain.

While CD1 showed strong inhibition of the growth of HSV-2, with an EC_{50} of $28.51 \pm 2.319 \mu\text{g/ml}$, CD2 showed no significant effect (Figure 22B). To alter the nature of the linker, CD3 with a nonalkyl linker and similar overall length to MUS was synthesized. The hypothesis was that removing the flexibility of the linker would result in stronger binding to the virus and improved overall antiviral effect. In a dose response assay, CD3 displayed enhanced antiviral effects, with an approximately threefold reduction in EC_{50} over the time course of a single-cycle infection compared to CD1. To determine whether the observed inhibition of HSV-2 growth was virustatic or virucidal, we pretreated viral solutions with CD1, CD2 and CD3. CD1 was highly virucidal, but this effect was markedly reduced when using CD2 and CD3 (Figure 22C). These findings for the first time assert the utility of long flexible linkers to provide a virucidal mode of action. CD1 also displayed broad-spectrum activity against a wide range of viruses belonging to different families (experimental results are omitted here).

MD simulations of CDns coupled with gB proteins

Systems and methods

MD simulations were performed for CDns interacting with Glycoprotein B (gB) of HSV. We extended the CDn categories with new CDns which are not present in experimental results. Six

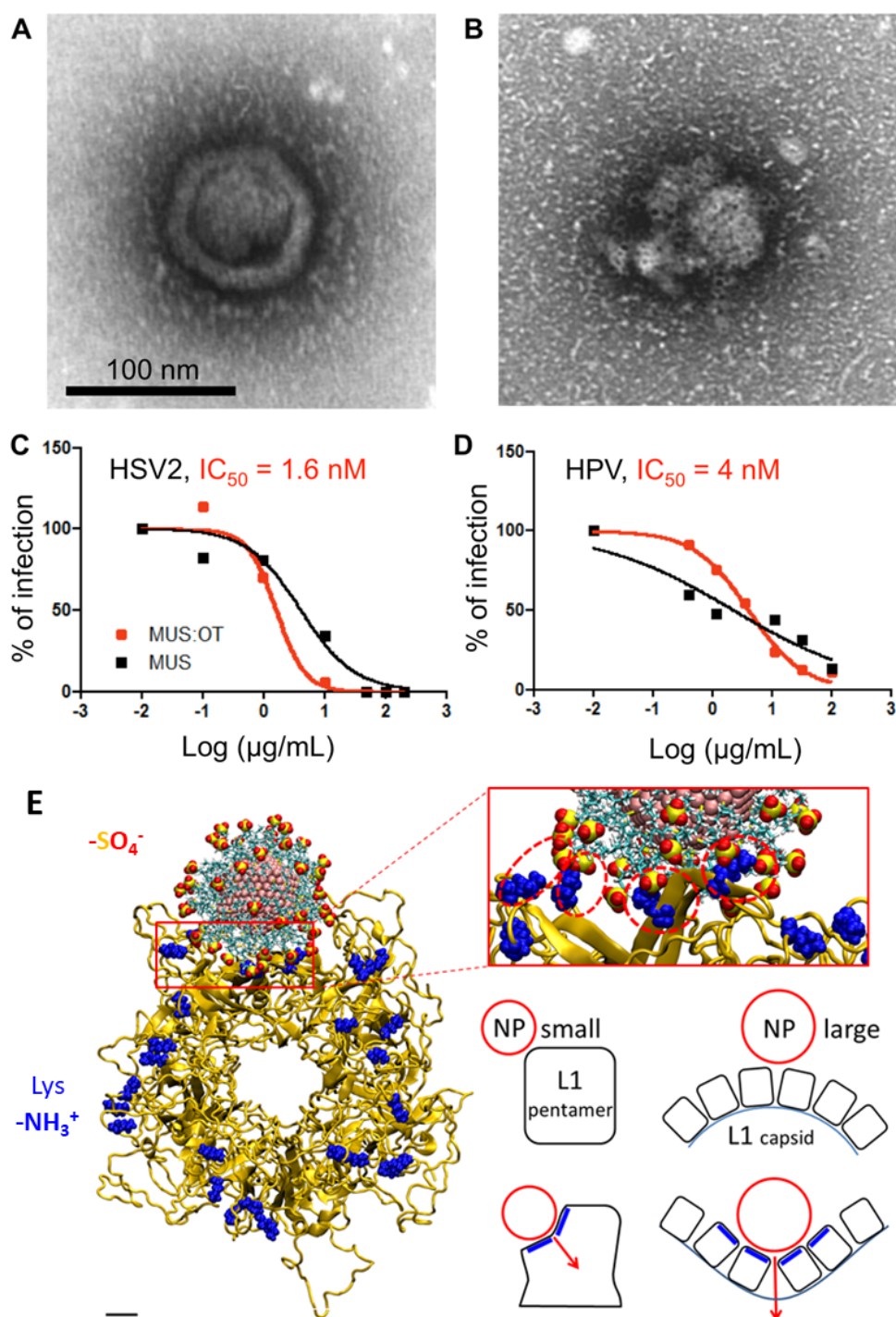


Figure 21: (A) Human Papillomavirus (HPV) by itself and (B) after 2 hours of incubation with 5 nm MUS:OT-NPs. Percentage of cells infected by HSV-2 (C) or HPV-16 (D), in dependent on the NPs concentration in the solution and the type of NP-ligands. (E) Top view of a small sulfonated MUS:OT-NP (2.4 nm core) selectively binding to HPV capsid L1 protein pentamer, after 25 ns of simulations; bottom right is the proposed mechanism of the NPs. Scale bars are 1 nm.

different β CDns including experimentally tested CDns were simulated. They are CD1 with 7 MUS ligands, Cyc5s with 5 MUS ligands, Cyc3s with 3 MUS ligands, Pegc7 with 7 PEG-SO₃ ligands ($CH_2 - (CH_2 - CH_2 - O)_2 - CH_2 - CH_2 - SO_3$), CD2 and CD3. The structure of gB is based on the PDB 5FZ2 [176]; each protein unit of the tetramer has residues 142 to 476, and the missing atoms in the structure were added with the VMD [73] plugin psfgen.

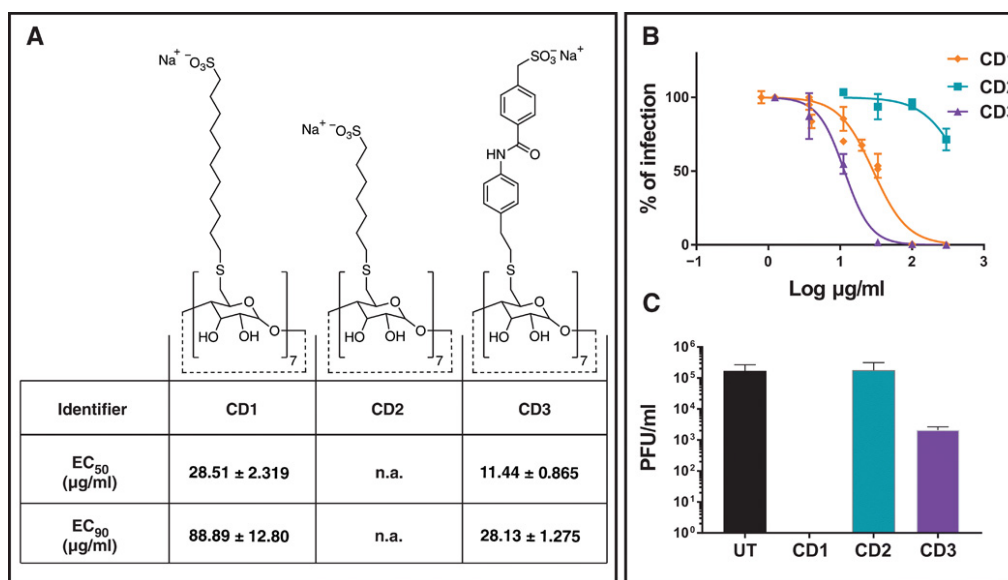


Figure 22: Structures and virucidal data for modified CDns. (A) Structures of modified CDns and relative effective concentrations of inhibition of HSV-2 growth. (B) Dose response assay in Vero cells. Serial dilutions of CD1, CD2, and CD3 were incubated for 1 hour at 37°C with HSV-2 and then added on cells for 2 hours at 37°C. Subsequently, cells were washed and overlaid with medium containing methylcellulose. Plaques were counted 24 hpi. Percentages of infections were calculated by comparing the number of plaques in treated and untreated wells. (C) Virucidal assays: HSV-2 was incubated with media or CDns (CD1, CD2, and CD3) at 300 µg/ml and then serially diluted on Vero cells to a negligible concentration of compound. Results are shown as the mean and SEM of three (for CD1) and two (for all other compounds) independent experiments. UT, untreated; n.a., not assessable.

In the simulations, 10 CDn molecules were initially placed near the fusion loops of gB and solvated in a 0.15 M NaCl solution. The key amino acid residues of gB fusion loop that are responsible for the cell fusion activity are known (Trp 174, Phe 175, Gly 176, Tyr 179, Ala 261, His 263, Arg

264) [177]. Unit cells of the simulated systems, containing CDns and gB in aqueous solution, had in total between 400,000 and 500,000 atoms.

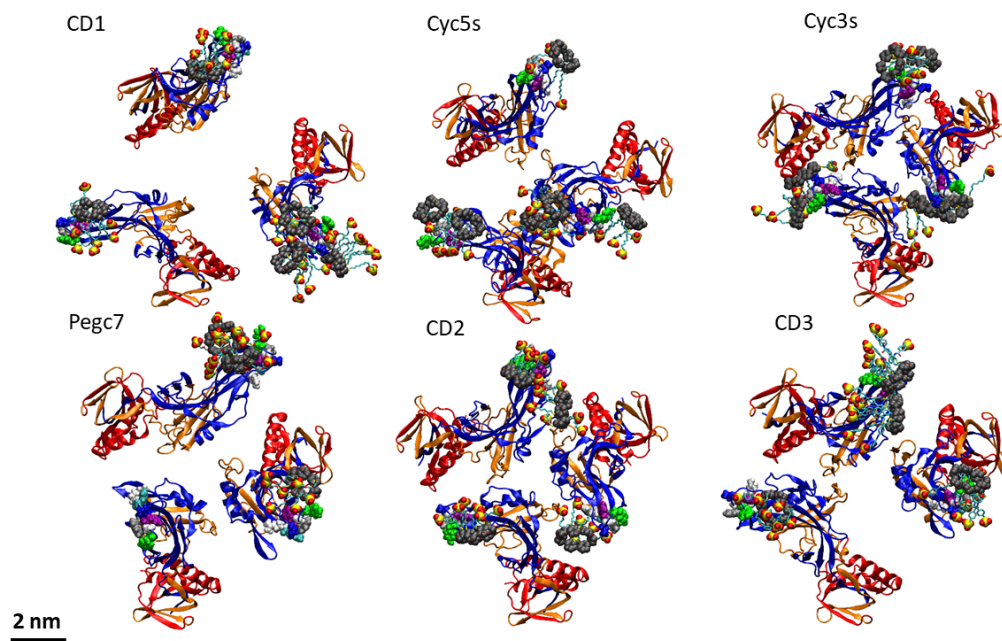


Figure 23: Snapshots of different β CDn interacting with gB after 55 ns of MD simulations. (CDns: gray rings with ligands in cyan; Trp 174: gray; Phe 175: purple; Gly 176: white; Tyr 179: green; Ala 261: blue; His 263: cyan; Arg 264: white)

The CDn ligands were described with the CHARMM general forcefield [69] and proteins were described with the CHARMM36 protein forcefield [63,64]. The simulations were performed with NAMD [58]. The PME method [62] was used for the evaluation of long-range Coulomb interactions. The time step was set to 2.0 fs, and long-range interactions were evaluated every 1 (van der Waals) and 2 timesteps (Coulombic). After 2,000 steps of minimization, ions and water molecules were equilibrated for 2 ns around gB and CDns, which were restrained using harmonic forces with a spring constant of 1 kcal/(mol Å²). For all the systems, the last frames of restrained systems were used to start simulations of partially restrained proteins (restraints were placed on the atoms of the bottom part of the protein) and free CDns. All the simulations were performed for 50 ns in the NPT

ensemble (pressure $p = 1$ bar and temperature $T = 300$ K), using the Langevin dynamics ($\gamma_{\text{Lang}} = 1 \text{ ps}^{-1}$).

Binding results for CDns

Figure 23 shows the snapshots of CDns interacting with gB at 50 ns. In each simulation, there are 10 CDns but only those bound to key amino acids of gB are shown. The numbers of bound CDns are quantified in Figure 24. CD1, Cyc5s and Cyc3s show similar numbers of bound CDns, while Pegc7, CD2 and CD3 have fewer CDns bound to the fusion loops (Figure 24A). As CD1 has more ligands than Cyc5s and Cyc3s, its negatively charged groups can interact with more residues of the fusion loops. When the charged groups accumulate on the fusion loops, they may increase the distance between the fusion loops due to the repulsion between charged groups in CDns. This is verified by Figure 24B, where the average distances $((d1+d2+d3)/3)$ between fusion loops of gB (the open tetramer) are far bigger in CD1 than in other cases. Cyc3s has the fewest ligands leading to the smallest average distance between the fusion loops. The separation or opening of the gB tetramer may reduce the fusion activity of gB. The binding of CDns to the fusion loops can block the initial virus entry to the cell.

Figure 24C shows the averaged binding energy per CDn to the key amino acids of gB fusion loops obtained from the last 10 ns of simulations, where the binding energy is composed of vdW and electrostatic contributions. The time averaged binding energy per CDn is -16.55 kcal/mol for CD1, -15.96 kcal/mol for Cyc5s, -15.47 kcal/mol for Cys3s, -14.55 kcal/mol for Pegc7, -15.48 kcal/mol for CD2 and -17.50 kcal/mol for CD3. Despite the fact that the binding energy shows a little difference among the six cases, it seems to have a clear trend. CD3 with Ar-ArSO3 ligands shows the strongest binding. CDns with long and more MUS ligands have a larger binding energy, while CDns with hydrophilic or fewer MUS ligands show smaller binding energies. Although the CD3 shows the

strongest binding energy with the fusion loop of gB, the binding number of CDns is smaller than that of CD1, Cys5s and Cys3s, which leads to smaller tetramer opening in the case of CD3.

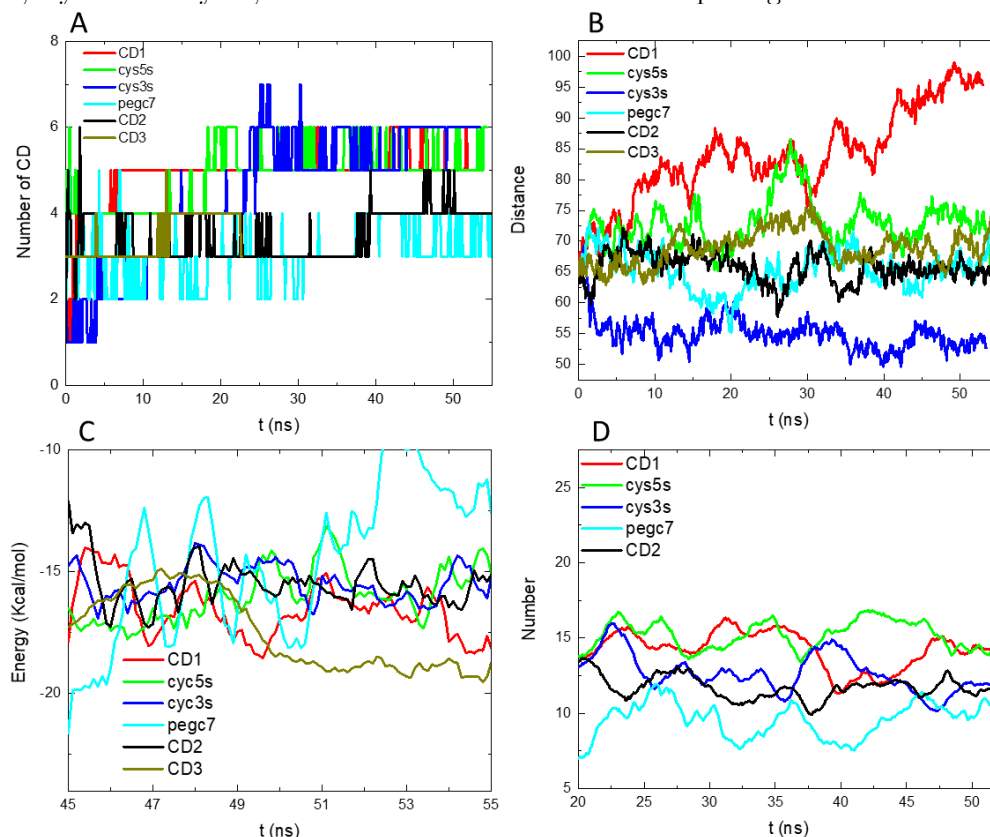


Figure 24: (A) Number of CDn within 5 Å of fusion loop key amino acids (Smoothing was performed to noisy data by adjacent averaging method). (B) Average distance between fusion loops of gB. (C) Averaged binding energy per CDn to gB fusion loop (Smoothing was performed to noisy data by adjacent averaging method). (D) Number of interacting alkyl groups per CDn with key amino acids of the fusion loop.

Figure 24D shows the number of interacting alkyl groups (within 5 Å of key amino acids of fusion loop) per CDn. The average number of interacting alkyl groups in the last 35 ns is 14 for CD1, 15 for Cys5s, 13 for Cys3s, and 12 for CD2, respectively. Alkyl groups of MUS ligands mainly bind to the hydrophobic amino acids of fusion loop. The binding number of alkyl groups is slightly smaller in the Cys3s and CD2 cases due to the reduced ligand number or length.

Conclusion

In summary, we propose that virucidal action of CDns originates in both blocking of the fusion loop and the conformational distortion of gB caused by the CDn binding (here, manifested by opening of the tetramer). The stronger binding strength of CDs to gB doesn't guarantee larger binding numbers of CDns, since the interaction between CDns may cause the accumulation of CDns on the binding site. Compared with CD3, CD1 shows less binding strength to gB but a larger binding number of CDns, which causes better blocking of fusion loop and opening of gB tetramer. As both alkyl groups and sulfonate charge groups bind to the key protein of gB fusion loop, the CDn binding is controlled by both hydrophobic and hydrophilic interactions.

4.3 Nanomolecules inhibiting protein–protein interactions

Adapted from Ref. [8–10] (*Nature Chem.* 2017, 9. DOI: 10.1038/NCHEM.2688; *Bioconjugate Chem.* 2019, 30. DOI: 10.1021/acs.bioconjchem.9b00526; *J. Am. Chem. Soc.* 2020, 142. DOI: 10.1021/jacs.9b10770) with the permissions from Nature and ACS Publishing Groups.

Introduction

Multivalency plays important roles in many biological processes [178]. In our own immune system, multivalent interactions modulate cell signaling, cell–cell interactions, and pathogen recognitions [179–181]. The specificity and affinity between glycoproteins and lectins can be significantly improved by multivalency. A model lectin concanavalin A (Con A) was selected to examine the multivalent efficiency of nanomolecule A, which use a dense layer of rigid pentafluoroaryl functional groups as scaffolds and glucose molecules as terminus. *PEG*₃₅₀ and monosaccharide (β -D-glucose) were used as control. To evaluate the application of such nanomolecules in the inhibition of viurs, DC-SIGN (dendritic cell-specific intercellular adhesion molecule-3-grabbing nonintegrin) [182] was

selected as the target. DC-SIGN plays an important role in transmitting HIV-1 to the T cells and enhancing the infection in early stages of HIV-1 invasion [183–185]. It is found to bind specifically with high-mannose glycoproteins and glycolipids. Nanomolecules C and D, with different length of scaffold, were designed to mimic those high-mannose structures. Uncovering the rules that govern the multivalent interactions between DC-SIGN and high-mannose glycoconjugates is important to design inhibitors against the DC-SIGN-dependent attachment and uptake of certain pathogens. With the development of synthesis method, it was found that the scaffold containing the phenyl group was promising [10]. Nanomolecules E, F, G, and H with phenyl scaffold and various sugar terminus were tested against their protein targets.

Experimental results

The structures of all the tested nanomolecules and their binding affinity were shown in Figure 25. Surface plasmon resonance (SPR) experiments were conducted to quantify binding interactions between the nanomolecule A and a model lectin ConA at pH 7.4. The measured binding response was dependent on the concentration of nanomolecule A in the injected sample. Furthermore, when two controls (PEG350 and β -D-glucose) were injected at the highest mass concentration of nanomolecule A (2.0 mg/L), minimal to no binding was observed. When the binding curves of nanomolecule A were fitted to the Langmuir 1:1 binding model, the K_d value was estimated to be 54 nM, which corresponds to a 6,500-fold increase in affinity when compared with the K_d between ConA and methyl D-glucopyranoside.

The binding interactions between the nanomolecules (C and D) and DC-SIGN were examined by SPR. In the first set of SPR-based direct binding experiments, the tetrameric DC-SIGN extracellular domain was immobilized on a commercial sensor chip via standard amide coupling, and

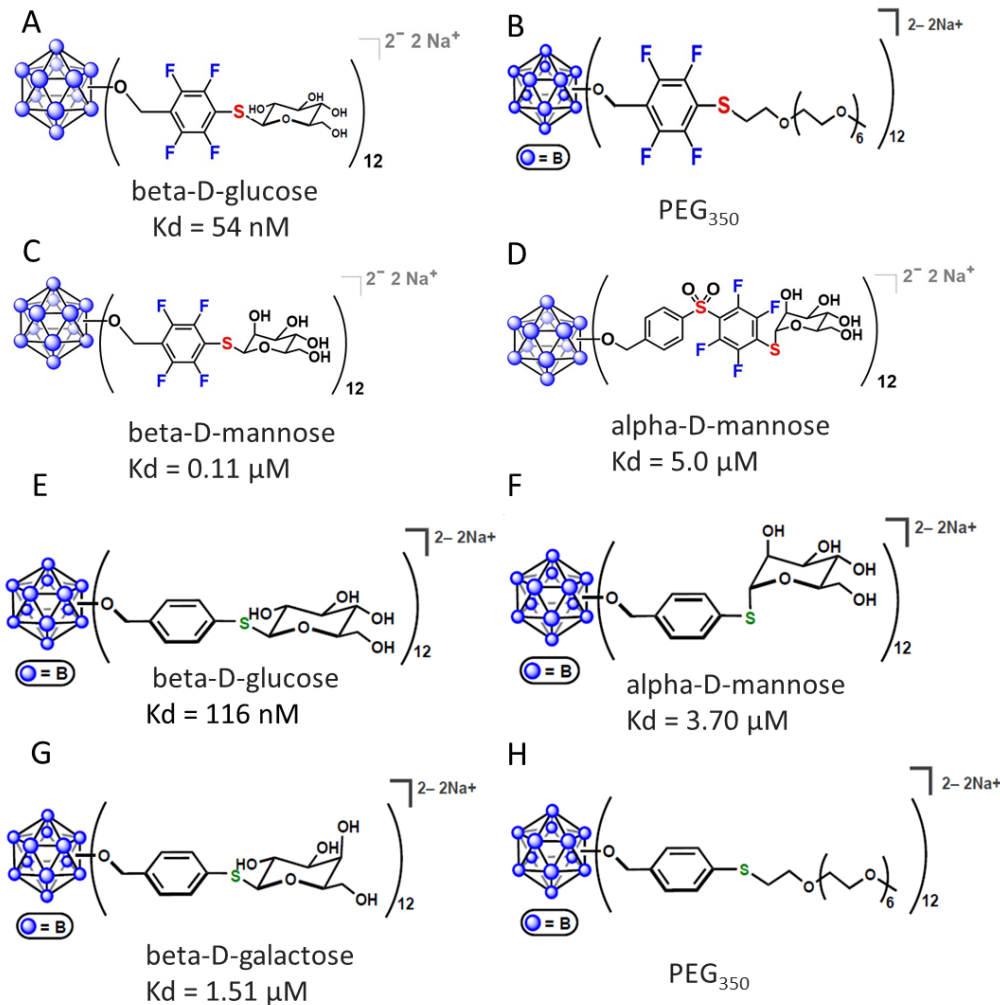


Figure 25: Structure of designed nanomolecules.

the mannose-functionalized nanomolecules C and D were injected over the protein surface for real-time visualization of their binding interactions with DC-SIGN. By fitting the Langmuir 1:1 binding model to the binding curves of the mannose-coated clusters, we estimated K_d values of $0.11 \mu\text{M}$ for nanomolecule C and $5.0 \mu\text{M}$ for nanomolecule D. Compared to D-mannose (low mM affinity), these multivalent systems exhibit avidities 3–4 orders of magnitude higher for DC-SIGN through the cluster glycoside effect.

The binding interaction of the nanomolecule E with ConA was determined to be 116 nM at pH 7.4 based on SPR binding experiments. This K_d value agrees well with the equilibrium constant determined for the previously developed dodecaborate perfluoroaryl analogue (54 nM) [186] with Con A under similar experimental conditions. When the PEGylated cluster control nanomolecule H was analyzed at the highest mass concentration of nanomolecule E evaluated (4 mg/L, 1 μ M), only minimal binding was observed, indicating that ConA binds nanomolecule E with a high degree of specificity. Similarly, a negligible response was observed when a solution of the D-glucose monomer was injected at a significantly higher concentration (40 mg/L, 200 μ M) over the protein surface, suggesting that the multivalent nature of nanomolecule E results in a dramatically enhanced binding profile per mole of saccharide.

SPR binding data reveal that nanomolecule F exhibits an enhanced dose-dependent avidity (K_d = 3.7 μ M) toward DC-SIGN when compared with the negligible responses observed for the D-mannose monosaccharide and PEGylated controls nanomolecule H at significantly higher mass concentration.

A K_d value of 1.51 μ M was determined for the binding of nanomolecule G with Stx1B by direct SPR studies. Even at high concentrations, the free D-galactose monomer does not bind to Stx1B (100 mg/L), and a phenylene-bridged disaccharide control (gal-C₆H₄-gal, 100 mg/L) fails to engage in significant binding with Stx1B as displayed by its minimal SPR response. These data suggest the multivalent binding properties of nanomolecule G are responsible for the enhancement in its binding capacity when compared with that of its mono- and divalent controls” [8–10].

MD simulations of nanomolecules coupled with target proteins

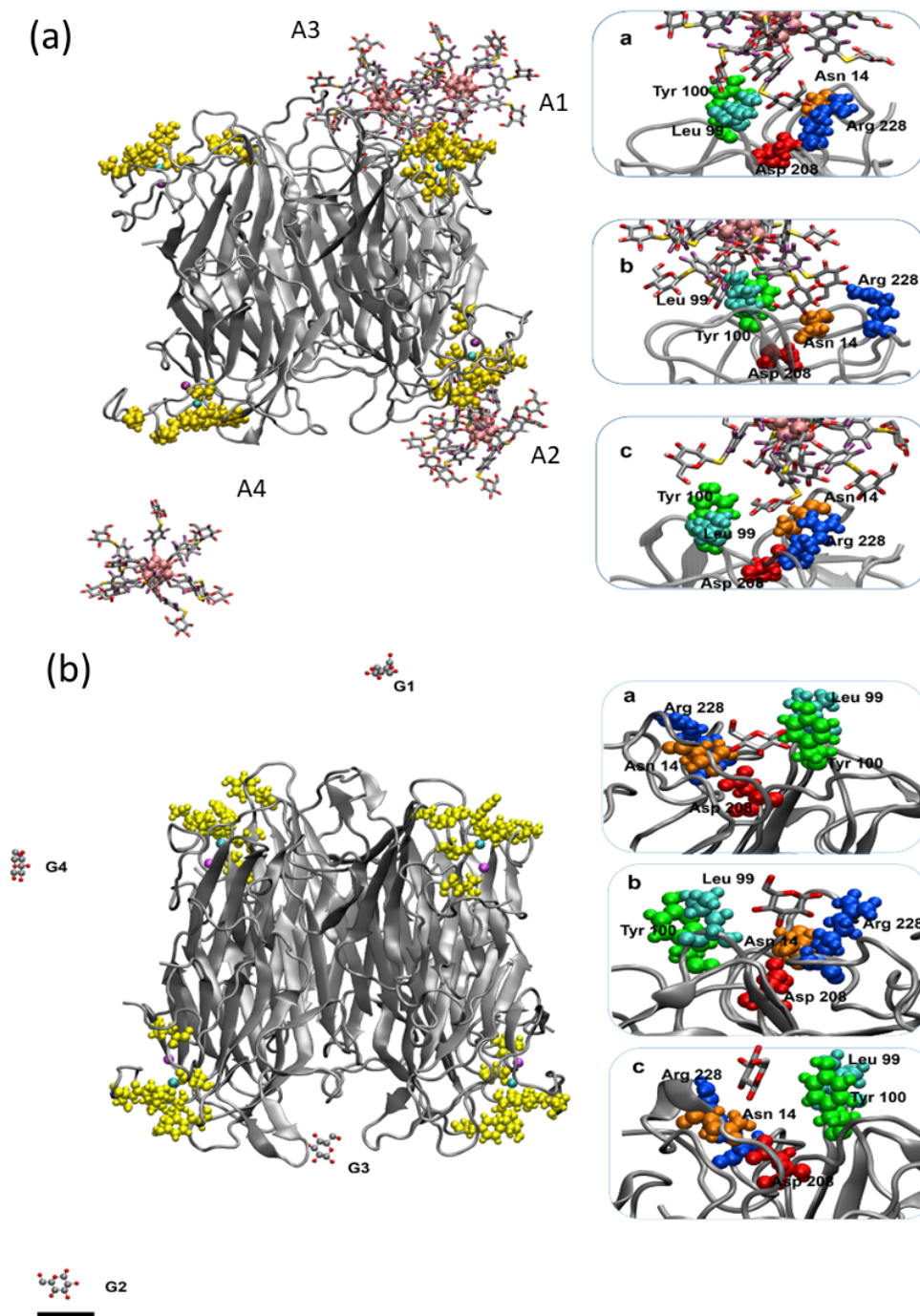
Methods

The proteins used in the simulations were described by a CHARMM36 [64] forcefield, while the organomimetic clusters were described by a CHARMM general forcefield [68]. The PME [62] method was used for the evaluation of long-range Coulombic interactions. The time step was set to 2.0 fs. The simulations were performed in the NPT ensemble ($p = 1$ bar and $T = 300$ K), using the Langevin dynamics ($\gamma_{\text{Lang}} = 1 \text{ ps}^{-1}$). After 2,000 steps of minimization, ions and water molecules were equilibrated for 2 ns around protein and cluster, which were restrained using harmonic forces with a spring constant of $1 \text{ kcal}/(\text{mol } \text{\AA}^2)$. The last frames of restrained equilibration were used to start simulations of free cluster and partial constrained protein (bottom part). The H-bonds number was analyzed by VMD [73] with a cutoff distance of 3.5 \AA and angle of 60° .

Interaction between nanomolecule A and Con A

MD simulations were performed to investigate multivalent binding of sugar-coated nanoparticles and proteins. Con A was chosen as the target protein to bind with multivalent sugar-coated nanomolecules A and monovalent β -D glucose (G), respectively.

Con A forms quaternary structures, giving at pH 7 a tetramer, having four carbohydrate binding sites (hydrogen bonds) [187]. In each Con A, up to 15 amino acids can be involved in the carbohydrate binding, while for the monosaccharide binding only five amino acids are involved, including Asn 14, Leu 99, Tyr 100, Asp 208, Arg 228. In our simulations, the tetramer structure of Con A used was based on X-ray diffraction data (PDB code 1ONA) [188]. Figure 26 shows the structures of tetramer of Con A with nanomolecule A and β -D glucose after 20 ns simulation. The metals manganese (magenta sphere) and calcium (cyan sphere) were added in Con A according to its metal



binding sites [188]. The monosaccharide binding sites are distinguished from the backbone of Con A by different colors. The Con A tetramer has four binding positions. We name the top right position as binding position 1 (B1), bottom right as B2, top left as B3, and bottom left as B4.

For the NPs binding, three nanomolecules (A1, A2 and A4) were initially put near the binding sites of chosen monomers. The last nanomolecule (A3) was placed in the cavity between the B1 and B3 binding positions. For the β -D glucose binding, three glucose molecules (G1, G2 and G3) are separately placed at the binding B1, B2 and B3 positions, while the last glucose molecule (G4) was placed between the B3 and B4 binding position. The two systems were immersed in water together with the counter-ions and the simulations were performed with NAMD [58].

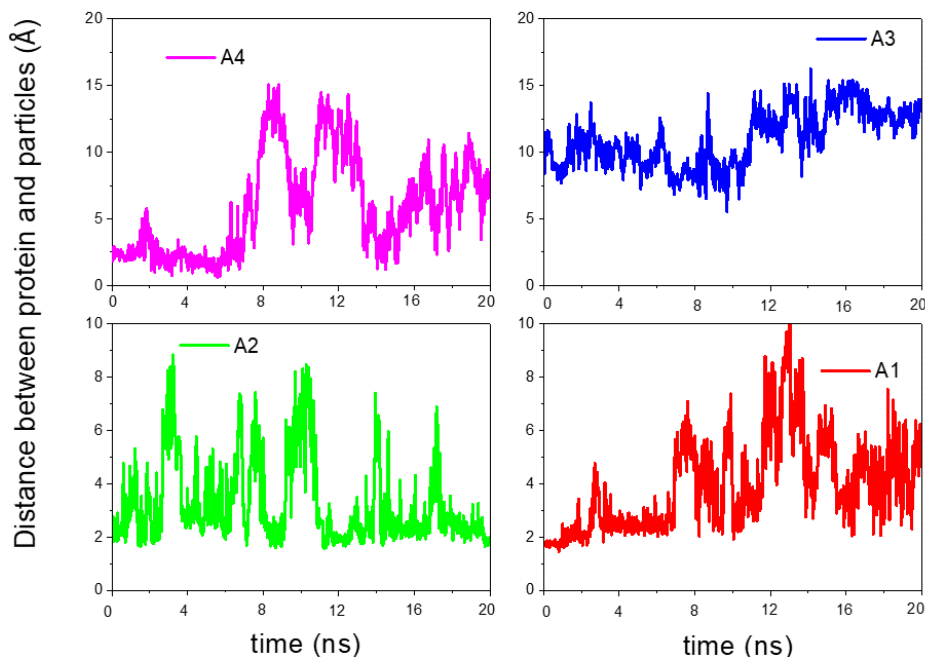


Figure 27: Nearest distances between nanomolecule A ligands and the Con A tetramer.

First, we modeled the coupling between nanomolecules A and the Con A tetramer. At each simulation time, we calculated a distance between each sugar binding site and its nearest ligand in the nanomolecule. Figure 27 shows a time-dependent distance between the nearest nanomolecule

ligands and the Con A tetramer. During the 20 ns simulations, A1 and A2 have an average distance of 4 Å, while A3 and A4 have an average distance of about 10 Å. Because the initial position of A3 is far from any binding site, it can't bind during the short simulations. From Figure 26, we can see that A3 competes with A1 for the B1 position, while A4 shows a different trend. Within 1 ns, A4 comes near to the Con A tetramer and binds to it. Then, it leaves away and binds again at 4 ns, when the binding lasts for about 4 ns. After 12 ns, A4 binds to the Con A tetramer again. Figure 27 reveals that when nanomolecules bind to the Con A tetramer, their binding distance is about 1.8-2 Å. nanomolecules occasionally gain and preserve for significant time periods these small binding distances. Figure 26 show details of A1, A2 and A4 binding to their binding sites. We can see that in all the cases only one of the nanomolecule ligands binds to the nearby binding site, composed of Asn 14, Leu 99, Tyr 100, Asp 208, Arg 228, which is the monosaccharide binding site shown in different color. Therefore, there is always one ligand of nanomolecule which performs like a monosaccharide when binding to the Con A tetramer. Because the nanomolecules have several ligands, when one ligand leaves, another nearby ligand comes and binds, which increases the binding probability of nanomolecules. In this way, nanomolecules act like multivalent binders.

In order to compare the binding ability of nanomolecules and β -D glucose systems, we simulated binding of β -D glucose and the Con A tetramer. Figure 28 shows the nearest distance between β -D glucose and Con A as a function of time. Figure 26 shows that G1 only binds to Con A at the first 1 ns and then leaves. G2 only binds at the very beginning and it doesn't bind later; G3 binds to Con A for about 4 ns at the beginning and after that it leaves away; G4 shows weak binding during the first 4 ns. The average distance between all the β -D glucose molecules and the Con A tetramer is more than 20 Å, except G3 whose average distance is about 12 Å. Figure 26 shows details of β -D glucose and the Con A tetramer binding. When β -D glucose binds to Con A, it binds to the

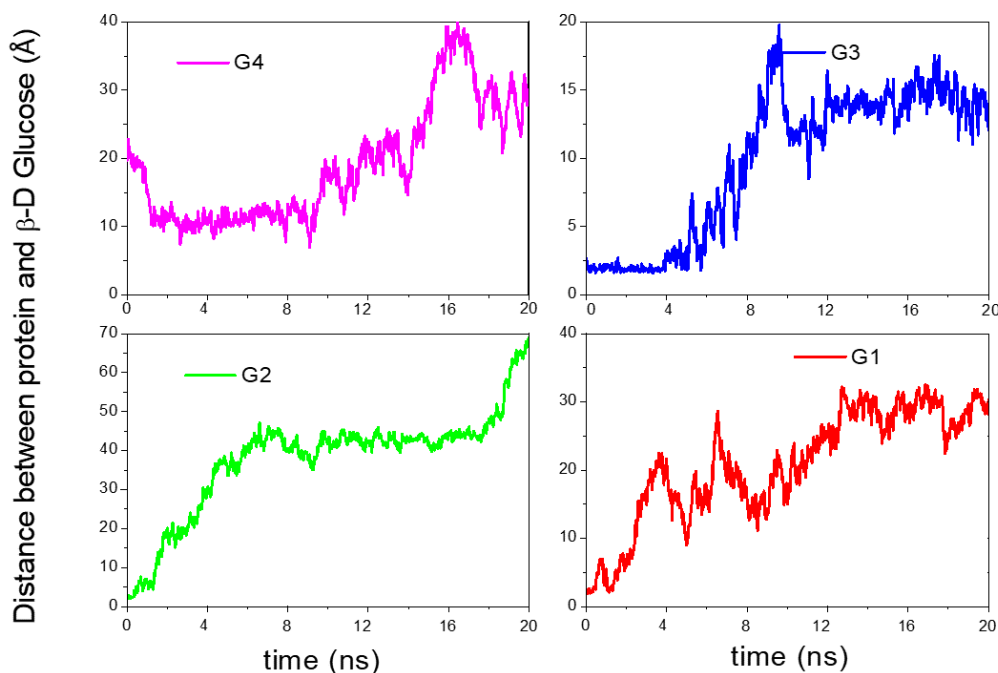


Figure 28: Nearest distances between β -D glucose molecules and the Con A tetramer.

typical monosaccharide binding sites. Because β -D glucose is monovalent, when one β -D glucose leaves, another β -D glucose from the surrounding solution might come nearby and bind. Overall, monovalent β -D glucose molecules show shorter binding times and longer binding distances than nanomolecules.

Simulation of nanomolecules C and D with their Target Protein DC-SIGN

In order to check the binding between nanomolecules (C and D) and DC-SIGN, atomistic MD simulations were performed by NAMD [58]. DC-SIGN (PDB 1k9I [189]) is a tetramer, having four carbohydrates binding sites with VAL, ASN, GLU and ASP involved. Two simulations were set up: nanomolecule C with DC-SIGN and nanomolecule D with DC-SIGN. Both systems were immersed in 150 mM NaCl solutions. Figure 29 shows the structures of tetramer of DC-SIGN with nanomolecule C or D after 40 ns simulation.

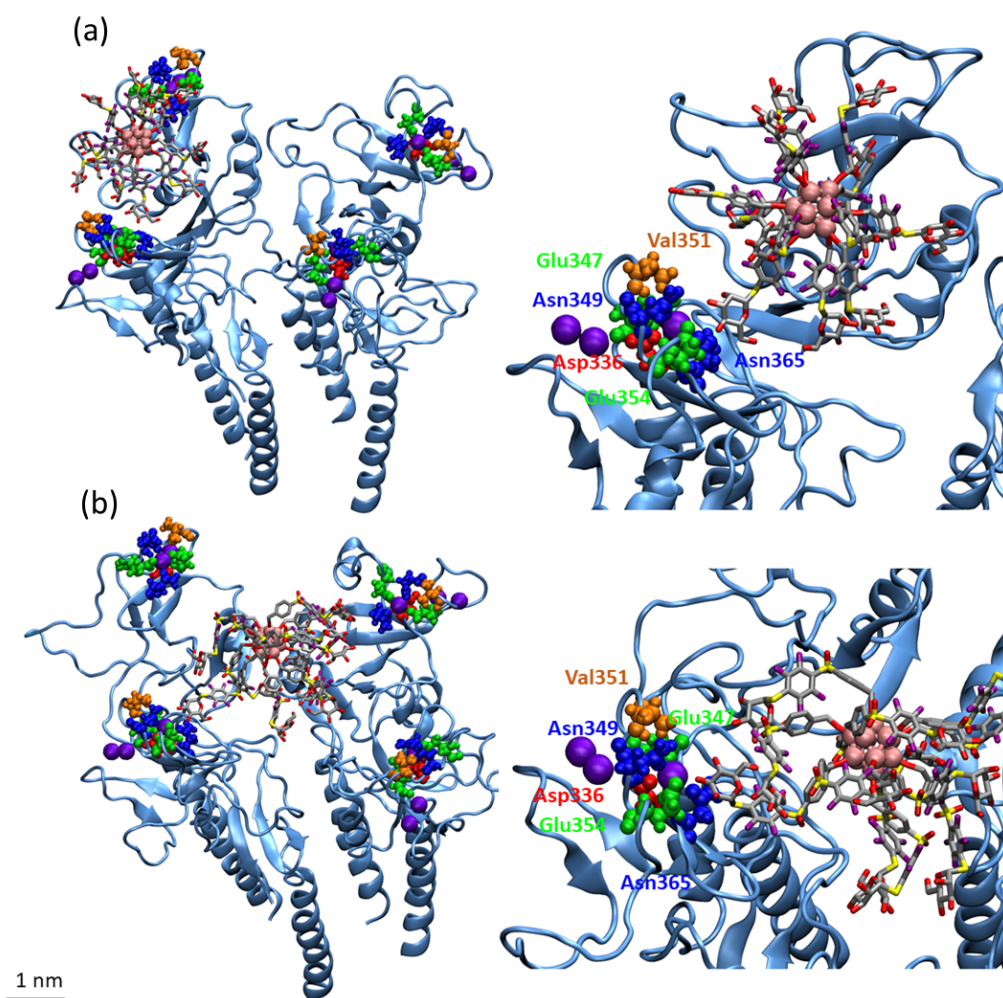


Figure 29: (a) Binding of nanomolecule C to DC-SIGN with details on the right side. (b) Binding of nanomolecule D to DC-SIGN with details on the right side. The protein is shown in light blue, and the ligands of the cluster are in gray, with boron, sulfur, fluorine, carbon, oxygen and calcium represented as pink, yellow, gray, red and purple, respectively.

Figure 29 top panels show how the nanomolecule C binds with DC-SIGN sugar binding pocket. The O3 and O4 of the mannose from nanomolecule C point towards the Calcium ion, while a similar binding of nanomolecule D to DC-SIGN can also be found in the bottom panels of Figure 29. To quantify the difference between the two binding cases, we checked the number of hydroxy group (containing O3 and O4) within 5 Å of Calcium ion. Nanomolecule C can bind with DC-SIGN for a

longer time than nanomolecule D as shown in Figure 30. The "2" means both 3-OH and 4-OH bind, "1" means only one of them binds, "0" means none of them binds. Nanomolecule D shows rapid switching among "2", "1" and "0" with a "1" state binding for 2 ns, while nanomolecule C stays with "2" for a longer time with a longest "2" state binding for 4 ns after switching between "0" and "1". The rapid switching of nanomolecule D may be induced by the stronger hydrophobic interaction within ligands which cause a higher dissociation constant.

The equatorial 3-OH and 4-OH groups on the cluster linked mannose residues engage in Ca^{2+} -mediated binding in the carbohydrate recognition sites. Furthermore, nanomolecule C was observed to stay longer than nanomolecule D near the binding site of the protein model Figure 30, which agrees with the lower Kd value of nanomolecule D determined from the SPR experiments. A possible explanation for the observed difference in avidity is the flexibility of the linker; while the extended linker in nanomolecule D is still rigid, it allows more flexibility compared to the benzylic linker in nanomolecule C. Although a moreflexible linker can relax the requirements for the precise positioning of ligands on a multivalent scaffold, it can also lower the overall affinity for a target protein.

Simulations of nanomolecules E, F, G, and H with their Target Proteins

In order to check the binding between different nanomolecules and their protein targets, atomistic MD simulations were performed. Con A (PDB 1ONA [188]) was chosen as target protein to bind with multivalent 1-thio-beta-D-glucose coated nanomolecule E; DC-SIGN (PDB 1k9I [189]) was used to bind with 1 - thio - α -D-mannose coated nanomolecule F; Stx1B (PDB 1CQF) was targeted to the nanomolecule G or H coated by 1-thio-beta-D-galactose or *PEG*₃₅₀.

Figure 31, Figure 32, Figure 33, Figure 34 show the snapshots of four nanomolecules binding with their target proteins. The proteins are shown in cartoon representation, and the ligands of the

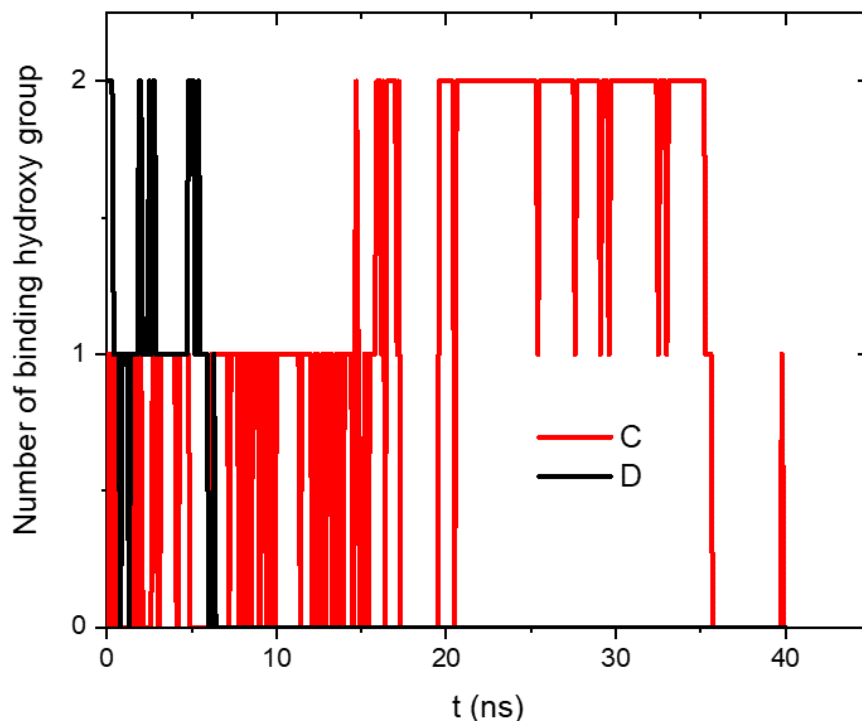


Figure 30: Number of binding hydroxy groups with time.

cluster are in gray, with boron, carbon, oxygen, calcium and manganese represented as pink, gray, red, purple, and cyan, respectively. The amino acids color scale is Asn: orange, Trp: purple, Asp: red, Arg: blue, Tyr: green, Leu: light blue, Val: ochre, Glu: pink.

Figure 35 show the number of ligands of the nanomolecules which are within 4 Å of the residues of the binding sites on the protein. Four nanomolecules E were initially put near the typical sugar binding sites of Con A (Tyr 12, Tyr 100, Pro 13, Asn 14, Thr 15, Asp 16, Asp 208, Arg 228, and Leu 229) which are highlighted in the Figure 31. After 20 ns simulation, only one nanomolecule (E1) binds into the exact sugar binding pocket as shown in Figure 31(c). E2 binds to the surrounding amino acids and E3 spans the binding pocket, while E4 dissociates from the protein eventually. From Figure 35, we can also see that there are on average 2 ligands from E1 and 2 ligands from

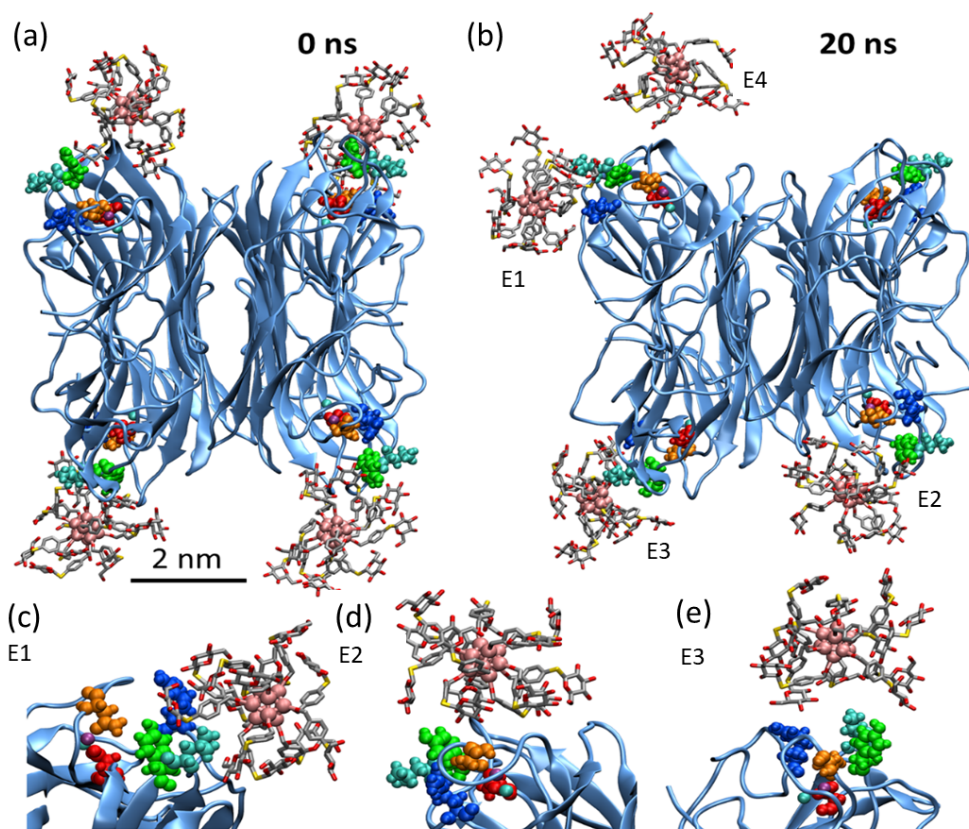


Figure 31: Binding of nanomolecule E to Con A. (a) Initial configuration of nanomolecule E and Con A; (b) one of the four E nanomolecules leaves the protein; (c) E1 binds into the sugar binding pocket; (d) E2 binds to the surrounding residues of the binding pocket; (e) ligands of the E3 span the binding pocket.

E2 binding with the amino acids of the binding pocket, while relatively less ligands from E3 and E4 bind to the surrounding amino acids. Since the four binding pockets are identical and separated with each other, we get the four different cases of binding. The ligands here without fluorination are more hydrophobic than the fluorinated ligand used in our previous work [8], which cause a relative stronger ligand to ligand interaction. The stronger ligand to ligand interaction thus interrupts the specific binding of ligand to its target protein.

Nanomolecule F was initially put near one binding pocket of DC-SIGN (Asp 336, Glu 347, Asn 349, Val 351, Glu 354, and Asn 365). It hopped from one monomer to another monomer with

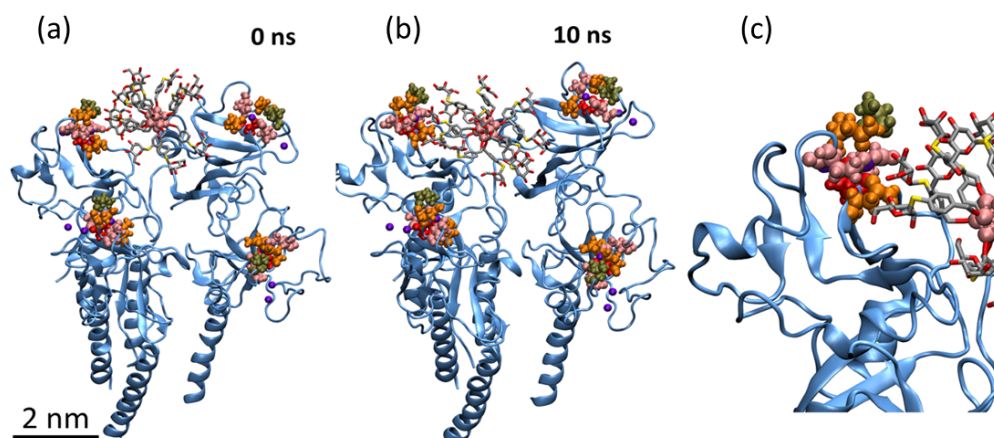


Figure 32: Binding of nanomolecule F to DC-SIGN. a) Initial configuration; b) binding of nanomolecule F to the surrounding residues of DC-SIGN at 20 ns.

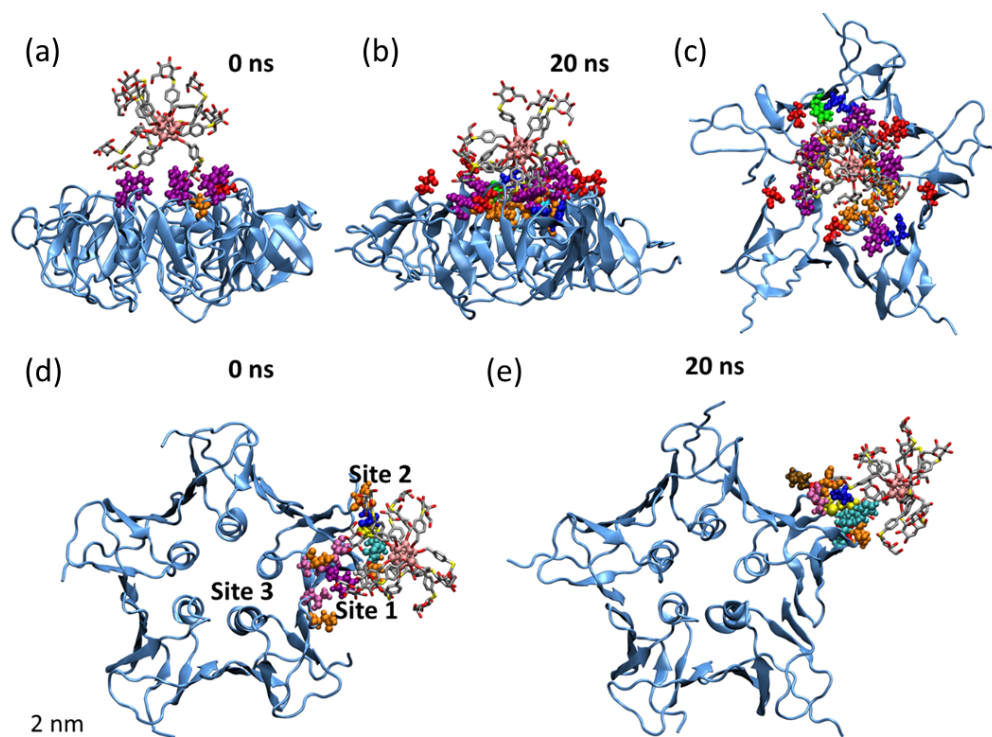


Figure 33: (a) Binding of nanomolecule G to the top of Stx1B (initial); (b) binding of nanomolecule G to the top of Stx1B at 20 ns; (c) top view of (b); d) binding of nanomolecule G to other sites (initial); (e) binding of nanomolecule G to other sites (20 ns).

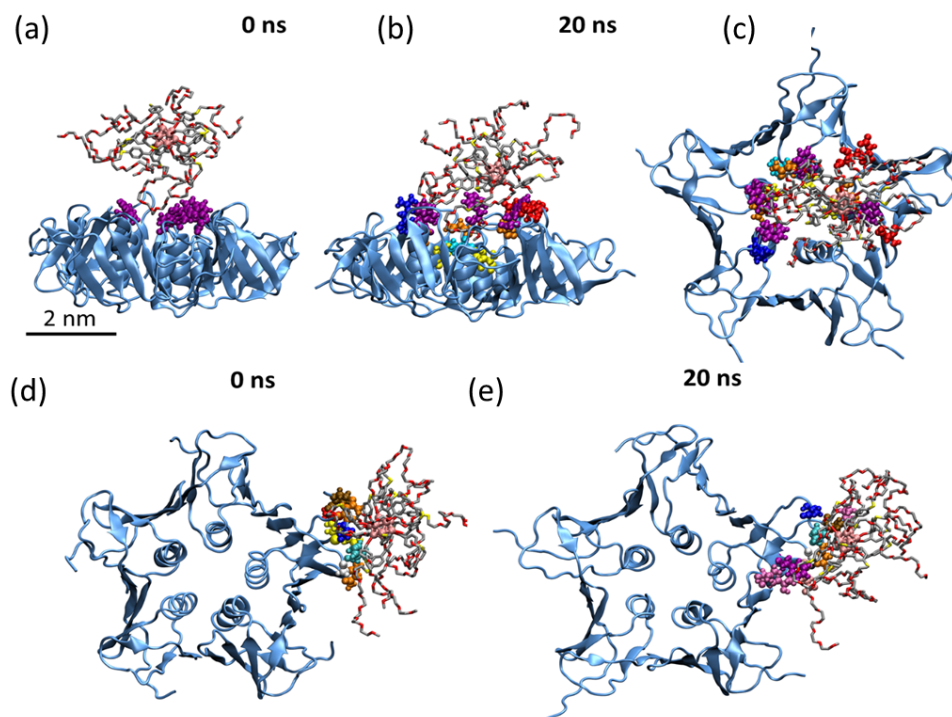


Figure 34: (a) Binding of nanomolecule H to the top of Stx1B (initial); (b) binding of nanomolecule H to the top of Stx1B at 20 ns; (c) top view of (b); d) binding of nanomolecule H to other sites (initial); (e) binding of nanomolecule H to other sites (20 ns).

maximum 3 ligands around the binding pocket, while none of them binds right into the binding pocket during 20 ns (Figure 32). This may be also caused by the ligand-ligand interaction within the nanomolecule F.

Nanomolecule G was initially placed on the top of Stx1B (site 3), it interacts with the Asn, Trp and Asp residues with the increased interacting number of ligands (up to 10) during the simulation as shown in Figure 35. When nanomolecule G and H were initially placed near site 1 and 2, the interacting ligands of nanomolecule G and H are very similar.

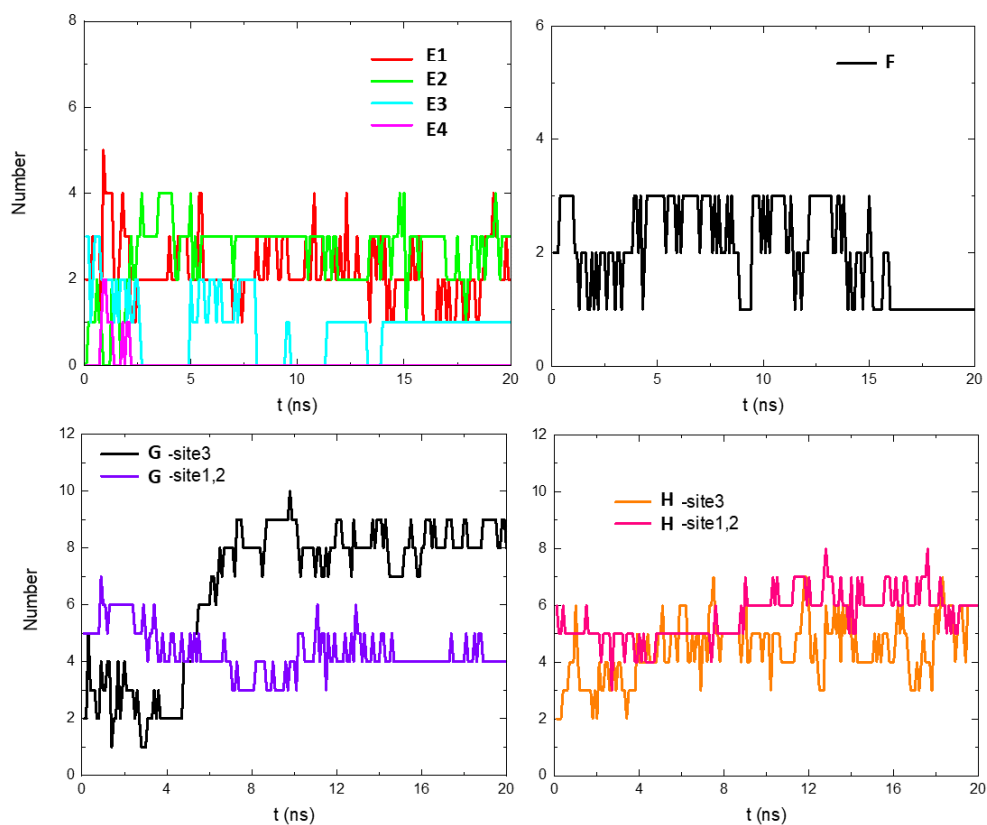


Figure 35: Number of ligands of nanomolecules (E, F, G, H) around the specific binding pocket of their target proteins (Con A, DC-SIGN, Stx1B, Stx1B).

Conclusion

The multivalent glycosylated B_{12} nanomolecules were tested to be capable of inhibiting protein–protein interactions. MD simulations captured special switching binding modes between nanomolecules and their protein targets. The thiolated saccharide ligands grafted on B_{12} cluster was found to bind in an alternative manner to the saccharide binding pockets, which enhance the multivalency. The designed glycosylated nanomolecules can serve as multivalent binders with dramatically enhanced affinity toward target lectins. The different K_d values among different nanomolecules arise from the intrinsic difference of sugar terminus and linkage between B_{12} cluster and sugars. The introduction

of hydrophobic moieties (benzene) in the ligands tends to diminish the flexibility of ligands which hinder the overall multivalent binding efficiency.

CHAPTER 5

SIMULATIONS OF POLYMER-BASED DRUG DELIVERY SYSTEMS

(Previously published as Malfanti, A., Mastrotto, F., Han, Y., Král, P., Balasso, A., et.al. Novel Oligo-Guanidyl-PEG Carrier Forming Rod-Shaped Polyplexes. *Molecular Pharmaceutics* **16**, 1678 (2019); Hsu, H.jui , Han, Y., Cheong, M., Král, P., Hong, S. Dendritic PEG Outer Shells Enhance Serum Stability of Polymeric Micelles. *Nanomedicine* **14**, 1879 (2018); Zhang, C., Moonshi, S. S., Han, Y., Puttick, S., Peng, H., et.al. PFPE-Based Polymeric 19F MRI Agents: A New Class of Contrast Agents with Outstanding Sensitivity. *Macromolecules* **50**, 5953 (2017); Zhang, C., Liu, T., Wang, W., Bell, C. A., Han, Y., et.al. Tuning of the Aggregation Behavior of Fluorinated Polymeric Nanoparticles for Improved Therapeutic Efficacy. *ACS Nano* **14**, 7425 (2020); Zhang, C., Moonshi, S. S., Wang, W., Ta, H. T., Han, Y., et.al. High F-Content Perfluoropolyether-Based Nanoparticles for Targeted Detection of Breast Cancer by 19F Magnetic Resonance and Optical Imaging. *ACS Nano* **12**, 9162 (2018).)

In this chapter, three polymer-based drug delivery vehicles synthesized by our collaborators were introduced. Maltotriose-based cationic polymers were designed to carry oligonucleotides. Micelles formed by dendritic or linear amphiphilic copolymers can encapsulate molecular drugs, whose stability were tested in the presence of serum proteins. Perfluoropolyether-based polymers with different content of Fluorine were synthesized to form nanoparticles, which show high cell permeability. MD simulations were conducted to check the conformation of different drug delivery systems and the interactions between polymers and their targets.

5.1 Novel oligonucleotide carriers

Adapted from Ref. [11] (*Mol. Pharmaceutics* 2019, 16. DOI: 10.1021/acs.molpharmaceut.9b00014) with the permission from ACS Publishing Group.

Introduction

Therapeutic oligonucleotides (ONs) have been applied as gene therapies [190–192]. ONs alone often suffer from degradation, low membrane transport rate, off-target profile and immunogenic response, which hinder their efficiency in therapeutic usages [193]. ON delivery carriers based on viral or nonviral platforms could help overcome these limitations. Viral vectors are limited by intrinsic toxicity and immunogenicity, low ON packaging, and difficult scale-up production [194–196]. Nonviral vectors which include cationic vesicles, nanoparticles, and macromolecules, have many advantages over viral carriers such as biosafety, easy scale-up production, low host immunogenicity, and controlled delivery [197].

Cationic supramolecular nanocarriers could form polyplexes with ONs by electrostatic interactions, which protect them from degradation and favor their internalization into the diseased cells [196,198,199]. Promising cationic macromolecules need to be non-cytotoxic, highly bio-compatible, less interactive with blood components and transfection efficient [200–202]. The introduction of PEG into the polycationic macromolecules was found to be beneficial in escaping the immunosystem and other clearance processes [203], reducing the carrier-induced hemolysis, protecting ONs from enzymatic degradation, and enhancing the colloidal stability, permeability and retention (EPR) effect [204].

Prof. Caliceti’s group developed a novel cationic supramolecular platform where an oligosaccharide core was functionalized with a polycationic “star-like head” formed by six guanidyl units and a

PEG “tail”. MD simulations were performed to characterize the conformations of the complexes of ONs and the new cationic macromolecules.

Experimental results

”The hybrid “head–tail” bioconjugate reported in this work ($Agm_6 - M - PEG - OCH_3$, Figure 36) was designed to develop an ON vector devoid of intrinsic biological activity and possessing high chemical stability, high biocompatibility, high transfection properties, and tailorable features. Maltotriose was selected as platform for the construction of the cationic block of the new carrier. It contains 10 hydroxyl groups of the C2, C3, C4 and C6 carbons that can be functionalized with guanidyl moieties to generate a star-like oligo-cationic ”head”. The PEG “tail” was introduced in the carrier structure to enhance the solubility, physical stability, and biocompatibility of micelle-like polyplexes [205], and prolong the residence time of the polyplexes in the bloodstream” [11].

Transmission electron microscopy (TEM) images of $Agm_6 - M - PEG - OCH_3$ /dsDNA with 3 and 5 N/P ratio revealed that the polyplexes have a rodshape structure (Figure 37 A and B). The gel electrophoresis image of $Agm_6 - M - PEG - OCH_3$ /ON samples with increasing N/P ratio ([guanidyl groups (N) of $Agm_6 - M - PEG - OCH_3$]/[phosphate groups (P) of ON]) reported in Figure 37 C shows that free dsDNA, stained with gelred nucleic acid gel stain was not detected at an N/P ratio 3 indicating that complete $Agm_6 - M - PEG - OCH_3$ /ON complexation was achieved. The degree of dsDNA complexation with $Agm_6 - M - PEG - OCH_3$ was evaluated by thiazole orange (TO) association assay Figure 37 D. The fluorescence of $Agm_6 - M - PEG - OCH_3$ /dsDNA polyplexes significantly decreases as the N/P ratio increases. This is a consequence of the decreased free dsDNA in solution and increased dsDNA complexed with $Agm_6 - M - PEG - OCH_3$. In particular, major fluorescence intensity reduction was observed at a 2–3 N/P ratio indicating that

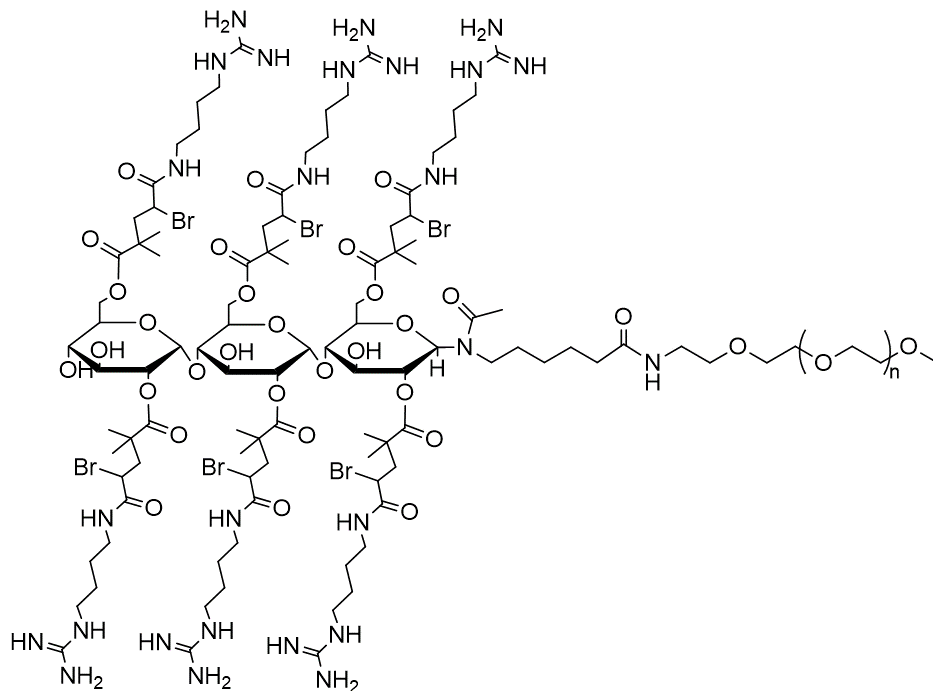


Figure 36: Star-like (*Agmatinyl*)₆ – *maltotriosyl* – *N* – *acetyl* – *amino* – *hexanoate* – *PEG*_{5kDa} – *OCH*₃(*Agm*₆ – *M* – *PEG* – *OCH*₃).

at and above this *Agm*₆ – *M* – *PEG* – *OCH*₃/dsDNA ratio, the ON undergoes extensive association with the macromolecular carrier.

The intracellular disposition of *Agm*₆ – *M* – *PEG* – *OCH*₃/ dsDNA polyplexes prepared with 3 and 5 N/P ratios after incubation with KB, MCF-7, and MC3T3-E1 cells were further investigated by confocal microscopy (Figure 38E). The cell membrane was stained with WGA-AlexaFluor488 (green), the nucleus with DAPI (blue), and the Cy3-dsDNA was visualized in red. The results underline the remarkable influence of the polyplex structure, size, shape, and aspect ratio on the cell uptake. The higher cell uptake was observed with the thick and short *Agm*₆ – *M* – *PEG* – *OCH*₃/ ON polyplexes (3 N/P ratio, 3.1 ± 0.9 aspect ratio) with respect to the thin and long structures (5 N/P ratio, 5.7 ± 1.5 aspect ratio). The different cell uptake obtained with the three different cell lines

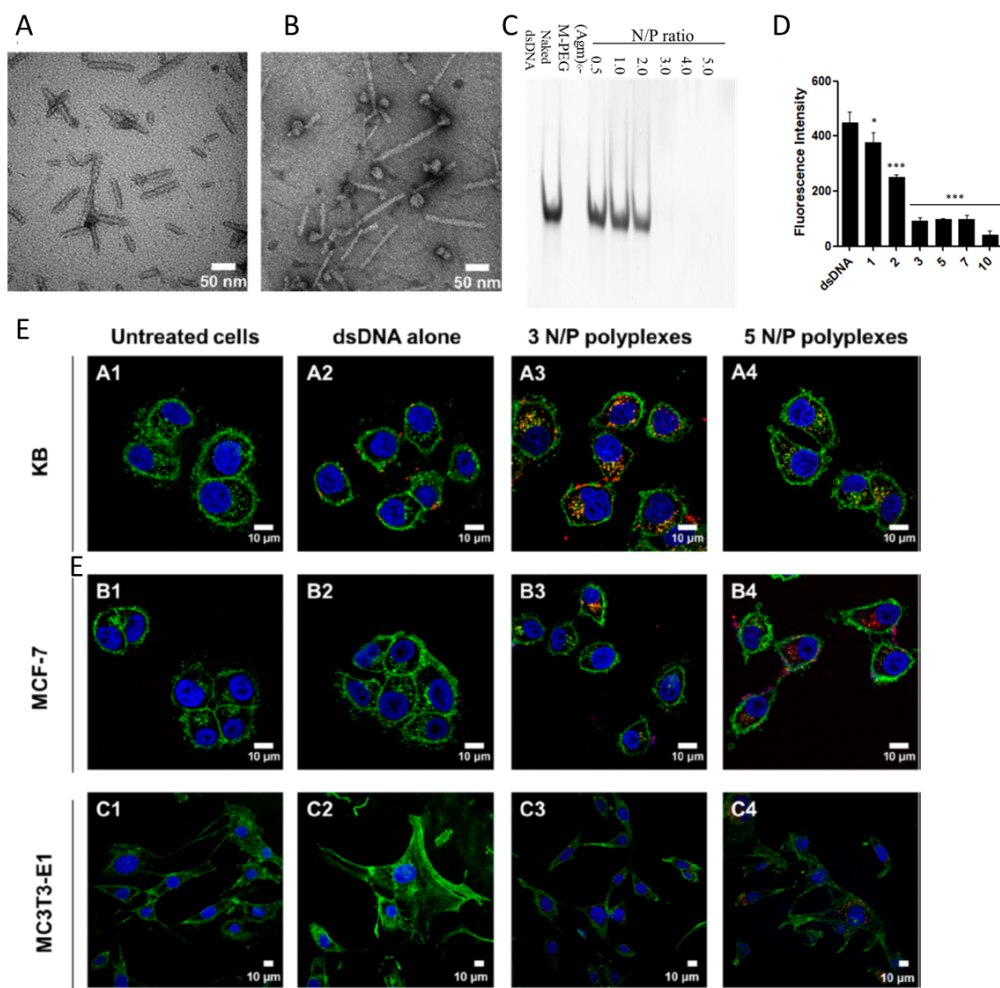


Figure 37: (A) TEM images of $Agm_6 - M - PEG - OCH_3$ /dsDNA polyplexes obtained with N/P ratio of 3 and (B) N/P ratio of 5 (scale bar: 50 nm). (C) Gel mobility profiles of $Agm_6 - M - PEG - OCH_3$ /dsDNA polyplexes with N/P ratio increasing from 0.5 to 5 at pH 7.4. The samples were run in polyacrylamide gel using TBE as running buffer. (D) Fluorescence intensities of thiazole orange (TO) association with free (noncomplexed) dsDNA polyplexes at increasing N/P ratios in PBS, pH 7.4. The analysis was replicated three times and the data are reported as fluorescence intensity mean \pm SD, * $p < 0.05$; ** $p < 0.01$; *** $p < 0.001$ versus naked dsDNA. (E) Confocal microscopy images of KB, MCF-7, and MC3T3-E1 cells: (A1, B1, C1) untreated cells (control); (A2, B2, C2) cells treated with Cy3-dsDNA; (A3, B3, C3) cells treated with N/P ratio of 3 $Agm_6 - M - PEG - OCH_3$ /Cy3-dsDNA polyplexes; (A4, B4, C4) cells treated with N/P ratio of 5 $Agm_6 - M - PEG - OCH_3$ /Cy3-dsDNA polyplexes. Scale bar indicates 10 μ m.

suggests that the polyplex internalization undergoes different mechanisms or rates of internalization with different cells.

MD simulations of DNA-polymer complexes

MD simulations were performed to show the interaction between the dsDNA and the $Agm_6 - M - PEG - OCH_3$ s. All the simulation was performed by NAMD [58] and mainly described by the CHARMM general forcefield [68]. The dsDNA were described by a CHARMM36 forcefield [66]. The PME [62] method was used for the evaluation of long-range coulombic interactions. The time step was set to 2.0 fs. The simulations were performed in the NPT ensemble ($p = 1$ bar and $T = 300$ K), using the Langevin dynamics ($\gamma_{\text{Lang}} = 1 \text{ ps}^{-1}$). After 2,000 steps of minimization, ions and water molecules were equilibrated for 2 ns around dsDNA and $Agm_6 - M - PEG - OCH_3$ s, which were restrained using harmonic forces with a spring constant of $1 \text{ kcal}/(\text{mol } \text{\AA}^2)$. The last frames of restrained equilibration were used to start simulations of free dsDNA and $Agm_6 - M - PEG - OCH_3$. All the simulations lasted for 20 ns.

To get deeper structural insight about the $Agm_6 - M - PEG - OCH_3/\text{ON}$ interaction, the interaction between $Agm_6 - M - PEG - OCH_3$ and dsDNA was simulated. Figure 38A shows a snapshot of 1 dsDNA molecule and 30 $Agm_6 - M - PEG - OCH_3$ molecules (corresponding to 5 N/P ratio, dsDNA-30) simulated in 150 mM NaCl solution. After 20 ns of equilibration, the positively charged groups (guanidyl groups) of $Agm_6 - M - PEG - OCH_3$ become oriented toward the negatively charged backbone of dsDNA, while the remaining chains are solvated around the formed polyplex. In total, 20 entangled $Agm_6 - M - PEG - OCH_3$ molecules (out of 30) were found around one dsDNA, which gives a N/P ratio of about 3 (each $Agm_6 - M - PEG - OCH_3$ molecule contains 6 guanidinium groups, while dsDNA has 38 phosphate groups), which is in very good agreement with the complete ON association at 3 N/P molar ratio calculated by gel-electrophoresis, fluorescence analysis, and

ITC. The stabilization of a limited number of charged $Agm_6 - M - PEG - OCH_3$ molecules is performed through a terminal self-assembly, where beyond certain total charge of the complex no more charged molecules can join the complex, due to a large Coulombic repulsion. Figure 39 shows that dsDNA is well covered by these 20 $Agm_6 - M - PEG - OCH_3$ chains.

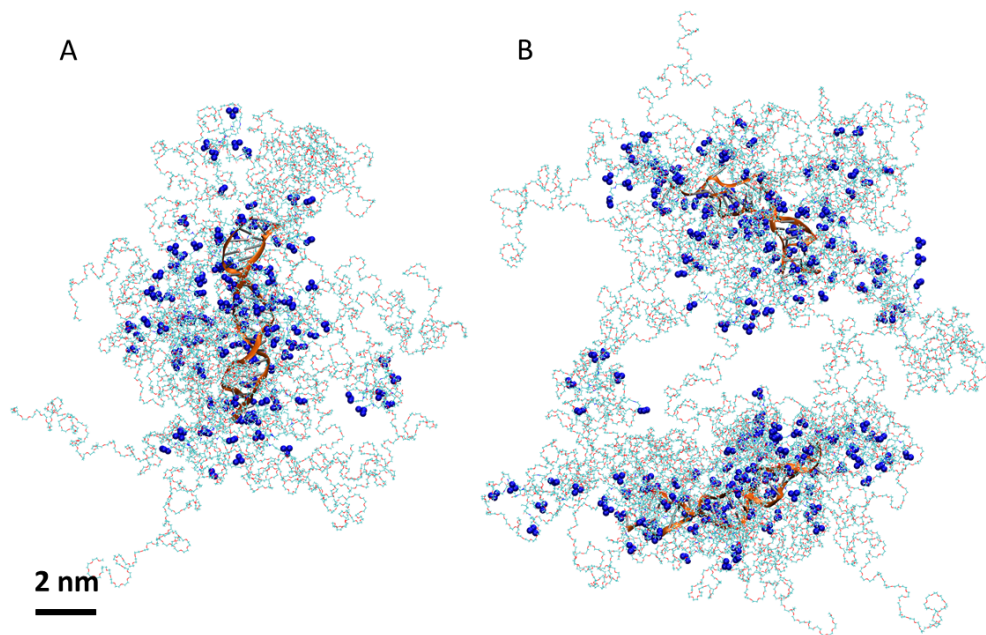


Figure 38: (A) MD simulations of 1 dsDNA and 30 $Agm_6 - M - PEG - OCH_3$ chains. After 20 ns, only 20 $Agm_6 - M - PEG - OCH_3$ assembled around 1 dsDNA, giving a 3 N/P ratio. (B) Two dsDNA strengths wrapped by 40 $Agm_6 - M - PEG - OCH_3$ chains are simulated for 20 ns. The $Agm_6 - M - PEG - OCH_3$ chains become entangled, forming a potential nucleus of a larger molecular complex. dsDNA is shown as orange ribbon with base pair in silver; $Agm_6 - M - PEG - OCH_3$ is shown as a chain with N atoms in blue (highlighted), O atoms in red, C atoms in cyan, S atoms in yellow, Br atoms in pink, and H atoms in white.

Next, we took from Figure 38A two polyplexes of 1 dsDNA with 20 $Agm_6 - M - PEG - OCH_3$ (still corresponding to a 3.3 N/P ratio) to make a complex system Figure 38B. During 20 ns simulations, some $Agm_6 - M - PEG - OCH_3$ chains bridged the two dsDNA assemblies, forming a larger complex, shown in Figure 38B. We can anticipate that in the same manner like a simple dsDNA complex which is stabilized by a terminal self-assembly of $Agm_6 - M - PEG - OCH_3$ chains, a large supercomplex of many dsDNA assemblies is stabilized in a terminal manner [42]. The decrease of

the Coulombic repulsion between the charged constituents of a large supercomplex of many dsDNA assemblies stabilized by terminal self-assembly of $Agm_6-M-PEG-OCH_3$ chains yields rod-shaped structures rather than spherical structures (Figure 38). As observed for other polycationic carriers used for ON delivery, we speculated that the rod-shaped structures could be originated from the combination of charge distribution of the $Agm_6-M-PEG-OCH_3$ and the relative stretching of ON molecules into the polyplexes [206]. Importantly, 40–80 nm rod shaped polyplexes have been reported to display longer in vivo circulation and more efficient cell up-take and gene silencing than sphereshaped polyplexes [207–209].

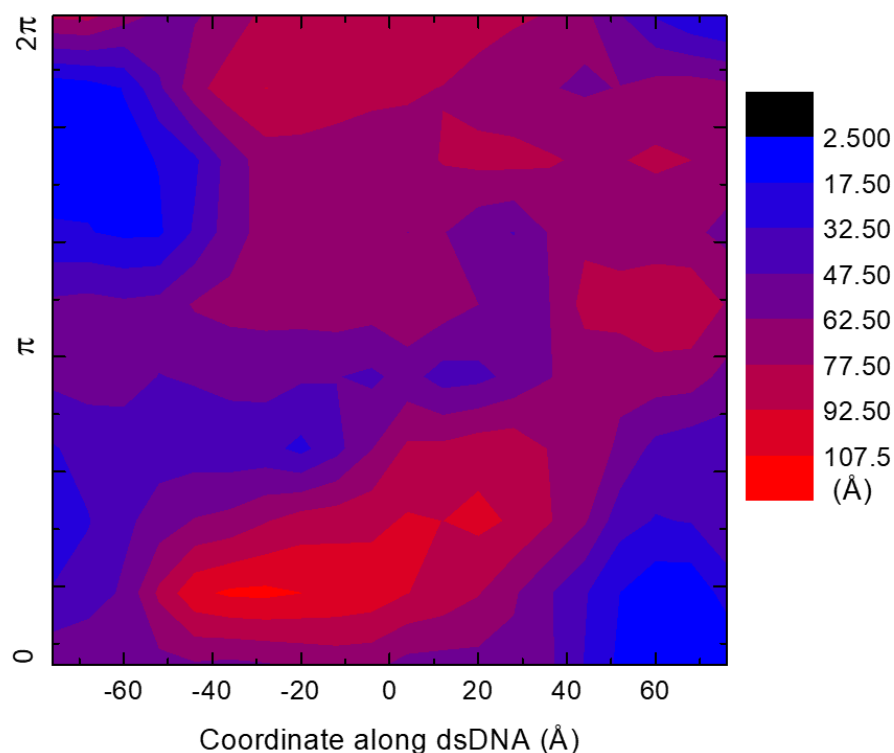


Figure 39: Thickness of $Agm_6-M-PEG-OCH_3$ chains around dsDNA. (cylinder coordinate is used, where the center of dsDNA is set to 0; dsDNA is in the range of -40 to 40 Å; different color stands for the thickness of $Agm_6-M-PEG-OCH_3$ chains.)

Conclusion

The experimental results show that the $Agm_6 - M - PEG - OCH_3$ molecules represent a novel platform with suitable physicochemical, structural, and biopharmaceutical properties for ONs delivery. $Agm_6 - M - PEG - OCH_3$ molecules possess strong interaction and form complexes with ONs as assessed by MD simulations and other analyses. The $Agm_6 - M - PEG - OCH_3$ molecules enclosed the ONs inside by the interactions between positively charged molecule "heads" and negatively charged ON backbones. Although the conformation of ONs subjected to change due to the interactions, no serve deformation of secondary structures was observed during simulations. The rod-shape structure of the polyplexes generated by the $Agm_6 - M - PEG - OCH_3$ and ONs exhibits promising advantage in intracellular access.

5.2 Polymeric micelles with dendritic PEG outer shells

Adapted from Ref. [12] (*Nanomedicine: NBM* 2018, 14. DOI: doi.org/10.1016/j.nano.2018.05.010) with the permission from ELSEVIER Publishing Group.

Introduction

Polymeric nanoparticles (PNPs) are promising drug delivery vehicles [210–213]. However, the interactions between PNPs and serum proteins could negatively affect the performance of nanocarriers (NCs). Serum proteins can attach onto NC surfaces and form "protein corona" [214,215]. These undesired NC-protein interactions can trigger opsonization-mediated NPs clearness by immune system, disturb the pharmacokinetic properties of NCs [216], block the targeting ligands attached on the NPs surface and diminish the specificity of the targeted PNPs [217–219]. The NC-protein interactions could fail the delivery of incorporated drugs to their targets [216,220,221]. Reducing the NC-protein interactions would substantially improve the effectiveness of these self-assembled NCs [221]. Intro-

ducing a highly hydrophilic polymer to the surface of NCs [222–224] is one of the most common strategies to reduce the NC-protein interactions. The PEG outer shells were found to decrease the protein adsorption to NCs and help to avoid the clearness of immune system, and thus prolong the circulation time of NCs [211, 225].

The linear configurations of PEG-conjugated hydrophobic polymers often result in less dense PEG outer shells, which provide limited protection to NCs [221, 226, 227]. Prof. Hong’s group synthesized the dendritic amphiphilic copolymers forming micelles which could provide high-density PEG outer shells. The dense PEG layers on the micelle surfaces were expected to reduce the undesired interactions with serum proteins. The effects of the dendritic PEG outer shells on the stability of micelles were systematically studied through both experiments and simulations.

Experimental results

”The dendritic amphiphilic copolymers tested in this study were developed previously. The PEGylated dendron-based copolymers (PDCs) consist of hydrophilic poly(ϵ -caprolactone) (PCL), polyester dendron, and multiple hydrophilic PEG chains (Figure 40) [228]. Due to their conical structure, these amphiphilic PDCs could self-assemble into dendron micelles with enhanced thermodynamic stability. The critical micelle concentrations (CMCs) of those dendron micelles were ranged from 10^{-7} to 10^{-8} M, which were up to two orders of magnitude lower than those of similar linear block copolymers (LBCs) [12].”

”The FRET-based technique was employed to compare the serum stability of DMs and LMs. To prepare FRET-micelles, DiO and DiI molecules were encapsulated into DMs or LMs through self-assembly. The stability of these FRET-micelles was first monitored in PBS buffer at 37°C up to 48 hours (Figure 41A). The FRET ratio ($I_{565}/(I_{501} + I_{565})$) of all the micelles tested remained

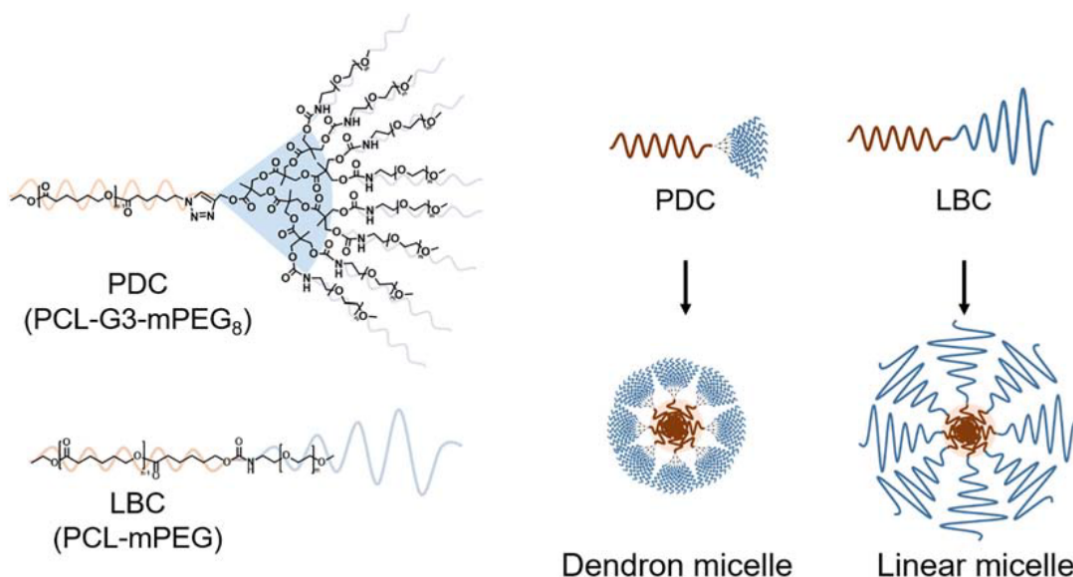


Figure 40: Schematic illustration of the structural difference between PEGylated dendron-based copolymer (PDC) and linear block copolymer (LBC).

constant throughout 48 hours, showing that all the micelles were stable in the absence of serum proteins. In sharp contrast, in 50% fetal bovine serum (FBS), the FRET ratios of the micelles rapidly decreased over time, indicating the integrity of the micelles was disrupted, as a result of the micelle serum protein interactions (Figure 41B). The serum stability of the micelles was generally proportional to the length (molecular weight) of the hydrophobic polymer (PCL) chains for both DMs and LMs [229]. With the same molecular weight of the PCL chains, DMs (both DM3.5K and DM14K) displayed a significantly slower decrease in FRET ratio over 48 hours compared to their LM counterparts (Figure 41B). This enhancement indicates that the incorporation of dendritic polymer architecture could improve the serum stability of the micelles” [12].

Simulations of serum proteins coupled with DM/LM

In order to better understand how different micelles become destabilized by serum proteins, we modeled these systems by MD simulations. BSA (Bovine serum albumin), a main component of

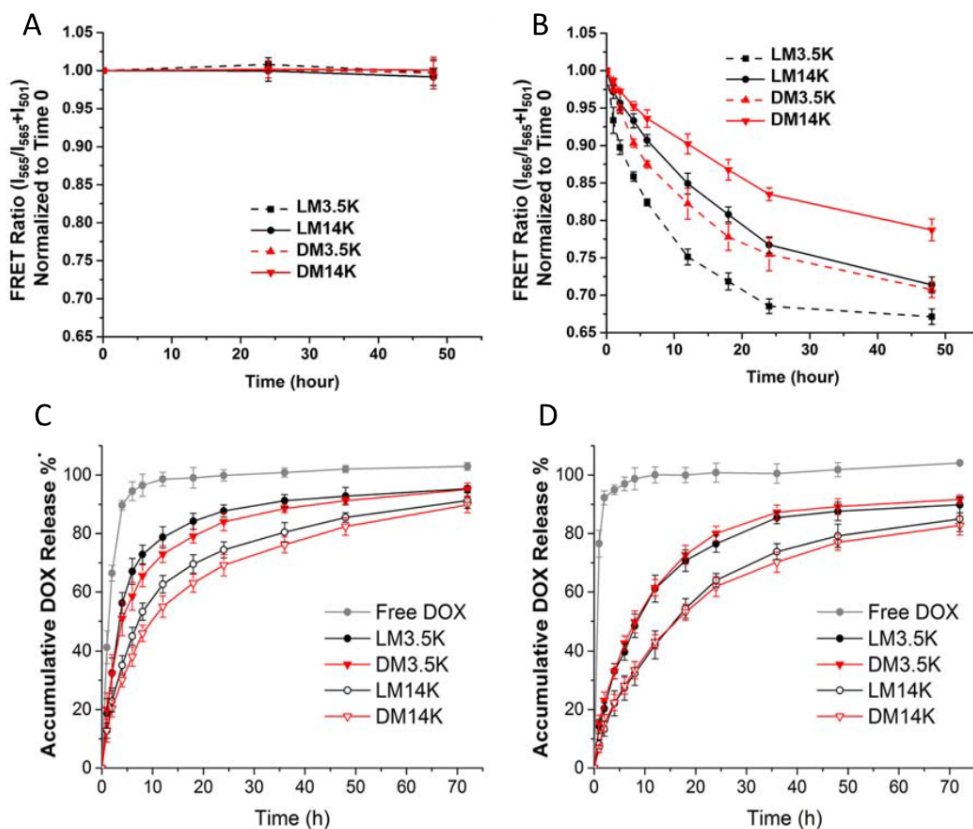


Figure 41: Fluorescence measurements of FRET pairs (DiI and DiO) encapsulated in LMs or DMs. Time-dependent FRET ratios ($I_{565}/(I_{565} + I_{501})$), normalized to time 0, in PBS (A) and 50% FBS (B). In vitro DOX release profiles from DMs and LMs in 50% FBS (C), and 1% Tween 80 (D) using a dialysis method. Results are presented as average \pm S.D. ($n = 3$).

the blood serum, was chosen as the target protein which interacted with LBC-based (LM3.5K) and dendron-based (DM3.5K) micelles. The polymer forming LM3.5K was PCL3.5k-PEG5k, while the polymer forming DM3.5K, PCL3.5k-G3-PEG600, had a dendritic structure (G3) in the middle of PCL core and PEG out-layer. Both micelles had the same terminal group (-CH₃) and the same number of monomers (60).

In the simulated system, six BSA proteins with different orientations were placed around each micelle in a 150 mM NaCl solution. The systems were simulated with NAMD [58] and the CHARMM forcefield [63,64] in a NPT ensemble at $P = 1$ bar and $T = 300$ K, using Langevin dynamics with

a damping constant of 0.01 ps^{-1} and a time step of 2 fs. Long-range electrostatic interactions were calculated by PME [62] in the presence of periodic boundary conditions.

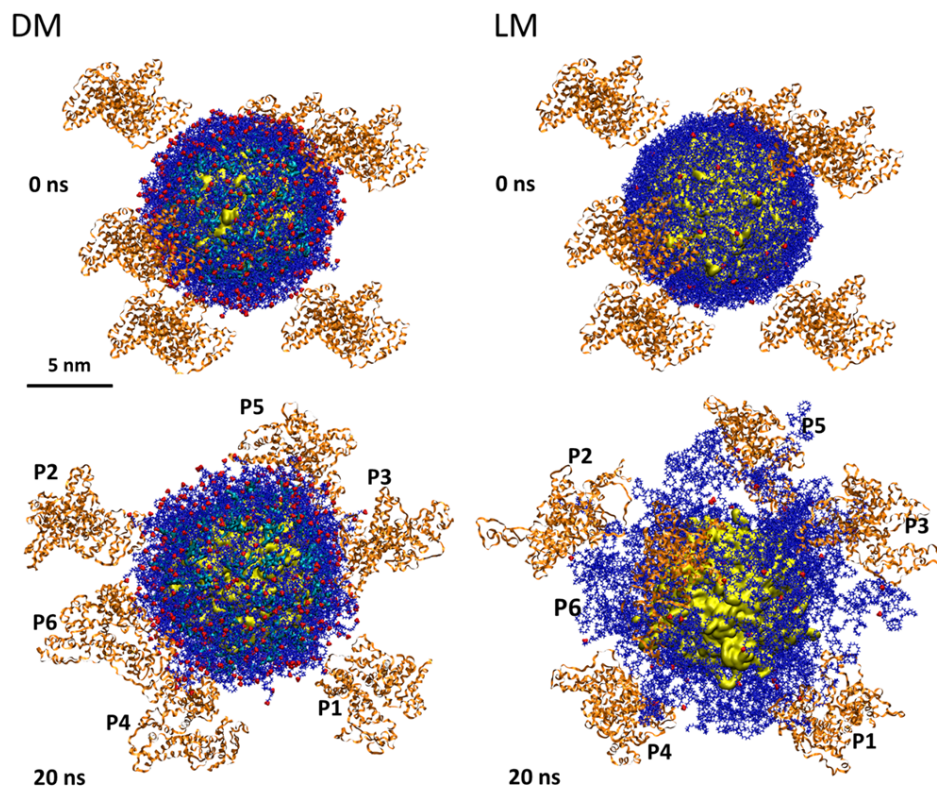


Figure 42: Structure of DM600 (left) and LM5k (right) micelles (BSA orange, PEG blue, G3 cyan, PCL core yellow, terminal group red, scale bar is 5 nm) at the beginning and after 20 ns of simulations in the presence of 6 BSAs.

Figure 42 displays the simulated systems after 20 ns of equilibration. The results show that the relaxed PEG chains in DM600 give a rather smooth micelle surface, providing a little room for strong BSA coupling. On the other hand, the relaxed PEG chains of LM5k give a highly loose surface allowing BSAs to submerge into. In order to quantify the strength of BSA-micelle coupling, we calculated the electrostatic and vdW coupling energies. Figure 43 gives the interaction energies averaged over the six BSAs, calculated with a dielectric constant of 1 (G3 was included in the whole interaction energy and PCL was taken as core of micelle). The average interaction energies of BSA

with DM and LM are -60.2 kcal/mol and -178.6 kcal/mol, respectively. Separate calculations were done for coupling energies between BSA and G3-PEG, and PCL (core). In DM600, they are about -37.3, and -22.9 kcal/mol, respectively, while in LM5k, they are -171.8 kcal/mol (PEG) and -6.8 kcal/mol (core). Therefore, the total coupling energy of BSAs with LM5k is about 3 times larger, which might explain why in experiments LM5k tends to be destabilized more. Even though most of this coupling in both DM600 and LM5k is associated with the PEG chains, the exposed PCL core chains in LM5k still have chance to significantly couple with BSAs, which can cause the micelle destabilization. In contrast, the PCL core in DM600 is highly protected by G3-PEG, even by much shorter PEG chains, since the energy between G3-PEG and BSA is -37.3 kcal/mol which is 6 times less than that of LM5k (-171.8 kcal/mol).

Figure 43C and D show the interaction energy of each of the six (differently oriented) BSA proteins with micelle; P1 stands for the first BSA protein, etc. In both cases, P5 has the lowest interaction energy during most of the simulation time. The interaction energies averaged over the whole simulation time in the case of DM600 are -71.8 kcal/mol for P1, -56.7 kcal/mol for P2, -41.0 kcal/mol for P3, -53.5 kcal/mol for P4, -90.9 kcal/mol for P5 and -47.5 kcal/mol for P6. In the case of LM5k, they are -182.0 kcal/mol for P1, -110.0 kcal/mol for P2, -174.1 kcal/mol for P3, -176.5 kcal/mol for P4, -306.4 kcal/mol for P5 and -123.3 kcal/mol for P6. Therefore, P5 has the lowest averaged interaction energy in both DM600 and LM5k cases.

We also counted the number of LYS and ARG within the proteins which have long side chains and may strongly interact with PEG chains. For the DM600, the averaged number, sum of LYS and ARG within 10 Å of PEG chains during the whole simulation time, is 7, 4, 4, 7, 8, 3 for P1, P2, P3, P4, P5, and P6, respectively. For the LM5k, it is 22, 17, 16, 20, 23, and 13, respectively. P5 has the largest number of LYS and ARG which interact with PEG chains in both cases. Moreover, the total

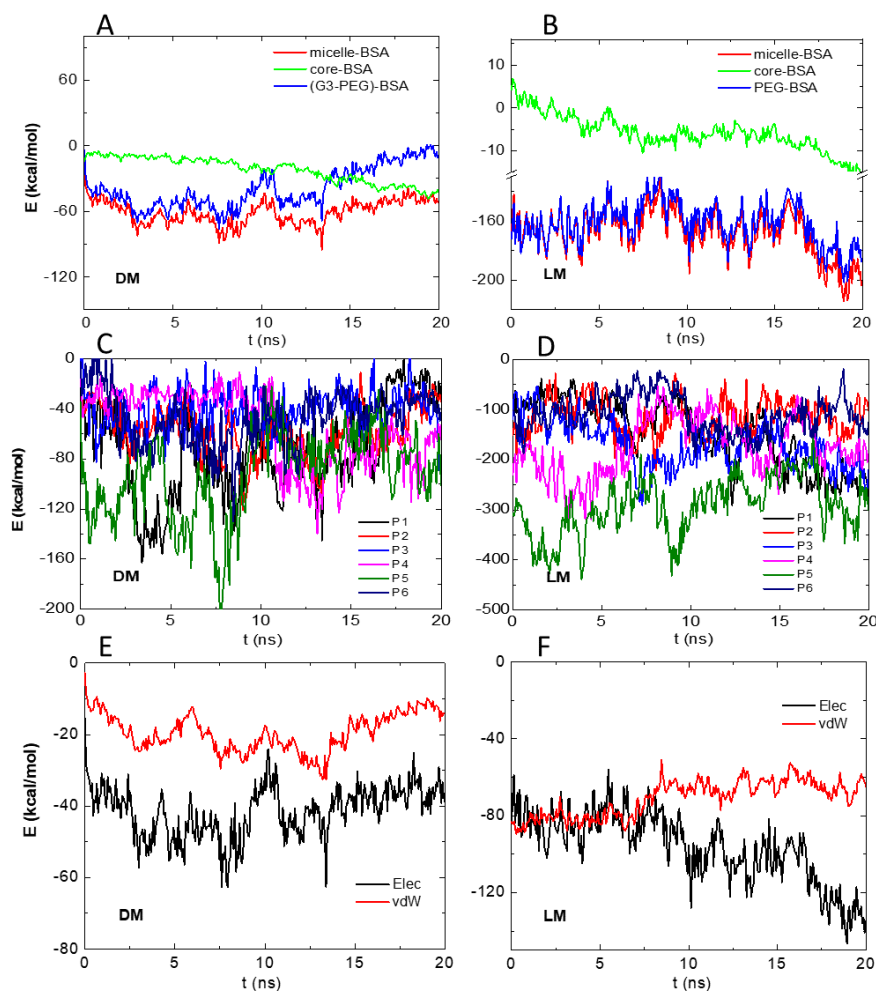


Figure 43: Interaction energies between micelles and proteins averaged over six BSAs (A-B); total interaction energy between micelles and each protein (C-D). Electrostatic and vdW energies between micelles and proteins averaged over six BSAs (E-F).

number of interacting LYS and ARG for LM5k is about 3.4 times of that for DM600. Figure 43E and F show that in DM600, the averaged electrostatic energy per protein is -105.3 kcal/mol, and the averaged vdW coupling energy is -73.3 kcal/mol. On the other side, the averaged electrostatic and vdW coupling energies in LM5k are -41.2 and -19.0 kcal/mol, respectively. Therefore, the vdW coupling energy of BSA with LM5k is almost 4 times of that with DM600, which is consistent with the results of the number of interacting amino acids (LYS and ARG). The increased vdW coupling

may be caused by the interaction between PEG chains and amino acids with long side chains in the BSAs.

Conclusion

Experimental results show that DMs exhibit 2-fold longer half-life in serum-containing solutions compared to their LM counterparts, suggesting that the dendritic PEG outer shell of DMs significantly reduces micelle-serum protein interactions. MD simulations reveal that the dendritic PEG outer shell prevents the penetration of serum proteins into the micelle core and thus weakens the protein binding. Interaction energy calculations indicated a strong binding energy in the case of LM with serum proteins. All of these results demonstrated that the dense dendritic architectures could enhance serum stability of DMs and reduce their non-specific interactions with serum proteins. The DMs exhibited a desired biological property as NCs. This design suggests a novel approach that can be potentially applied to improve the effectiveness of many self-assembled polymers as drug delivery vehicles.

5.3 High F-content perfluoropolyether-based nanoparticles

Adapted from Ref. [13–15] (*Macromolecules* 2017, 50. DOI: 10.1021/acs.macromol.7b01285; *ACS Nano* 2020, 14. DOI: 10.1021/acsnano.0c02954; *ACS Nano* 2018, 12. DOI: 10.1021/acsnano.8b03726) with the permission from ACS Publishing Group.

Introduction

Many experimental results have shown that substitution of hydrogen by fluorine could improve the efficiency of certain drugs in cellular uptake and crossing of cellular membranes [230, 231]. Fluorine has been widely used to tailor the properties and behavior of molecules and particles for

biomedical applications [13–15]. In this section, Prof. Whittaker’s group prepared a series of fluorinated polymeric nanoparticles. The nanoparticles have hydrophobic perfluoropolyether (PFPE) as the cores and oligo(ethylene glycol) methyl ether acrylate (OEGA) as the hydrophilic chains. The synthesizing process is called reversible addition–fragmentation chain transfer(RAFT) polymerization (Figure 44A). The synthesized nanoparticles have well-controlled aggregation behavior in solution. The fluorine content was found to be the factor determining the formation of multiple-chain nanoaggregates or single-chain nanoparticles [13]. A combination of experimental and computational techniques was employed to investigate the relations between the aggregation behavior of these PFPE-containing nanoparticles and their therapeutic efficacy. The experimental results suggest that a single-chain folding conformation (lower fluorine content) of fluorinated polymeric nanoparticles facilitate a significant drug delivery efficiency to living cells [14]. MD simulations were performed to check the different aggregations of different PFPE-polymers and the interactions between aggregates and three different lipid bilayers. The single-chain folding polymers show a larger proportion of hydrophobic PFPE segments exposed to solvent, which could provide enhanced cellular internalization and improve their therapeutic efficacy.

Experimental results

”The chemical structure of the poly(OEGA)_m-PFPE polymer is shown in Figure 44A, with $m = 5, 10$ and 20 , respectively. The uptake of Cy5.5-labeled PFPE nanoparticles by MCF-7 cells after exposure for 24 h was visualized using confocal microscopy. The Z-slices through the center of the cells clearly show red staining, indicating localization of the PFPE nanoparticles within the cell body (Figure 44D-F). The confocal images show stronger red fluorescence and, hence, greater extent of uptake of P20 single-chain unimers compared to P5 and P10, agreeing well with the observations by

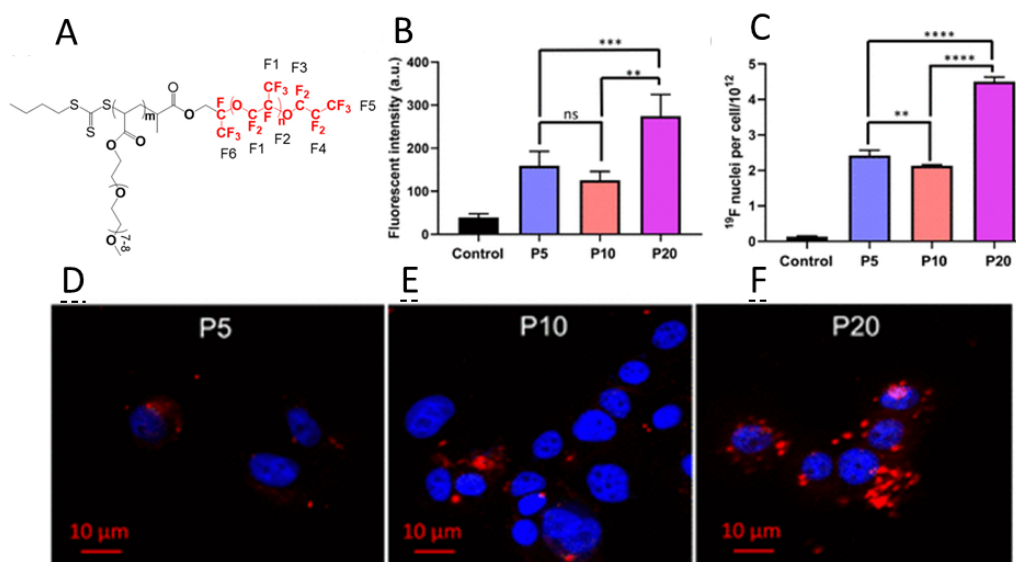


Figure 44: (A) The chemical structure of the poly(OEGA)m-PFPE polymer; (B) flow cytometry, based on the detection of fluorescence intensity per cell, and (C) ¹⁹F NMR spectroscopy, based on the quantification of the ¹⁹F NMR signal intensity per cell. Experiments were performed in triplicate to obtain mean and standard deviation values (shown as error bars); ns, not significant; $p > 0.05$; ** $p < 0.01$; *** $p < 0.001$, **** $p < 0.0001$ (t test). The total cell number was determined using a hemocytometer with Trypan blue exclusion. (D-F) Confocal microscopy of MCF-7 cells incubated with Cy5.5-labeled PFPE nanoparticles (red) at same dye concentration (0.25 mM) for 24 h at 37 °C. Cell nuclei were counter stained with DAPI (blue).

flow cytometry and ¹⁹F NMR analysis (Figure 44B and C). These results confirm that P20 is taken up most efficiently, and that the extent of uptake of the polymers correlates with the proportion of PFPE segments exposed in an aqueous solution” [13–15].

MD simulations of polymer-based nanoparticles

Systems and methods

MD simulations of self-assembled polymers adsorbed on membrane were performed. The model self-assembled polymers had different number of monomers, P1 with 8 monomers, P2 with 4 monomers, P3 with one monomer, and P3-A based on P3 with an adaptor at the end of polymer. Three different membrane surfaces were prepared based on a POPC (phosphatidylcholine) bilayer: M1 (perfect

POPC membrane), M2 (POPC membrane with one protrusion, which means one POPC molecule with its hydrophobic tail towards outside), M3 (POPC membrane with HSP70 protein spanning across). Since HSP70 was found in the tumor cells membrane [232], which may have a specific polymer recognition function, we first placed the HSP70 across membrane with C-terminal domain toward outside (predicted by Botzler et. al. [233]) and then equilibrate the membrane around HSP70 for 10 ns to get M3. We modeled the adsorption of P1, P2 and P3 on the M1 and M2 membrane, and the adsorption of P3 and P3-A on M3. The structure of the HSP70 in our model is based on the PDB ID (5e84) [234] with an open state [235], containing residues 24 to 629, and the missing atoms in the structure were added with the VMD plugin psfgen [73]. In the simulations, P1, P2 and P3 were initially placed near the outside surface of membrane M1 and above the protrusion of M2; P3 and P3-A were placed near the C-terminal domain of HSP70. All the systems were placed in a 0.15 M NaCl solution. Unit cells of systems, containing P1, P2 and P3 with M1 and M2 in aqueous solution, had in total between 123,000 and 136,000 atoms, while the unit cell containing P3 and P3-A with M3 had around 194,000 atoms. The simulations were performed in the same way as described in the previous chapters.

Adsorption of polymers on different membranes

Figure 45 shows how these amphiphilic copolymers assemble in water. In 20 ns simulations, 5 P1 polymers aggregate by van der Waals (vdW) and hydrophobic forces into a big cluster with the hydrophobic groups present in its core, like in micelles. In a similar manner, the P2 copolymers aggregate, as shown in Figure 45B. However, only 4 P2 copolymers are seen to aggregate, since there is not enough room in the cluster for the remaining P2. Finally, Figure 45C shows that P3 copolymers tend to be wrapped with their own PEG chains, rather than forming a compact cluster with a hydrophobic core. In this case, the steric and entropic forces between displaced PEG chains,

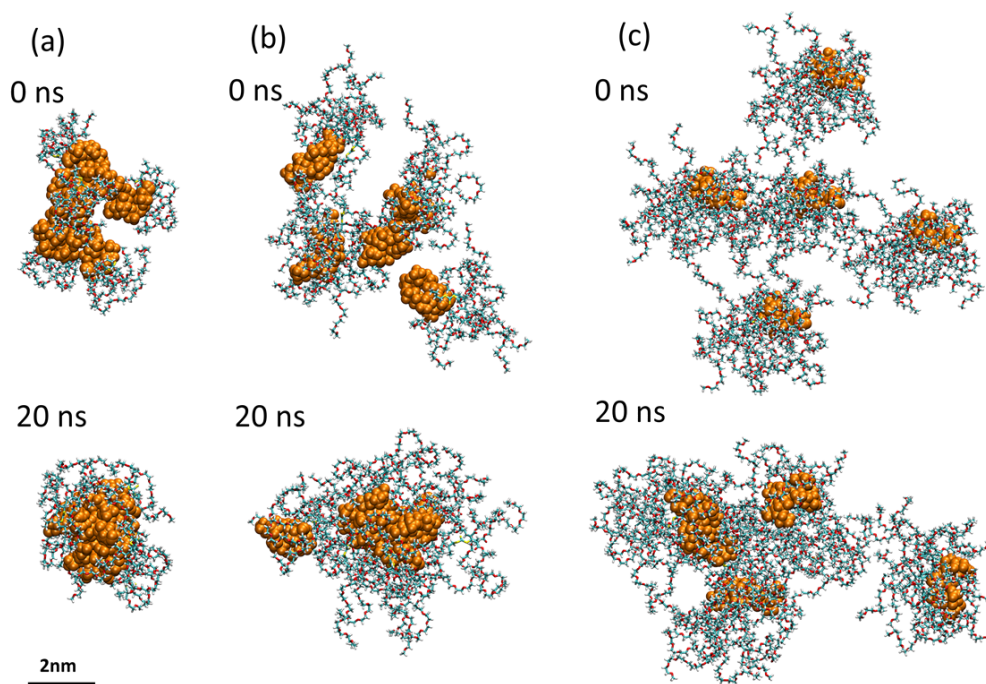


Figure 45: Self-assembly of 5 copolymers in solution. (a) P1, (b) P2, (c) P3

associated with bringing the hydrophobic parts together, would be too large to overcome. However, at longer times, we can expect that P3 dimers and occasionally trimers can form in the system. Since the P3 copolymers tend to be individually wrapped, the coverage of hydrophilic chains is less thick than those in the cluster of P2 and P1 cases.

These results are consistent with our experimental findings and further confirm that the P1 and P2 nanoaggregates can form micelle-like assemblies (eight and four polymer chains for P1 and P2, respectively), with the OEGA side chains within the shell and the PFPE blocks constituting the core. In contrast, the P3 adopts a single-chain folded conformation, indicating that the longer OEGA segment is able to stabilize a single fluorocarbon block.

Interactions between PFPE nanoparticles and cell membranes were not observed within the simulation time frame for membranes without lipid tail protrusion (Figure 46). As some defects

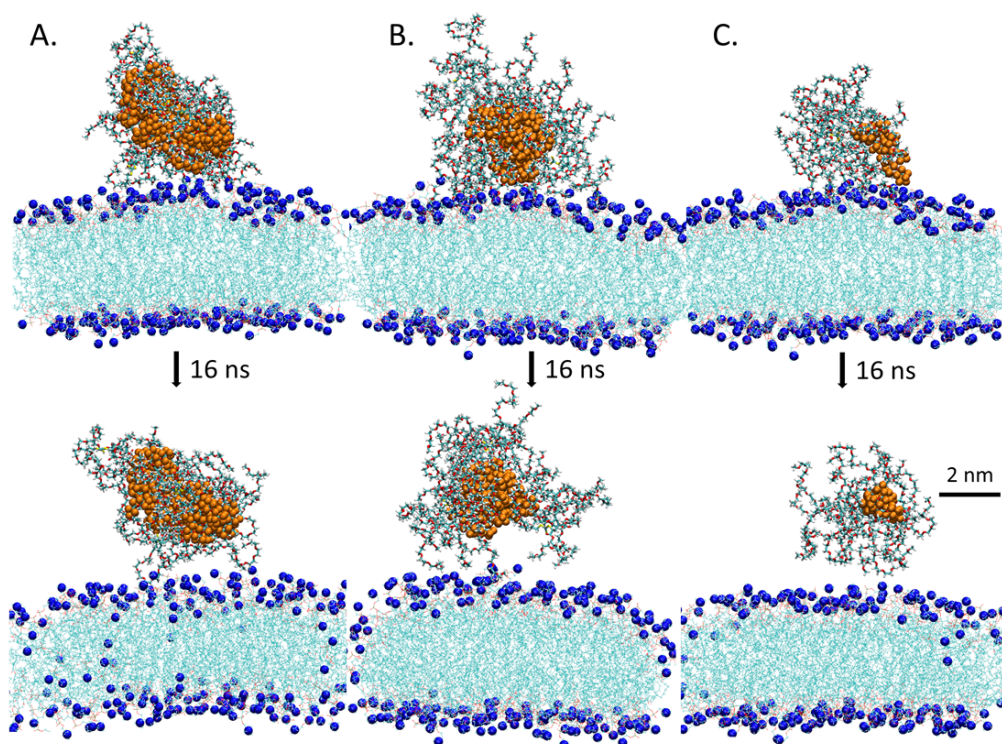


Figure 46: Side view of the interactions of polymers with M1 at 0 ns and 16 ns of the simulation. (A) P1 with M1; (B) P2 with M1; (C) P3 with M1. (Polymer hydrophobic parts are shown in orange surrounded by hydrophilic chains; Membranes show in cyan highlighted with the N atoms at the outside edge.)

may appear on the membrane in the real case [236], a biological membrane, consisting of a phosphatidylcholine (POPC) bilayer with stochastic protrusion of an aliphatic lipid tail into solution, was simulated under the same conditions. PFPE nanoparticles were then placed within 5 Å of the membrane, and simulation of the whole system was performed (Figure 47). Over the time course of 40 ns simulations, interactions between PFPE nanoparticles and the cell membrane were recorded. The proportion of hydrophobic PFPE and hydrophilic PEG segments exposed to the cell membrane (within 3 Å distance) was calculated to be 10.8, 11.3, and 13.3% for P1, P2, and P3, respectively. At 40 ns, the nanoparticles of P1 and P2 moved toward and stably settled on the surface of the membrane without noticeable changes in conformation, whereas the P3 single-chain unimers with

more hydrophobic PFPE segments exposed to the cell membrane were observed to insert and fuse within the lipid membrane (Figure 47C), presumably due to stronger hydrophobic interactions with the exposed lipid tail. We should also note that P3 has a much smaller hydrophobic core (one PFPE chain per nanoparticle) compared with P1 and P2 with eight and four PFPE chains per nanoparticle, respectively, leading to faster diffusion across barriers of cell membrane. These simulation results further support the experimental observations and highlight how exposure of hydrophobic PFPE segments to the cell surface can promote interactions with membranes and hence enhance uptake. The simulations also illustrate that a critical step to initiate cellular uptake is the hydrophobic–hydrophobic contact between the fluorinated segments and the lipid chains, and that stochastic protrusion of an aliphatic lipid tail of the bilayer into the solution is important. A similar observation was reported by Van Lehn et. al. in their studies of insertion of gold nanoparticles into model cell membranes [237].

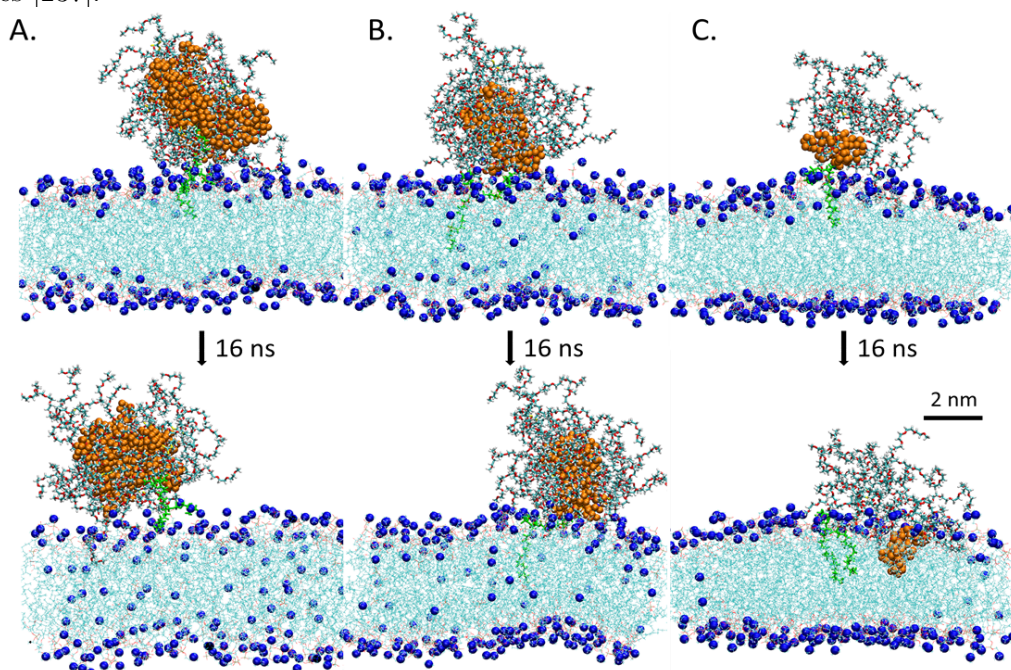


Figure 47: Side view of the interactions of polymers with M2 at 0 ns and 16 ns of the simulation. (A) P1 with M2; (B) P2 with M2; (C) P3 with M2. (protrusion is shown in green)

Figure 48 shows snapshots from the MD simulations of the interactions between the polymers and cell membrane with Hsp70 protein. In the case of P3 with M3 (Figure 48A), the polymer was not observed to interact with the Hsp70 protein for further insertion into the interior of the lipid bilayer. Therefore, the cellular uptake of P3 was not a result of the specific binding and recognition with the Hsp70 protein. However, other uptake pathways, such as passive diffusion, could still be operative. However, the incorporation of the aptamer in P3 changes dramatically the behavior. The aptamer was observed to specifically bind to the C-terminus of the SBD domain of the Hsp70 protein (Figure 48B), leading to extended retention of P3-A on the surface of cell membrane and thereby facilitating higher cellular uptake. The combination of MD simulations and experimental FACS and confocal studies of cellular uptake leads to a more complete understanding of how the highly fluorinated polymer interacts with the cell membrane in the presence of the Hsp70 protein.

We determined the number of contact points between polymers and membrane. The contacts points involve hydrophobic part, hydrophilic part and adaptor of polymer within 4 Å of the membrane or HSP70 protein (Figure 49). Figure 49A shows the decreasing hydrophilic contacts between P1, P2 and P3 with M1, respectively. The hydrophobic contacts are almost zero in all the three cases, which indicated a weak interaction between polymers and M1. With protrusion (Figure 49B), P3 shows increasing of both hydrophobic and hydrophilic contacts with M2. Compared with the interacting with M1, P1 and P2 obtained enhanced hydrophobic and hydrophilic contacts with M2. Figure 49C shows that all the contacts between P3 and HSP70 decreased to zero after 16 ns simulation, which means HSP70 has no recognition of P3. However, the P3 adaptor shows a relative stable contact with HSP70 (average 60 atoms), and the hydrophilic interaction of P3-A increase from 20 to 80 with a few hydrophobic contacts (about 10). All these indicated that HSP70 can recognize the adaptor of P3,

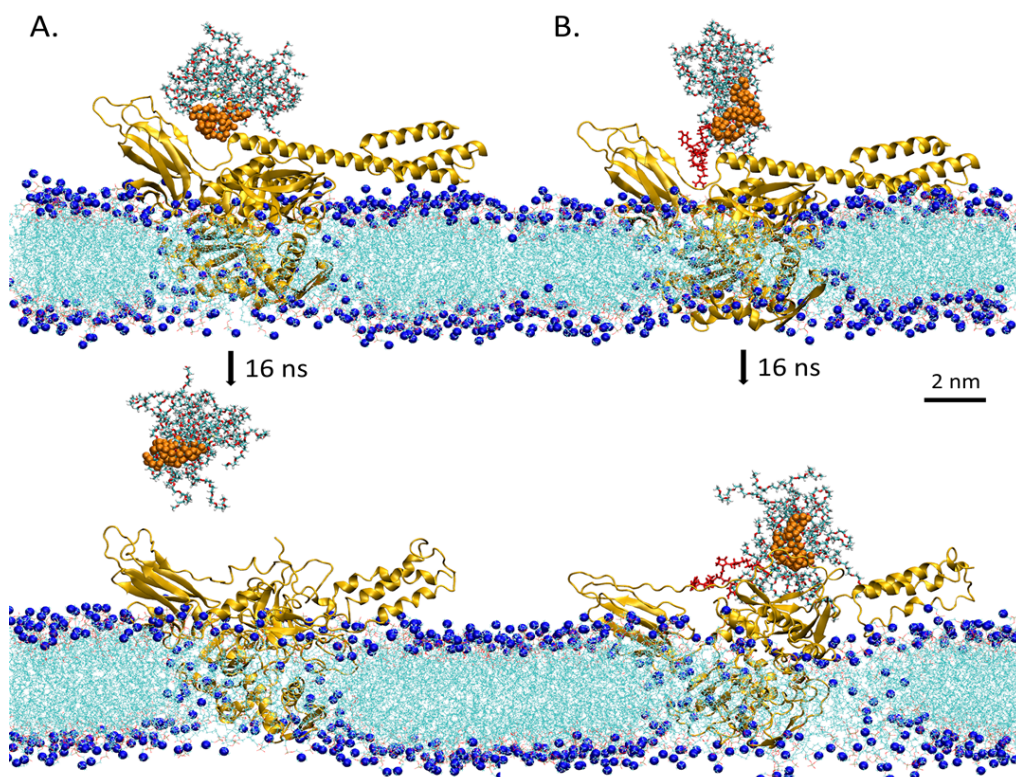


Figure 48: (A) Side view of the interactions of P3 with M3 at 0 ns and 16 ns of the simulation; (B) P3-A with M3 (Adaptor shows in red and HSP70 shows in yellow.)

and the interaction between adaptor and HSP70 could strengthen the P3 adsorption on membrane surface.

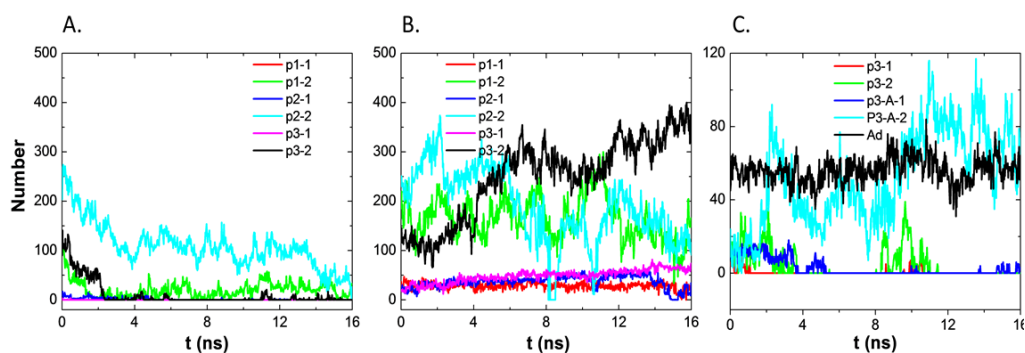


Figure 49: Number of different types of contacts between polymers and membrane during 16 ns trajectory. (A) P1, P2 and P3 with M1; (B) P1, P2 and P3 with M2; (C) P3 and P3-A with M3 (-1 means hydrophobic contacts number, -2 means hydrophilic contacts number, and Ad stands for the interaction number of adaptor with membrane.)

Conclusion

The polymeric PFPE-based platform was used to examine how aggregation behavior affects interactions between fluorinated nanoparticles and living cells at the molecular level [13–15]. P3 nanoparticles in the form of unimers contain fewer hydrophobic PFPE segments which are more extensively exposed to the solution and hence to the cell surface on encountering cells. Experimental results show that the P3 single-chain polymers show an approximately 2-fold higher uptake by MCF-7 cells, more extensive penetration into 3D MCF-7 tumor spheroids, and higher therapeutic efficacy compared to the P1 and P2 nano-aggregates which form micelles [13, 14]. MD simulations revealed that P3 with smaller size and bigger exposed hydrophobic cores is more efficient in penetrating lipid bilayer. Here, the hydrophobic interactions between PFPE parts and lipid tails provide the main driven forces. When there is protein in the membrane, the specific adaptor functionlized on P3 facilitates the interactions between P3-A and protein, which indicates the significance of specific recognition in cellular internalization of polymers.

CHAPTER 6

MODELING OF DYNAMICAL NANOSYSTEMS

(Previously published as Han, Y., Langer, M., Medved, M., Otyepka, M., Král, P. Biomimetic Materials: Stretch-Healable Molecular Nanofibers. *Advanced Theory and Simulations* **3**, 2070023 (2020); Zheng, L., Zhao, H., Han, Y., Qian, H., Vukovic, L., et.al. Catalytic Transport of Molecular Cargo Using Diffusive Binding along a Polymer Track. *Nature Chemistry* **11**, 359 (2019); Chu, Z., Han, Y., Bian, T., De, S., Král, P., Klajn, R. Supramolecular Control of Azobenzene Switching on Nanoparticles. *Journal of the American Chemical Society* **141**, 1949 (2019); Chu, Z., Han, Y., Král, P., Klajn, R. “Precipitation on Nanoparticles”: Attractive Intermolecular Interactions Stabilize Specific Ligand Ratios on the Surfaces of Nanoparticles. *Angewandte Chemie International Edition* **57**, 7023 (2018).)

In this chapter, intermolecular interactions in dynamical nanosystems were studied. The intermolecular interactions are the factors controlling the stretch-healable process of nanofibers, the diffusive motions of molecular sliders on polymer tracks, the self-assembly of NPs, and the isomerization of azobenzene ligands on NP surfaces. MD simulations were used to check the intermolecular interactions in different cases in atomistic details.

6.1 Stretch-healable molecular nanofibers

Adapted from Ref. [16] (*Adv. Theory Simul.* 2020, 3. DOI: 10.1002/adts.202070023) with the permission from Wiley Online Library.

Introduction

The self-assembly of various nanostructures [238–240] and nanoparticles [241] could be directed by solvents [44], pH [42], salinity [242], temperature [41], electric [243], optical [20] and magnetic fields [43], and other parameters. Once the coarsened materials are formed, they usually stop reorganizing, with a few exceptions, e.g., liquid crystals can be reorganized by electric fields [244]. In contrast, most biological systems retain their ability to reorganize during their entire lifetimes. Dynamically reorganizable and healable low-D materials can have applications in electronics, photonics, energy storage, and medicine, both in dry and wet forms.

It would be particularly appealing to synthesize highly stretchable (spider silk-like) and possibly electrically conducting nanofibers. Such nanofibers might be based on molecular flakes formed from graphene, graphene-like structures and other 2D materials [245], which are covalently linked into chains. The π -conjugated flakes could form conducting fibers, with structures dependent on their charging. Such molecular nanowires could transfer electric and mechanical signals from/into cellular environments [246, 247].

In this work, we combine classical molecular dynamics (MD) simulations with quantum electronic structure calculations to study nanofibers formed by functionalized, covalently linked, and self-assembled molecular flakes based on coronene and perfluorocoronene molecules. We examine the stability of these nanofibers and their ability to reversibly stretch and reassemble (self-heal) in bulk water and air of different humidities.

Methods

In the MD simulations, the partial atomic charges of flakes with different charges (-1 , $+1$ and 0) were derived using the RESP method at the MP2/6-31G(d) level by Gaussian 09 [248] in water

implicit solvent. The systems of free and linked stacked flakes were simulated by NAMD [58] and the CHARMM general forcefield [249]. The PME method was used for the evaluation of long-range Coulomb interactions. The time step was set to 2 fs. The simulations were performed in the NPT ensemble ($p = 1$ bar and $T = 298$ K), using the Langevin dynamics with a damping constant of 1 ps^{-1} .

To gain more physical insight into the coupling of CORs and PERs dimers, the coupling energies were calculated by DFT and SAPT0 methods on dimers optimized in vacuum. The dimers and monomers were first optimized at the $\omega\text{B97x-D}/6\text{-}31\text{++G(d,p)}$ level of theory, which was followed by single-point calculations with $\omega\text{B97x-D}$ and ωB97x functionals with the $6\text{-}31\text{++G(d,p)}$ basis set (Gaussian09). The SAPT0 and sSAPT0 [56] (i.e., modified SAPT0 method with empirically scaled exchange terms evaluated in S^2 approximation) calculations were performed in the Psi4 code [250] with the aug-cc-pVDZ basis set, on the previously optimized geometries.

The MM interaction energies were calculated by the NAMD energy plugin, which evaluates Coulombic and Lennard-Jones (LJ) 6 – 12 potential energy contributions. The two adjacent flakes in the middle of the columnar structures (Figure 54 a, d and g) were selected as the interacting CORs, PERs and CORs/PERs dimers. The MM energies were averaged over the last 2 ns (50 frames). The parameters in the potentials were taken from the CHARMM general forcefield with charges calculated as in Figure 50. The dielectric constant was set to 1.

Interactions between free flakes

We used classical MD simulations to model systems of many coronene $\text{C}_{24}\text{H}_{12}$ (COR) and perfluorocoronene $\text{C}_{24}\text{F}_{12}$ (PER) molecules in different charge states. Their partial atomic charges (Figure 50) were calculated in water implicit solvent by Gaussian 09 [248]. In neutral PER, highly elec-

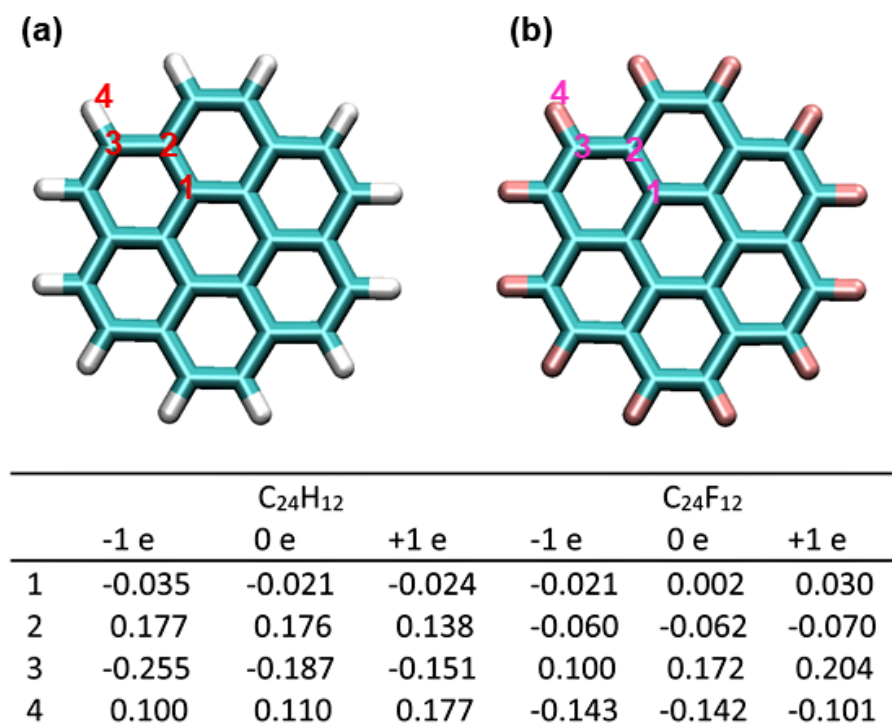


Figure 50: Partial charges distribution of (a) coronene and (b) perfluorocoronene. Labeling of 1 – 4 atoms refers to the table that displays partial atomic charges used in MD simulations for negatively, neutral and positively charged flakes.

tronegative F atoms have negative charges and neighboring C atoms have positive charges, whereas in neutral COR, less electronegative H atoms have positive charges and neighboring C atoms have negative charges. Similar charge distributions are present in benzene (C_6H_6) and hexafluorobenzene (C_6F_6), which form stable alternating stacks [251–253]. In the charged CORs and PERs, the charge distributions show the same trend as their neutral cases, except the inner C atoms of PERs (labeled as 1 in Figure 50).

To understand coupling of such flakes, we calculated their coupling energies in vacuum by different methods. The benchmarking of coupling energies calculated by selected density functional theory (DFT) methods for different molecules coupled with COR indicates that the ω B97x-D method [254]

fairly reproduces the trend revealed by the reference CCSD(T)/CBS method (Table 1 and Table 1), overestimating the coupling energies by ca 1.6 – 3.8 kcal/mol. The interaction energies of the COR/PER, PER/PER, and COR/COR dimers, calculated by DFT methods, the symmetry-adapted perturbation theory (SAPT) [54], and the Molecular Mechanics potential (MM), are shown in Table 2, Figure 51 and Table 3. Under the DFT framework, the ω B97x-D and ω B97x [255] functionals with the 6-31++G(d,p) basis set were used. The interaction energies of COR/PER, PER/PER, and COR/COR dimers calculated with ω B97x-D are –37.0, –33.9, and –27.0 kcal/mol, respectively (Table 2). These results are in a reasonable agreement with the SAPT0 method [55] giving the interaction energies of –48.0, –40.6 and –37.8 kcal/mol for these pairs of flakes, respectively (Table 3). Figure 51b shows the decomposition of the SAPT0 interaction energies, where the dispersion interactions contribute by more than 50 % to attractive energy in all three cases. Dispersion interactions originates from electron correlations, which tend to be large in unsaturated systems (aromatic), where electrons can occupy many unoccupied orbitals and thus stabilize binding of the structures. Therefore, the dispersion interactions play a significant role in stabilization of the flake COR and PER systems. Stacking of aromatic systems are known to be stabilized to a large extend by dispersion interactions, as shown in many research papers [256,257]. However, the stability of different flake dimers (CORs, PERs and CORs/PERs dimers) is a result of a complex interplay of noncovalent interactions. Using the partial charges calculated in water implicit solvent, MM predicts somewhat smaller interaction energies, but reproduces the trend predicted by the QM methods calculated in vacuum. These energy values could provide a rough physical insight about the assembling patterns observed in the MD simulations.

The interaction energies ΔE_{int} of two flakes are calculated as an energy difference of a flake dimer and two flake monomers having the geometries of the dimer. The physical insight into the strengths

of coupling of CORs, PERs and CORs/PERs was deciphered by DFT calculations, SAPT0 [55] calculations, and Molecular Mechanics potential in vacuum. In the DFT calculations, the ω B97x-D [254] and ω B97x functionals [255] with the 6-31++G(d,p) basis set were chosen. The empirical atom-atom dispersion potential in ω B97x-D accounts for the dispersion interaction between molecules in the dimer.

First, the validity of the ω B97x-D functional was benchmarked against the CCSD(T)/CBS method in calculations of the interaction energies for small organic molecules weakly bound to coronene [258]. The interaction energies of seven organic molecules adsorbed on coronene were calculated using Gaussian 09 [248] with the ω B97x-D functional and the same B97D geometries as in the CCSD(T)/CBS calculations, kindly provided by the authors [258] (Table 1). The ω B97x-D functional correctly sorted molecules according to their interaction energies (Table 1) (for the absolute values, please see Table 1). Therefore, this functional was used in the DFT calculation of interaction of COR/COR, COR/PER and PER/PER dimers, together with ω B97x and MM potential (Table 2, Figure 51a).

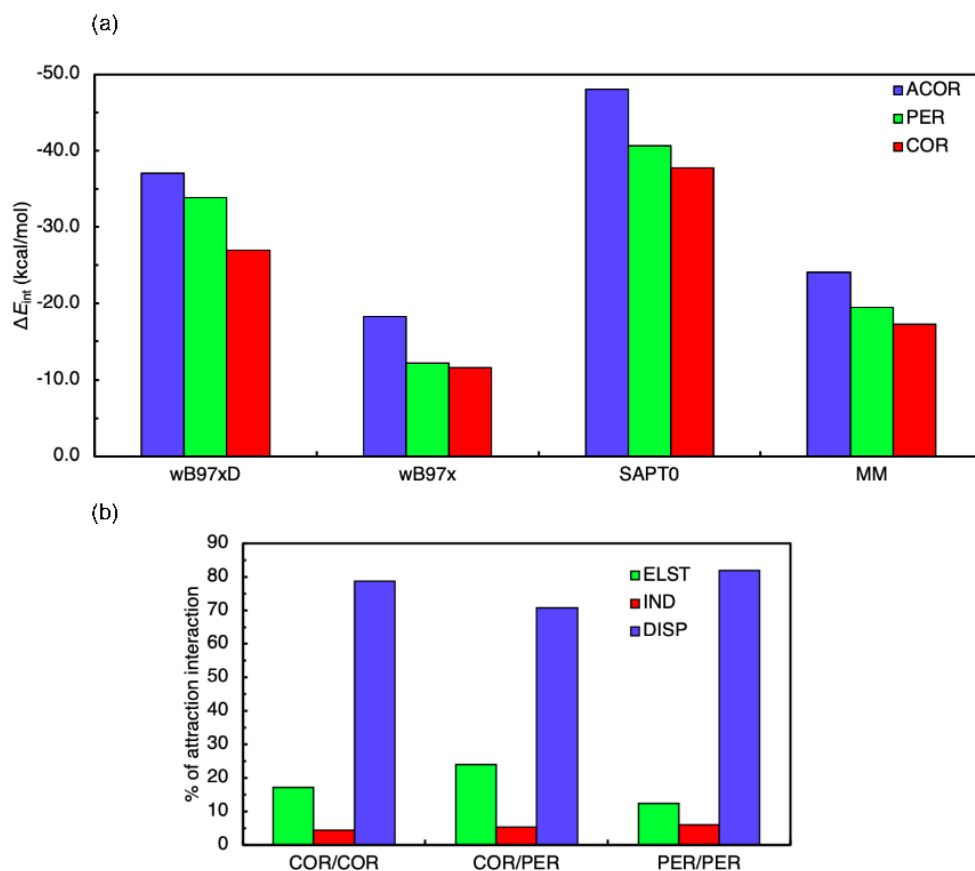


Figure 51: (a) Interaction ΔE_{int} (in kcal/mol) of COR, COR/PER and PER dimer, calculated with two different functionals and Molecular Mechanics (MM) potential. (b) Decomposition of the attractive contributions to the interaction energy from *SAPT0*.

Table 1 clearly shows that in the absence of dispersion interactions, the interaction energies calculated with $\omega B97x$ are energetically higher for all three cases, which indicates that stacks are mainly stabilized by dispersion interactions. Furthermore, SAPT [54–56], which is a suitable method to estimate the role of dispersion and other terms, demonstrated that dispersions largely contribute to attractive forces between the dimers (see Figure 51 and Table 3). Both DFT and SAPT calculations revealed that CORs/PERs formed the most stable dimer, followed by PERs and CORs. The same trend was also obtained from the calculations performed with a molecular mechanics (MM) potential,

composed of Coulombic and Lennard-Jones (LJ) 6 – 12 potentials (the parameters were taken from CHARMM general force field with the charges recalculated as shown in Figure 50).

Table 1: Interaction energies ΔE_{int} (in kcal/mol) of seven studied molecules on coronene calculated by ω B97x-D, ω B97x functionals, and other methods. [258]

compound	ω B97x-D/ 6-31++G(d,p) ^a	ω B97x/ 6-31++G(d,p) ^a	optB88-vdW/ PW ^b	M06-2X/ cc-pVTZ ^b	SCS(MI)-MP2/ CBS ^{a,b}	CCSD(T)/ CBS ^{a,b}
acetone	-9.0	-5.3	-8.5	-7.5	-7.9	-7.6
acetonitrile	-6.9	-4.3	-6.6	-5.4	-6.6	-6.2
dichlormethane	-7.4	-4.6	-6.8	-5.4	-7.0	-6.7
ethanol	-8.7	-5.4	-7.8	-7.1	-7.1	-7.1
ethyl acetate	-11.5	-6.6	-10.5	-9.1	-9.7	-9.7
hexane	-13.5	-6.7	-11.6	-9.9	-10.7	-10.4
toluene	-13.7	-6.7	-12.1	-9.7	-13.5	-11.9

^a B97D geometries; ^b Taken from the literature.

Table 2: Interaction ΔE_{int} (in kcal/mol) of COR, COR/PER (ACOR) and PER dimer, calculated with two different functionals and Molecular Mechanics (MM) potential.

Method	ω B97x-D/ 6-31++G(d,p) ^a			ω B97x/ 6-31++G(d,p) ^a			MM dimer in MD ^b		
System	COR	ACOR	PER	COR	ACOR	PER	COR	ACOR	PER
ΔE_{int}	-27.0	-37.0	-33.9	-11.7	-18.3	-12.2	-17.3	-24.1	-19.5

^a ω B97x-D geometries. ^b dimer taken from MD simulations (Figure 54a, d, g).

MD simulations of free flakes

Next, we used classical MD simulations to model the self-assembly of free molecular flakes with partial charges from Figure 50. Initially, alternating stacks of neutral CORs and PERs were simulated in water. Within 10 ns, the stacks arranged into a hexagonal lattice, as shown in Figure 52a and Figure 53. The flakes rotated [258] and became slightly tilted, due to interactions between neighboring stacks.

In the following model simulations, all flakes were charged in the same way, each with elementary charges of +e or -e (Figure 50), but no chemical reactions of flakes with water and each other were considered. The charged flakes quickly reorganized, as shown in Figure 52b (negative) and

Table 3: SAPT0 [55] and sSAPT0 [56] interaction energy decomposition (in kcal/mol), calculated with aug-cc-pVDZ basis set in Psi4 code [250].

System	COR/COR		COR/PER		PER/PER	
Basis set	aug-cc-pVDZ		aug-cc-pVDZ		aug-cc-pVDZ	
	SAPT0	sSAPT0	SAPT0	sSAPT0	SAPT0	sSAPT0
Electrostatics	-12.2	-12.2	-21.3	-21.3	-9.4	-9.4
Exchange	34.0	34.0	41.0	41.0	36.5	36.5
Induction	-3.1	-3.2	-4.7	-4.7	-4.6	-4.6
Dispersion	-56.4	-56.5	-62.9	-62.9	-63.1	-63.1
TOTAL	-37.8	-37.8	-48.0	-48.0	-40.6	-40.7

Figure 52d (positive), collected after 30 ns. In the system with negative flakes, PERs formed columnar structures, but CORs were mostly free. On the other hand, in the system with positive flakes, CORs formed columnar structures, but PERs were mostly free. The presence of different structures, due to different charging, shown in Figure 52b, d, is in line with Figure 54c, e. Figure 54 shows that columnar structures of 8 CORs can be maintained when CORs are neutral or positively charged. Neutral PER stacks are dimerized (Figure 54d), but negative PER (Figure 54e) and alternating neutral COR/PER (Figure 54g) stacks are stable.

When the flakes in Figure 52b, d were discharged, they reorganized in a random way where stacks were mixed preferably in a COR/PER pattern, as shown in Figure 52c, e (as in Figure 54a, g). The same system was also simulated in a 150 mM NaCl aqueous solution (Figure 55). Here, the columnar structures formed by charged flakes were shorter, which is attributed to screening. Our simulations show that the self-assembling of free flakes can be controlled by their composition, charging and solvent environment.

Figure 53 shows the initial and final structures of neutral CORs and PERs stacks, modeled by MD simulations and discussed further in Figure 52. After 10 ns, the stacks rearranged into a hexagonal lattice and the alternating CORs and PERs arrangement was maintained.

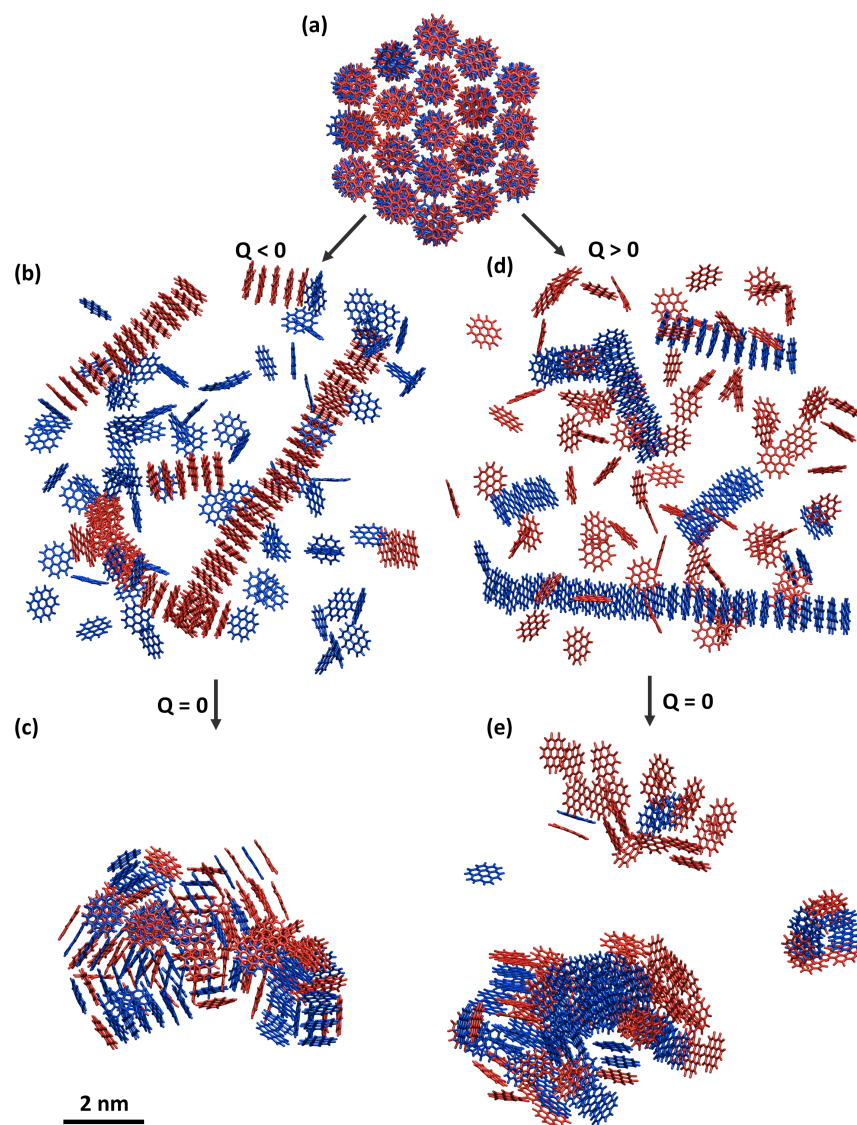


Figure 52: MD simulation snapshots showing differently stacked CORs (blue) and PERs (red) in water with NaCl counterions. (a) Initially pre-assembled and thermalized system after 10 ns of simulations. (b, d) Then, the flakes in (a) were negatively and positively charged by $-e$ or $+e$ according to Figure 50. After 30 ns simulations, the flakes reorganized differently. (c, e) Then, the flakes in (b, d) were discharged. After another 30 ns, they reassembled into structures with mixed CORs and PERs. For clarity, water and ions are not displayed.

To reexamine the observations in Figure 52, eight columnar flakes of neutral, positive, and negative CORs, PERs, and alternating CORs/PERs (ACORs) were separately prepared and simulated

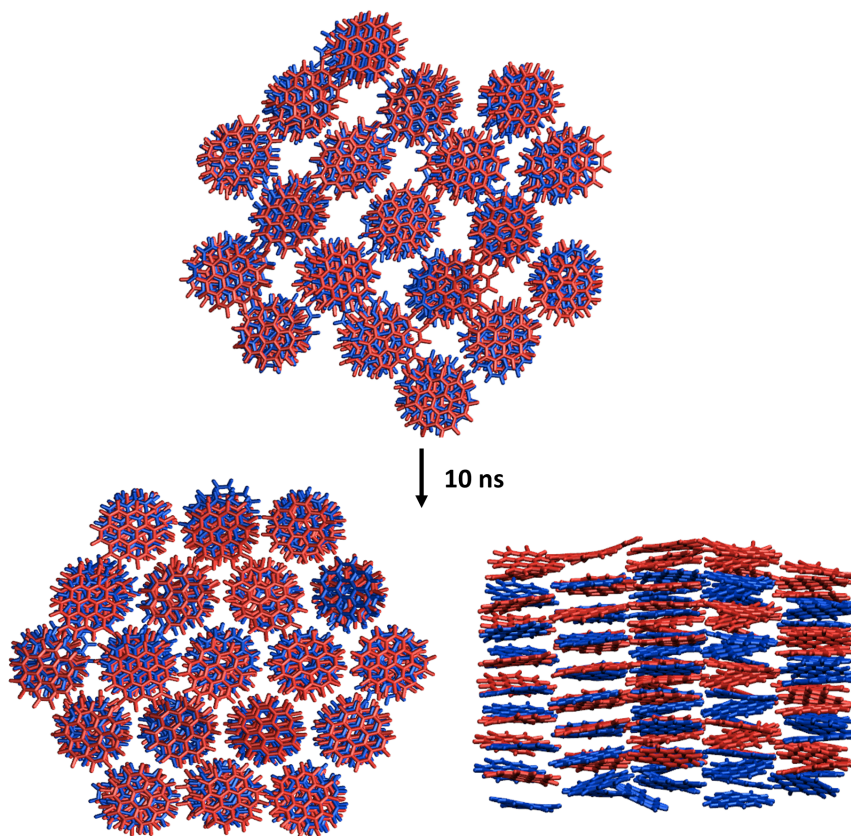


Figure 53: The stacks of neutral flakes were stable after 10 ns simulations in water. The stacks arranged into hexagonal shape (see top view) and the alternating HFHFHF pattern was preserved (see side view). Coloring scheme: blue – CORs; red – PERs.

in water. When the flakes were charged by $+e$ or $-e$ with the partial atomic charges shown in the table of Figure 50, they were simulated with counterions. These simulations gave similar results as Figure 52 in the main text: after 30 ns, the neutral and positively charged CORs, the neutral ACORs and the negatively charged PERs were all stable (see Figure 54). PERs tend to form dimers rather than columnar structure as shown in Figure 54d. This could be explained by a weaker electrostatic energy of the dimer coupling (-9.4 kcal/mol, Table 3).

To check how the ionic solution influence the formation of stacked flakes, the system in Figure 52 was also simulated in a 150 mM ionic solution (NaCl). Once the flakes in the original stacks were

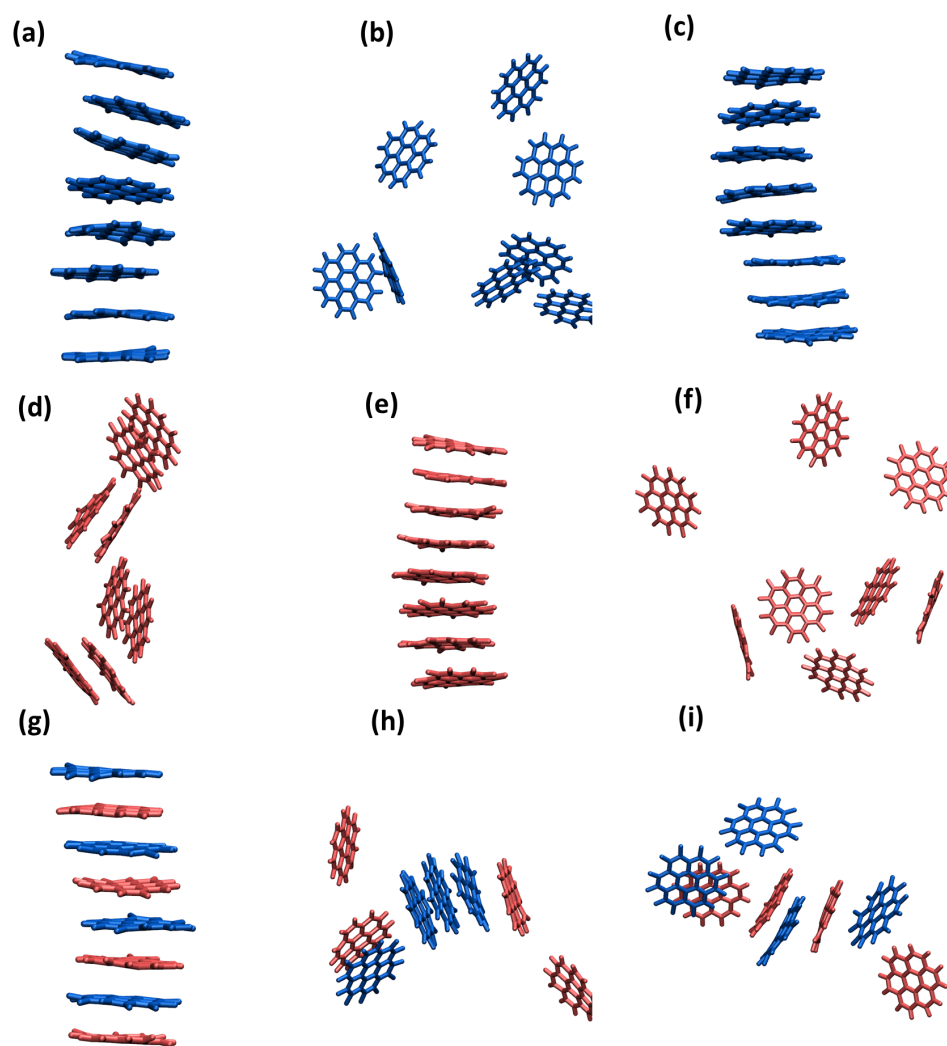


Figure 54: (a-c) The final structures of coronene stacks with neutral, negative, and positive charges, (d-f) The final structures of perfluorocoronene stacks with neutral, negative, and positive charges, (g-i) The final structures of alternating coronene stacks with neutral, negative, and positive charges. Counterions and water are not presented. Coloring scheme: blue – CORs; red – PERs.

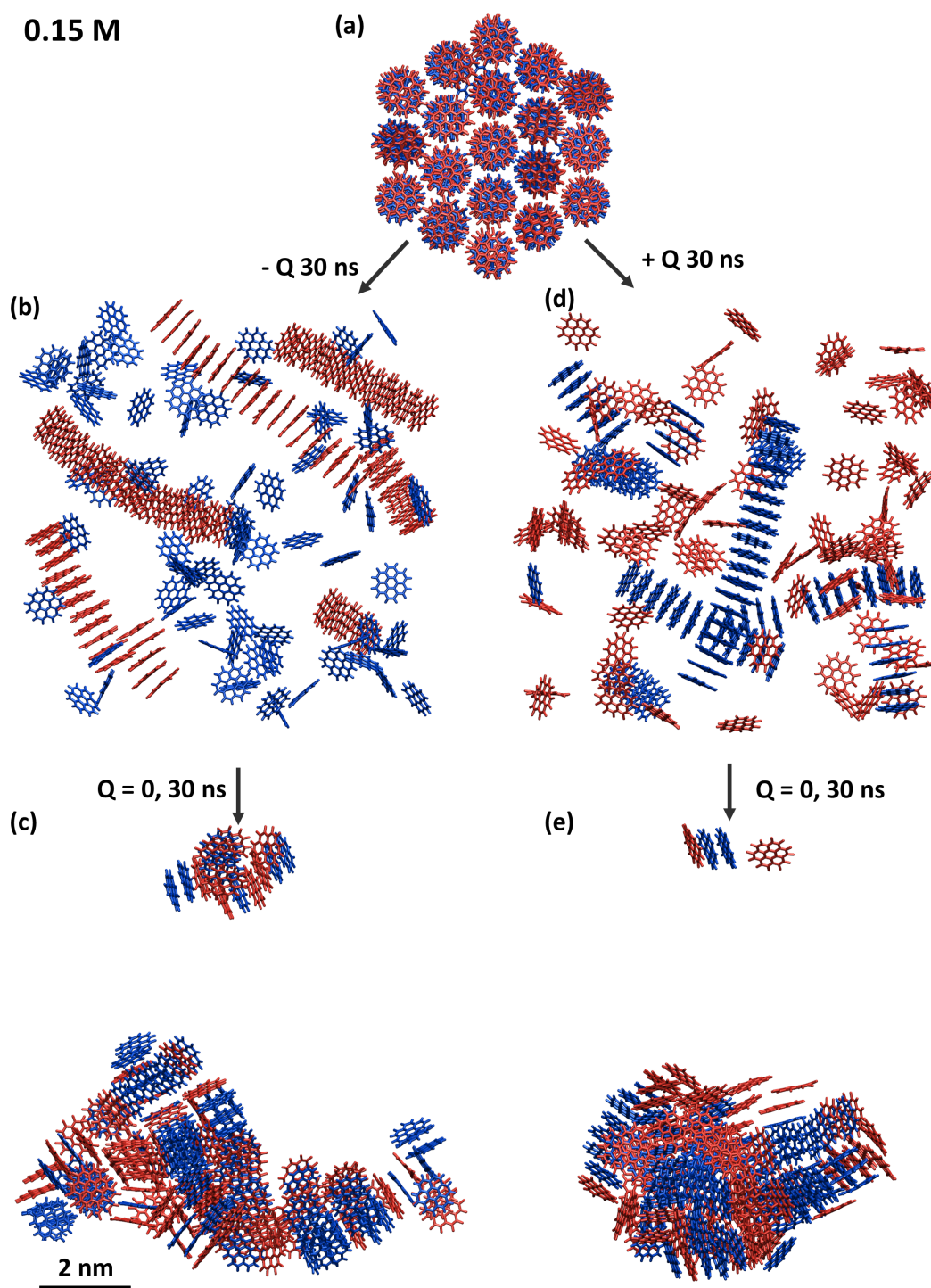


Figure 55: Snapshots of MD simulations showing differently stacked CORs and PERs in 150 mM NaCl solution. (a) Initially pre-stacked and thermalized system after 10 ns of simulations. (b, d) Then, each flake in (a) was negatively or positively charged by $-e$ or $+e$ with the partial charges shown in Figure 50. After 30 ns of simulations, they reorganized differently. (c, e) Then, the flakes in (b, d) were discharged. After another 30 ns, they re-assembled into structures with mixed CORs and PERs. For clarity, water and ions are not displayed. Coloring scheme: blue – CORs; red – PERs.

negatively or positively charged (each one was charged by $-e$ or $+e$ according to Figure 50), columnar structures formed in Figure 55(b, d) similar to those in Figure 52(b, d). The difference is that shorter columnar stacks were formed in the ionic solutions after charging the flakes, compared with that in water Figure 52(b, d). This is attributed to the screening effect of ions. After all the stacks were discharged, alternating structures of CORs and PERs and random stacks were formed in Figure 55(c, e).

MD simulations of linked flakes

Highly-defined "spider silk-like fibrils" could be prepared when the molecular flakes, which tend to self-assemble, are covalently linked by short and flexible bridging molecules. To explore this possibility, we linked the neutral COR and PER (COR/PER pattern) flakes by short oligomeric polyvinyl alcohol (PVA) chains: 8 flakes were connected by 7 PVA chains ($-[\text{CH}_2\text{-CH}(\text{OH})]\text{-}$), each with 5 vinyl alcohol monomeric units, where carbon atoms of PVA connected to carbon atoms of the flakes in the trans configurations. These short linear stacks were simulated in bulk water, in the presence of water nanodroplets (vapor), and in vacuum, as shown in Figure 56 and Figure 59.

Stacks of linked neutral CORs and CORs/PERs were first prepared and stabilized for 30 ns in vacuum. Then, these stacks were placed in bulk water, close to nanodroplets, or left in a vacuum (Figure 56a, Figure 59a). In these media, the stacks were gradually stretched by a force of $F = 200$ pN, applied to the right terminal flakes (one atom on the left terminal flakes was fixed), as shown in Figure 59a. In all media, the flakes at the two ends of the chains started to unfold first. In the systems with water droplets (humidity), their surface tension caused the droplets to embrace groups of self-assembled flakes and to resist their dis-assembly by the stretching force. Since the applied force is large, the linked flakes stretched fast into chains. Once the force was turned off, the stretched chains started to collapse in a stepwise manner. They did not form the same structures

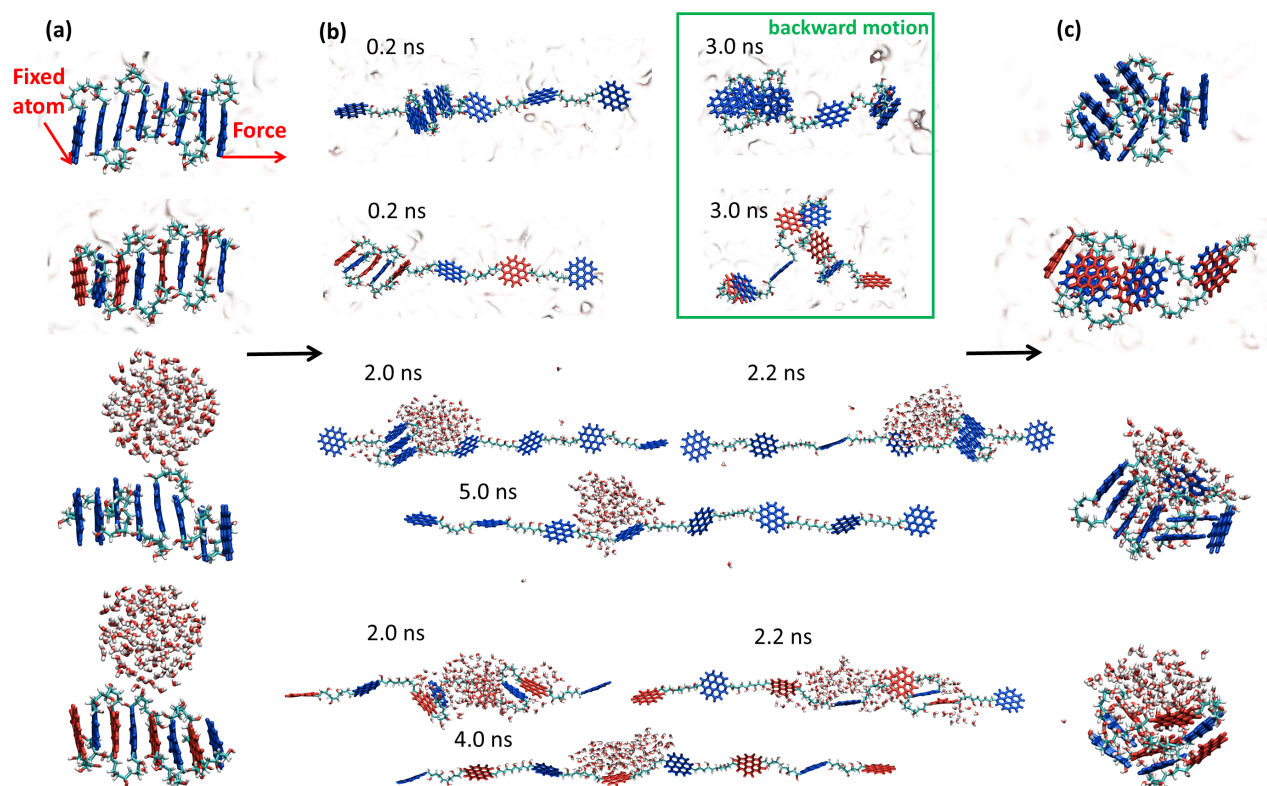


Figure 56: (a) COR and COR/PER flakes linked and pre-assembled into linear stacks in bulk water and with small water droplet (top to bottom). (b) Intermediate and fully stretched chains; top 4 panels at 0.2 ns (forward motion) and 3.0 ns (backward motion, marked in blue box). (c) Re-assembled structures. Coloring scheme: blue – CORs; red – PERs.

as at the beginning (Figure 56a, Figure 59a), but more random assemblies embracing water droplets (Figure 56c, Figure 59c). Figure 56b shows some intermediate steps of stretching and collapsing (healing) nanofibers in different media.

Figure 57 shows time-dependent lengths of the above nanofibers, which were stretched by a force of $F = 200$ pN and then spontaneously released (no force). In bulk water (Figure 57a), the CORs and CORs/PERs stacks were stretched to full lengths within 1.5 ns, with relatively smooth trajectories, where the featured conformations are shown in the plots. When the force was turned off, the structures collapsed in ≈ 4 ns. In the presence of water droplets (Figure 57b, c), the droplets release in a stepwise manner with the assembled flakes solvated in their interior, which led to a

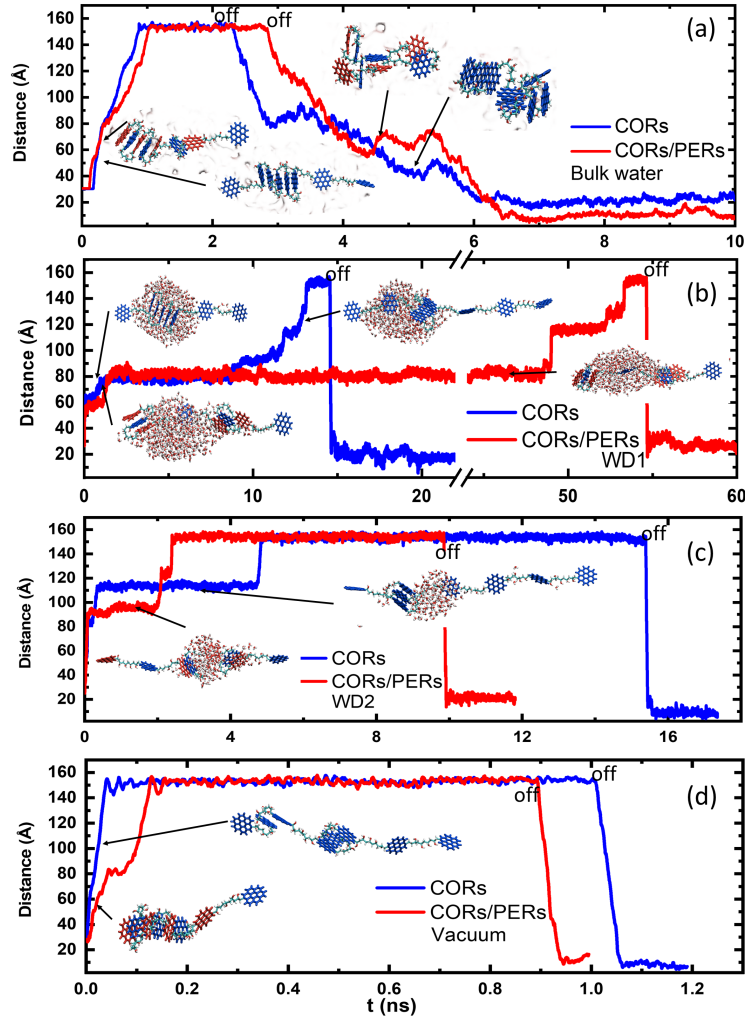


Figure 57: Stretching of neutral CORs and neutral CORs/PERs fibers: The distance between the two fiber ends under a stretching force of $F = 200$ pN (a) in bulk water, (b) with a big water droplet, (c) with a small water droplet, and (d) in vacuum. The force is turned off at times when the chain lengths are seen to drop from their maximum values (marked as off). Coloring scheme: blue – CORs; red – PERs.

slow stepwise stretching of the fibers. The stronger the flakes bind to water, the more significant is this effect. For larger droplets (Figure 57b), a full stretching of the CORs and CORs/PERs stacks took 12.5 ns and 53 ns, respectively, when the CORs/PERs trajectory developed five plateaus. For smaller droplets (Figure 57c), the CORs and CORs/PERs stacks were fully stretched within 5.0 ns and 2.5 ns, respectively. In vacuum (Figure 57d), the stretching processes took < 0.2 ns. Here, CORs

(binding energy of -27.0 kcal/mol) stretch quicker than CORs/PERs (-37.0 kcal/mol) in bulk water and vacuum, since the mixed flakes have a stronger coupling (Figure 51, Table 1, Table 2). In all simulated systems, except bulk water (slow diffusion), the structures collapsed extremely fast (< 0.03 ns).

Figure 58 also shows the stretching dynamics of nanofibers in bulk water under different forces applied to their two ends. At $F = 100$ pN, a full stretching of CORs and CORs/PERs took 25 ns and 12 ns, respectively (Figure 58a), while at $F = 200$ pN, it took just 0.9 ns and 1.2 ns (Figure 58b). The CORs were stretched faster than PERs during earlier stretching times, as shown in Figure 58 a and b, which is in line with cases in Figure 57 a-d. However, the overall stretching time is affected by fluctuations. In general, at smaller stretching forces, the prolongation was slow with typical steps, while at larger forces it was fast and smooth. The steps are caused by energy barriers associated with the dis-assembly of individual flakes from the stacks. Larger forces can easily overcome these barriers, giving fast and smooth prolongation of the nanofibers.

To better understand the fluctuations in elongation of these nanofibers during their stretching, three separate replicas of neutral CORs and CORs/PERs fibers were separately stretched in bulk water by a force of 85 pN. As shown in Figure 58 (c-d), the elongation steps and simulation times that were necessary for these nanofibers to fully stretch were slightly different in the three replicas. These differences may be related to slightly different initial arrangements of the structures and fluctuations present in each replica. However, these effects should average out in ensembles of such fibers, i.e., in longer fibers or many parallel fibers.

The stacks of neutral CORs and neutral CORs/PERs covalently connected by short linkers were put in bulk water, water droplets and vacuum (Figure 56, Figure 59). The water droplets were placed on top of stacks in the middle position as shown in Figure 59a. The stacks were stretched by applied

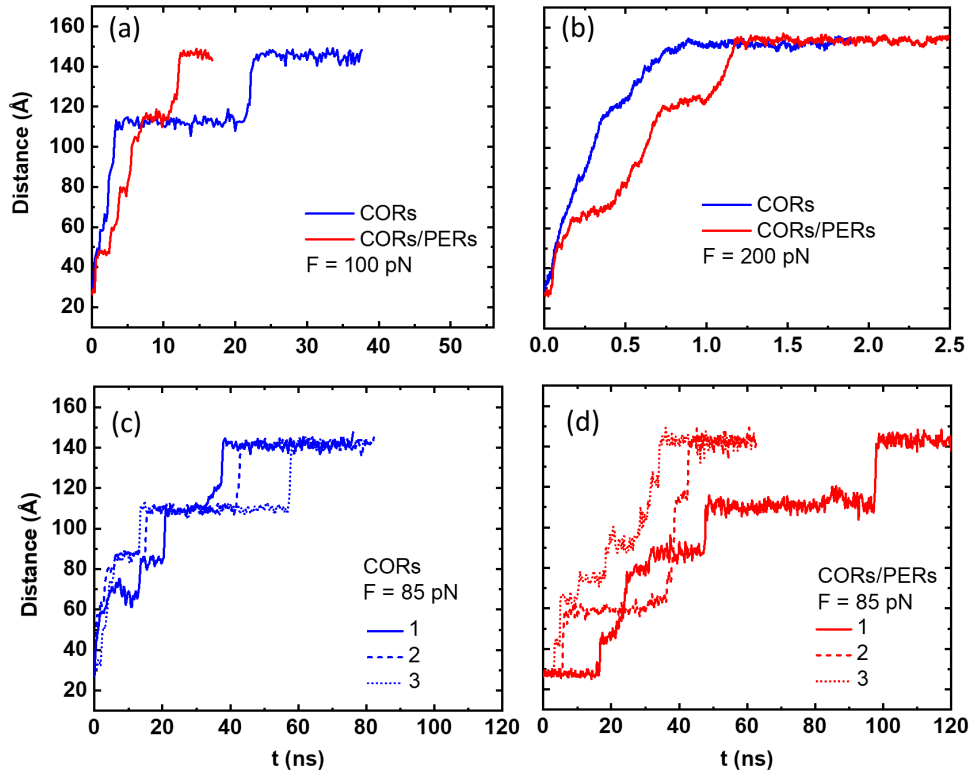


Figure 58: (a-b) Stretching of neutral COR and COR/PER nanofibers in bulk water: The lengths of nanofibers under a stretching force of (a) $F = 100$ pN, (b) 200 pN. (c-d) Three replicas stretched separately with a force of 85 pN: (c) neutral CORs, (d) neutral CORs/PERs.

forces of $F = 200$ pN to their terminal flakes on the right with an atom on the left end fixed (top panel of Figure 59a). Once the stacks were fully stretched into chains, as shown in Figure 59b, the forces were disconnected. Figure 59c reveals that the stretched chains re-assembled back, but they did not form exactly the same structures as at the beginning (Figure 59a). Figure 59b shows part of the intermediate structures with the applied forces at different time. The flakes at the two ends of the chains start to unfold first which is independent of the water environment. The big water droplet tends to embrace the unfolded flakes to resist the stretching force. Due to the limit of the surface tension of the water droplet, the embracing force is quickly overcome by the applied force which lead to the full stretching of the chain. Without water environment, the applied force only need to

overcome the interaction between the CORs and CORs/PERs flakes, which cause faster stretching.

The intermediate stretching steps at $t = 0.03$ ns are shown in Figure 59b (bottom two panels).

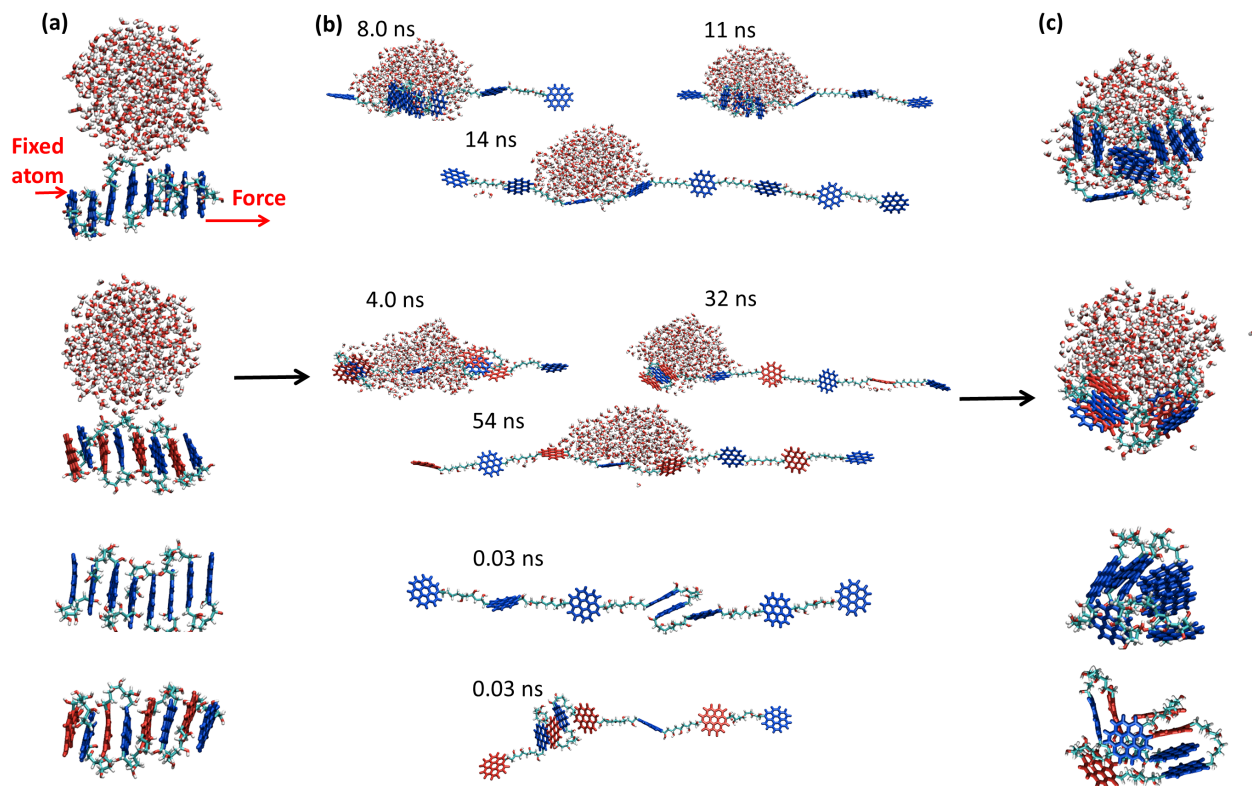


Figure 59: (a) CORs and CORs/PERs flakes linked and pre-assembled into linear stacks (top to bottom): with a big water droplet and in vacuum. (b) Intermediate and fully stretched chains. (c) Re-assembled structures. Coloring scheme: blue – CORs; red – PERs.

Conclusion

In summary, using MD simulations and electronic structure methods, we have shown that coronene and perfluorocoronene molecules can self-assemble into stacks in environments of different humidities. When the molecular flakes within such stacks are covalently linked, they can form stretchable and healable nanofibers [259]. These ultra-stretchable and possibly electrically conducting nanofibers can have many diverse applications in materials, electronics, and sensing.

6.2 Cargo-carrying peptide sliders on polymer tracks

Adapted from Ref. [17] (*Nat. Chem.* 2019, 11. DOI: 10.1038/s41557-018-0204-7) with the permission from Nature Publishing Group.

Introduction

Inspired by the natural transport systems e.g. transport of vesicles along microtubular tracks [260], scientists want to develop synthesized transport systems with the ultimate goal of developing molecular robotics and assembly lines [261]. Most artificial systems have employed DNA architectures as programmable devices for the transport of DNA strands [262] or gold nanoparticles [263]. However, most of the designs need the supply of energy to trigger the transporting motions [264]. In contrast, diffusive transport is energy independent and can have comparable efficacy as active transport [265]. A number of interesting examples of molecular-scale walkers have been developed which were based on reversible supramolecular interactions or dynamic covalent bonds [17, 266]. We are inspired by the efficient sliding and hopping motion of proteins along polynucleotides, as this form of diffusive transport does not require a chemical fuel [267]. Here, we present a synthetic diffusive transport system which is capable of picking up, transporting and ultimately depositing molecular cargo [17].

By functionalizing the molecular sliders with different reactive groups, we can study the changes in reaction rates between freely diffusing molecules and systems with reduced dimensionality [17]. Furthermore, MD simulations were performed to study the diffusive binding modes of sliders on polymeric tracks. The experimental observed rate enhancement was well explained in combination of diffusion constant calculations.

Experimental results

”As a model reaction, we chose the reaction between an alkylthiol and bromo-substituted N-methylmaleimide, which yields a fluorescent product on substitution of the bromide by the thiolate. This reaction is typically slow in the absence of tracks, as seen in Figure 60C and D where μM concentrations of reactants ($6\ \mu\text{M}$ thiols and $5\ \mu\text{M}$ maleimides, respectively) were used. However, following the addition of polycations, the reaction rates were enhanced significantly, with either slider reaching nearly full conversion within minutes on both pLys and pArg tracks (Figure 60C and D). The concentrations of pArg and pLys were chosen such that the charged monomer concentration equivalents were 1.76mM , that is, the concentration of positive charges on the track was at least 50-fold greater than the measured dissociation constants between polymers and sliders. It follows that over 98% of the reactants are bound on the polycations (at the μM concentrations used). We calculated the relative rate enhancements from the initial slopes of the reactions. The reaction between slider 1 and the bromo-substituted N-methylmaleimide-1 conjugate was accelerated by 113- and 110-fold by pArg and pLys, respectively. Similarly, slider 2 gave enhancements of 149- and 77-fold by pArg and pLys, respectively. As a control, the addition of 1.76mM arginine (the same concentration of opposite charge, but no polymeric backbone) showed only a marginal increase in the reaction rate, confirming the essential role of the polymeric ‘tracks’ in increasing the rates of bimolecular reactions” [17].

MD simulations of sliders with tracks

Systems and methods

In order to clarify the observed reaction rates of molecular sliders and their bromo-substituted N-methyl-Maleimide conjugates taking part on polycation tracks, atomistic MD simulations of the

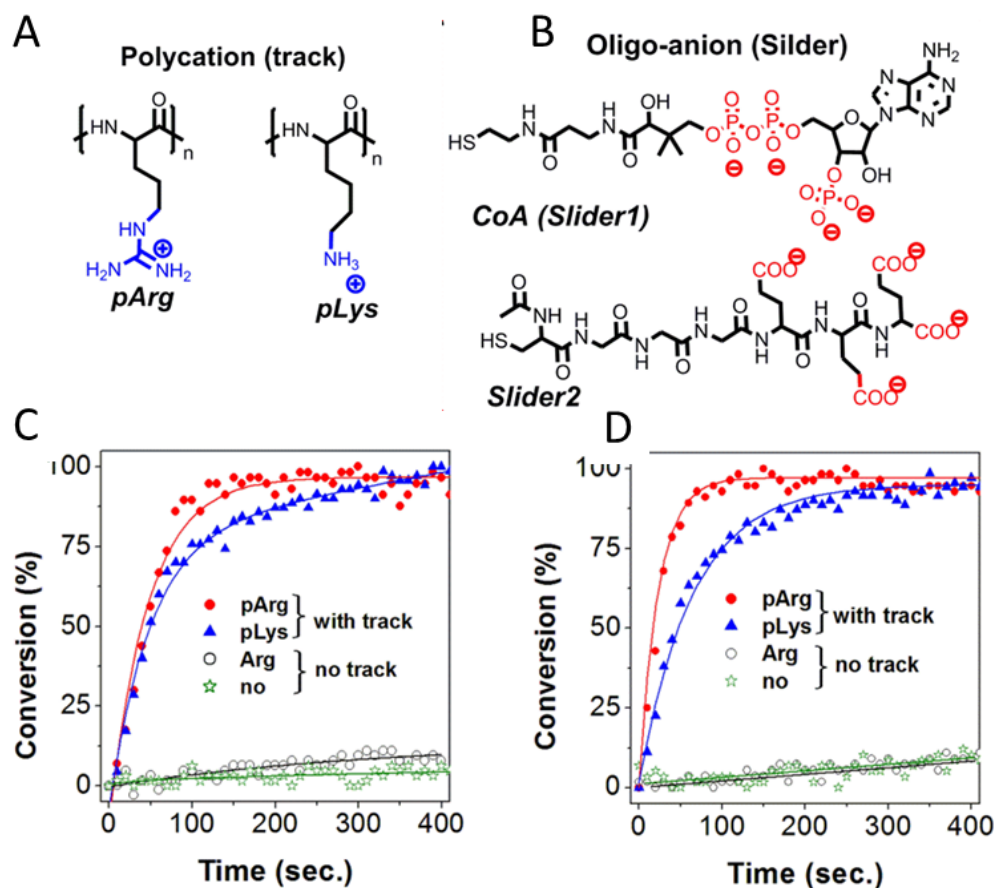


Figure 60: (A) Two types of molecular tracks; (B) functionalized (reactive) sliders; (C) The kinetics of the reaction between slider 1 and bromo-substituted N-methylmaleimide-1 are accelerated significantly by the presence of polycations. (D) The kinetics of reaction between slider 2 and bromo-substituted N-methylmaleimide-2 are also accelerated significantly by the presence of polycations.

sliders' motion on these tracks were performed. These cases were simulated: slider 1-*pArg*/*pLys*, with one slider 1 and one polyArginine or polyLysine track of 95 Arginine or Lysine residues placed in a 25 mM MES solution; slider 2-*pArg*/*pLys*, with one slider 2 and one polyarginine/polylysine track of 95 arginine/lysine residues placed in a 22 mM MOPS solution. A 95-residues long track with a molecular weight of 15,000 Da was selected to represent a polycation track. The positive charge arising from the polycation chain is close to 96 mM (3,000 folds larger than the dissociation

constant of slider), which means that a slider practically does not leave the polycations during the simulations.

The charges and dihedrals parameters for the tail of slider1 (between the thiol group and phosphate group) were separately calculated by a ForceField Toolkit [72] from VMD [73] after performing a geometry optimization at the MP2 level by GAUSSIAN 09 [248]. The polycation tracks were described by a CHARMM36 forcefield [249]. The PME [62] method was used for the evaluation of long-range Coulombic interactions. The time step was set to 2.0 fs. The simulations were performed in the NPT ensemble ($p = 1$ bar and $T = 300$ K), using the Langevin dynamics ($\gamma_{\text{Lang}} = 1 \text{ ps}^{-1}$). After 2,000 steps of minimization, ions and water molecules were equilibrated for 2 ns around sliders and tracks, which were restrained using harmonic forces with a spring constant of $1 \text{ kcal}/(\text{mol } \text{\AA}^2)$. The last frames of restrained equilibration were used to start simulations of free sliders and tracks. Then, 200 ns trajectories were used to compute MSD at a variety of lag times (τ). A diffusion coefficient $D(\tau)$ was computed from $D(\tau) = \text{MSD}(\tau)/2E\tau$, where E is the integer dimensionality of the system (1, 2 or 3) [268]. The H-bonds number was analyzed by VMD with a cutoff distance of 3.5 \AA and angle of 60° . The free energy calculation was performed using an umbrella sampling (US) method. The coordinate, which was defined as the distance between the center of charged groups of slider and the center of pARG track (11 units of ARG), was partitioned into 40 windows of 1 \AA width, where confinement potential were introduced in the form of harmonic restraints with a force constant of $3 \text{ kcal}/(\text{mol } \text{\AA}^2)$. During sampling, three backbone atoms of pARG track were held by restraints performed by collective variables (colvars [81]). Each US window was run for 10 ns. The weighted histogram analysis method (WHAM) [82–84] was used to reconstruct the potential of mean force (PMF). A MC bootstrap error analysis was performed with the WHAM algorithm (with

num_MC_trials set to 3). The histograms of the US windows used to reconstruct the PMF were examined and shown to have an appropriate overlap.

Diffusion of sliders on polycation tracks

To examine a diffusive motion of the sliders on different tracks, we used the coordinates of charged groups centers within each slider to calculate their mean square displacement (MSD) and diffusion coefficient $D(\tau)$ at various lag times τ in 3D, while being on the track, and in 1D along the track (with respect to its longitudinal coordinate).

Figure 61A and B show that MSD and $D(\tau)$ in 3D for both sliders and at most lag times (τ) are larger on pLYS than on pARG. These results include jumping between bent loops of pLYS and pARG. Since the sliders bind to their tracks, their 3D motion also reflects the tracks' motion. To separately study the sliders diffusion with respect to the tracks, we find in each slider a backbone atom which is nearest to the charge group center of each slider. By using the residue number (CA) of this atom as the coordinate, we study 1D diffusion along the track and calculate $D(\tau)$ in units of $\text{residue}^2/\text{ns}$ and MSD in units of residue^2 . Figure 61C shows that the sliders moved by 4-5 residues along tracks (1D) at a lag time of 100 ns. Contrary to the 3D diffusion, results in Figure 61D reveal that for most of the lag times, the 1D diffusion constants are larger on pARG than on pLYS. At a lag time of 100 ns, $D(\tau)$ reaches 0.10/0.15 $\text{residue}^2/\text{ns}$ in the cases of Slider1/Slider2-pARG and 0.09/0.13 $\text{residue}^2/\text{ns}$ in the cases of Slider1/Slider2-pLYS. This trend is consistent with an enhancement of the reaction rates, observed in experiments: Slider1-pARG (enhanced by 113-fold) > Slider1-pLYS (110) and Slider2-pARG (149) > Slider2-pLYS (77). Since most of the reactions between the sliders occur on the tracks (50-fold more sliders binding positions in the experiment), we can conclude that the experimentally observed increase of reaction rates is related to the 1D diffusion of sliders along the tracks.

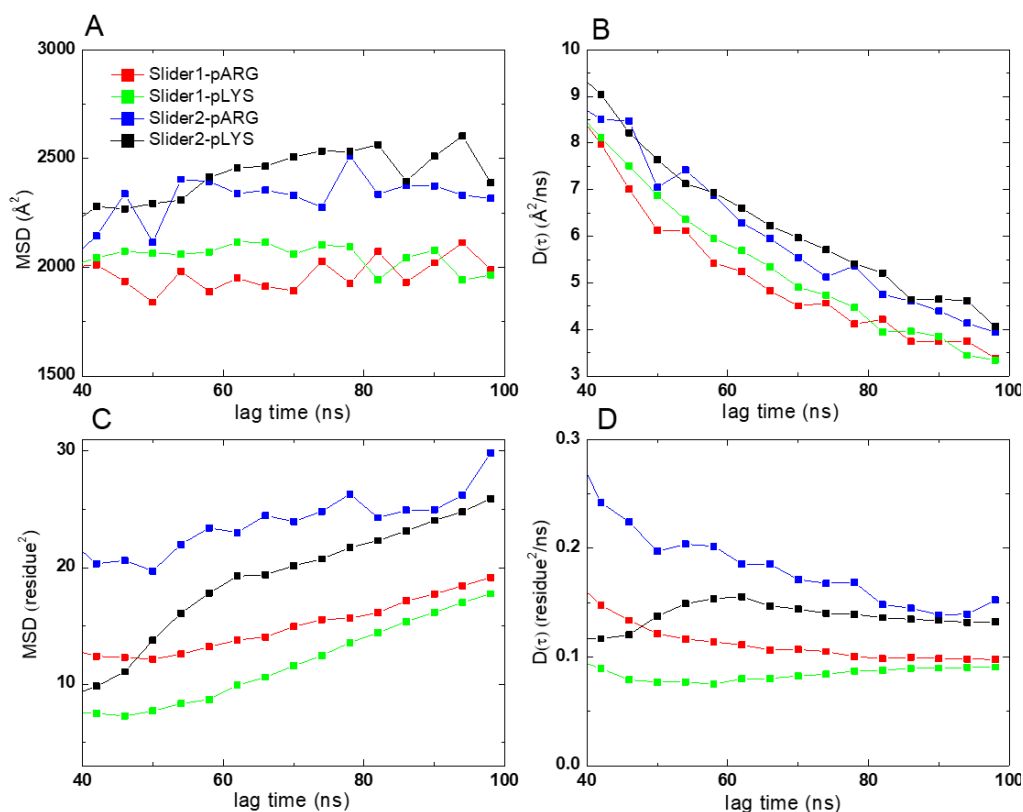


Figure 61: (A and B) MSD and $D(\tau)$ for a 3D diffusion of sliders on tracks in solution; (C and D) The same for 1D diffusion of sliders along tracks.

Motion of polycation tracks caused by sliders

The simulation snapshots in Figure 62 and Figure 63 show that both sliders can make transient loops by attracting the track with different charged groups of sliders. It seems that loops are easier to make on the pARG tracks (better coupling of the charged groups of sliders with track), especially by Slider1 which has more localized charged groups.

To examine the looping of tracks in the absence/presence of sliders, resembling track condensation, we quantified the radius of gyration (R_g) of the tracks and the number of H-bonds within the tracks. Figure 64A shows that, during the 150-200 ns simulations, $R_g=12/39$ Å for Slider1/Slider2-pARG, while $R_g=45/55$ Å for Slider1/Slider2-pLYS. R_g is smaller for pARG in the presence of both

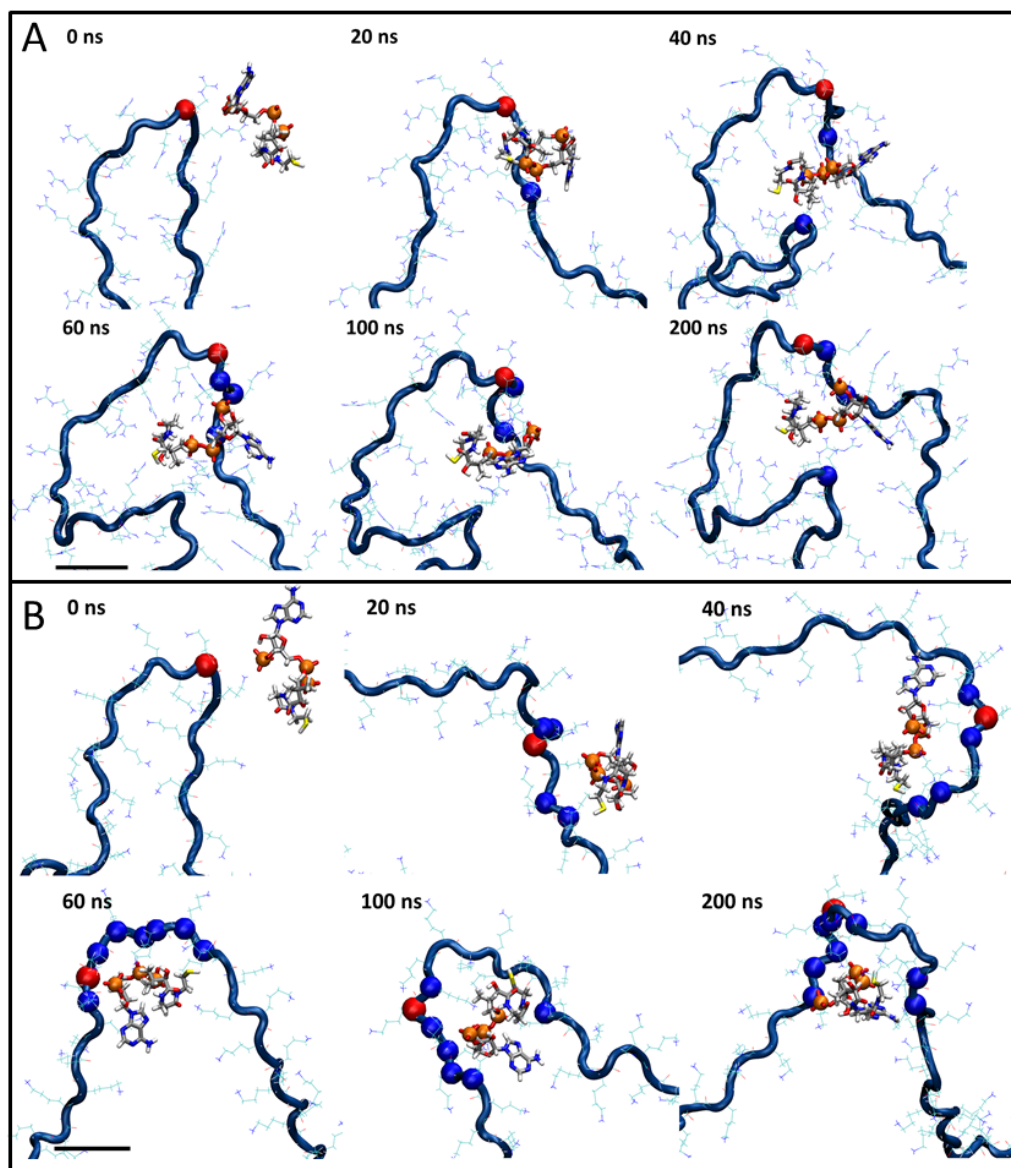


Figure 62: (A) Slider1 on pARG track; (B) Slider1 on pLYS track. Track is shown in dark blue with side chains of ARG, and the slider is shown in grey, with P atom in orange, O in red, N in blue, S in yellow and H in white. Red point on the track is the initial nearest backbone atom from track to slider, and blue points are the backbone atoms within 7 Å of slider during the simulation. Scale bar 1 nm.

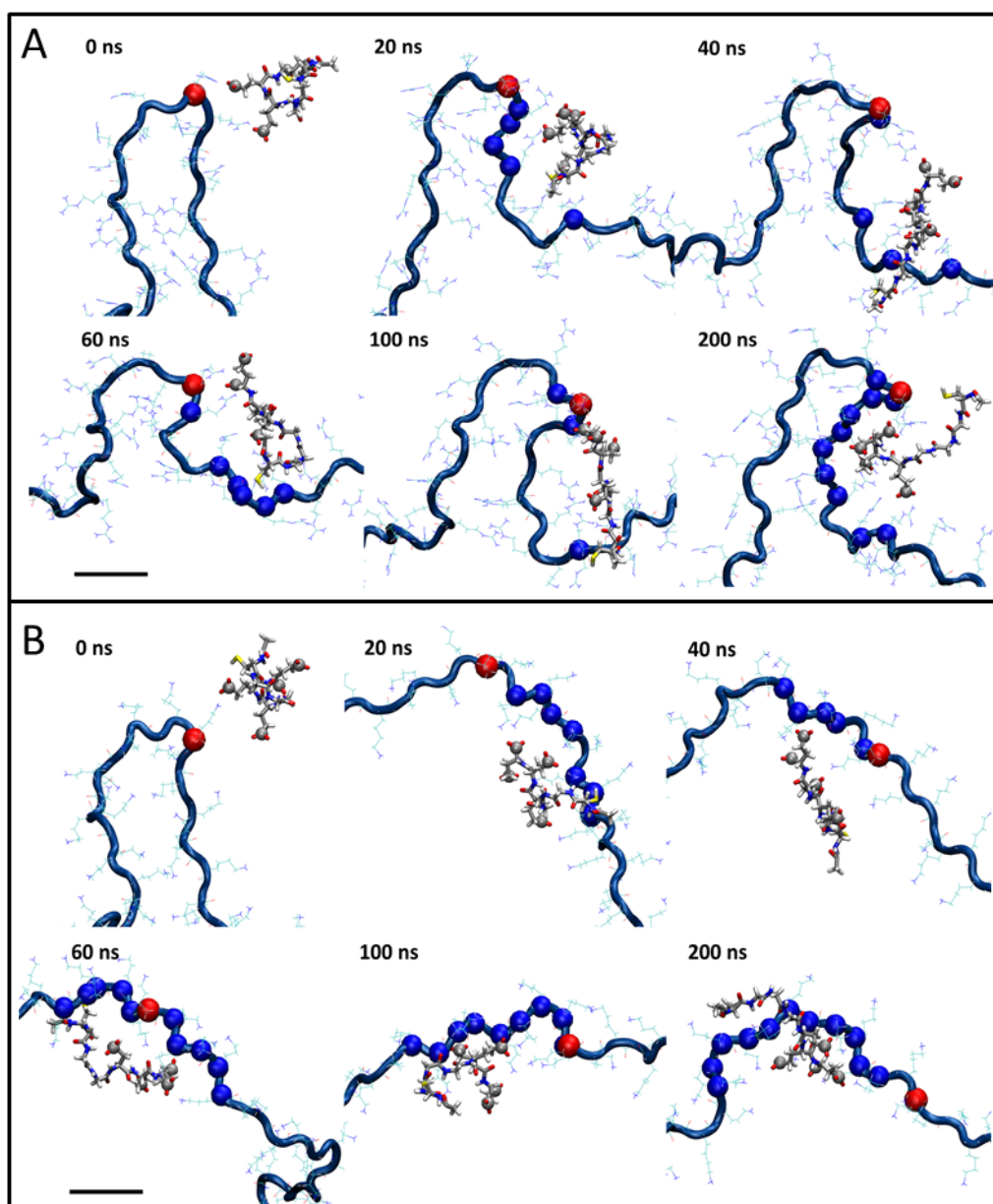


Figure 63: (A) Slider2 on pARG track; (B) Slider2 on pLYS track. Track is shown in dark blue with side chains of ARG, and slider is shown in grey, with P atom in orange, O in red, N in blue, S in yellow and H in white. Red point on the track is the initial nearest backbone atom from track to slider, and blue points are the backbone atoms within 7 Å of slider during the simulation. Scale bar 1 nm.

sliders, especially Slider1. This means that the pARG chains are more condensed than pLYS chains, which increases their intra-track connection and a 1D diffusion of the attached sliders (switching between different loops). On the other hand, the tracks folding can slow down a 3D diffusion of the sliders. Figure 64(B) shows for both sliders that pARG has at least 4 times more H-bonds within the track than pLYS. The increased number of H-bonds also indicates a higher chance of looping in the pARG track.

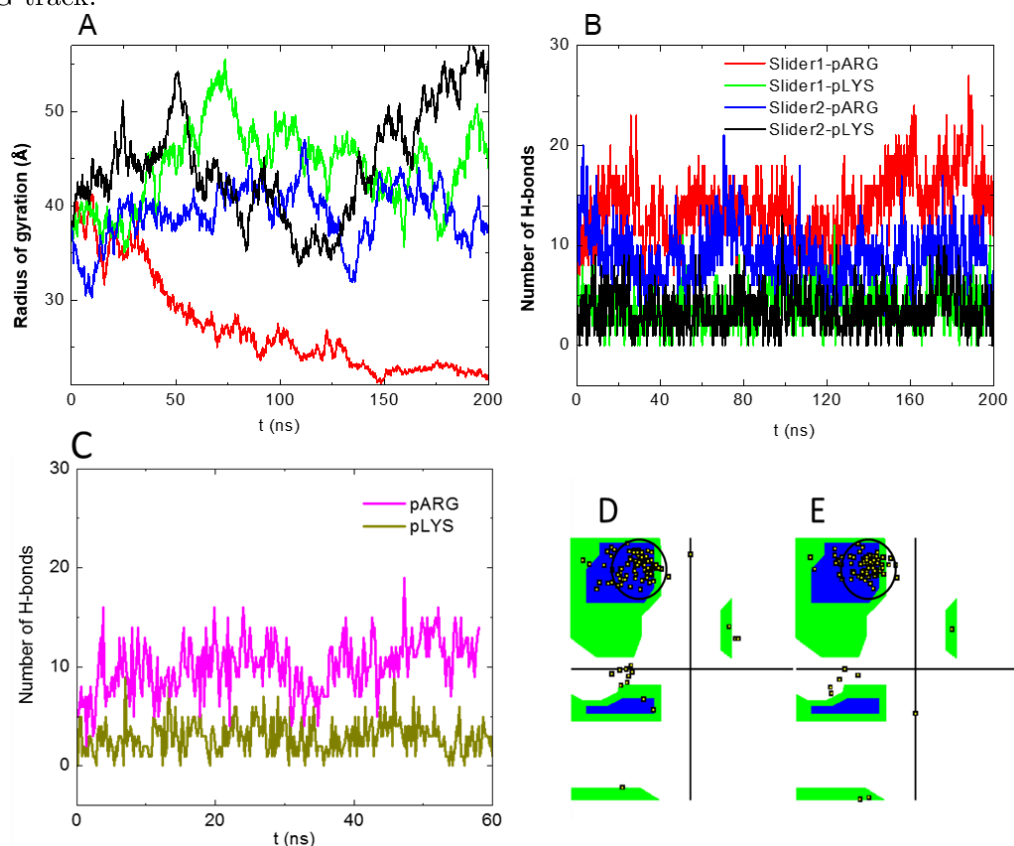


Figure 64: (A) Radius of gyration; (B) number of H-bonds within polycation track itself (with cutoff distance of 3.5 Å and angle of 60°). (C) number of H-bonds within polycation track itself; (D). pARG Ramachandran plot at 60 ns; (E) pLYS Ramachandran plot at 60 ns. Scale bar is 2 nm and the PPII helix region is circled.

We still need to clarify whether the looping of pARG/pLYS tracks is autonomous or caused by the sliders. Figure 64D and E show that after 60 ns of simulations both tracks are curved in a PPII helix form, but pARG has almost 4-fold more H-bonds than pLYS even in the absence of sliders

(Figure 64C). However, the number of H-bonds is smaller than in the presence of sliders (Figure 64B). Therefore, pARG has a higher tendency of looping than pLYS, and this looping tendency is further increased in the presence of sliders. Thus, a relative high 1D diffusion observed in Figure 61 on pARG tracks is related to their spontaneous looping. Figure 61D also reveals that Slider2 with more separate charged groups has a faster 1D diffusion because of a more flexible multivalent binding to the tracks. Therefore, both the structures of tracks and sliders influence this 1D diffusion, where a more flexible track and a slider with more separated charged group guarantee a faster diffusion.

Free energy calculation

To understand better the interaction between sliders and polycation track, we calculated the Gibbs free energy of binding of slider1/slider2 to the pARG track. Compared with experimental free energy values -7.05/-8.02 kcal/mol, the calculated values (-4.9/-5.1 kcal/mol) are smaller for slider1/2-pARG, which may due to the insufficient sampling and the restraints on the pARG. Based on the calculated PMF, the energy barrier for slider1/2 unbinding is estimated to be about 5.6/5.8 kcal/mol Figure 65A. According to the Arrhenius equation and method used in [269], this will give us an estimation of the slider1 unbinding rate of $1.54 \times 10^6 \text{ s}^{-1}$ and the binding time of 0.6 μs (assuming the Arrhenius frequency factor as $2.5 \times 10^{10} \text{ s}^{-1}$). Similarly, the binding time of slider2 is estimated to be 0.7 μs . We assume that the average contact number per second is equal to the Arrhenius frequency, which is predicted from average contact number between sliders and side chains of polycation track (Figure 65C). The contact number defined as the number of side chains of polycation track within 4 Å of slider charge group was collected every 0.2 ns Figure 65B.

We further simulated the system of slider 2 interacting with two short pLYS tracks (25 and 29-residues long). Initially, slider 2 was put in between the two tracks as shown in the snapshot at 0 ns (Figure 66). After 18 ns interaction with both tracks, slider 2 dissociates from one track

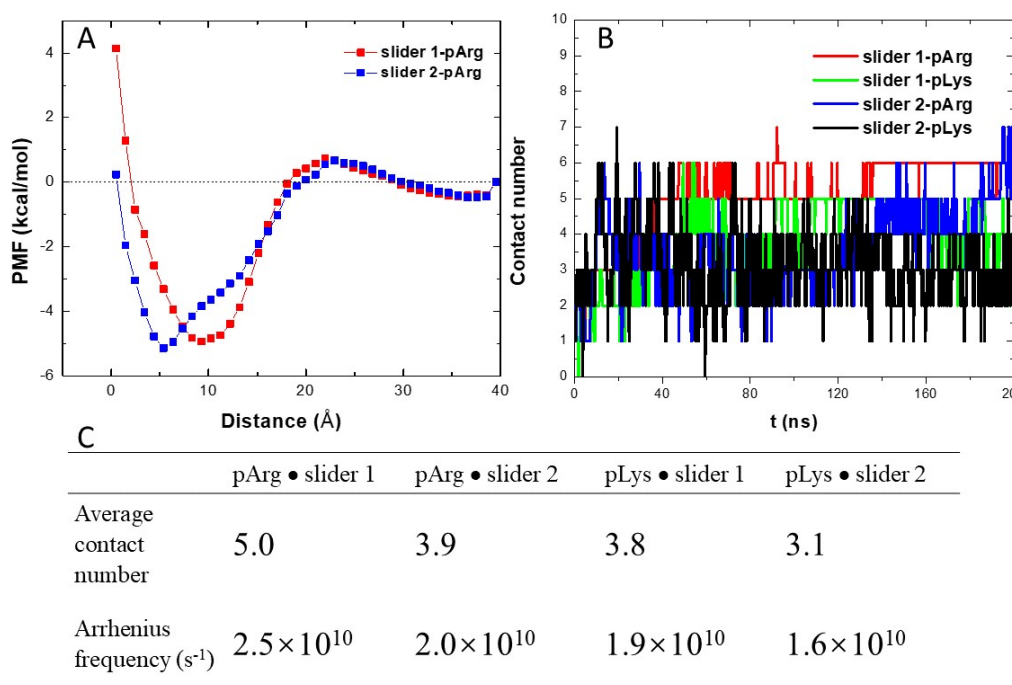


Figure 65: (A) Free energy profile of slider1/2 unbinding from the pArg track. (B) The contact number change between sliders and side chains of pARG/LYS during 200 ns trajectory (data collect every 0.2 ns). (C) Average contact number and Arrhenius frequency

and completely binds to the other nearby track at 22 ns. The unbinding of slider 2 from one track was observed at 44 ns, which is the only unbinding event observed during 0.9 μs simulation. This is consistent with our binding time prediction. The dissociated slider finally jumped back to the original track at 46 ns. We propose that the slider have a chance to bind with the other track, if the other track is nearby (just like in the first 22 ns).

Conclusion

We have presented examples of rate enhancement of reactions mediated by diffusive binding and hopping of a molecular slider on polymer tracks. Our system is inspired by the efficient 1D Brownian motion of proteins along polynucleotides found in nature, but adapted to a generally applicable

route for functional nanosystems. MD simulations revealed the sliding and hopping motions of slider molecules on their polymer tracks. The tracks provide enormous binding sites for sliders which facilitate the diffusive motions of sliders along tracks, which can be explained by 1D diffusion models. In contrast to the free sliders in solutions, the binding sliders on tracks gained increased collision rates with each other. The diffusive motions also counterpart part of the intrinsic Coulombic repulsions between negatively charged sliders, which resulted in significantly increased reaction rates in both slider systems. We anticipate that our work will inspire new applications based on Brownian motion, including reaction diffusion systems and other spatially encoded smart materials [17].

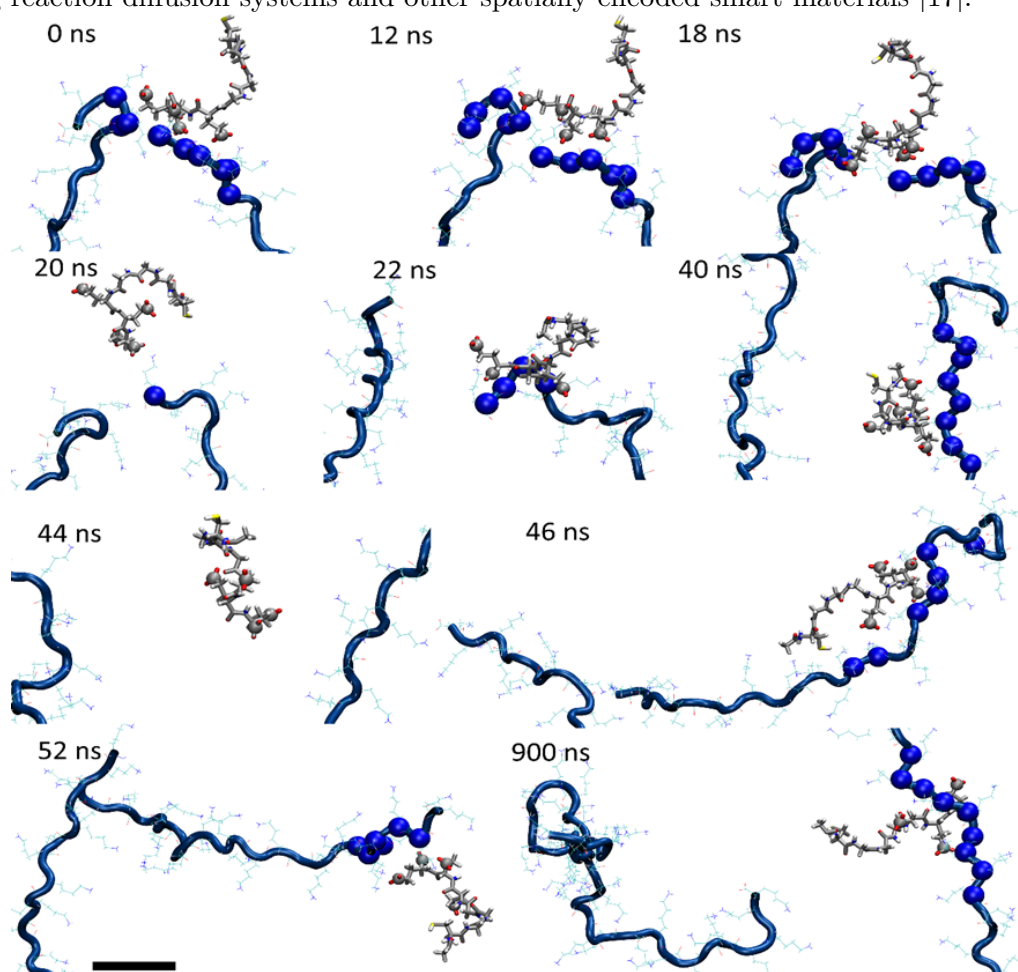


Figure 66: Snapshots of slider2 interacting with two short pLYS tracks. Scale bar 1 nm.

6.3 Intermolecular interactions stabilize ligand ratios on nanoparticles

Adapted from Ref. [18] (*Angew. Chem.* 2018, 130. DOI: 10.1002/anie.201800673) with the permission from Wiley Online Library.

Introduction

Gold NPs covered with two novel thiol ligands with different ratios were synthesized in Prof. Klajn's lab. In solution, these thiols are solvated and do not interact with each other. Once attached onto NPs, the ratio of the two ligands favor a narrow range which is independent of the initial ratio in solutions [18]. The adsorption of free ligands on pre-assembled NPs were modeled to explain the saturated ratio of ligands on NPs. The intermolecular interactions were analyzed based on simulation results, which favor the electrostatic interactions.

Experimental results

"A schematic representation of a ligand exchange reaction on nanoparticles (NPs) involving a mixture of two incoming thiol ligands is shown in Figure 67. The molar fraction of thiol **1** (MV) in the initial solution is denoted as θ and on the resulting NPs as κ .

The dependence of κ on θ followed a roughly linear curve with a slope of about 0.15 (see the red data points in Figure 68 c), which indicates that NPs have a propensity to stabilize a narrow range of 1:2 ratios, suggesting the presence of attractive electrostatic interactions between immobilized **1** and **2**.

Next, we investigated the effect of NP size on the mutual stabilization of both ligands. To this end, we functionalized 2.4 nm gold NPs (Figure 68d with different mixtures of **1** and **2**. Similar to 5.9 nm NPs, the smaller particles exhibited a narrow range of ζ -potentials (+ 32 to + 49 mV;

Atomistic MD simulations of gold NPs functionalized with mixed-ligands (F-NPs) were performed to clarify the observed experimental results. F-NPs are ligated with different molar ratio of positively

double charged **1** (MV) and zwitterionic **2** (SB). To clarify why the number of immobilized **1** on NPs surfaces saturate when their concentration in solution is increased, we tested the adsorption of free **1** and **2** on F-NP. We also tested the self-assembly of different F-NPs.

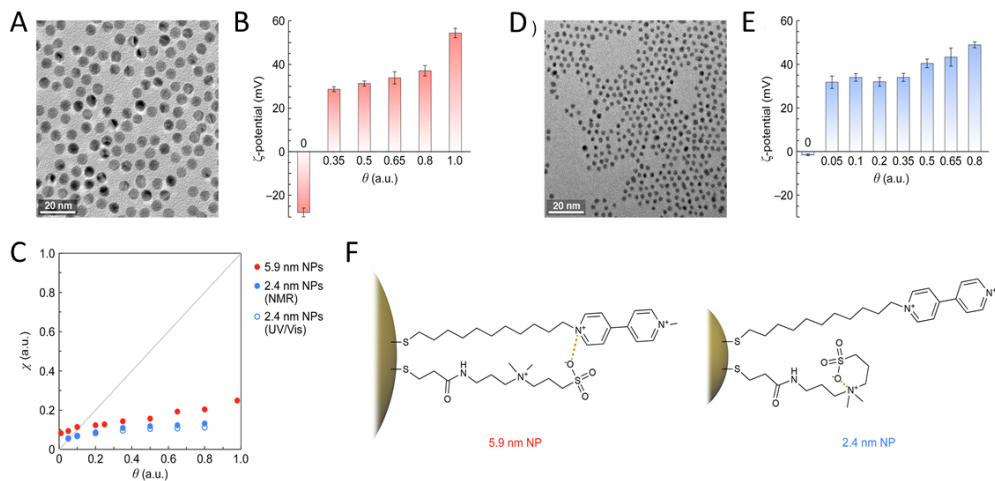


Figure 68: (A) representative TEM image of 5.9 nm gold NPs. (B) ζ -potentials of 5.9 nm gold NPs functionalized with mixtures of **1** and **2** as a function of κ . (C) as a function of θ for 5.9 nm (red) and 2.4 nm (blue) gold NPs estimated using NMR (solid markers) and UV/Vis absorption spectroscopy (empty markers). The gray line corresponds to $\theta = \kappa$. (D) A representative TEM image of 2.4 nm gold NPs. (E) ζ -potentials of 2.4 nm gold NPs functionalized with mixtures of **1** and **2** as a function of θ . (F) Proposed modes of dominating inter- and intramolecular electrostatic interactions on 5.9 nm (left) and 2.4 nm (right) NPs.

First, we studied the adsorption of free ligands on partly functionalized F-NPs, rather than considering their direct attachment through thiolated coupling. F-NP1s, with 400 surface-attached **1/2** (κ account for 0.205), were placed into chloroform with different concentrations of free **1/2** ligands (50,000 chloroform molecules in a box of $200 \times 200 \times 200 \text{ \AA}^3$): F-NP1-A (F-NP1 with 23 **1** and 23 **2** free ligands), F-NP1-B (F-NP1 with 33 **1** and 23 **2** free ligands), F-NP1-C (F-NP1 with 43 **1** and 23 **2** free ligands). Second, to analyze the solubility of different F-NPs, we separately modeled the self-assembly of two F-NP2s ($\kappa = 0.157$, ligands immobilized) or F-NP3s ($\kappa = 0.094$, ligands immobilized) in water or 0.5 M NaCl solution. In these four simulations, F-NPs were initially placed apart from each other in a water solvent ($80,000$ water molecules in a box of $220 \times 115 \times 115 \text{ \AA}^3$).

The ligands were described by the CHARMM general forcefield [68, 69] and the charge were obtained from electrostatic potential fitting using the CHELPG algorithm by GAUSSIAN 09 package [248]. The simulations were performed with NAMD [58]. The PME [62] method was used for evaluation of long-range Coulombic interactions. A van der Waals (vdW) coupling between the NPs core was separately added in the simulations [20]. The time step was set to 2.0 fs. The simulations were performed in the NPT ensemble ($p = 1$ bar and $T = 300$ K), using the Langevin dynamics ($\gamma_{\text{Lang}} = 1 \text{ ps}^{-1}$). After 2,000 steps of minimization, the equilibration of F-NP1s lasted for 40-50 ns, and the self-assembly of F-NP2s and F-NP3s lasted for 8 ns.

Adsorption of **1** and **2** on the F-NPs surfaces

During the simulations, the freely solvated ligands interact with the 400 ligands (**1** 20.5% and **2** 79.5%) constrained to F-NP1s, but these ligands are free to move on the F-NP1s surfaces. Figure 69 shows the distributions of free **1/2** ligands as a function of their distance from the F-NP1s centers. These distributions are obtained by averaging results from the last 500,000 steps (1 ns) of 40-50 ns long simulations. Free ligands present within 55 Å from the NPs centers are considered to be adsorbed on F-NP1s. Figure 69A-C show that there are 7, 10, 9 (**1**) and 13, 9, 8 (**2**) ligands for concentrations denoted above are adsorbed to F-NP1. The time evolution of the free ligands distribution is shown in the Figure 70. With the increasing concentration of free **1**, the number of such ligands adsorbed on F-NP1s reaches saturation, where **1** replace the adsorbed **2**. This self-limiting process is caused by Coulombic repulsion of **1**, in analogy to terminal assemblies of charged NPs clusters.

Self-assembly of F-NP2s and F-NP3s

Figure 71 (B, C) show that in 8 ns simulations F-NP2s with a higher ligand **1** ratio ($\kappa = 0.157$) on their surfaces never aggregate both in water and salt solutions. However, F-NP3s ($\kappa = 0.094$)

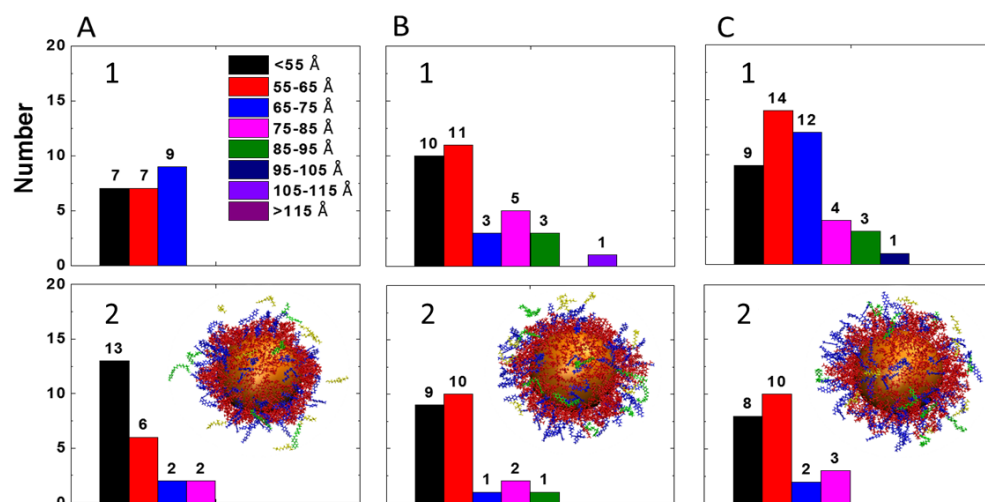


Figure 69: Free ligand distribution: A. F-NP1-A (23 **1** and 23 **2** in solution); B. F-NP1-B (33 **1** and 23 **2** in solution); C. F-NP1-C (43 **1** and 23 **2** in solution). Inset: F-NP1 with **1** and **2** within 55 Å of its center (blue: immobilized **1**; red: immobilized **2**; green: free **1**; yellow: free **2**; orange: gold nanoparticles)

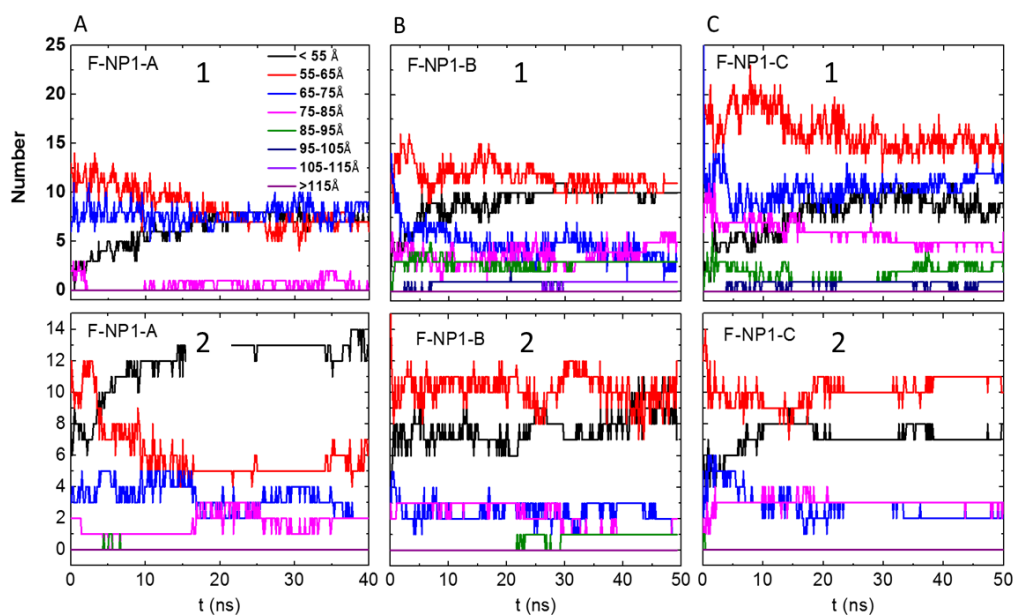


Figure 70: Time evolution of free ligand distributions: A. F-NP1-A (23 **1** and 23 **2** in solution); B. F-NP1-B (33 **1** and 23 **2** in solution); C. F-NP1-C (43 **1** and 23 **2** in solution).

aggregate in water after 7.5 ns, but stay separated in the salt solution. All these results agree with the experimental observations. The distance between F-NP2s (more charged) keeps a relative stable value during the simulations, but F-NP3 (less charged) shows large fluctuations both in water and salt solutions.

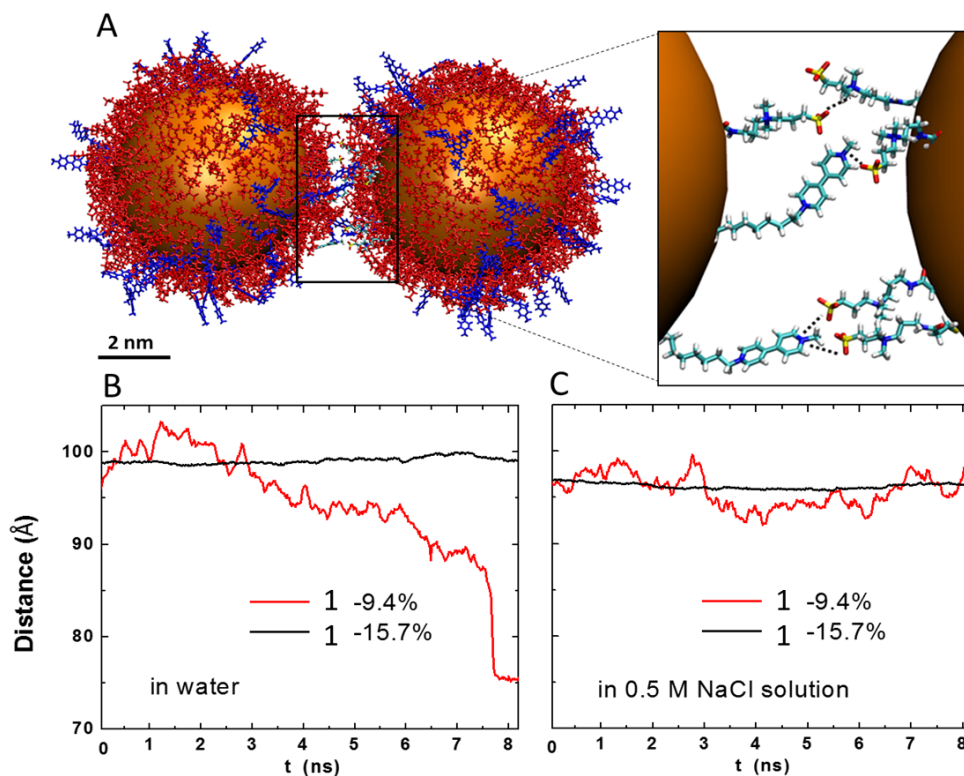


Figure 71: A. Snapshot of F-NP3 aggregation in water; Enlarged figure: closest ligand to ligand contacts. B. Center to center distance between F-NPs in water. C. Center to center distance between F-NPs in salt solution.

The self-assembly of F-NP3s is possible due to a reduced Coulombic repulsion between these less charged NPs. Once the center-to-center distance of F-NP3s is within the effective distance of the bulk vdW coupling, the particles are pulled closer. Figure 71 shows that when F-NP3s are nearby, similar to Liu et. al. [270], the positively charged group of **1** further interact with the negatively charged group of **2** and the negatively charged group of one **2** ligand interact with the positively charge group

of different **2** ligands. When the ionic strength is larger, the salt ions screen this Coulombic coupling between charged groups, which causes weakening of the attraction between F-NP3s and prevents their self-assembly.

Conclusion

Co-adsorption of a positively charged viologen-based ligand (MV) and a zwitterionic sulfobetaine ligand (SB) onto metallic nanoparticles favors a narrow range of molar ratios of these two ligands on the functionalized particles [18]. Molecular dynamics simulations revealed that this result could be attributed to attractive electrostatic interactions between the two ligands upon adsorption onto the NPs. The Coulombic repulsion between positive charged MV ligands is the factor limiting the accumulation of MV ligands on NP surfaces, which cause the saturated ratio of the two ligands with increasing free ligands concentration in solution. The self-assembly of NPs is driven by the intermolecular interactions between different NPs. The intermolecular interactions can be screened by increasing the concentration of ions which can explain the different self-assembly behaviors observed in different ionic solutions.

6.4 Supramolecular control of azobenzene switching on nanoparticles

Adapted from Ref. [19] (*J. Am. Chem. Soc.* 2019, 141. DOI: doi.org/10.1021/jacs.8b09638) with the permission from ACS Publishing Group.

Introduction

Prof. Klajn's lab synthesized cofunctionalized NPs with mixtures of polar and apolar ligands. They developed a modified NP functionalization procedure that allowed to predictably control the molar ratio of the two ligands on the NPs. These NPs were used to systematically investigate how the

background ligand influenced the switching properties of azobenzene-based ligands in solution. MD simulations were performed to characterize the conformations of different NPs functionalized with different pairs of ligands. The ligand switching mechanism was proposed based on the combination of simulation and experimental results.

Experimental results

We functionalized gold NPs with different combinations of thiolated azobenzenes Am ($m = 1$ through 6) and background (“dummy”) thiols Bn ($n = 1$ through 9) (Figure 72).

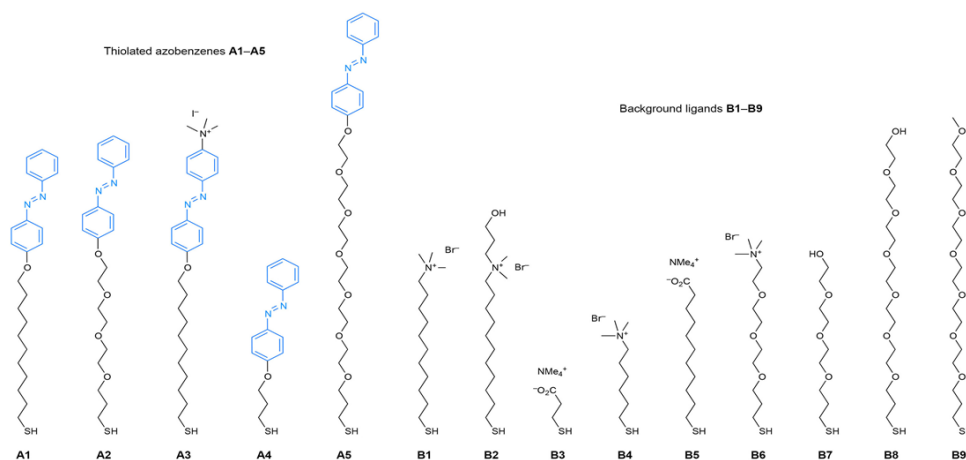


Figure 72: Structural formulas of thiolate ligands used in this study.

”It was of critical importance to verify that azobenzenes adsorbed on the surfaces of gold NPs retain their photoswitchable properties. Figure 73A shows changes in the UV/vis spectra of A1/B1-functionalized 2.5 nm NPs ($\kappa = 0.17$) resulting from exposure to a low-intensity ($\sim 0.7 \text{ mW} \cdot \text{cm}^{-2}$) hand-held UV light source. Within several minutes of UV irradiation, the band at $\sim 350 \text{ nm}$ decreased nearly to the background level, indicative of $\text{trans} \rightarrow \text{cis}$ azobenzene isomerization. Notably, azobenzene switching did not affect the high colloidal stability of the NPs (no absorption increase in the long-wavelength region, Figure 73A). Therefore, these NPs behave differently than the azobenzene-

coated NPs do in hydrophobic solvents, which, upon UV irradiation, readily assemble into metastable aggregates to minimize contact with the nonpolar environment. To accurately determine the photoisomerization yield of azobenzene on NPs, we developed a procedure based on a combination of UV/vis absorption and NMR spectroscopies. Using this method, we found that the photostationary state (PSS) under UV light contained 92% of the cis isomer (Figure 73B). Subsequent exposure to blue light (we worked with a 460 nm light-emitting diode) triggered a fast back isomerization reaction; the PSS was reached within <2 min, and it consisted of 84% trans-azobenzene.

Next, we investigated the effect of ligand length on the switching properties of NP-bound azobenzene. To this end, we functionalized AuNPs with a mixture of a short thiolated azobenzene A4 and background ligand B3 and found that the resulting NPs were readily soluble in water. However, exposure to UV did not induce any changes in the absorption spectra of these NPs, indicating that trans-azobenzene groups residing close to the gold surface are difficult to photoisomerize. This can be attributed to the quenching of the excited state of azobenzene by gold, in agreement with previous literature reports [271–273]. We therefore considered combining the short background ligand, B3, and the long-chain azobenzene, A1 (Figure 73C and D). Similar to A1/B1-coated NPs, azobenzene A1 coadsorbed with B3 could be readily switched for many cycles, and the reversible isomerization was not accompanied by NP aggregation.

To investigate the effect of background ligand on the switching properties of azobenzene, we prepared 2.5 nm NPs cofunctionalized with A2 and several different background ligands (all NPs were at $\kappa \approx 0.15$). We found that shortening the alkyl chain of B1 by five methylene groups (i.e., ligand B4) had no effect on the kinetics of the back-isomerization reaction (Figure 77E; $k \approx 0.024 \text{ h}^{-1}$). Likewise, replacing the terminal positively charged group of B1 with the negatively charged carboxylate (ligand B5) had little effect ($k \approx 0.030 \text{ h}^{-1}$). In contrast, replacing B1's alkyl chain

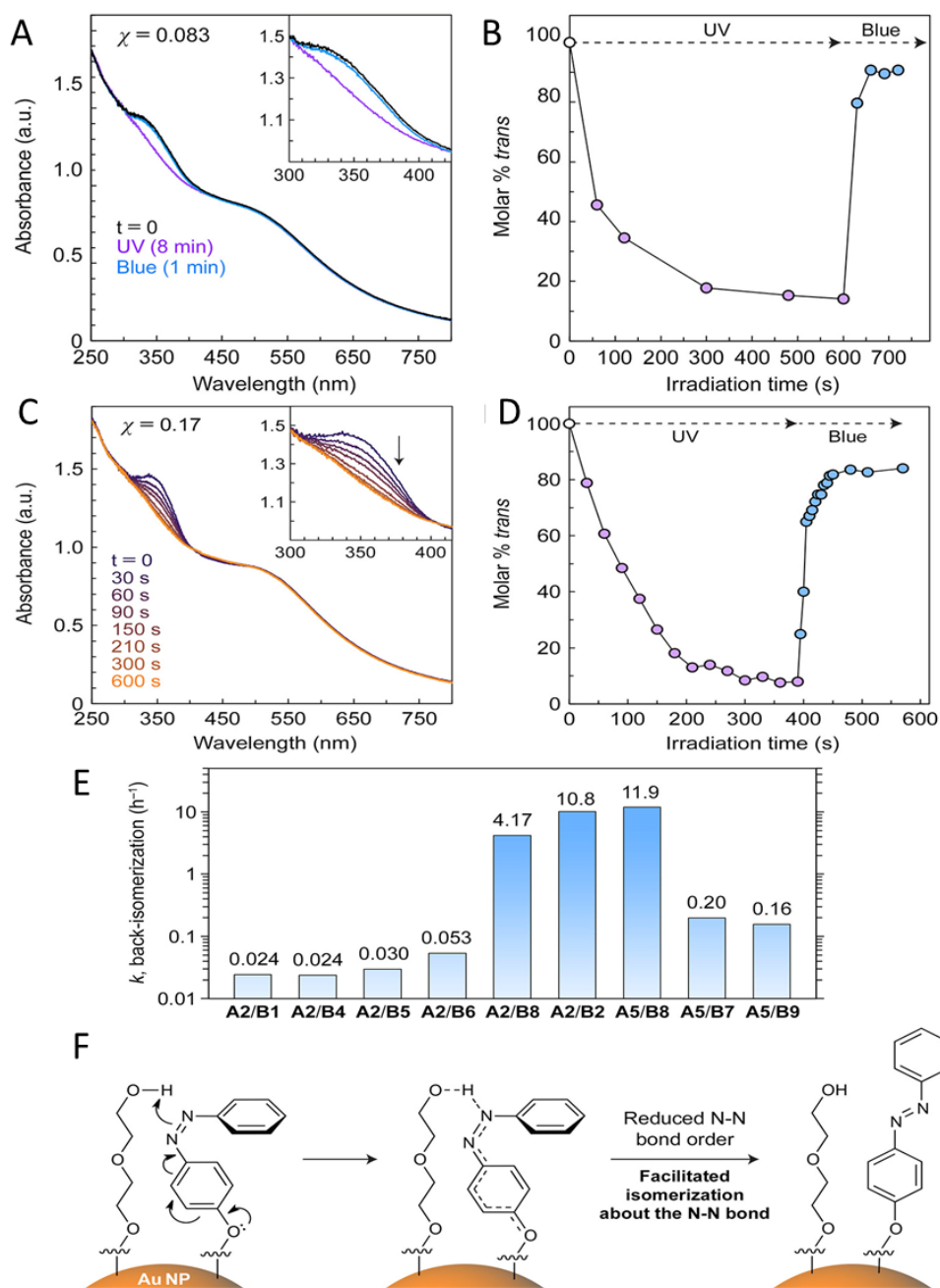


Figure 73: (A) Evolution of the UV/vis absorption spectra of an aqueous solution of A1/B1-functionalized 2.5 nm Au NPs ($\kappa = 0.17$) under UV light exposure. (B) Reversible photoswitching of A1 on A1/B1-functionalized 2.5 nm Au NPs. (C) UV/vis absorption spectra of an aqueous solution of A1/B3-functionalized 2.5 nm Au NPs before (black) and after (purple) exposure to UV light and after subsequent exposure to blue light (in blue). (D) Reversible photoswitching of A1 on the same NPs. (E) Dependence of the thermal back-isomerization of cis-A2 and cis-A5 on 2.5 nm Au NPs as a function of background ligand Bn (note the logarithmic scale). The surface coverage of azobenzene, κ , corresponded to 0.15 for all NPs. (F) Proposed mechanism for back-isomerization of cis-azobenzene assisted by a neighboring hydroxy group.

with a tris(ethylene glycol) chain of similar overall length (B6) increased the rate of relaxation approximately 2-fold ($k \approx 0.053 \text{ h}^{-1}$). We hypothesized that this increase might be related to the high flexibility of OEG chains [274] (compared to alkyl chains), resulting in more conformational freedom available to the terminal azobenzene groups. To verify the critical role of the hydroxy group, we also prepared NPs cofunctionalized with A2 + B2 and found that the rate of thermal relaxation was even faster, $k \approx 10.8 \text{ h}^{-1}$ (Figure 73E). This can be explained by the higher propensity for H-bond formation between A2 (where the distance between the S atom and the center of mass of the N=N moiety is $d_{S-N} = 21.1 \text{ \AA}$) and B2 (the distance between the S and terminal O atoms is $d_{S-O} = 20.1 \text{ \AA}$; $\Delta d_{A2/B2} = 1.0 \text{ \AA}$) than between A2 and B8 ($d_{S-O} = 26.7 \text{ \AA}$, $\Delta d_{A2/B8} = 5.6 \text{ \AA}$; all distances were calculated for extended structures using GaussView software [275]). Overall, our results show that the rate of azobenzene back-isomerization in water can be tuned by a factor of ~ 500 simply by changing the background ligand with which it is coadsorbed on gold NPs.

Extending the OEG chain of A2 by three EG units (i.e., ligand A5) again resulted in a fast back-isomerization reaction ($k \approx 11.9 \text{ h}^{-1}$ on A5/B8-functionalized 2.5 nm NPs, corresponding to a $\tau_{1/2}$ value of 3.5 min). Although this result may appear surprising given the relatively large $\Delta d_{A5/B8} = 5.5 \text{ \AA}$ (d_{S-N} in A5 = 32.2 \AA), it can be explained by the high flexibility of long OEG chains, which can facilitate interactions between H-bond donors and acceptors. When, however, the distance between the donor and acceptor sites was increased to $\delta d = 16.3 \text{ \AA}$ (using the A5 + B7 combination; d_{S-O} in B7 = 15.9 \AA), the rate of back-isomerization dropped substantially ($k \approx 0.20 \text{ h}^{-1}$; see Figure 73E)” [19].

MD simulations of azobenzene-functionalized nanoparticles

Systems and methods

A thiolated AuNP with a diameter of 2.5 nm was modeled as an icosahedron decorated with 91 ligands (14 thiolated azobenzenes Am and 77 background ligands Bn). We considered nine systems: trans-A1/B1-, cis-A1/B1-, trans-A1/B3-, cis-A1/B3-, trans-A3/B1-, and cis-A3/B1-, trans-A5/B8-, cis-A5/B8-, and cis-A5/B9-functionalized nanoparticle. The ligands were described by a forcefield used in our previous studies [20]. Electric charges were calculated from the electrostatic potential fitting in the implicit solvent of water using GAUSSIAN 09 [248]. The simulations were performed with NAMD [58] in the NPT ensemble ($p = 1$ bar and $T = 300$ K), using Langevin dynamics ($\gamma_{\text{Lang}} = 1 \text{ ps}^{-1}$) with a time step of 2.0 fs. Initially, the simulated NPs were placed in water with counterions (in a box of $100 \times 100 \times 100 \text{ \AA}^3$). The PME [62] method was used for evaluating long-range Coulombic interactions. After 2,000 steps of minimization, the equilibration of the functionalized NPs lasted for ~ 10 -20 ns. The hydrogen bond numbers were analyzed by VMD [73] with a cutoff distance of 4 Å and an angle of 60° . The distance between the NP center and the N=N moiety was averaged over all the ligands. The local number of water molecules was averaged over the last 5 ns.

Reversible Isomerization of Azobenzene on Water Soluble Nanoparticles.

To help better understand the high solubility and efficient switching of A1/B1-functionalized NPs in water, we studied these particles by means of atomistic MD simulations. In these studies, an icosahedral gold nanoparticle functionalized with a densely packed monolayer of randomly distributed trans-A1 and background ligands B1 was first constructed. The size of the metallic core was 2.5 nm, and κ amounted to 0.15 (which corresponds to 14 A1 ligands and 77 B1 ligands; Figure 74A, left), in agreement with a typical experimental situation, and the NP was allowed to equilibrate

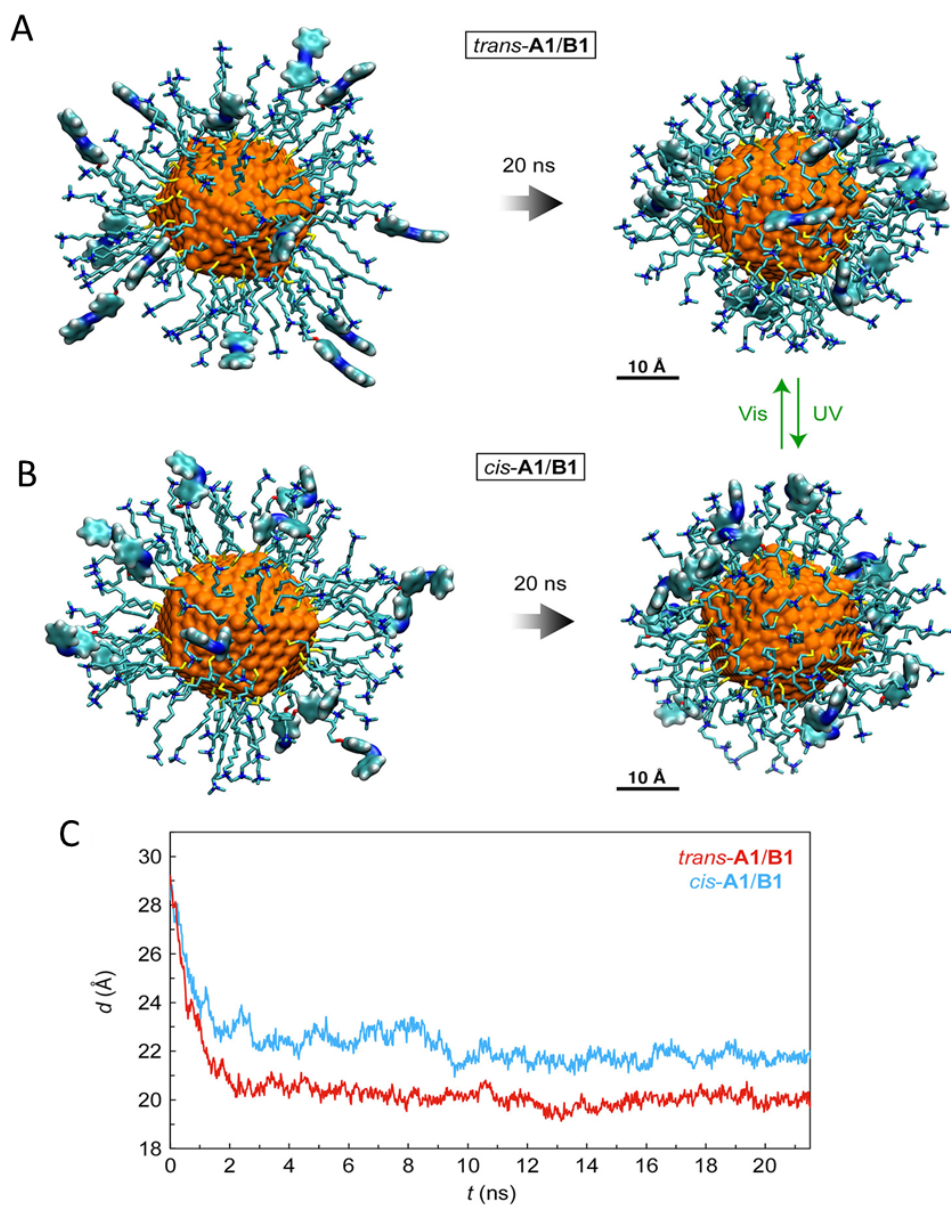


Figure 74: Snapshots from molecular dynamics (MD) simulations of an A1/B1-coated gold NP in the *trans* (A) and *cis* (B) state of azobenzene. The images on the left correspond to $t = 0$, and those on the right correspond to $t = 20$ ns. Color codes: C, cyan; N, blue; O, red; S, yellow. (C) Average distance between the center of the NP and the center of mass of the N=N moiety of the *trans* (red) and *cis* (blue) isomer of A1 as a function of time.

(20 ns) in a box of water. We found that in their energy-minimized state (Figure 74A, right) these NPs featured trans-azobenzene moieties buried within the ligand monolayer; in other words, the high energy of trans-A1 in water was decreased by solvation with long alkyl chains. The positively charged ammonium groups of B1, on the other hand, retained their initial protruding configuration, which can explain the excellent water solubility of these NPs despite the presence of the hydrophobic trans-azobenzene groups. We separately considered a cis-A1/B1-coated NP (Figure 74B). Similar to their trans isomers, the cis-azobenzene groups became buried within the nonpolar monolayer, albeit to a lesser (by ~ 2 Å) extent, which can be visualized by plotting the average distance of the center of mass of the N=N moiety to the center of the NP (Figure 74C). This result can be rationalized by the more hydrophilic character of the cis form, which can interact with water molecules via its nitrogens' lone electron pairs [20, 276]. On the basis of these results, we postulate that azobenzene switching in A1/B1-functionalized NPs occurs within the nonpolar nanoenvironment of the NP bound alkyl chains [277] (Figure 74, green arrows) rather than in the aqueous phase.

We then proceeded to study azobenzene photoswitching on NPs functionalized with other Am/Bn combinations. A3/B1-functionalized 2.5 nm NPs behaved analogously to A1/B1 NPs, with the photoisomerization reactions completed within 10 min for the trans \rightarrow cis and ~ 2 min for the cis \rightarrow trans reaction, respectively (Figure 75).

The good colloidal stability of A1/B3-functionalized NPs in water may be surprising, given the lack of background ligands' long alkyl chains capable of solvating the azobenzene groups (compare with the right panels of Figure 74A and B). To help explain the efficient hydration of these NPs, we performed additional MD simulations and found that energy-minimized configurations of these NPs in water featured small bundles (aggregates) of azobenzene (Figure 76A,B). As expected, the trans isomer of A1 exhibited a higher propensity to aggregate, with aggregates of up to five azobenzene

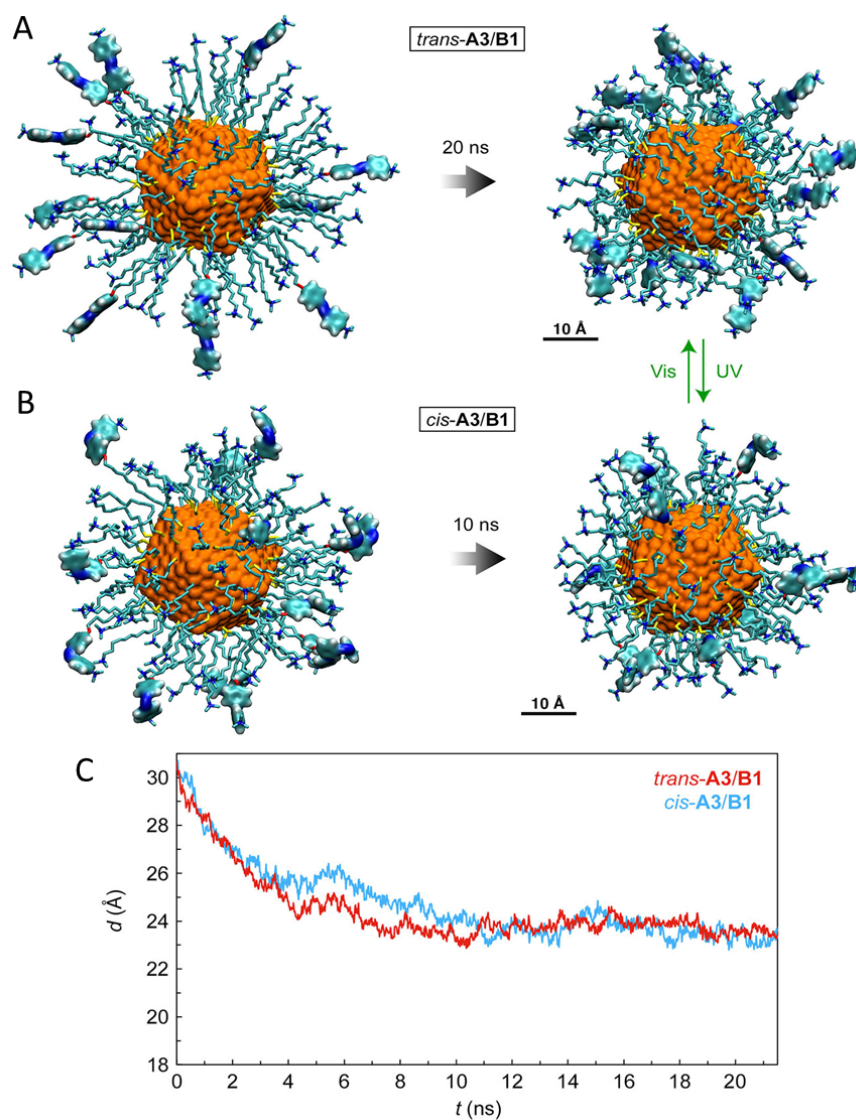


Figure 75: Snapshots from MD simulations of a *trans*-A3/B1-coated 2.5 nm gold NP (A) and a *cis*-A3/B1-coated 2.5 nm gold NP (B). (C) Average distance between the center of the NP and the center of mass of the N=N moiety of the *trans* (red) and *cis* (blue) isomer of A3 as a function of time. Note that over time, the average distance in both cases equilibrates to ~ 23.5 Å, which is similar to the distance between *cis*-A1's N=N moiety and the NP center, but considerably more than that between *trans*-A1's N=N moiety and the NP center (compare with Figure 74 in the main text).

units, whereas the more polar *cis*-A1 afforded a $\sim 1:1$ mixture of free and dimerized azobenzenes.

These results indicate that in the absence of a nonpolar nanoenvironment on the NP surfaces, the surface energy of the NP–water interface is decreased by stacking the azobenzene units.

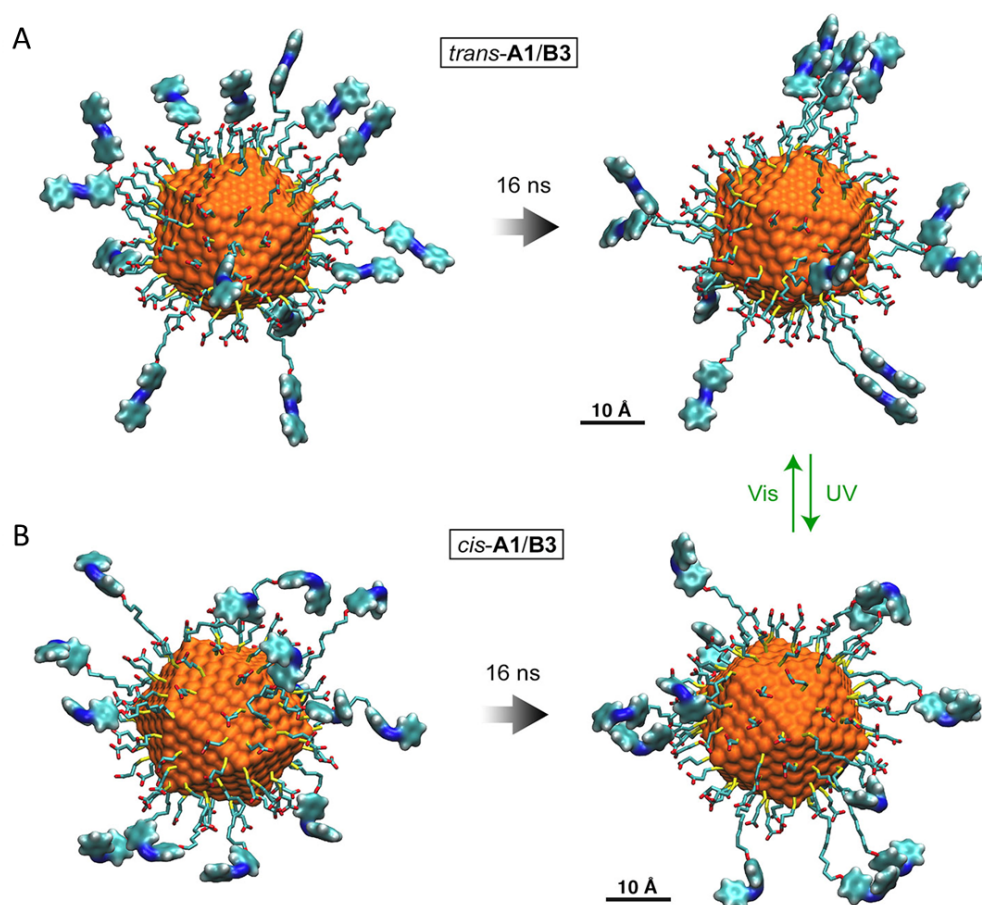


Figure 76: Snapshots from MD simulations of an A1/B3-coated gold NP in the trans (A) and cis (B) state of azobenzene. The images on the left correspond to $t = 0$ and those on the right correspond to $t = 16$ ns.

Effect of Background Ligands on the Kinetics of Azobenzene Isomerization

To verify the importance of hydrogen bonding between coadsorbed azobenzene- and hydroxy-terminated thiols on the kinetics of azobenzene isomerization on gold nanoparticles, we performed MD simulations for cis-A5/B8, trans-A5/B8 and cis-A5/B9 Figure 77 Figure 78.

This on-nanoparticle H-bonding investigated by MD simulations revealed that the presence of H-bonds between cis-A5 and B8 residing on the same NPs (Figure 77). In sharp contrast, the terminal

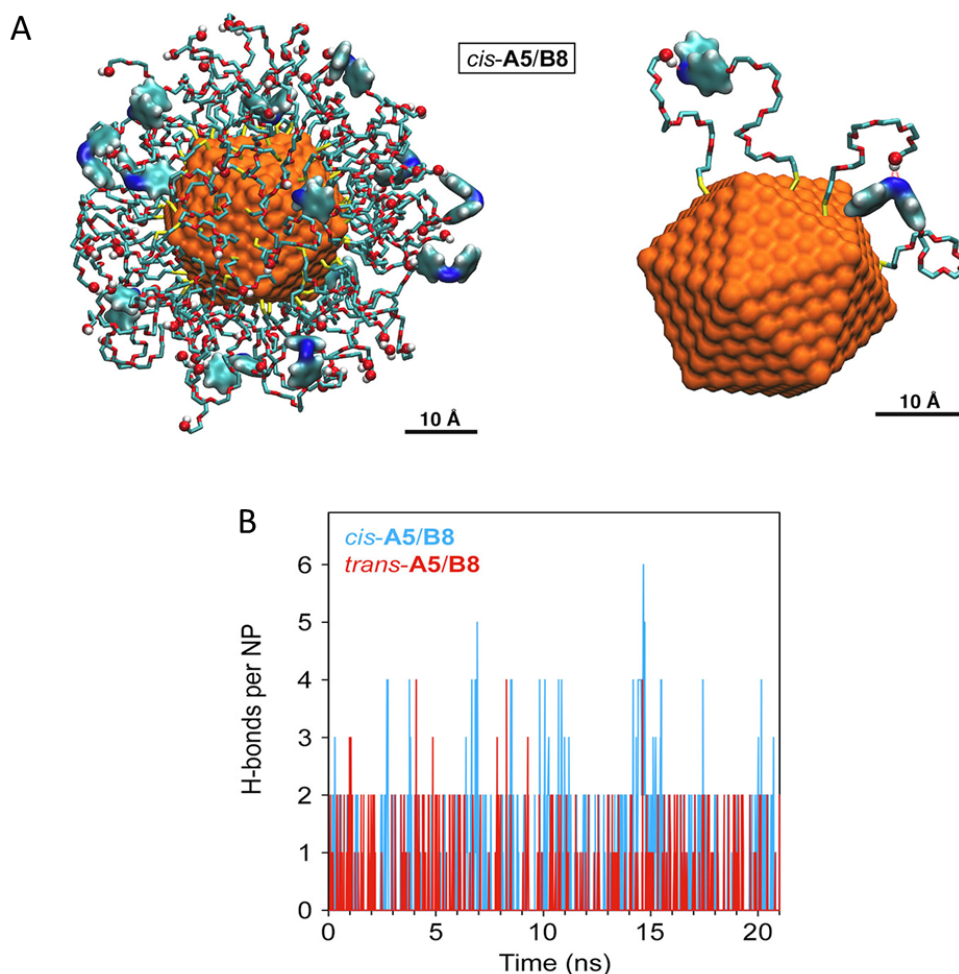


Figure 77: (A) Snapshots from MD simulations of a cis-A5/B8-coated 2.5 nm gold NP. (B) Number of hydrogen bonds (by MD simulations) between B8 and trans- vs. cis-A5 over a period of 20 ns.

methoxy groups of B9 were exposed to the solvent (Figure 78A). The trans isomer of A5 may also be capable of forming H-bonds with B8's hydroxy group (Figure 78B and C), thus possibly reducing the double-bond character of the N=N group and increasing the rate of the trans \rightarrow cis forward isomerization. To verify this hypothesis experimentally, we exposed NPs functionalized with trans-A5/B8 and trans-A5/B9 to UV light for increasing periods and found that, indeed, isomerization proceeded faster with the OH-terminated B8 as the background ligand. The difference in rates, however, was much smaller than in the case of back-isomerization (≈ 4 and ≈ 74 , respectively), which

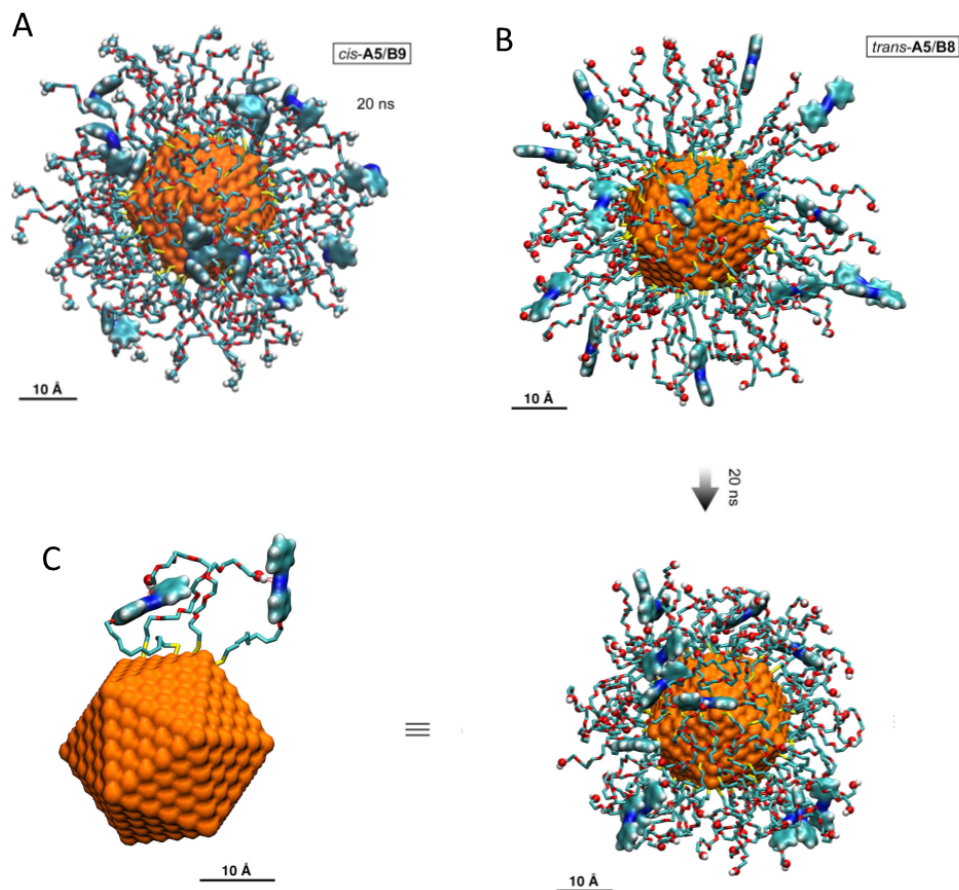


Figure 78: (A) Snapshot from MD simulations of a *cis*-A5/B9-coated 2.5 nm gold NP. (B), (C) Snapshots from MD simulations of a *trans*-A5/B8-coated 2.5 nm gold NP.

can be accounted for by the lower percentage of *trans*-A5 vs *cis*-A5 engaged in H-bonding with B8 (estimated as 0.7% and 1.9%, respectively, over a period of 20 ns; Figure 77B) and by the lower strength of H-bonds formed by *trans*-A5 (a significant distortion from planarity in the O—H · · · N moiety (Figure 78C);

To verify that the increased rate of relaxation by replacing alkyl chain (B1) with a tris(ethylene glycol) chain of similar overall length (B6) is related to the high flexibility of OEG chains [278–280] (Figure 73E), which results in more conformational freedom available to the terminal azobenzene groups. We performed MD simulations of *cis*-A2/B1- and *cis*-A2/B6-functionalized 2.5 nm gold NPs

and analyzed the position of the azobenzene group in time. To this end, we calculated the root-mean-square deviation (RMSD) of the N=N moiety (Figure 79A). The results (Figure 79A) confirm that the azobenzene group moves a larger distance (with respect to the 1-ns reference frame) in the presence of background ligand B6. This reasoning is further confirmed by analyzing the distance of the azobenzene group in cis-A2/B1- vs. cis-A2/B6-functionalized 2.5 nm Au NPs from the surface of gold. As Figure 79B shows, the average distance between the center of mass of the N=N moiety and the surface of gold is smaller for B6, indicating that this background ligand offers more room for the azobenzene groups. In Figure 79C, we plotted the total number of atoms within an arbitrary distance (we selected 3 Å) of the A2 ligands. It can be seen that cis-A2 resides in a less congested environment on A2/B6-functionalized NPs compared with A2/B1-functionalized NPs (Figure 80). To verify that the different kinetics of back-isomerization in cis-A2/B1- and cis-A2/B6-coated AuNPs are not due to the different degrees of azobenzene aggregation, we analyzed the snapshots from the simulations at $t = 20$ ns (Figure 80). Indeed, we found that the aggregation was negligible in both cases (see also Figure 79D).

Conclusion

In sum, nanoparticles co-adsorbed with the inherently hydrophobic azobenzene ligands and water-solubilizing ligands can be water-soluble by precisely fine-tuning the amount of azobenzene ligands which is observed in the lab of Prof. Rafal Klajn. Molecular dynamics simulations helped to identify two distinct supramolecular architectures (depending on the length of the background ligand) on these nanoparticles, which can explain their excellent aqueous solubilities. The background ligands with hydroxy (OH) groups show a slightly bigger number of H-bonds with cis-azobenzene than with trans-azobenzene ligands, which might be the reason for the observed increased rate of back

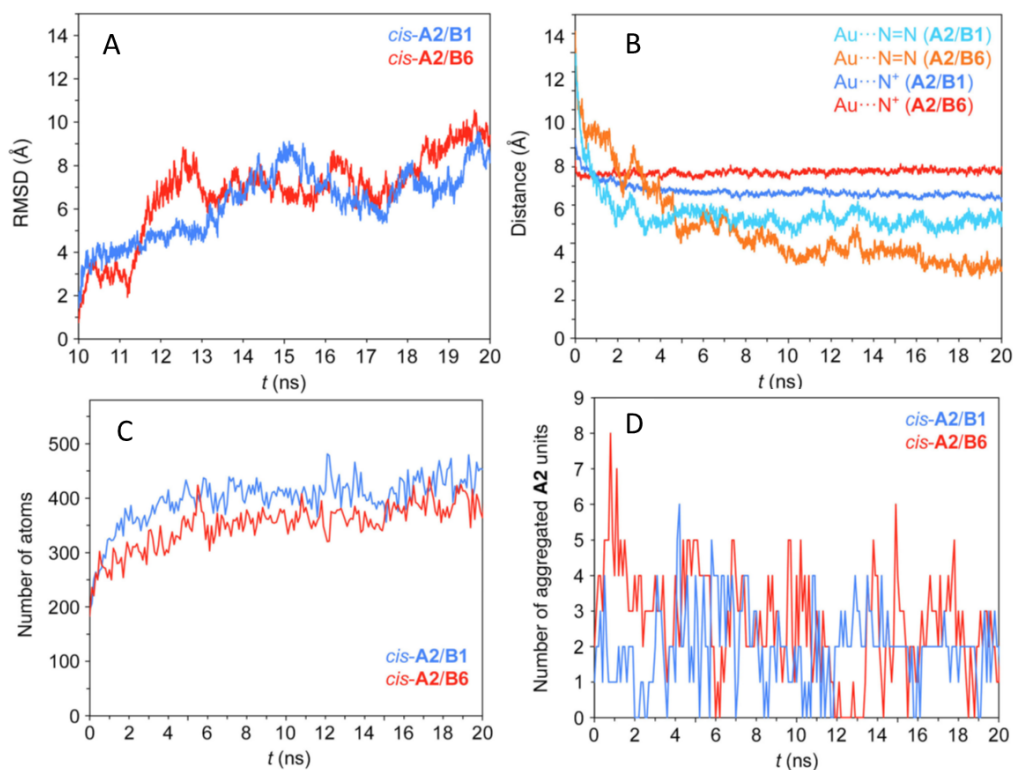


Figure 79: (A) Root-mean-square deviation of the N=N moiety in cis-A2 co-adsorbed on 2.5 nm AuNPs with B1 (blue) and B6 (red). (B) Average distance of the center of mass of A2's N=N moiety from the surface of gold on cis-A2/B1- functionalized 2.5 nm Au NPs (cyan) vs. cis-A2/B6- functionalized 2.5 nm Au NPs (blue). For comparison, average distances between B1's and B6's ammonium N atoms and the gold surface are also plotted. (C) The total number of atoms present within 3 Å of A2 ligands on an A2/B1- vs. an A2/B6- functionalized NP. (D) An attempt to quantify the aggregation of cis-A2 on an A2/B1- vs. an A2/B6-coated 2.5 nm Au NP. An azobenzene group of an A2 ligand is considered aggregated when there are at least six atoms of another A2's azobenzene group within a distance of 4 Å.

isomerization. RMSD and N=N moiety distance measurements indicated stronger intermolecular interactions between ligands with similar length, which could accelerate the isomerization rate.

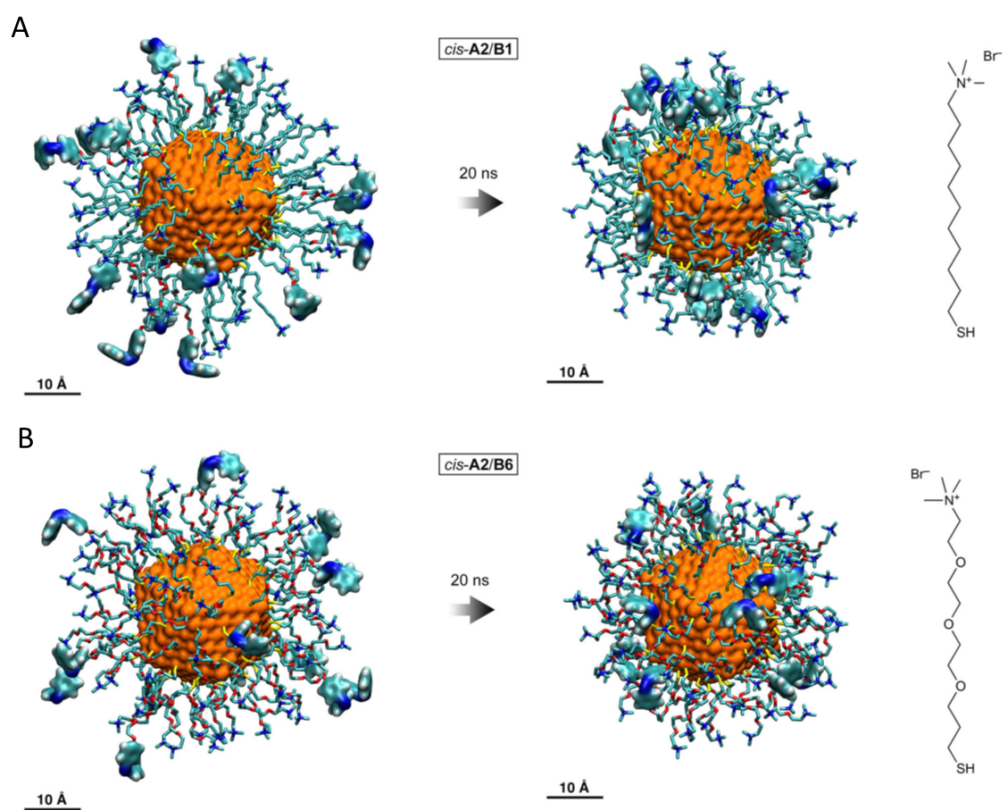


Figure 80: (A) Snapshots from MD simulations of a cis-A2/B1-coated 2.5 nm gold NP. (B) Snapshots from MD simulations of a cis-A2/B6-coated 2.5 nm gold NP.

CHAPTER 7

CONCLUDING REMARKS

This thesis includes projects spanning three main research blocks: Design and simulations of inhibitors against various pathogens, simulations and analysis of drug delivery systems, and modeling of dynamical nanosystems. Most of the works are based on collaborations with experimental groups. MD simulation methods were used to design the systems, test them by simulations, interpret experimental observations and explain mechanisms. *Ab initio* calculations were used to analyze some delicate interactions and prepare forcefields for MD simulations. Besides those collaborative works, we also used MD simulations for designing protein inhibitors and boosters against virus causing pandemics, where a new adaptive evolution algorithm was developed. The major results of our studies are summarized below:

7.1 A: Design of inhibitors and boosters for SARS-CoV-2

Section 1 - Design of ACE2-based peptide inhibitors of SARS-CoV-2: Four SARS-CoV-2 inhibitors with different template scaffolds were designed based on ACE2, which is the cellular receptor of the coronavirus. A computational strategy was developed to adaptively evolve peptides that could selectively inhibit mutating S protein receptor binding domains (RBDs) of different SARS-CoV-2 viral strains. Starting from suitable peptide templates, we gradually modified the templates by random mutations and Monte Carlo decisions, while retaining those mutations that maximize their RBD-binding free energies. The computational search could provide libraries of optimized therapeutics capable of reducing the SARS-CoV-2 infection on a global scale [1,2].

Section 2 - Retrained generic antibodies can recognize SARS-CoV-2: The dramatic impact which novel viruses can have on the human society could be mitigated without the need of vaccination if antibodies present within the population are retrained to recognize these viruses. With this idea in mind, double-faced peptide-based boosters are designed and evaluated computationally to allow recognition of SARS-CoV-2 by Hepatitis B antibodies. One booster face is made of ACE2-mimic peptides that can bind to the receptor binding domain (RBD) of SARS-CoV-2. The other booster face is composed of a Hepatitis B core-antigen, targeting the Hepatitis B antibody fragment. Molecular dynamics simulations revealed that the designed boosters have a highly specific and stable binding both to RBD and the antibody fragment (AF). This approach can provide a cheap and efficient neutralization of emerging pathogens [3].

Section 3 - Glycodendrimer inhibitors of HIV and SARS-CoV-2: By mimicking HSPGs, several hexavalent sulfoglycodendrimers (SGDs) were synthesized and found to be promising in inhibiting the early stages of viral binding/entry of HIV-1 mediated through gp120. MD simulations demonstrated that the sulfation level, number of sugars, orientations of polar groups and overall arrangement of sugars in SGDs determines the strength of their multivalent interactions with gp120. Since coronaviruses also utilize HSPGs during their cell entry, cellobiose and lactose SGDs were evaluated for binding to the RBD of the S protein in SARS-CoV-2 using MD. SGDs were found to bind both the top region (ACE2-RBD binding interface) and the middle part (HSPG binding region) of RBD, while GDs only target the top region of RBD. These combined results illustrate the potential of using SGDs to prevent transmission of the HIV-1 and SARS-CoV-2 pathogens [4].

7.2 B: Design of inhibitors against cancer and other viral pathogens

Section 1 - Peptide-conjugated dendrimers as cancer immunotherapies : β -Hairpin peptides present great potential as antagonists against β -sheet-rich protein surfaces. A peptide–dendrimer conjugate (PDC) approach was designed to stabilize the β -hairpin structure of the peptide via intermolecular forces and the excluded volume effect in the lab of Prof. Seungpyo Hong. The PDCs based on a β -hairpin peptides isolated from an engineered programmed death-1 (PD-1) protein showed significantly higher affinity (avidity) to their binding counterpart, programmed death ligand 1 (PD-L1). MD simulation results conformed the stable conformations of peptides on dendrimer surface. The interactions between dendrimers and peptides were quantified. The results demonstrate the potential of the PDC system as a novel class of inhibitors targeting β -strand-rich protein surfaces, such as PD-1 and PD-L1, displaying its potential as a new cancer immunotherapy platform [5].

Section 2 - Modified nanoparticles and cyclodextrins as broad-spectrum antivirals: Antiviral AuNPs with long and flexible linkers mimicking HSPG were designed in the lab of Prof. Francesco Stellacci. The strong and multivalent binding between AuNPs and the repeating units of viral capsid was captured by MD simulations. The functionalized AuNPs could generate forces (~ 190 pN) that eventually lead to irreversible viral deformation. Virucidal assays, electron microscopy images, and MD simulations support the proposed mechanism. In order to design nontoxic antival agents, the naturally occurring glucose derivatives, CDns, were functionalized by different sulfonated ligands mimicking HSPGs. Some of the CDns exhibit virucidal properties against various viruses. MD simulations of six types of CDns interacting with envelope protein gB of HSV implied that virucidal action of CDns originates in both blocking of the fusion loop and causing conformational change of gB through multivalent binding modes [6, 7].

Section 3 - Boron clusters inhibiting protein–protein interactions: Using a structurally characterized boron cluster-based organometallic building block, several Boron clusters were systematically synthesized and tested in binding with different protein targets in the lab of Prof. Alexander Spokoiny. MD simulations demonstrated the topological rigidity of the resulting Boron clusters and their multivalent binding capabilities to complex protein targets. Combining elements of inorganic cluster chemistry, organometallic synthesis, nanobiotechnology and MD simulations, we have provided a basis for the generation of robust and programmable hybrid Boron clusters with unique applications targeting molecular recognition [8–10].

7.3 C: Simulations of polymer-based drug delivery systems

Section 1 - Novel oligonucleotide carrier: The synthesized nonviral cationic supramolecular polymers (in the lab of Prof. Paolo Caliceti) represent a novel platform with suitable physicochemical, structural, and biopharmaceutical properties for oligonucleotides delivery. Both experiments and simulations show that polyplexes formed by certain ratio of cationic polymers and oligonucleotides preserve a rod-shape structure, which play a key role in the intracellular access of the nanocarrier and thus the delivery of the ON payload [11].

Section 2 - Polymeric micelles with dendritic PEG outer shells: A higher surface density of poly(ethylene glycol) (PEG) on polymeric micelles enhances their stability in serum, leading to improved plasma circulation, observed in the lab of Prof. Seungpyo Hong. The dendron micelles exhibited a better serum stability (longer half-life) and thus a slower release profile than the linear micelles. Fluorescence quenching assays and molecular dynamics (MD) simulations revealed that the high serum stability of the dendron micelles can be attributed to the reduced micelle-serum protein interactions, owing to their dendritic, dense PEG outer shell. These results provided an important design cue for various polymeric micelles and nanoparticles [12].

Section 3 - High F-content perfluoropolyether-based nanoparticles: Copolymers with different fluorine contents were prepared in the lab of Prof. Andrew Whittaker. The simulations have shown that the copolymers can aggregate in solution in a manner dependent on the fluorine content. Dynamic light scattering and MD simulations were conducted and demonstrated that $poly(OEGA)_m - PFPE$ with the longest $poly(OEGA)_m$ segments ($m = 20$) undergoes single-chain folding in water while $poly(OEGA)_{10} - PFPE$ and $poly(OEGA)_4 - PFPE$ with shorter OEGA segments experience multiple-chain aggregation. The aggregation behavior of these fluorinated polymers plays a critical role in internalization and transport in living cells and 3D spheroids, providing important design criteria for the preparation of highly effective delivery agents [13–15].

7.4 D: Modeling of dynamical nanosystems

Section 1 - Stretch-healable molecular nanofibers: *Ab initio* calculations were used to analyze the dedicated noncovalent interactions between coronene or perfluorocoronene molecular flakes. The interaction energy was interpreted by both SAPT and molecular mechanics potential. MD simulations show that mixed coronene and perfluorocoronene molecular flakes in aqueous solutions form linear stacks having predominantly an alternating pattern. When such molecular flakes are covalently connected by short flexible molecular linkers into chains of various organizations, they can form stretchable and healable fibers with parameters dependent on humidity [16].

Section 2 - Cargo-carrying peptide sliders on polymer tracks: The oligoanionic molecular sliders were designed that exploit Brownian motion and diffusive binding on polycationic tracks in the lab of Prof. Wilhelm Huck. The presence of the polymer tracks increases the rate of bimolecular reactions between modified sliders by over two orders of magnitude. Molecular dynamics simulations showed that the sliders not only diffuse, but also jump and hop surprisingly efficiently along the polymer tracks. The concept of diffusive binding can also be utilized for the spatially controlled

transport of chemical groups across gels. This work represents a new concept for designing functional nanosystems based on random Brownian motion [17].

Section 3 - Intermolecular interactions stabilize ligand ratios on nanoparticles: Confining organic molecules to the surfaces of inorganic nanoparticles can induce intermolecular interactions between them, observed in the lab of Prof. Rafal Klajn. A narrow range of molar ratios of the two ligands (positively and zwitterionic ligand) can be preserved on the functionalized particles. Molecular dynamics simulations revealed that this self-limiting process could be attributed to attractive electrostatic interactions between the two ligands upon adsorption onto the NPs [18].

Section 4 - Supramolecular control of azobenzene switching on nanoparticles: Nanoparticles co-adsorbed with the inherently hydrophobic azobenzenes and water-solubilizing ligands can be water-soluble by precisely fine-tune the amount of azobenzene, observed in the lab of Prof. Rafal Klajn. Molecular dynamics simulations helped to identify two distinct supramolecular architectures (depending on the length of the background ligand) on these nanoparticles, which can explain their excellent aqueous solubilities [19].

Most of our simulations are in close agreement with experimental results. Combining the experimental observations, theoretical analysis, and computational simulations, we provided a comprehensive view of the studied systems. Based on the experience gained from the collaborative projects, we further developed the usage of MD simulations in drug discovery. A series of peptide inhibitors were designed and tested with the binding affinity against their target protein. The computational search could provide libraries of optimized therapeutics capable of reducing the virus infection.

CITED LITERATURE

1. Han, Y., Král, P. Computational Design of ACE2-Based Peptide Inhibitors of SARS-CoV-2. *ACS Nano* **14**, 5143 (2020).
2. Chaturvedi, P., Han, Y., Král, P., Vukovic, L. Adaptive Evolution of Peptide Inhibitors for Mutating SARS-CoV-2. *Advanced Theory and Simulations* **3**, 2000156 (2020).
3. Han, Y., McReynolds, K., Kral, P. Retrained Generic Antibodies Can Recognize SARS-CoV-2. *The Journal of Physical Chemistry Letters* **submitted**, (2020).
4. Wells, L., Vierra, C., Hardman, J., Han, Y., Dimas, D., Gwarada, L., Blackeye, R., Eggers, D. K., LaBranche, C. C., Král, P., McReynolds, K. D. Sulfoglycodendrimer Therapeutics for HIV-1 and SARS-CoV-2. *Advanced Therapeutics* **submitted**, (2020).
5. Jeong, W.-j., Bu, J., Han, Y., Drelich, A. J., Nair, A., Král, P., Hong, S. Nanoparticle Conjugation Stabilizes and Multimerizes β -Hairpin Peptides To Effectively Target PD-1/PD-L1 β -Sheet-Rich Interfaces. *Journal of the American Chemical Society* **142**, 1832 (2020).
6. Cagno, V., Andreozzi, P., D'Alicarnasso, M., Silva, P. J., Mueller, M., Galloux, M., Le Goffic, R., Jones, S. T., Vallino, M., Hodek, J., Weber, J., Sen, S., Janeček, E.-R., Bekdemir, A., Sanavio, B., Martinelli, C., Donalisio, M., Rameix Welti, M.-A., Eleouet, J.-F., Han, Y., Kaiser, L., Vukovic, L., Tapparel, C., Král, P., Krol, S., Lembo, D., Stellacci, F. Broad-spectrum non-toxic antiviral nanoparticles with a virucidal inhibition mechanism. *Nature Materials* **102**, 195 (2018).
7. Jones, S. T., Cagno, V., Janeček, M., Ortiz, D., Gasilova, N., Piret, J., Gasbarri, M., Constant, D. A., Han, Y., Vuković, L., Král, P., Kaiser, L., Huang, S., Constant, S., Kirkegaard, K., Boivin, G., Stellacci, F., Tapparel, C. Modified cyclodextrins as broad-spectrum antivirals. *Science Advances* **6**, eaax9318 (2020).
8. Qian, E. A., Wixtrom, A. I., Axtell, J. C., Saebi, A., Jung, D., Rehak, P., Han, Y., Mouly, E. H., Mosallaei, D., Chow, S., Messina, M. S., Wang, J. Y., Royappa, A. T., Rheingold, A. L., Maynard, H. D., Král, P., Spokoyny, A. M. Atomically precise organomimetic cluster nanomolecules assembled via perfluoroaryl-thiol SNAr chemistry. *Nature Chemistry* **9**, 333 (2017).
9. Qian, E. A., Han, Y., Messina, M. S., Maynard, H. D., Král, P., Spokoyny, A. M. Multi-valent Cluster Nanomolecules for Inhibiting Protein-Protein Interactions. *Bioconjugate Chemistry* **30**, 2594 (2019).

CITED LITERATURE (Continued)

10. Stauber, J. M., Qian, E. A., Han, Y., Rheingold, A. L., Král, P., Fujita, D., Spokoyny, A. M. An Organometallic Strategy for Assembling Atomically Precise Hybrid Nanomaterials. *Journal of the American Chemical Society* **142**, 327 (2020).
11. Malfanti, A., Mastrotto, F., Han, Y., Král, P., Balasso, A., Scomparin, A., Pozzi, S., Satchi-Fainaro, R., Salmaso, S., Caliceti, P. Novel Oligo-Guanidyl-PEG Carrier Forming Rod-Shaped Polyplexes. *Molecular Pharmaceutics* **16**, 1678 (2019).
12. Hsu, H.jui , Han, Y., Cheong, M., Král, P., Hong, S. Dendritic PEG outer shells enhance serum stability of polymeric micelles. *Nanomedicine: Nanotechnology, Biology and Medicine* **14**, 1879 (2018).
13. Zhang, C., Moonshi, S. S., Han, Y., Puttick, S., Peng, H., Magoling, B. J. A., Reid, J. C., Bernardi, S., Searles, D. J., Král, P., Whittaker, A. K. PFPE-Based Polymeric ¹⁹F MRI Agents: A New Class of Contrast Agents with Outstanding Sensitivity. *Macromolecules* **50**, 5953 (2017).
14. Zhang, C., Liu, T., Wang, W., Bell, C. A., Han, Y., Fu, C., Peng, H., Tan, X., Král, P., Gaus, K., Gooding, J. J., Whittaker, A. K. Tuning of the Aggregation Behavior of Fluorinated Polymeric Nanoparticles for Improved Therapeutic Efficacy. *ACS Nano* **14**, 7425 (2020).
15. Zhang, C., Moonshi, S. S., Wang, W., Ta, H. T., Han, Y., Han, F. Y., Peng, H., Král, P., Rolfe, B. E., Gooding, J. J., Gaus, K., Whittaker, A. K. High F-Content Perfluoropolyether-Based Nanoparticles for Targeted Detection of Breast Cancer by ¹⁹F Magnetic Resonance and Optical Imaging. *ACS Nano* **12**, 9162 (2018).
16. Han, Y., Langer, M., Medved, M., Otyepka, M., Král, P. Biomimetic Materials: Stretch-Healable Molecular Nanofibers. *Advanced Theory and Simulations* **3**, 2070023 (2020).
17. Zheng, L., Zhao, H., Han, Y., Qian, H., Vukovic, L., Mecinović, J., Král, P., Huck, W. T. S. Catalytic transport of molecular cargo using diffusive binding along a polymer track. *Nature Chemistry* **11**, 359 (2019).
18. Chu, Z., Han, Y., Král, P., Klajn, R. "Precipitation on Nanoparticles": Attractive Intermolecular Interactions Stabilize Specific Ligand Ratios on the Surfaces of Nanoparticles. *Angewandte Chemie International Edition* **57**, 7023 (2018).
19. Chu, Z., Han, Y., Bian, T., De, S., Král, P., Klajn, R. Supramolecular Control of Azobenzene Switching on Nanoparticles. *Journal of the American Chemical Society* **141**, 1949 (2019).
20. Zhao, H., Sen, S., Udayabhaskararao, T., Sawczyk, M., Kucanda, K., Manna, D., Kundu, P. K., Lee, J.-W., Král, P., Klajn, R. Reversible trapping and reaction acceleration within dynamically self-assembling nanoflasks. *Nature Nanotechnology* **11**, 82 (2015).

CITED LITERATURE (Continued)

21. Abraham, F. F. Computational statistical mechanics methodology, applications and supercomputing. *Advances in Physics* **35**, 1 (1986).
22. Winsberg, E., *The Stanford Encyclopedia of Philosophy*, Zalta, E. N., ed. (Metaphysics Research Lab, Stanford University, 2019), winter 2019 edn.
23. Iftimie, R., Minary, P., Tuckerman, M. E. Ab initio molecular dynamics: Concepts, recent developments, and future trends. *Proceedings of the National Academy of Sciences* **102**, 6654 (2005).
24. Groenhof, G., *Introduction to QM/MM Simulations* (Humana Press, Totowa, NJ, 2013), pp. 43–66.
25. Iftimie, R., Minary, P., Tuckerman, M. E. Ab initio molecular dynamics: Concepts, recent developments, and future trends. *Proceedings of the National Academy of Sciences* **102**, 6654 (2005).
26. Casalino, L., Gaieb, Z., Goldsmith, J. A., Hjorth, C. K., Dommer, A. C., Harbison, A. M., Fogarty, C. A., Barros, E. P., Taylor, B. C., McLellan, J. S., Fadda, E., Amaro, R. E. Beyond Shielding: The Roles of Glycans in the SARS-CoV-2 Spike Protein. *ACS Central Science* **6**, 1722 (2020).
27. Tarasova, E., Farafonov, V., Khayat, R., Okimoto, N., Komatsu, T. S., Taiji, M., Nerukh, D. All-Atom Molecular Dynamics Simulations of Entire Virus Capsid Reveal the Role of Ion Distribution in Capsid’s Stability. *The Journal of Physical Chemistry Letters* **8**, 779 (2017).
28. Khot, A., Shiring, S. B., Savoie, B. M. Evidence of information limitations in coarse-grained models. *The Journal of Chemical Physics* **151**, 244105 (2019).
29. Ramezanpour, M., Leung, S., Delgado-Magnero, K., Bashe, B., Thewalt, J., Tieleman, D. Computational and experimental approaches for investigating nanoparticle-based drug delivery systems. *Biochimica et Biophysica Acta (BBA) - Biomembranes* **1858**, 1688 (2016).
30. Hospital, A., Goni, J. R., Orozco, M., Gelpi, J. L. Molecular dynamics simulations: advances and applications. *Advances and Applications in Bioinformatics and Chemistry* **8**, 37 (2015).
31. Brown, L. V., Gaffney, E. A., Wagg, J., Coles, M. C. Applications of mechanistic modelling to clinical and experimental immunology: an emerging technology to accelerate immunotherapeutic discovery and development. *Clinical and Experimental Immunology* **193**, 284 (2018).

CITED LITERATURE (Continued)

32. Khalkhali, M., Mohammadinejad, S., Khoeini, F., Rostamizadeh, K. Vesicle-like structure of lipid-based nanoparticles as drug delivery system revealed by molecular dynamics simulations. *International Journal of Pharmaceutics* **559**, 173 (2019).
33. Sen, S., Han, Y., Rehak, P., Vuković, L., Král, P. Computational studies of micellar and nanoparticle nanomedicines. *Chemical Society Reviews* **47**, 3849 (2018).
34. Han, Y., Yang, C.-L. Molecular Dynamics Study on Encapsulation of Double Stranded Nucleic Acids into Carbon Nanotubes. *The Journal of Physical Chemistry C* **122**, 19236 (2018).
35. Bae, J. W., Pearson, R. M., Patra, N., Sunoqrot, S., Vukovic, L., Král, P., Hong, S. Dendron-mediated self-assembly of highly PEGylated block copolymers: a modular nanocarrier platform. *Chemical Communications* **47**, 10302 (2011).
36. Hsu, H.-j., Sen, S., Pearson, R. M., Uddin, S., Král, P., Hong, S. Poly(ethylene glycol) Corona Chain Length Controls End-Group-Dependent Cell Interactions of Dendron Micelles. *Macromolecules* **47**, 6911 (2014).
37. Pearson, R. M., Sen, S., Hsu, H.-j., Pasko, M., Gaske, M., Král, P., Hong, S. Tuning the Selectivity of Dendron Micelles Through Variations of the Poly(ethylene glycol) Corona. *ACS Nano* **10**, 6905 (2016).
38. Boisseau, P., Loubaton, B. Nanomedicine, nanotechnology in medicine. *Comptes Rendus Physique* **12**, 620 (2011).
39. Dogra, P., Butner, J. D., Chuang, Y.-l., Caserta, S., Goel, S., Brinker, C. J., Cristini, V., Wang, Z. Mathematical modeling in cancer nanomedicine: a review. *Biomedical Microdevices* **21**, 40 (2019).
40. Nune, S. K., Gunda, P., Thallapally, P. K., Lin, Y. Y., Forrest, M. L., Berkland, C. J. Nanoparticles for biomedical imaging. *Expert Opinion on Drug Delivery* **6**, 1175 (2009).
41. Grzelczak, M., Vermant, J., Furst, E. M., Liz-Marzán, L. M. Directed Self-Assembly of Nanoparticles. *ACS Nano* **4**, 3591 (2010).
42. Yang, M., Chan, H., Zhao, G., Bahng, J. H., Zhang, P., Král, P., Kotov, N. A. Self-assembly of nanoparticles into biomimetic capsid-like nanoshells. *Nature Chemistry* **9**, 287 (2017).
43. Lee, S., Kumari, N., Jeon, K.-W., Kumar, A., Kumar, S., Koo, J. H., Lee, J., Cho, Y.-K., Lee, I. S. Monofacet-Selective Cavitation within Solid-State Silica-Nanoconfinement toward Janus Iron Oxide Nanocube. *Journal of the American Chemical Society* **140**, 15176 (2018).

CITED LITERATURE (Continued)

44. Korevaar, P. A., Schaefer, C., Greef, T. F. A. de, Meijer, E. W. Controlling Chemical Self-Assembly by Solvent-Dependent Dynamics. *Journal of the American Chemical Society* **134**, 13482 (2012).
45. Cohen, E., Weissman, H., Pinkas, I., Shimoni, E., Rehak, P., Král, P., Rybtchinski, B. Controlled Self-Assembly of Photofunctional Supramolecular Nanotubes. *ACS Nano* **12**, 317 (2018).
46. Evans, S. D., Flynn, T. M., Ulman, A. Self-Assembled Multilayer Formation on Predefined Templates. *Langmuir* **11**, 3811 (1995).
47. Levine, I. N., *Quantum Chemistry* (Pearson Education, New Jersey, 2009).
48. Szabo, A., Ostlund, N. S., *Modern Quantum Chemistry* (Dover Publications, New York, 1989).
49. Muller, C., Paulus, B. Wavefunction-based electron correlation methods for solids. *Physical Chemistry Chemical Physics* **14**, 7605 (2012).
50. Hohenberg, P., Kohn, W. Inhomogeneous Electron Gas. *Physical Review* **136**, B864 (1964).
51. Friesner, R. A. Ab initio quantum chemistry: Methodology and applications. *Proceedings of the National Academy of Sciences* **102**, 6648 (2005).
52. Johnson, B. G., Gill, P. M. W., Pople, J. A. The performance of a family of density functional methods. *The Journal of Chemical Physics* **98**, 5612 (1993).
53. Becke, A. D. Density functional thermochemistry. III. The role of exact exchange. *The Journal of Chemical Physics* **98**, 5648 (1993).
54. Jeziorski, B., Moszynski, R., Szalewicz, K. Perturbation Theory Approach to Intermolecular Potential Energy Surfaces of van der Waals Complexes. *Chemical Reviews* **94**, 1887 (1994).
55. Duijneveldt, F. B. van, Rijdt, J. G. C. M. van Duijneveldt-van de, Lenthe, J. H. van State of the Art in Counterpoise Theory. *Chemical Reviews* **94**, 1873 (1994).
56. Parrish, R. M., Sherrill, C. D. Spatial assignment of symmetry adapted perturbation theory interaction energy components: The atomic SAPT partition. *The Journal of Chemical Physics* **141**, 044115 (2014).
57. Bhandarkar, M., Bhatele, A., Bohm, E., Brunner, R., Buelens, F., Chipot, C., Dalke, A., Dixit, S., Fiorin, G., Freddolino, P., Grayson, P., Gullingsrud, J., Gursoy, A., Hardy, D., Harrison, C., Hénin, J., Humphrey, W., Hurwitz, D., Hynninen, A., Jain, N., Krawetz,

CITED LITERATURE (Continued)

- N., Kumar, S., Kunzman, D., Lai, J., Lee, C., McGreevy, R., Mei, C., Nelson, M., Phillips, J., Radak, B., Sarood, O., Shinozaki, A., Tanner, D., Wells, D., Zheng, G., Zhu, F., *NAMD User's Guide* (Theoretical Biophysics Group, University of Illinois and Beckman Institute, 2016).
58. Phillips, J. C., Braun, R., Wang, W., Gumbart, J., Tajkhorshid, E., Villa, E., Chipot, C., Skeel, R. D., Kalé, L., Schulten, K. Scalable molecular dynamics with NAMD. *Journal of Computational Chemistry* **26**, 1781 (2005).
 59. Spreiter, Q., Walter, M. Classical Molecular Dynamics Simulation with the Velocity Verlet Algorithm at Strong External Magnetic Fields. *Journal of Computational Physics* **152**, 102 (1999).
 60. Martyna, G. J., Tobias, D. J., Klein, M. L. Constant pressure molecular dynamics algorithms. *The Journal of Chemical Physics* **101**, 4177 (1994).
 61. Feller, S. E., Zhang, Y., Pastor, R. W., Brooks, B. R. Constant pressure molecular dynamics simulation: The Langevin piston method. *The Journal of Chemical Physics* **103**, 4613 (1995).
 62. Darden, T., York, D., Pedersen, L. Particle mesh Ewald: An $N \log(N)$ method for Ewald sums in large systems. *The Journal of Chemical Physics* **98**, 10089 (1993).
 63. MacKerell, A. D., Bashford, D., Bellott, M., Dunbrack, R. L., Evanseck, J. D., Field, M. J., Fischer, S., Gao, J., Guo, H., Ha, S., Joseph-McCarthy, D., Kuchnir, L., Kuczera, K., Lau, F. T. K., Mattos, C., Michnick, S., Ngo, T., Nguyen, D. T., Prodhom, B., Reiher, W. E., Roux, B., Schlenkrich, M., Smith, J. C., Stote, R., Straub, J., Watanabe, M., Wiórkiewicz-Kuczera, J., Yin, D., Karplus, M. All-Atom Empirical Potential for Molecular Modeling and Dynamics Studies of Proteins. *The Journal of Physical Chemistry B* **102**, 3586 (1998).
 64. Huang, J., MacKerell, A. D. CHARMM36 all-atom additive protein force field: Validation based on comparison to NMR data. *Journal of Computational Chemistry* **34**, 2135 (2013).
 65. Klauda, J. B., Venable, R. M., Freites, J. A., O'Connor, J. W., Tobias, D. J., Mondragon-Ramirez, C., Vorobyov, I., MacKerell, A. D., Pastor, R. W. Update of the CHARMM All-Atom Additive Force Field for Lipids: Validation on Six Lipid Types. *The Journal of Physical Chemistry B* **114**, 7830 (2010).
 66. Hart, K., Foloppe, N., Baker, C. M., Denning, E. J., Nilsson, L., MacKerell, A. D. Optimization of the CHARMM Additive Force Field for DNA: Improved Treatment of the BI/BII Conformational Equilibrium. *Journal of Chemical Theory and Computation* **8**, 348 (2012).

CITED LITERATURE (Continued)

67. Denning, E. J., Priyakumar, U. D., Nilsson, L., Mackerell Jr., A. D. Impact of 2'-hydroxyl sampling on the conformational properties of RNA: Update of the CHARMM all-atom additive force field for RNA. *Journal of Computational Chemistry* **32**, 1929 (2011).
68. Vanommeslaeghe, K., Hatcher, E., Acharya, C., Kundu, S., Zhong, S., Shim, J., Darian, E., Guvench, O., Lopes, P., Vorobyov, I., Mackerell, A. D. CHARMM general force field: A force field for drug-like molecules compatible with the CHARMM all-atom additive biological force fields. *Journal of Computational Chemistry* **31**, 671 (2010).
69. Vanommeslaeghe, K., MacKerell, A. D. Automation of the CHARMM General Force Field (CGenFF) I: Bond Perception and Atom Typing. *Journal of Chemical Information and Modeling* **52**, 3144 (2012).
70. Vanommeslaeghe, K., Raman, E. P., MacKerell, A. D. Automation of the CHARMM General Force Field (CGenFF) II: Assignment of Bonded Parameters and Partial Atomic Charges. *Journal of Chemical Information and Modeling* **52**, 3155 (2012).
71. Hu, H., Lu, Z., Yang, W. Fitting Molecular Electrostatic Potentials from Quantum Mechanical Calculations. *Journal of Chemical Theory and Computation* **3**, 1004 (2007).
72. Mayne, C. G., Saam, J., Schulten, K., Tajkhorshid, E., Gumbart, J. C. Rapid parameterization of small molecules using the Force Field Toolkit. *Journal of Chemical Theory and Computation* **34**, 2757 (2013).
73. Humphrey, W., Dalke, A., Schulten, K. VMD: Visual molecular dynamics. *Journal of Molecular Graphics* **14**, 33 (1996).
74. Pulay, P., Fogarasi, G., Pang, F., Boggs, J. E. Systematic ab initio gradient calculation of molecular geometries, force constants, and dipole moment derivatives. *Journal of the American Chemical Society* **101**, 2550 (1979).
75. Vanommeslaeghe, K., Hatcher, E., Acharya, C., Kundu, S., Zhong, S., Shim, J., Darian, E., Guvench, O., Lopes, P., Vorobyov, I., Mackerell, A. D. CHARMM general force field: A force field for drug-like molecules compatible with the CHARMM all-atom additive biological force fields. *Journal of Computational Chemistry* **31**, 671 (2010).
76. Mark, P., Nilsson, L. Structure and Dynamics of the TIP3P, SPC, and SPC/E Water Models at 298 K. *The Journal of Physical Chemistry A* **105**, 9954 (2001).
77. Guvench, O., MacKerell, A. D. Automated conformational energy fitting for force-field development. *Journal of Molecular Modeling* **14**, 667 (2008).
78. Hamaker, H. The London—van der Waals attraction between spherical particles. *Physica* **4**, 1058 (1937).

CITED LITERATURE (Continued)

79. McQuarrie, D. A., *Statistical mechanics Donald A. McQuarrie* (Harper & Row New York, 1975).
80. Kastner, J. Umbrella sampling. *WIREs Computational Molecular Science* **1**, 932 (2011).
81. Fiorin, G., Klein, M. L., HÅ©nin, J. Using collective variables to drive molecular dynamics simulations. *Molecular Physics* **111**, 3345 (2013).
82. Grossfield, A. *WHAM: the weighted histogram analysis method. version 2.0*, http://membrane.urmc.rochester.edu/wordpress/?page_id=126 .
83. Kumar, S., Rosenberg, J. M., Bouzida, D., Swendsen, R. H., Kollman, P. A. The weighted histogram analysis method for free-energy calculations on biomolecules. I. The method. *Journal of Computational Chemistry* **13**, 1011 (1992).
84. Roux, B. The calculation of the potential of mean force using computer simulations. *Computer Physics Communications* **91**, 275 (1995).
85. Homeyer, N., Gohlke, H. Free Energy Calculations by the Molecular Mechanics Poisson–Boltzmann Surface Area Method. *Molecular Informatics* **31**, 114 (2012).
86. Vergara-Jaque, A., Comer, J., Monsalve, L., González-Nilo, F. D., Sandoval, C. Computationally Efficient Methodology for Atomic-Level Characterization of Dendrimer-Drug Complexes: A Comparison of Amine- and Acetyl-Terminated PAMAM. *The Journal of Physical Chemistry B* **117**, 6801 (2013).
87. Tanner, D. E., Chan, K.-Y., Phillips, J. C., Schulten, K. Parallel Generalized Born Implicit Solvent Calculations with NAMD. *Journal of Chemical Theory and Computation* **7**, 3635 (2011).
88. Abroshan, H., Akbarzadeh, H., Parsafar, G. A. Molecular dynamics simulation and MM-PBSA calculations of sickle cell hemoglobin in dimer form with Val, Trp, or Phe at the lateral contact. *Journal of Physical Organic Chemistry* **23**, 866 (2010).
89. Massova, I., Kollman, P. A. Computational Alanine Scanning To Probe Protein–Protein Interactions: A Novel Approach To Evaluate Binding Free Energies. *Journal of the American Chemical Society* **121**, 8133 (1999).
90. Enriquez, H., Rolando, P., Pavan, S., Benedetti, F., Tossi, A., Savoini, A., Berti, F., Laio, A. Designing Short Peptides with High Affinity for Organic Molecules: A Combined Docking, Molecular Dynamics, And Monte Carlo Approach. *J. Chem. Theory Comput.* **8**, 1121 (2012).

CITED LITERATURE (Continued)

91. Russo, A., Scognamiglio, P. L., Hong Enriquez, R. P., Santambrogio, C., Grandori, R., Marasco, D., Giordano, A., Scoles, G., Fortuna, S. In Silico Generation of Peptides by Replica Exchange Monte Carlo: Docking-Based Optimization of Maltose-Binding-Protein Ligands. *PLOS ONE* **10**, e0133571 (2015).
92. Gorbalenya, A. E., Baker, S. C., Baric, R. S., Groot, R. J.de , Drosten, C., Gulyaeva, A. A., Haagmans, B. L., Lauber, C., Leontovich, A. M., Neuman, B. W., Penzar, D., Perlman, S., Poon, L. L. M., Samborskiy, D. V., Sidorov, I. A., Sola, I., Ziebuhr, J. The species Severe acute respiratory syndrome-related coronavirus: classifying 2019-nCoV and naming it SARS-CoV-2. *Nature Microbiology* **5**, 536 (2020).
93. Chen, N., Zhou, M., Dong, X., Qu, J., Gong, F., Han, Y., Qiu, Y., Wang, J., Liu, Y., Wei, Y., Xia, J., Yu, T., Zhang, X., Zhang, L. Epidemiological and clinical characteristics of 99 cases of 2019 novel coronavirus pneumonia in Wuhan, China: a descriptive study. *Lancet* **395**, 507 (2020).
94. Huang, C., Wang, Y., Li, X., Ren, L., Zhao, J., Hu, Y., Zhang, L., Fan, G., Xu, J., Gu, X., Cheng, Z., Yu, T., Xia, J., Wei, Y., Wu, W., Xie, X., Yin, W., Li, H., Liu, M., Xiao, Y., Gao, H., Guo, L., Xie, J., Wang, G., Jiang, R., Gao, Z., Jin, Q., Wang, J., Cao, B. Clinical features of patients infected with 2019 novel coronavirus in Wuhan, China. *Lancet* **395**, 497 (2020).
95. Wrapp, D., Wang, N., Corbett, K. S., Goldsmith, J. A., Hsieh, C. L., Abiona, O., Graham, B. S., McLellan, J. S. Cryo-EM structure of the 2019-nCoV spike in the prefusion conformation. *Science* **367**, 1260 (2020).
96. Li, F. Structure, Function, and Evolution of Coronavirus Spike Proteins. *Annual Review of Virology* **3**, 237 (2016).
97. Bosch, B. J., Zee, R.van der , Haan, C. A.de , Rottier, P. J. The coronavirus spike protein is a class I virus fusion protein: structural and functional characterization of the fusion core complex. *Journal of Virology* **77**, 8801 (2003).
98. Wan, Y., Shang, J., Graham, R., Baric, R. S., Li, F. Receptor Recognition by the Novel Coronavirus from Wuhan: an Analysis Based on Decade-Long Structural Studies of SARS Coronavirus. *Journal of Virology* , e00127 (2020).
99. Yan, R., Zhang, Y., Li, Y., Xia, L., Guo, Y., Zhou, Q. Structural basis for the recognition of SARS-CoV-2 by full-length human ACE2. *Science* **367**, 1444 (2020).
100. Wu, C., Liu, Y., Yang, Y., Zhang, P., Zhong, W., Wang, Y., Wang, Q., Xu, Y., Li, M., Li, X., Zheng, M., Chen, L., Li, H. Analysis of therapeutic targets for SARS-CoV-2 and discovery of potential drugs by computational methods. *Acta Pharmaceutica Sinica B* **10**, 766 (2020).

CITED LITERATURE (Continued)

101. Wang, J. Fast Identification of Possible Drug Treatment of Coronavirus Disease -19 (COVID-19) Through Computational Drug Repurposing Study. *Chemrxiv preprint*, (2020).
102. Leader, B., Baca, Q. J., Golan, D. E. Protein therapeutics: a summary and pharmacological classification. *Nature Reviews Drug Discovery* **7**, 21 (2008).
103. Bodier-Montagutelli, E., Mayor, A., Vecellio, L., Respaud, R., Heuz?-Vourc'h, N. Designing inhaled protein therapeutics for topical lung delivery: what are the next steps?. *Expert Opinion on Drug Delivery* **15**, 729 (2018).
104. Yao, H., Lu, X., Chen, Q., Xu, K., Chen, Y., Cheng, L., Liu, F., Wu, Z., Wu, H., Jin, C., Zheng, M., Wu, N., Jiang, C., Li, L. Patient-derived mutations impact pathogenicity of SARS-CoV-2. *medRxiv preprint*, 2020.04.14.20060160 (2020).
105. Ou, J., Zhou, Z., Dai, R., Zhang, J., Lan, W., Zhao, S., Wu, J., Seto, D., Cui, L., Zhang, G., Zhang, Q. Emergence of RBD mutations in circulating SARS-CoV-2 strains enhancing the structural stability and human ACE2 receptor affinity of the spike protein. *bioRxiv preprint*, 2020.03.15.991844 (2020).
106. Korber, B., Fischer, W. M., Gnanakaran, S., Yoon, H., Theiler, J., Abfalterer, W., Foley, B., Giorgi, E. E., Bhattacharya, T., Parker, M. D., Partridge, D. G., Evans, C. M., Freeman, T. M., Silva, T. I. de , LaBranche, C. C., Montefiori, D. C. Spike mutation pipeline reveals the emergence of a more transmissible form of SARS-CoV-2. *bioRxiv preprint*, 2020.04.29.069054 (2020).
107. Liu, Z., Xiao, X., Wei, X., Li, J., Yang, J., Tan, H., Zhu, J., Zhang, Q., Wu, J., Liu, L. Composition and divergence of coronavirus spike proteins and host ACE2 receptors predict potential intermediate hosts of SARS-CoV-2. *Journal of Medical Virology* **92**, 595 (2020).
108. Baum, A., Fulton, B. O., Wloga, E., Copin, R., Pascal, K. E., Russo, V., Giordano, S., Lanza, K., Negron, N., Ni, M., Wei, Y., Atwal, G. S., Murphy, A. J., Stahl, N., Yancopoulos, G. D., Kyratsous, C. A. cocktail to SARS-CoV-2 spike protein prevents rapid mutational escape seen with individual antibodies. *Science* **365**, 1014 (2020).
109. Grant, O. C., Montgomery, D., Ito, K., Woods, R. J. Analysis of the SARS-CoV-2 spike protein glycan shield: implications for immune recognition. *bioRxiv preprint*, 2020.04.07.030445 (2020).
110. Watanabe, Y., Allen, J. D., Wrapp, D., McLellan, J. S., Crispin, M. Site-specific glycan analysis of the SARS-CoV-2 spike. *Science* **369**, 330 (2020).

CITED LITERATURE (Continued)

111. Vankadari, N., Wilce, J. A. Emerging COVID-19 coronavirus: glycan shield and structure prediction of spike glycoprotein and its interaction with human CD26. *Emerging Microbes & Infections* **9**, 601 (2020).
112. Qiao, B., Cruz, M., Olvera de la Cruz, M. The Distal Polybasic Cleavage Sites of SARS-CoV-2 Spike Protein Enhance Spike Protein-ACE2 Binding. *bioRxiv preprint*, 2020.06.09.142877 (2020).
113. Wang, Q., Zhang, Y., Wu, L., Niu, S., Song, C., Zhang, Z., Lu, G., Qiao, C., Hu, Y., Yuen, K.-Y., Wang, Q., Zhou, H., Yan, J., Qi, J. Structural and Functional Basis of SARS-CoV-2 Entry by Using Human ACE2. *Cell* **181**, 894 (2020).
114. Darden, T., York, D., Pedersen, L. Particle mesh Ewald: An $N \log(N)$ method for Ewald sums in large systems. *The Journal of Chemical Physics* **98**, 10089 (1993).
115. Hadfield, J., Megill, C., Bell, S. M., Huddleston, J., Potter, B., Callender, C., Sagulenko, P., Bedford, T., Neher, R. A. Nextstrain: real-time tracking of pathogen evolution. *Bioinformatics* **34**, 4121 (2018).
116. Procko, E. The sequence of human ACE2 is suboptimal for binding the S spike protein of SARS coronavirus 2. *bioRxiv preprint*, 2020.03.16.994236 (2020).
117. Montgomery, J., Donnelly, J. A., Fanning, S. W., Speltz, T. E., Shangguan, X., Coukos, J. S., Greene, G. L., Moellering, R. E. Versatile Peptide Macrocyclization with Diels-Alder Cycloadditions. *Journal of the American Chemical Society* **141**, 16374 (2019).
118. Gil, C., Ginex, T., Maestro, I., Nozal, V., Barrado-Gil, L., Cuesta-Geijo, M. A., Urquiza, J., Ramírez, D., Alonso, C., Campillo, N. E., Martínez, A. COVID-19: Drug targets and potential treatments. *Journal of Medicinal Chemistry* **63**, 12359–12386 (2020).
119. Stawiski, E. W., Diwanji, D., Suryamohan, K., Gupta, R., Fellouse, F. A., Sathirapongsasuti, J. F., Liu, J., Jiang, Y.-P., Ratan, A., Mis, M., Santhosh, D., Somasekar, S., Mohan, S., Phalke, S., Kuriakose, B., Antony, A., Junutula, J. R., Schuster, S. C., Jura, N., Seshagiri, S. Human ACE2 receptor polymorphisms predict SARS-CoV-2 susceptibility. *bioRxiv preprint*, 2020.04.07.024752 (2020).
120. Belay, E. D., Kile, J. C., Hall, A. J., Barton-Behravesh, C., Parsons, M. B., Salyer, S., Walke, H. Zoonotic Disease Programs for Enhancing Global Health Security. *Emerging Infectious Diseases* **23**, S65 (2017).
121. Ali, I., Alharbi, O. M. L. COVID-19: Disease, management, treatment, and social impact. *Science of the Total Environment* **728**, 138861 (2020).

CITED LITERATURE (Continued)

122. Jeyanathan, M., Afkhami, S., Smaill, F., Miller, M. S., Lichty, B. D., Xing, Z. Immunological considerations for COVID-19 vaccine strategies. *Nature Reviews Immunology* **20**, 615 (2020).
123. Ledford, H. Coronavirus: Will the World Benefit From Antibody Therapies?. *Nature* **584**, 333 (2020).
124. Jahanshahlu, L., Rezaei, N. Monoclonal antibody as a potential anti-COVID-19. *Biomedicine & Pharmacotherapy* **129**, 110337 (2020).
125. Yoo, J. H. Uncertainty about the Efficacy of Remdesivir on COVID-19. *Journal of Korean Medical Science* **35**, e221 (2020).
126. Wu, R., Wang, L., Kuo, H. D., Shannar, A., Peter, R., Chou, P. J., Li, S., Hudlikar, R., Liu, X., Liu, Z., Poiani, G. J., Amorosa, L., Brunetti, L., Kong, A. N. An Update on Current Therapeutic Drugs Treating COVID-19. *Current Pharmacology Reports* **11**, 1 (2020).
127. Abd Ellah, N. H., Gad, S. F., Muhammad, K., EÂ Batiha, G., Hetta, H. F. Nanomedicine as a promising approach forÂ diagnosis, treatment and prophylaxis against COVID-19. *Nanomedicine* **15**, 2085 (2020).
128. Wu, C., Liu, Y., Yang, Y., Zhang, P., Zhong, W., Wang, Y., Wang, Q., Xu, Y., Li, M., Li, X., Zheng, M., Chen, L., Li, H. Analysis of therapeutic targets for SARS-CoV-2 and discovery of potential drugs by computational methods. *Acta Pharm. Sin. B* **10**, 766 (2020).
129. Cao, L., Goreshnik, I., Coventry, B., Case, J. B., Miller, L., Kozodoy, L., Chen, R. E., Carter, L., Walls, A. C., Park, Y.-J., Strauch, E.-M., Stewart, L., Diamond, M. S., Veisler, D., Baker, D. De novo design of picomolar SARS-CoV-2 miniprotein inhibitors. *Science* **370**, 426 (2020).
130. Humphrey, J. H. Antibodies-structure and biological function. *Journal of the Royal Society of Medicine* **60**, 591 (1967).
131. Eren, E., Watts, N. R., Dearborn, A. D., Palmer, I. W., Kaufman, J. D., Steven, A. C., Wingfield, P. T. Structures of Hepatitis B Virus Core- and e-Antigen Immune Complexes Suggest Multi-point Inhibition. *Structure* **26**, 1314 (2018).
132. Cagno, V., Tseligka, E. D., Jones, S. T., Tapparel, C. Heparan Sulfate Proteoglycans and Viral Attachment: True Receptors or Adaptation Bias?. *Viruses* **11**, (2019).
133. Ito, M., Baba, M., Sato, A., Pauwels, R., De Clercq, E., Shigeta, S. Inhibitory effect of dextran sulfate and heparin on the replication of human immunodeficiency virus (HIV) in vitro. *Antiviral Research* **7**, 361 (1987).

CITED LITERATURE (Continued)

134. Nakashima, H., Kido, Y., Kobayashi, N., Motoki, Y., Neushul, M., Yamamoto, N. Purification and characterization of an avian myeloblastosis and human immunodeficiency virus reverse transcriptase inhibitor, sulfated polysaccharides extracted from sea algae. *Antimicrobial Agents and Chemotherapy* **31**, 1524 (1987).
135. Hatanaka, K., Kurihara, Y., Uryu, T., Yoshida, O., Yamamoto, N., Mimura, T., Kaneko, Y. A strong inhibition of HIV-induced cytopathic effects by synthetic (1—6)-alpha-D-mannopyranan sulfate. *Carbohydrate Research* **214**, 147 (1991).
136. Katsuraya, K., Ikushima, N., Takahashi, N., Shoji, T., Nakashima, H., Yamamoto, N., Yoshida, T., Uryu, T. Synthesis of sulfated alkyl malto- and laminara-oligosaccharides with potent inhibitory effects on AIDS virus infection. *Carbohydrate Research* **260**, 51 (1994).
137. Meng, G., Wei, X., Wu, X., Sellers, M. T., Decker, J. M., Moldoveanu, Z., Orenstein, J. M., Graham, M. F., Kappes, J. C., Mestecky, J., Shaw, G. M., Smith, P. D. Primary intestinal epithelial cells selectively transfer R5 HIV-1 to CCR5+ cells. *Nature Medicine* **8**, 150 (2002).
138. Clayton, R., Hardman, J., LaBranche, C. C., McReynolds, K. D. Evaluation of the synthesis of sialic acid-PAMAM glycodendrimers without the use of sugar protecting groups, and the anti-HIV-1 properties of these compounds. *Bioconjugate Chemistry* **22**, 2186 (2011).
139. McReynolds, K. D., Gervay-Hague, J. Chemotherapeutic Interventions Targeting HIV Interactions with Host-Associated Carbohydrates. *Chemical Reviews* **107**, 1533 (2007).
140. Zhang, Q., Chen, C. Z., Swaroop, M., Xu, M., Wang, L., Lee, J., Pradhan, M., Shen, M., Luo, Z., Xu, Y., Huang, W., Zheng, W., Ye, Y. Targeting heparan sulfate proteoglycan-assisted endocytosis as a COVID-19 therapeutic option. *bioRxiv preprint*, (2020).
141. Spillmann, D. Heparan sulfate: Anchor for viral intruders?. *Biochimie* **83**, 811 (2001).
142. Choi, Y., Chung, H., Jung, H., Couchman, J. R., Oh, E.-S. Syndecans as cell surface receptors: Unique structure equates with functional diversity. *Matrix Biology* **30**, 93 (2011).
143. Kamhi, E., Joo, E. J., Dordick, J. S., Linhardt, R. J. Glycosaminoglycans in infectious disease. *Biological Reviews* **88**, 928 (2013).
144. Lee, J. H., Andrabi, R., Su, C. Y., Yasmeen, A., Julien, J. P., Kong, L., Wu, N. C., McBride, R., Sok, D., Pauthner, M., Cottrell, C. A., Nieusma, T., Blattner, C., Paulson, J. C., Klasse, P. J., Wilson, I. A., Burton, D. R., Ward, A. B. A Broadly Neutralizing Antibody Targets the Dynamic HIV Envelope Trimer Apex via a Long, Rigidified, and Anionic Î²-Hairpin Structure. *Immunity* **46**, 690 (2017).

CITED LITERATURE (Continued)

145. Feinberg, H., Castelli, R., Drickamer, K., Seeberger, P., Weis, W. Multiple modes of binding enhance the affinity of DC-SIGN for high mannose N-linked glycans found on viral glycoproteins. *Journal of Biological Chemistry* **282**, 4202 (2007).
146. Hao, W., Ma, B., Li, Z., Wang, X., Gao, X., Li, Y., Qin, B., Shang, S., Cui, S., Tan, Z. Binding of the SARS-CoV-2 Spike Protein to Glycans. *bioRxiv preprint*, 10.1101/2020.05.17.100537 (2020).
147. Kim, S. Y., Jin, W., Sood, A., Montgomery, D. W., Grant, O. C., Fuster, M. M., Fu, L., Dordick, J. S., Woods, R. J., Zhang, F., Linhardt, R. J. Glycosaminoglycan binding motif at S1/S2 proteolytic cleavage site on spike glycoprotein may facilitate novel coronavirus (SARS-CoV-2) host cell entry. *bioRxiv preprint*, 10.1101/2020.04.14.041459 (2020).
148. Mycroft-West, C., Su, D., Elli, S., Guimond, S., Miller, G., Turnbull, J., Yates, E., Guerrini, M., Fernig, D., Lima, M., Skidmore, M. The 2019 coronavirus (SARS-CoV-2) surface protein (Spike) S1 Receptor Binding Domain undergoes conformational change upon heparin binding. *bioRxiv preprint*, 2020.02.29.971093 (2020).
149. Ribas, A., Wolchok, J. D. Cancer immunotherapy using checkpoint blockade. *Science* **359**, 1350 (2018).
150. Tang, J., Yu, J. X., Hubbard-Lucey, V. M., Neftelinov, S. T., Hodge, J. P., Lin, Y. Trial watch: The clinical trial landscape for PD1/PDL1 immune checkpoint inhibitors. *Nature Reviews Drug Discovery* **17**, 854 (2018).
151. Tang, H., Liang, Y., Anders, R. A., Taube, J. M., Qiu, X., Mulgaonkar, A., Liu, X., Harrington, S. M., Guo, J., Xin, Y., Xiong, Y., Nham, K., Silvers, W., Hao, G., Sun, X., Chen, M., Hannan, R., Qiao, J., Dong, H., Peng, H., Fu, Y. X. PD-L1 on host cells is essential for PD-L1 blockade-mediated tumor regression. *Journal of Clinical Investigation* **128**, 580 (2018).
152. Crews, C. M. Targeting the undruggable proteome: the small molecules of my dreams. *Chemistry & Biology* **17**, 551 (2010).
153. Leader, B., Baca, Q. J., Golan, D. E. Protein therapeutics: a summary and pharmacological classification. *Nature Reviews Drug Discovery* **7**, 21 (2008).
154. Lau, J. L., Dunn, M. K. Therapeutic peptides: Historical perspectives, current development trends, and future directions. *Bioorganic & Medicinal Chemistry* **26**, 2700 (2018).
155. Jeong, W.-j., Choi, S.-H., Jin, K. S., Lim, Y.-b. Tuning Oligovalent Biomacromolecular Interfaces Using Double-Layered α -Helical Coiled-Coil Nanoassemblies from Lariat-Type Building Blocks. *ACS Macro Letters* **5**, 1406 (2016).

CITED LITERATURE (Continued)

156. Klein, M. Stabilized helical peptides: overview of the technologies and its impact on drug discovery. *Expert Opinion on Drug Discovery* **12**, 1117 (2017).
157. Jeong, W. J., Choi, S. J., Choi, J. S., Lim, Y. B. Chameleon-like self-assembling peptides for adaptable biorecognition nanohybrids. *ACS Nano* **7**, 6850 (2013).
158. Watkins, A. M., Arora, P. S. Anatomy of β -strands at protein-protein interfaces. *ACS Chemical Biology* **9**, 1747 (2014).
159. Khakshoor, O., Demeler, B., Nowick, J. S. Macrocyclic β -Sheet Peptides That Mimic Protein Quaternary Structure through Intermolecular β -Sheet Interactions. *Journal of the American Chemical Society* **129**, 5558 (2007).
160. Maute, R. L., Gordon, S. R., Mayer, A. T., McCracken, M. N., Natarajan, A., Ring, N. G., Kimura, R., Tsai, J. M., Manglik, A., Kruse, A. C., Gambhir, S. S., Weissman, I. L., Ring, A. M. Engineering high-affinity PD-1 variants for optimized immunotherapy and immuno-PET imaging. *Proceedings of the National Academy of Sciences of the United States of America* **112**, E6506 (2015).
161. Pascolutti, R., Sun, X., Kao, J., Maute, R. L., Ring, A. M., Bowman, G. R., Kruse, A. C. Structure and Dynamics of PD-L1 and an Ultra-High-Affinity PD-1 Receptor Mutant. *Structure* **24**, 1719 (2016).
162. De Clercq, E. Strategies in the design of antiviral drugs. *Nature Reviews Drug Discovery* **1**, 13 (2002).
163. McCormack, S., Ramjee, G., Kamali, A., Rees, H., Crook, A. M., Gafos, M., Jentsch, U., Pool, R., Chisembele, M., Kapiga, S., Mutemwa, R., Vallely, A., Palanee, T., Sookrajh, Y., Lacey, C. J., Darbyshire, J., Grosskurth, H., Profy, A., Nunn, A., Hayes, R., Weber, J. PRO2000 vaginal gel for prevention of hiv-1 infection (microbicides development programme 301): A phase 3, randomised, double-blind, parallel-group trial. *Lancet* **376**, 1329 (2010).
164. Pirrone, V., Wigdahl, B., Krebs, F. C. The rise and fall of polyanionic inhibitors of the human immunodeficiency virus type 1. *Antiviral Research* **90**, 168 (2011).
165. Van Damme, L., Govinden, R., Mirembe, F. M., Guedou, F., Solomon, S., Becker, M. L., Pradeep, B. S., Krishnan, A. K., Alary, M., Pande, B., Ramjee, G., Deese, J., Crucitti, T., Taylor, D., Murphy, S., Wahala, L., Callahan, M., Gabelnick, H., Acevedo, N., Johnson, L., Dube, K., Chalkley, L., Carayon-Lefebvre d'Hellencourt, F., Combes, S., Commins, M., Tolley, E., Corneli, A., Law, M., Rountree, W., Saylor, L., Fransen, K., Beelaert, G., Abdellati, S., Mangelschots, M., Buv?, A., Moses, S., Blanchard, J., Washington, R. G., Satyanarayana, R., Mendonca, K., Minani, I., Massinga Loemb?,

CITED LITERATURE (Continued)

- M., Anagonou, S., Geraldo, N., Ganesh, A. K., Johnson, S., Vasudevan, C. K., Murugavel, K. G., Edward, V., Raju, E., Singh, R., Vasant, U., Khoza, N., Ganesh, S., Nakabiito, C., Nakintu, N., Tenywa, T., Musuuza, C., Nagganda, J., Nakimuli, M., Gati, B., Kagoda, J., Kaddu, R., Kintu, G., Luzze, M., Saunders, C. Lack of effectiveness of cellulose sulfate gel for the prevention of vaginal HIV transmission. *The New England Journal of Medicine* **359**, 463 (2008).
166. Rusnati, M., Vicenzi, E., Donalisio, M., Oreste, P., Landolfo, S., Lembo, D. Sulfated K5 Escherichia coli polysaccharide derivatives: A novel class of candidate antiviral microbicides. *Pharmacology & Therapeutics* **123**, 310 (2009).
167. Baram-Pinto, D., Shukla, S., Gedanken, A., Sarid, R. Inhibition of HSV-1 attachment, entry, and cell-to-cell spread by functionalized multivalent gold nanoparticles. *Small (Weinheim an der Bergstrasse, Germany)* **6**, 1044 (2010).
168. Abe, M., Kaneko, K., Ueda, A., Otsuka, H., Shiosaki, K., Nozaki, C., Goto, S. Effects of several virucidal agents on inactivation of influenza, Newcastle disease, and avian infectious bronchitis viruses in the allantoic fluid of chicken eggs. *Japanese Journal of Infectious Diseases* **60**, 342 (2007).
169. Haute, D. V., Berlin, J. M. Challenges in realizing selectivity for nanoparticle biodistribution and clearance: lessons from gold nanoparticles. *Therapeutic Delivery* **8**, 763 (2017).
170. Davis, M. E., Brewster, M. E. Cyclodextrin-based pharmaceuticals: past, present and future. *Nat Rev Drug Discov* **3**, 1023 (2004).
171. Anand, R., Nayyar, S., Pitha, J., Merril, C. R. Sulphated Sugar Alpha-Cyclodextrin Sulphate, a Uniquely Potent Anti-HIV Agent, Also Exhibits Marked Synergism with AZT, and Lymphoproliferative Activity. *Antiviral Chemistry and Chemotherapy* **1**, 41 (1990).
172. Moriya, T., Kurita, H., Matsumoto, K., Otake, T., Mori, H., Morimoto, M., Ueba, N., Kunita, N. Potent inhibitory effect of a series of modified cyclodextrin sulfates (mCDS) on the replication of HIV-1 in vitro. *Journal of Medicinal Chemistry* **34**, 2301 (1991).
173. Otake, T., Schols, D., Witvrouw, M., Naesens, L., Nakashima, H., Moriya, T., Kurita, H., Matsumoto, K., Ueba, N., Clercq, E. D. Modified Cyclodextrin Sulphates(mCDS11) have Potent Inhibitory Activity against HIV and High Oral Bioavailability. *Antiviral Chemistry and Chemotherapy* **5**, 155 (1994).
174. Dasgupta, J., Bienkowska-Haba, M., Ortega, M. E., Patel, H. D., Bodevin, S., Spillmann, D., Bishop, B., Sapp, M., Chen, X. S. Structural basis of oligosaccharide receptor recognition by human papillomavirus. *Journal of Biological Chemistry* **286**, 2617 (2011).

CITED LITERATURE (Continued)

175. Melcrov?, A., Pokorna, S., Pullanchery, S., Kohagen, M., Jurkiewicz, P., Hof, M., Jungwirth, P., Cremer, P. S., Cwiklik, L. The complex nature of calcium cation interactions with phospholipid bilayers. *Scientific Reports* **6**, 38035 (2016).
176. Zeev-Ben-Mordehai, T., Vasishtan, D., Hernandez Duran, A., Vollmer, B., White, P., Prasad Pandurangan, A., Siebert, C. A., Topf, M., Grunewald, K. Two distinct trimeric conformations of natively membrane-anchored full-length herpes simplex virus 1 glycoprotein B. *Proceedings of the National Academy of Sciences of the United States of America* **113**, 4176 (2016).
177. Hannah, B. P., Cairns, T. M., Bender, F. C., Whitbeck, J. C., Lou, H., Eisenberg, R. J., Cohen, G. H. Herpes simplex virus glycoprotein B associates with target membranes via its fusion loops. *Journal of Virology* **83**, 6825 (2009).
178. Mammen, M., Choi, S. K., Whitesides, G. M. Polyvalent Interactions in Biological Systems: Implications for Design and Use of Multivalent Ligands and Inhibitors. *Angewandte Chemie* **37**, 2754 (1998).
179. Weis, W. I., Taylor, M. E., Drickamer, K. The C-type lectin superfamily in the immune system. *Immunological Reviews* **163**, 19 (1998).
180. Lundquist, J. J., Toone, E. J. The cluster glycoside effect. *Chemical Reviews* **102**, 555 (2002).
181. Wolfert, M. A., Boons, G. J. Adaptive immune activation: glycosylation does matter. *Nature Chemical Biology* **9**, 776 (2013).
182. Geijtenbeek, T. B., Torensma, R., Vliet, S. J. van, Duijnhoven, G. C. van, Adema, G. J., Kooyk, Y. van, Figdor, C. G. Identification of DC-SIGN, a novel dendritic cell-specific ICAM-3 receptor that supports primary immune responses. *Cell* **100**, 575 (2000).
183. Kooyk, Y. van, Geijtenbeek, T. B. DC-SIGN: escape mechanism for pathogens. *Nature Reviews Immunology* **3**, 697 (2003).
184. Geijtenbeek, T. B., Kwon, D. S., Torensma, R., Vliet, S. J. van, Duijnhoven, G. C. van, Middel, J., Cornelissen, I. L., Nottet, H. S., KewalRamani, V. N., Littman, D. R., Figdor, C. G., Kooyk, Y. van DC-SIGN, a dendritic cell-specific HIV-1-binding protein that enhances trans-infection of T cells. *Cell* **100**, 587 (2000).
185. Chung, N. P., Breun, S. K., Bashirova, A., Baumann, J. G., Martin, T. D., Karamchandani, J. M., Rausch, J. W., Le Grice, S. F., Wu, L., Carrington, M., Kewalramani, V. N. HIV-1 transmission by dendritic cell-specific ICAM-3-grabbing nonintegrin (DC-SIGN) is regulated by determinants in the carbohydrate recognition domain that are absent in liver/lymph node-SIGN (L-SIGN). *Journal of Biological Chemistry* **285**, 2100 (2010).

CITED LITERATURE (Continued)

186. Messina, M. S., Axtell, J. C., Wang, Y., Chong, P., Wixtrom, A. I., Kirlikovali, K. O., Upton, B. M., Hunter, B. M., Shafaat, O. S., Khan, S. I., Winkler, J. R., Gray, H. B., Alexandrova, A. N., Maynard, H. D., Spokoyny, A. M. Visible-Light-Induced Olefin Activation Using 3D Aromatic Boron-Rich Cluster Photooxidants. *Journal of the American Chemical Society* **138**, 6952 (2016).
187. Borrok, M. J., Kiessling, L. L. Non-carbohydrate inhibitors of the lectin DC-SIGN. *Journal of the American Chemical Society* **129**, 12780 (2007).
188. Loris, R., Maes, D., Poortmans, F., Wyns, L., Bouckaert, J. A structure of the complex between concanavalin A and methyl-3,6-di-O-(alpha-D-mannopyranosyl)-alpha-D-mannopyranoside reveals two binding modes. *Journal of Biological Chemistry* **271**, 30614 (1996).
189. Feinberg, H., Mitchell, D. A., Drickamer, K., Weis, W. I. Structural basis for selective recognition of oligosaccharides by DC-SIGN and DC-SIGNR. *Science* **294**, 2163 (2001).
190. Cross, D., Burmester, J. K. Gene therapy for cancer treatment: past, present and future. *Clinical Medicine & Research* **4**, 218 (2006).
191. Pack, D. W., Hoffman, A. S., Pun, S., Stayton, P. S. Design and development of polymers for gene delivery. *Nature Reviews Drug Discovery* **4**, 581 (2005).
192. Putnam, D. Polymers for gene delivery across length scales. *Nature Materials* **5**, 439 (2006).
193. Geary, R. S., Norris, D., Yu, R., Bennett, C. F. Pharmacokinetics, biodistribution and cell uptake of antisense oligonucleotides. *Advanced Drug Delivery Reviews* **87**, 46 (2015).
194. Kay, M. A., Glorioso, J. C., Naldini, L. Viral vectors for gene therapy: the art of turning infectious agents into vehicles of therapeutics. *Nature Medicine* **7**, 33 (2001).
195. Baum, C., Kustikova, O., Modlich, U., Li, Z., Fehse, B. Mutagenesis and oncogenesis by chromosomal insertion of gene transfer vectors. *Human Gene Therapy* **17**, 253 (2006).
196. Thomas, C. E., Ehrhardt, A., Kay, M. A. Progress and problems with the use of viral vectors for gene therapy. *Nature Reviews Genetics* **4**, 346 (2003).
197. Bessis, N., GarciaCozar, F. J., Boissier, M. C. Immune responses to gene therapy vectors: influence on vector function and effector mechanisms. *Gene therapy* **11**, S10 (2004).
198. Boussif, O., Lezoualc'h, F., Zanta, M. A., Mergny, M. D., Scherman, D., Demeneix, B., Behr, J. P. A versatile vector for gene and oligonucleotide transfer into cells in culture and in vivo: polyethylenimine. *Proceedings of the National Academy of Sciences of the United States of America* **92**, 7297 (1995).

CITED LITERATURE (Continued)

199. Whitehead, K. A., Langer, R., Anderson, D. G. Knocking down barriers: advances in siRNA delivery. *Nature Reviews Drug Discovery* **8**, 129 (2009).
200. Matini, T., Francini, N., Battocchio, A., Spain, S. G., Mantovani, G., Vicent, M. J., Sanchis, J., Gallon, E., Mastrotto, F., Salmaso, S., Caliceti, P., Alexander, C. Synthesis and characterization of variable conformation pH responsive block co-polymers for nucleic acid delivery and targeted cell entry. *Polymer Chemistry* **5**, 1626 (2014).
201. Duncan, R., Gaspar, R. Nanomedicine(s) under the microscope. *Molecular Pharmaceutics* **8**, 2101 (2011).
202. Marguet, M., Bonduelle, C., Lecommandoux, S. Multicompartmentalized polymeric systems: towards biomimetic cellular structure and function. *Chemical Society Reviews* **42**, 512 (2013).
203. Nelson, C. E., Kintzing, J. R., Hanna, A., Shannon, J. M., Gupta, M. K., Duvall, C. L. Balancing cationic and hydrophobic content of PEGylated siRNA polyplexes enhances endosome escape, stability, blood circulation time, and bioactivity in vivo. *ACS Nano* **7**, 8870 (2013).
204. Matsumura, Y., Maeda, H. A new concept for macromolecular therapeutics in cancer chemotherapy: mechanism of tumorotropic accumulation of proteins and the antitumor agent smancs. *Cancer Research* **46**, 6387 (1986).
205. Ikeda, Y., Nagasaki, Y. Impacts of PEGylation on the gene and oligonucleotide delivery system. *Journal of Applied Polymer Science* **131**, 40293 (2014).
206. Mann, A., Richa, R., Ganguli, M. DNA condensation by poly-L-lysine at the single molecule level: role of DNA concentration and polymer length. *Journal of Controlled Release* **125**, 252 (2008).
207. Zhao, Y., Wang, Y., Ran, F., Cui, Y., Liu, C., Zhao, Q., Gao, Y., Wang, D., Wang, S. A comparison between sphere and rod nanoparticles regarding their in vivo biological behavior and pharmacokinetics. *Scientific Reports* **7**, 4131 (2017).
208. Gratton, S. E., Ropp, P. A., Pohlhaus, P. D., Luft, J. C., Madden, V. J., Napier, M. E., DeSimone, J. M. The effect of particle design on cellular internalization pathways. *Proceedings of the National Academy of Sciences of the United States of America* **105**, 11613 (2008).
209. Kolhar, P., Anselmo, A. C., Gupta, V., Pant, K., Prabhakarpanth, B., Ruoslahti, E., Mitragotri, S. Using shape effects to target antibody-coated nanoparticles to lung and brain endothelium. *Proceedings of the National Academy of Sciences* **110**, 10753 (2013).

CITED LITERATURE (Continued)

210. Lee, C. C., MacKay, J. A., Fréchet, J. M., Szoka, F. C. Designing dendrimers for biological applications. *Nature Biotechnology* **23**, 1517 (2005).
211. Peer, D., Karp, J. M., Hong, S., Farokhzad, O. C., Margalit, R., Langer, R. Nanocarriers as an emerging platform for cancer therapy. *Nature Nanotechnology* **2**, 751 (2007).
212. Duncan, R. The dawning era of polymer therapeutics. *Nature Reviews Drug Discovery* **2**, 347 (2003).
213. Wurm, F., Frey, H. Linear–dendritic block copolymers: The state of the art and exciting perspectives. *Progress in Polymer Science* **36**, 1 (2011).
214. Cedervall, T., Lynch, I., Lindman, S., Berggård, T., Thulin, E., Nilsson, H., Dawson, K. A., Linse, S. Understanding the nanoparticle–protein corona using methods to quantify exchange rates and affinities of proteins for nanoparticles. *Proceedings of the National Academy of Sciences* **104**, 2050 (2007).
215. Pearson, R. M., Juettner, V. V., Hong, S. Biomolecular corona on nanoparticles: a survey of recent literature and its implications in targeted drug delivery. *Frontiers in Chemistry* **2**, 108 (2014).
216. Kim, S., Shi, Y., Kim, J. Y., Park, K., Cheng, J. X. Overcoming the barriers in micellar drug delivery: loading efficiency, in vivo stability, and micelle–cell interaction. *Expert Opinion on Drug Delivery* **7**, 49 (2010).
217. Dai, Q., Walkey, C., Chan, W. C. Polyethylene glycol backfilling mitigates the negative impact of the protein corona on nanoparticle cell targeting. *Angewandte Chemie* **53**, 5093 (2014).
218. Salvati, A., Pitek, A. S., Monopoli, M. P., Prapainop, K., Bombelli, F. B., Hristov, D. R., Kelly, P. M., Aberg, C., Mahon, E., Dawson, K. A. Transferrin-functionalized nanoparticles lose their targeting capabilities when a biomolecule corona adsorbs on the surface. *Nature Nanotechnology* **8**, 137 (2013).
219. Pearson, R. M., Sen, S., Hsu, H.-j., Pasko, M., Gaske, M., Král, P., Hong, S. Tuning the Selectivity of Dendron Micelles Through Variations of the Poly(ethylene glycol) Corona. *ACS Nano* **10**, 6905 (2016).
220. Chen, H., Kim, S., Li, L., Wang, S., Park, K., Cheng, J. X. Release of hydrophobic molecules from polymer micelles into cell membranes revealed by Forster resonance energy transfer imaging. *Proceedings of the National Academy of Sciences of the United States of America* **105**, 6596 (2008).
221. Owen, S. C., Chan, D. P., Shoichet, M. S. Polymeric micelle stability. *Nano Today* **7**, 53 (2012).

CITED LITERATURE (Continued)

222. Oerlemans, C., Bult, W., Bos, M., Storm, G., Nijssen, J. F., Hennink, W. E. Polymeric micelles in anticancer therapy: targeting, imaging and triggered release. *Pharmaceutical Research* **27**, 2569 (2010).
223. Deng, C., Jiang, Y., Cheng, R., Meng, F., Zhong, Z. Biodegradable polymeric micelles for targeted and controlled anticancer drug delivery: Promises, progress and prospects. *Nano Today* **7**, 467 (2012).
224. Cabral, H., Kataoka, K. Progress of drug-loaded polymeric micelles into clinical studies. *Journal of Controlled Release* **190**, 465 (2014).
225. Biswas, S., Kumari, P., Lakhani, P. M., Ghosh, B. Recent advances in polymeric micelles for anti-cancer drug delivery. *European Journal of Pharmaceutical Sciences* **83**, 184 (2016).
226. Hsu, H.-j., Sen, S., Pearson, R. M., Uddin, S., Král, P., Hong, S. Poly(ethylene glycol) Corona Chain Length Controls End-Group-Dependent Cell Interactions of Dendron Micelles. *Macromolecules* **47**, 6911 (2014).
227. Logie, J., Owen, S. C., McLaughlin, C. K., Shoichet, M. S. PEG-Graft Density Controls Polymeric Nanoparticle Micelle Stability. *Chemistry of Materials* **26**, 2847 (2014).
228. Bae, J. W., Pearson, R. M., Patra, N., Sunoqrot, S., Vukovic, L., Král, P., Hong, S. Dendron-mediated self-assembly of highly PEGylated block copolymers: a modular nanocarrier platform. *Chemical Communications* **47**, 10302 (2011).
229. Miller, T., Rachel, R., Besheer, A., Uezguen, S., Weigandt, M., Goepferich, A. Comparative investigations on in vitro serum stability of polymeric micelle formulations. *Pharmaceutical Research* **29**, 448 (2012).
230. Metelev, V., Zhang, S., Zheng, S., Kumar, A. T. N., Bogdanov, A. Fluorocarbons Enhance Intracellular Delivery of Short STAT3-sensors and Enable Specific Imaging. *Theranostics* **7**, 3354 (2017).
231. Dafik, L., Kalsani, V., Leung, A. K. L., Kumar, K. Fluorinated Lipid Constructs Permit Facile Passage of Molecular Cargo into Living Cells. *Journal of the American Chemical Society* **131**, 12091 (2009).
232. Gross, C., Koelch, W., DeMaio, A., Arispe, N., Multhoff, G. Cell surface-bound heat shock protein 70 (Hsp70) mediates perforin-independent apoptosis by specific binding and uptake of granzyme B. *Journal of Biological Chemistry* **278**, 41173 (2003).
233. Multhoff, G., Hightower, L. E. Distinguishing integral and receptor-bound heat shock protein 70 (Hsp70) on the cell surface by Hsp70-specific antibodies. *Cell Stress Chaperones* **16**, 251 (2011).

CITED LITERATURE (Continued)

234. Yang, J., Nune, M., Zong, Y., Zhou, L., Liu, Q. Close and Allosteric Opening of the Polypeptide-Binding Site in a Human Hsp70 Chaperone BiP. *Structure* **23**, 2191 (2015).
235. Balchin, D., Hayer-Hartl, M., Hartl, F. U. In vivo aspects of protein folding and quality control. *Science* **353**, aac4354 (2016).
236. Van Lehn, R. C., Alexander-Katz, A. Pathway for insertion of amphiphilic nanoparticles into defect-free lipid bilayers from atomistic molecular dynamics simulations. *Soft Matter* **11**, 3165 (2015).
237. Van Lehn, R. C., Ricci, M., Silva, P. H., Andreozzi, P., Reguera, J., Voitchovsky, K., Stellacci, F., Alexander-Katz, A. Lipid tail protrusions mediate the insertion of nanoparticles into model cell membranes. *Nature Communications* **5**, 4482 (2014).
238. Patra, N., Wang, B., Král, P. Nanodroplet Activated and Guided Folding of Graphene Nanostructures. *Nano Letters* **9**, 3766 (2009).
239. Patra, N., Song, Y., Král, P. Self-Assembly of Graphene Nanostructures on Nanotubes. *ACS Nano* **5**, 1798 (2011).
240. Cohen, E., Weissman, H., Pinkas, I., Shimoni, E., Rehak, P., Král, P., Rybtchinski, B. Controlled Self-Assembly of Photofunctional Supramolecular Nanotubes. *ACS Nano* **12**, 317 (2018).
241. Grzelczak, M., Liz-Marzán, L. M., Klajn, R. Stimuli-responsive self-assembly of nanoparticles. *Chemical Society Reviews* **48**, 1342 (2019).
242. Clark, B. D., Molina, A. R., Martin, G. G., Wang, J. W., Spain, E. M. Au nanoparticle clusters from deposition of a coalescing emulsion. *Journal of Colloid and Interface Science* **450**, 417 (2015).
243. Bera, M. K., Chan, H., Moyano, D. F., Yu, H., Tatur, S., Amoanu, D., Bu, W., Rotello, V. M., Meron, M., Král, P., Lin, B., Schlossman, M. L. Interfacial Localization and Voltage-Tunable Arrays of Charged Nanoparticles. *Nano Letters* **14**, 6816 (2014).
244. Miyajima, D., Tashiro, K., Araoka, F., Takezoe, H., Kim, J., Kato, K., Takata, M., Aida, T. Liquid Crystalline Corannulene Responsive to Electric Field. *Journal of the American Chemical Society* **131**, 44 (2009).
245. Geim, A. K., Grigorieva, I. V. Van der Waals heterostructures. *Nature* **499**, 419 (2013).
246. Pearson, R. G. Hard and Soft Acids and Bases. *Journal of the American Chemical Society* **85**, 3533 (1963).

CITED LITERATURE (Continued)

247. Zheng, J., Luo, C., Shabbir, B., Wang, C., Mao, W., Zhang, Y., Huang, Y., Dong, Y., Jasieniak, J. J., Pan, C., Bao, Q. Flexible photodetectors based on reticulated SWNT/perovskite quantum dot heterostructures with ultrahigh durability. *Nanoscale* **11**, 8020 (2019).
248. Frisch, M. J., Trucks, G. W., Schlegel, H. B., Scuseria, G. E., Robb, M. A., Cheeseman, J. R., Scalmani, G., Barone, V., Mennucci, B., Petersson, G. A., Nakatsuji, H., Caricato, M., Li, X., Hratchian, H. P., Izmaylov, A. F., Bloino, J., Zheng, G., Sonnenberg, J. L., Hada, M., Ehara, M., Toyota, K., Fukuda, R., Hasegawa, J., Ishida, M., Nakajima, T., Honda, Y., Kitao, O., H. Nakai, a. T. V., Montgomery, J. A., Jr., J. E. P., Ogliaro, F., Bearpark, M., Heyd, J. J., Brothers, E., Kudin, K. N., Staroverov, V. N., Kobayashi, R., Normand, J., Raghavachari, K., Rendell, A., Burant, J. C., Iyengar, S. S., Tomasi, J., Cossi, M., Rega, N., Millam, J. M., Klene, M., Knox, J. E., Cross, J. B., Bakken, V., Adamo, C., Jaramillo, J., Gomperts, R., Stratmann, R. E., Yazyev, O., Austin, A. J., Cammi, R., Pomelli, C., Ochterski, J. W., Martin, R. L., Morokuma, K., Zakrzewski, V. G., Voth, G. A., Salvador, P., Dannenberg, J. J., Dapprich, S., Daniels, A. D., Farkas, O., Foresman, J. B., Ortiz, J. V., Cioslowski, J., Fox, D. J., Gaussian 09 Revision C.01 (2009). Gaussian Inc. Wallingford CT.
249. Brooks, B. R., Brooks, C. L., Mackerell, A. D., Nilsson, L., Petrella, R. J., Roux, B., Won, Y., Archontis, G., Bartels, C., Boresch, S., Caffisch, A., Caves, L., Cui, Q., Dinner, A. R., Feig, M., Fischer, S., Gao, J., Hodoscek, M., Im, W., Kuczera, K., Lazaridis, T., Ma, J., Ovchinnikov, V., Paci, E., Pastor, R. W., Post, C. B., Pu, J. Z., Schaefer, M., Tidor, B., Venable, R. M., Woodcock, H. L., Wu, X., Yang, W., York, D. M., Karplus, M. CHARMM: the biomolecular simulation program. *Journal of Computational Chemistry* **30**, 1545 (2009).
250. Parrish, R. M., Burns, L. A., Smith, D. G. A., Simmonett, A. C., DePrince, A. E., Hohenstein, E. G., Bozkaya, U., Sokolov, A. Y., Di Remigio, R., Richard, R. M., Gonthier, J. F., James, A. M., McAlexander, H. R., Kumar, A., Saitow, M., Wang, X., Pritchard, B. P., Verma, P., Schaefer, H. F., Patkowski, K., King, R. A., Valeev, E. F., Evangelista, F. A., Turney, J. M., Crawford, T. D., Sherrill, C. D. Psi4 1.1: An Open-Source Electronic Structure Program Emphasizing Automation, Advanced Libraries, and Interoperability. *Journal of Chemical Theory and Computation* **13**, 3185 (2017).
251. Tsuzuki, S., Honda, K., Uchimaru, T., Mikami, M., Tanabe, K. Origin of Attraction and Directionality of the π - π Interaction:â€‰ Model Chemistry Calculations of Benzene Dimer Interaction. *Journal of the American Chemical Society* **124**, 104 (2002).
252. Williams, J. H., Cockcroft, J. K., Fitch, A. N. Structure of the Lowest Temperature Phase of the Solid Benzene-Hexafluorobenzene Adduct. *Angewandte Chemie International Edition in English* **31**, 1655 (1992).
253. Spano, F. C. The Spectral Signatures of Frenkel Polarons in H- and J-Aggregates. *Accounts of Chemical Research* **43**, 429 (2010).

CITED LITERATURE (Continued)

254. Chai, J.-D., Head-Gordon, M. Long-range corrected hybrid density functionals with damped atom-atom dispersion corrections. *Physical Chemistry Chemical Physics* **10**, 6615 (2008).
255. Chai, J. D., Head-Gordon, M. Systematic optimization of long-range corrected hybrid density functionals. *The Journal of Chemical Physics* **128**, 084106 (2008).
256. Kumar Tummanapelli, A., Vasudevan, S. Communication: Benzene dimer-The free energy landscape. *The Journal of Chemical Physics* **139**, 201102 (2013).
257. Hwang, J., Dial, B. E., Li, P., Kozik, M. E., Smith, M. D., Shimizu, K. D. How important are dispersion interactions to the strength of aromatic stacking interactions in solution?. *Chemical Science* **6**, 4358 (2015).
258. Palonc yov , M., Langer, M., Otyepka, M. Structural Dynamics of Carbon Dots in Water and N,N-Dimethylformamide Probed by All-Atom Molecular Dynamics Simulations. *Journal of Chemical Theory and Computation* **14**, 2076 (2018).
259. Wang, S., Urban, M. Self-healing polymers. *Nature Reviews Materials* **5**, 562 (2020).
260. Schliwa, M., Woehlke, G. Molecular motors. *Nature* **422**, 759 (2003).
261. Kinbara, K., Aida, T. Toward Intelligent Molecular Machines: Directed Motions of Biological and Artificial Molecules and Assemblies. *Chemical Reviews* **105**, 1377 (2005).
262. Wickham, S. F. J., Endo, M., Katsuda, Y., Hidaka, K., Bath, J., Sugiyama, H., Turberfield, A. J. Direct observation of stepwise movement of a synthetic molecular transporter. *Nature Nanotechnology* **6**, 166 (2011).
263. Gu, H., Chao, J., Xiao, S.-J., Seeman, N. C. A proximity-based programmable DNA nanoscale assembly line. *Nature* **465**, 202 (2010).
264. Delius, M.von , Geertsema, E. M., Leigh, D. A. A synthetic small molecule that can walk down a track. *Nature Chemistry* **2**, 96 (2010).
265. Kopperger, E., Pirzer, T., Simmel, F. C. Diffusive Transport of Molecular Cargo Tethered to a DNA Origami Platform. *Nano Letters* **15**, 2693 (2015).
266. Perl, A., Gomez-Casado, A., Thompson, D., Dam, H. H., Jonkh ijm, P., Reinhoudt, D. N., Huskens, J. Gradient-driven motion of multivalent ligand molecules along a surface functionalized with multiple receptors. *Nature Chemistry* **3**, 317 (2011).
267. Givaty, O., Levy, Y. Protein Sliding along DNA: Dynamics and Structural Characterization. *Journal of Molecular Biology* **385**, 1087 (2009).

CITED LITERATURE (Continued)

268. Giorgino, T. Computing diffusion coefficients in macromolecular simulations: the Diffusion Coefficient Tool for VMD. *GitHub* **22**, (2015).
269. Zhang, D., Gullingsrud, J., McCammon, J. A. Potentials of mean force for acetylcholine unbinding from the $\alpha 7$ nicotinic acetylcholine receptor ligand-binding domain. *Journal of the American Chemical Society* **128**, 3019 (2006).
270. Liu, X., Li, H., Jin, Q., Ji, J. Surface Tailoring of Nanoparticles via Mixed-Charge Monolayers and Their Biomedical Applications. *Small* **10**, 4230 (2014).
271. Klajn, R. Immobilized azobenzenes for the construction of photoresponsive materials. *Pure and Applied Chemistry* **82**, 2247 (2010).
272. Zhang, J., Whitesell, J. K., Fox, M. A. Photoreactivity of Self-assembled Monolayers of Azobenzene or Stilbene Derivatives Capped on Colloidal Gold Clusters. *Chemistry of Materials* **13**, 2323 (2001).
273. Thomas, K. G., Kamat, P. V. Chromophore-functionalized gold nanoparticles. *Accounts of Chemical Research* **36**, 888 (2003).
274. Ahmed, S. A., Tanaka, M. Synthesis of Oligo(ethylene glycol) toward 44-mer. *The Journal of Organic Chemistry* **71**, 9884 (2006).
275. Dennington, R., Keith, T., Millam, J. Gauss View. *Semichem Inc. Shawnee Mission*, Software (2009).
276. Moldt, T., Przyrembel, D., Schulze, M., Bronsch, W., Boie, L., Brete, D., Gahl, C., Klajn, R., Tegeder, P., Weinelt, M. Differing Isomerization Kinetics of Azobenzene-Functionalized Self-Assembled Monolayers in Ambient Air and in Vacuum. *Langmuir* **32**, 10795 (2016).
277. Taguchi, T., Isozaki, K., Miki, K. Enhanced catalytic activity of self-assembled-monolayer-capped gold nanoparticles. *Advanced Materials Weinheim* **24**, 6462 (2012).
278. Ahmed, S. A., Tanaka, M. Synthesis of Oligo(ethylene glycol) toward 44-mer. *The Journal of Organic Chemistry* **71**, 9884 (2006).
279. Han, J.-M., Pan, J.-L., Lei, T., Liu, C., Pei, J. Smart Macrocyclic Molecules: Induced Fit and Ultrafast Self-Sorting Inclusion Behavior through Dynamic Covalent Chemistry. *Chemistry A European Journal* **16**, 13850 (2010).
280. Chen, X., Zhang, Z., Liu, J., Wang, L. A polymer electron donor based on isoindigo units bearing branched oligo(ethylene glycol) side chains for polymer solar cells. *Polymer Chemistry* **8**, 5496 (2017).



Tuning of the Aggregation Behavior of Fluorinated Polymeric Nanoparticles for Improved Therapeutic Efficacy



Author: Cheng Zhang, Tianqing Liu, Wenqian Wang, et al

Publication: ACS Nano

Publisher: American Chemical Society

Date: Jun 1, 2020

Copyright © 2020, American Chemical Society

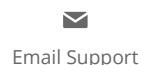
PERMISSION/LICENSE IS GRANTED FOR YOUR ORDER AT NO CHARGE

This type of permission/license, instead of the standard Terms & Conditions, is sent to you because no fee is being charged for your order. Please note the following:

- Permission is granted for your request in both print and electronic formats, and translations.
- If figures and/or tables were requested, they may be adapted or used in part.
- Please print this page for your records and send a copy of it to your publisher/graduate school.
- Appropriate credit for the requested material should be given as follows: "Reprinted (adapted) with permission from (COMPLETE REFERENCE CITATION). Copyright (YEAR) American Chemical Society." Insert appropriate information in place of the capitalized words.
- One-time permission is granted only for the use specified in your request. No additional uses are granted (such as derivative works or other editions). For any other uses, please submit a new request.

[BACK](#)

[CLOSE WINDOW](#)



High F-Content Perfluoropolyether-Based Nanoparticles for Targeted Detection of Breast Cancer by ¹⁹F Magnetic Resonance and Optical Imaging



Author: Cheng Zhang, Shehzahdi Shebbrin Moonshi, Wenqian Wang, et al

Publication: ACS Nano

Publisher: American Chemical Society

Date: Sep 1, 2018

Copyright © 2018, American Chemical Society

PERMISSION/LICENSE IS GRANTED FOR YOUR ORDER AT NO CHARGE

This type of permission/license, instead of the standard Terms & Conditions, is sent to you because no fee is being charged for your order. Please note the following:

- Permission is granted for your request in both print and electronic formats, and translations.
- If figures and/or tables were requested, they may be adapted or used in part.
- Please print this page for your records and send a copy of it to your publisher/graduate school.
- Appropriate credit for the requested material should be given as follows: "Reprinted (adapted) with permission from (COMPLETE REFERENCE CITATION). Copyright (YEAR) American Chemical Society." Insert appropriate information in place of the capitalized words.
- One-time permission is granted only for the use specified in your request. No additional uses are granted (such as derivative works or other editions). For any other uses, please submit a new request.

[BACK](#)

[CLOSE WINDOW](#)



PFPE-Based Polymeric ¹⁹F MRI Agents: A New Class of Contrast Agents with Outstanding Sensitivity



Author: Cheng Zhang, Shehzahdi Shebbrin Moonshi, Yanxiao Han, et al

Publication: Macromolecules

Publisher: American Chemical Society

Date: Aug 1, 2017

Copyright © 2017, American Chemical Society

PERMISSION/LICENSE IS GRANTED FOR YOUR ORDER AT NO CHARGE

This type of permission/license, instead of the standard Terms & Conditions, is sent to you because no fee is being charged for your order. Please note the following:

- Permission is granted for your request in both print and electronic formats, and translations.
- If figures and/or tables were requested, they may be adapted or used in part.
- Please print this page for your records and send a copy of it to your publisher/graduate school.
- Appropriate credit for the requested material should be given as follows: "Reprinted (adapted) with permission from (COMPLETE REFERENCE CITATION). Copyright (YEAR) American Chemical Society." Insert appropriate information in place of the capitalized words.
- One-time permission is granted only for the use specified in your request. No additional uses are granted (such as derivative works or other editions). For any other uses, please submit a new request.

[BACK](#)

[CLOSE WINDOW](#)



Novel Oligo-Guanidyl-PEG Carrier Forming Rod-Shaped Polyplexes



Author: Alessio Malfanti, Francesca Mastrotto, Yanxiao Han, et al

Publication: Molecular Pharmaceutics

Publisher: American Chemical Society

Date: Apr 1, 2019

Copyright © 2019, American Chemical Society

PERMISSION/LICENSE IS GRANTED FOR YOUR ORDER AT NO CHARGE

This type of permission/license, instead of the standard Terms & Conditions, is sent to you because no fee is being charged for your order. Please note the following:

- Permission is granted for your request in both print and electronic formats, and translations.
- If figures and/or tables were requested, they may be adapted or used in part.
- Please print this page for your records and send a copy of it to your publisher/graduate school.
- Appropriate credit for the requested material should be given as follows: "Reprinted (adapted) with permission from (COMPLETE REFERENCE CITATION). Copyright (YEAR) American Chemical Society." Insert appropriate information in place of the capitalized words.
- One-time permission is granted only for the use specified in your request. No additional uses are granted (such as derivative works or other editions). For any other uses, please submit a new request.

[BACK](#)

[CLOSE WINDOW](#)



Multivalent Cluster Nanomolecules for Inhibiting Protein-Protein Interactions



Author: Elaine A. Qian, Yanxiao Han, Marco S. Messina, et al

Publication: Bioconjugate Chemistry

Publisher: American Chemical Society

Date: Oct 1, 2019

Copyright © 2019, American Chemical Society

PERMISSION/LICENSE IS GRANTED FOR YOUR ORDER AT NO CHARGE

This type of permission/license, instead of the standard Terms & Conditions, is sent to you because no fee is being charged for your order. Please note the following:

- Permission is granted for your request in both print and electronic formats, and translations.
- If figures and/or tables were requested, they may be adapted or used in part.
- Please print this page for your records and send a copy of it to your publisher/graduate school.
- Appropriate credit for the requested material should be given as follows: "Reprinted (adapted) with permission from (COMPLETE REFERENCE CITATION). Copyright (YEAR) American Chemical Society." Insert appropriate information in place of the capitalized words.
- One-time permission is granted only for the use specified in your request. No additional uses are granted (such as derivative works or other editions). For any other uses, please submit a new request.

[BACK](#)

[CLOSE WINDOW](#)



Email Support



Yanxiao Han ▾

Atomically precise organomimetic cluster nanomolecules assembled via perfluoroaryl-thiol SNAr chemistry

SPRINGER NATURE

Author: Elaine A. Qian et al

Publication: Nature Chemistry

Publisher: Springer Nature

Date: Dec 19, 2016

Copyright © 2016, Springer Nature

Author Request

If you are the author of this content (or his/her designated agent) please read the following. If you are not the author of this content, please click the Back button and select no to the question "Are you the Author of this Springer Nature content?".

Ownership of copyright in original research articles remains with the Author, and provided that, when reproducing the contribution or extracts from it or from the Supplementary Information, the Author acknowledges first and reference publication in the Journal, the Author retains the following non-exclusive rights:

To reproduce the contribution in whole or in part in any printed volume (book or thesis) of which they are the author(s).

The author and any academic institution, where they work, at the time may reproduce the contribution for the purpose of course teaching.

To reuse figures or tables created by the Author and contained in the Contribution in oral presentations and other works created by them.

To post a copy of the contribution as accepted for publication after peer review (in locked Word processing file, of a PDF version thereof) on the Author's own web site, or the Author's institutional repository, or the Author's funding body's archive, six months after publication of the printed or online edition of the Journal, provided that they also link to the contribution on the publisher's website.

Authors wishing to use the published version of their article for promotional use or on a web site must request in the normal way.

If you require further assistance please read Springer Nature's online [author reuse guidelines](#).

For full paper portion: Authors of original research papers published by Springer Nature are encouraged to submit the author's version of the accepted, peer-reviewed manuscript to their relevant funding body's archive, for release six months after publication. In addition, authors are encouraged to archive their version of the manuscript in their institution's repositories (as well as their personal Web sites), also six months after original publication.

v1.0

BACK

CLOSE WINDOW



Dendritic PEG outer shells enhance serum stability of polymeric micelles

Author: Hao-jui Hsu, Yanxiao Han, Michael Cheong, Petr Král, Seungpyo Hong

Publication: Nanomedicine: Nanotechnology, Biology and Medicine

Publisher: Elsevier

Date: August 2018

© 2018 Elsevier Inc. All rights reserved.

Please note that, as the author of this Elsevier article, you retain the right to include it in a thesis or dissertation, provided it is not published commercially. Permission is not required, but please ensure that you reference the journal as the original source. For more information on this and on your other retained rights, please visit: <https://www.elsevier.com/about/our-business/policies/copyright#Author-rights>

[BACK](#)

[CLOSE WINDOW](#)

© 2020 Copyright - All Rights Reserved | [Copyright Clearance Center, Inc.](#) | [Privacy statement](#) | [Terms and Conditions](#)
Comments? We would like to hear from you. E-mail us at customercare@copyright.com



An Organometallic Strategy for Assembling Atomically Precise Hybrid Nanomaterials



Author: Julia M. Stauber, Elaine A. Qian, Yanxiao Han, et al

Publication: Journal of the American Chemical Society

Publisher: American Chemical Society

Date: Jan 1, 2020

Copyright © 2020, American Chemical Society

PERMISSION/LICENSE IS GRANTED FOR YOUR ORDER AT NO CHARGE

This type of permission/license, instead of the standard Terms & Conditions, is sent to you because no fee is being charged for your order. Please note the following:

- Permission is granted for your request in both print and electronic formats, and translations.
- If figures and/or tables were requested, they may be adapted or used in part.
- Please print this page for your records and send a copy of it to your publisher/graduate school.
- Appropriate credit for the requested material should be given as follows: "Reprinted (adapted) with permission from (COMPLETE REFERENCE CITATION). Copyright (YEAR) American Chemical Society." Insert appropriate information in place of the capitalized words.
- One-time permission is granted only for the use specified in your request. No additional uses are granted (such as derivative works or other editions). For any other uses, please submit a new request.

[BACK](#)

[CLOSE WINDOW](#)



Email Support



Yanxiao Han ▾

Catalytic transport of molecular cargo using diffusive binding along a polymer track

SPRINGER NATURE

Author: Lifei Zheng et al

Publication: Nature Chemistry

Publisher: Springer Nature

Date: Jan 21, 2019

Copyright © 2019, Springer Nature

Author Request

If you are the author of this content (or his/her designated agent) please read the following. If you are not the author of this content, please click the Back button and select no to the question "Are you the Author of this Springer Nature content?".

Ownership of copyright in original research articles remains with the Author, and provided that, when reproducing the contribution or extracts from it or from the Supplementary Information, the Author acknowledges first and reference publication in the Journal, the Author retains the following non-exclusive rights:

To reproduce the contribution in whole or in part in any printed volume (book or thesis) of which they are the author(s).

The author and any academic institution, where they work, at the time may reproduce the contribution for the purpose of course teaching.

To reuse figures or tables created by the Author and contained in the Contribution in oral presentations and other works created by them.

To post a copy of the contribution as accepted for publication after peer review (in locked Word processing file, of a PDF version thereof) on the Author's own web site, or the Author's institutional repository, or the Author's funding body's archive, six months after publication of the printed or online edition of the Journal, provided that they also link to the contribution on the publisher's website.

Authors wishing to use the published version of their article for promotional use or on a web site must request in the normal way.

If you require further assistance please read Springer Nature's online [author reuse guidelines](#).

For full paper portion: Authors of original research papers published by Springer Nature are encouraged to submit the author's version of the accepted, peer-reviewed manuscript to their relevant funding body's archive, for release six months after publication. In addition, authors are encouraged to archive their version of the manuscript in their institution's repositories (as well as their personal Web sites), also six months after original publication.

v1.0

BACK

CLOSE WINDOW



Email Support



Yanxiao Han ▾

Broad-spectrum non-toxic antiviral nanoparticles with a virucidal inhibition mechanism

Author: Valeria Cagno et al

Publication: Nature Materials

Publisher: Springer Nature

Date: Dec 18, 2017

Copyright © 2017, Nature Publishing Group

Author Request

If you are the author of this content (or his/her designated agent) please read the following. If you are not the author of this content, please click the Back button and select no to the question "Are you the Author of this Springer Nature content?".

Ownership of copyright in original research articles remains with the Author, and provided that, when reproducing the contribution or extracts from it or from the Supplementary Information, the Author acknowledges first and reference publication in the Journal, the Author retains the following non-exclusive rights:

To reproduce the contribution in whole or in part in any printed volume (book or thesis) of which they are the author(s).

The author and any academic institution, where they work, at the time may reproduce the contribution for the purpose of course teaching.

To reuse figures or tables created by the Author and contained in the Contribution in oral presentations and other works created by them.

To post a copy of the contribution as accepted for publication after peer review (in locked Word processing file, of a PDF version thereof) on the Author's own web site, or the Author's institutional repository, or the Author's funding body's archive, six months after publication of the printed or online edition of the Journal, provided that they also link to the contribution on the publisher's website.

Authors wishing to use the published version of their article for promotional use or on a web site must request in the normal way.

If you require further assistance please read Springer Nature's online [author reuse guidelines](#).

For full paper portion: Authors of original research papers published by Springer Nature are encouraged to submit the author's version of the accepted, peer-reviewed manuscript to their relevant funding body's archive, for release six months after publication. In addition, authors are encouraged to archive their version of the manuscript in their institution's repositories (as well as their personal Web sites), also six months after original publication.

v1.0

BACK

CLOSE WINDOW



Nanoparticle Conjugation Stabilizes and Multimerizes β -Hairpin Peptides To Effectively Target PD-1/PD-L1 β -Sheet-Rich Interfaces



Author: Woo-jin Jeong, Jiyeon Bu, Yanxiao Han, et al

Publication: Journal of the American Chemical Society

Publisher: American Chemical Society

Date: Jan 1, 2020

Copyright © 2020, American Chemical Society

PERMISSION/LICENSE IS GRANTED FOR YOUR ORDER AT NO CHARGE

This type of permission/license, instead of the standard Terms & Conditions, is sent to you because no fee is being charged for your order. Please note the following:

- Permission is granted for your request in both print and electronic formats, and translations.
- If figures and/or tables were requested, they may be adapted or used in part.
- Please print this page for your records and send a copy of it to your publisher/graduate school.
- Appropriate credit for the requested material should be given as follows: "Reprinted (adapted) with permission from (COMPLETE REFERENCE CITATION). Copyright (YEAR) American Chemical Society." Insert appropriate information in place of the capitalized words.
- One-time permission is granted only for the use specified in your request. No additional uses are granted (such as derivative works or other editions). For any other uses, please submit a new request.

[BACK](#)

[CLOSE WINDOW](#)

JOHN WILEY AND SONS LICENSE TERMS AND CONDITIONS

Dec 20, 2020

This Agreement between University of Illinois at Chicago -- Yanxiao Han ("You") and John Wiley and Sons ("John Wiley and Sons") consists of your license details and the terms and conditions provided by John Wiley and Sons and Copyright Clearance Center.

License
Number 4973240652972

License date Dec 20, 2020

Licensed
Content
Publisher John Wiley and Sons

Licensed
Content
Publication Angewandte Chemie

Licensed
Content Title "Precipitation on Nanoparticles": Attractive Intermolecular Interactions
Stabilize Specific Ligand Ratios on the Surfaces of Nanoparticles

Licensed
Content Author Rafal Klajn, Petr Král, Yanxiao Han, et al

Licensed
Content Date May 15, 2018

Licensed
Content
Volume 130

Licensed
Content Issue 24

Licensed 5
Content Pages

Type of use Dissertation/Thesis

Requestor type Author of this Wiley article

Format Print and electronic

Portion Full article

Will you be
translating? No

Title Molecular Dynamics Simulations of Bioactive Complexes, Nanoparticles
and Polymers

Institution
name University of Illinois at Chicago

Expected
presentation
date Dec 2020

Requestor
Location University of Illinois at Chicago
845 W Taylor St
CHICAGO, IL 60607
United States
Attn: University of Illinois at Chicago

Publisher Tax
ID EU826007151

Total 0.00 USD

Terms and Conditions

228
TERMS AND CONDITIONS

This copyrighted material is owned by or exclusively licensed to John Wiley & Sons, Inc. or one of its group companies (each a "Wiley Company") or handled on behalf of a society with which a Wiley Company has exclusive publishing rights in relation to a particular work (collectively "WILEY"). By clicking "accept" in connection with completing this licensing transaction, you agree that the following terms and conditions apply to this transaction (along with the billing and payment terms and conditions established by the Copyright Clearance Center Inc., ("CCC's Billing and Payment terms and conditions"), at the time that you opened your RightsLink account (these are available at any time at <http://myaccount.copyright.com>).

Terms and Conditions

- The materials you have requested permission to reproduce or reuse (the "Wiley Materials") are protected by copyright.
- You are hereby granted a personal, non-exclusive, non-sub licensable (on a stand-alone basis), non-transferable, worldwide, limited license to reproduce the Wiley Materials for the purpose specified in the licensing process. This license, **and any CONTENT (PDF or image file) purchased as part of your order**, is for a one-time use only and limited to any maximum distribution number specified in the license. The first instance of republication or reuse granted by this license must be completed within two years of the date of the grant of this license (although copies prepared before the end date may be distributed thereafter). The Wiley Materials shall not be used in any other manner or for any other purpose, beyond what is granted in the license. Permission is granted subject to an appropriate acknowledgement given to the author, title of the material/book/journal and the publisher. You shall also duplicate the copyright notice that appears in the Wiley publication in your use of the Wiley Material. Permission is also granted on the understanding that nowhere in the text is a previously published source acknowledged for all or part of this Wiley Material. Any third party content is expressly excluded from this permission.
- With respect to the Wiley Materials, all rights are reserved. Except as expressly granted by the terms of the license, no part of the Wiley Materials may be copied, modified, adapted (except for minor reformatting required by the new Publication), translated, reproduced, transferred or distributed, in any form or by any means, and no derivative works may be made based on the Wiley Materials without the prior permission of the respective copyright owner. **For STM Signatory Publishers clearing permission under the terms of the [STM Permissions Guidelines](#) only, the terms of the license are extended to include subsequent editions and for editions in other languages, provided such editions are for the work as a whole in situ and does not involve the separate exploitation of the permitted figures or extracts,** You may not alter, remove or suppress in any manner any copyright, trademark or other notices displayed by the Wiley Materials. You may not license, rent, sell, loan, lease, pledge, offer as security, transfer or assign the Wiley Materials on a stand-alone basis, or any of the rights granted to you hereunder to any other person.
- The Wiley Materials and all of the intellectual property rights therein shall at all times remain the exclusive property of John Wiley & Sons Inc, the Wiley Companies, or their respective licensors, and your interest therein is only that of having possession of and the right to reproduce the Wiley Materials pursuant to Section 2 herein during the continuance of this Agreement. You agree that you own no right, title or interest in or to the Wiley Materials or any of the intellectual property rights therein. You shall have no rights hereunder other than the license as provided for above in Section 2. No right,

license or interest to any trademark, trade name, service mark or other branding ("Marks") of WILEY or its licensors is granted hereunder, and you agree that you shall not assert any such right, license or interest with respect thereto

- NEITHER WILEY NOR ITS LICENSORS MAKES ANY WARRANTY OR REPRESENTATION OF ANY KIND TO YOU OR ANY THIRD PARTY, EXPRESS, IMPLIED OR STATUTORY, WITH RESPECT TO THE MATERIALS OR THE ACCURACY OF ANY INFORMATION CONTAINED IN THE MATERIALS, INCLUDING, WITHOUT LIMITATION, ANY IMPLIED WARRANTY OF MERCHANTABILITY, ACCURACY, SATISFACTORY QUALITY, FITNESS FOR A PARTICULAR PURPOSE, USABILITY, INTEGRATION OR NON-INFRINGEMENT AND ALL SUCH WARRANTIES ARE HEREBY EXCLUDED BY WILEY AND ITS LICENSORS AND WAIVED BY YOU.
- WILEY shall have the right to terminate this Agreement immediately upon breach of this Agreement by you.
- You shall indemnify, defend and hold harmless WILEY, its Licensors and their respective directors, officers, agents and employees, from and against any actual or threatened claims, demands, causes of action or proceedings arising from any breach of this Agreement by you.
- IN NO EVENT SHALL WILEY OR ITS LICENSORS BE LIABLE TO YOU OR ANY OTHER PARTY OR ANY OTHER PERSON OR ENTITY FOR ANY SPECIAL, CONSEQUENTIAL, INCIDENTAL, INDIRECT, EXEMPLARY OR PUNITIVE DAMAGES, HOWEVER CAUSED, ARISING OUT OF OR IN CONNECTION WITH THE DOWNLOADING, PROVISIONING, VIEWING OR USE OF THE MATERIALS REGARDLESS OF THE FORM OF ACTION, WHETHER FOR BREACH OF CONTRACT, BREACH OF WARRANTY, TORT, NEGLIGENCE, INFRINGEMENT OR OTHERWISE (INCLUDING, WITHOUT LIMITATION, DAMAGES BASED ON LOSS OF PROFITS, DATA, FILES, USE, BUSINESS OPPORTUNITY OR CLAIMS OF THIRD PARTIES), AND WHETHER OR NOT THE PARTY HAS BEEN ADVISED OF THE POSSIBILITY OF SUCH DAMAGES. THIS LIMITATION SHALL APPLY NOTWITHSTANDING ANY FAILURE OF ESSENTIAL PURPOSE OF ANY LIMITED REMEDY PROVIDED HEREIN.
- Should any provision of this Agreement be held by a court of competent jurisdiction to be illegal, invalid, or unenforceable, that provision shall be deemed amended to achieve as nearly as possible the same economic effect as the original provision, and the legality, validity and enforceability of the remaining provisions of this Agreement shall not be affected or impaired thereby.
- The failure of either party to enforce any term or condition of this Agreement shall not constitute a waiver of either party's right to enforce each and every term and condition of this Agreement. No breach under this agreement shall be deemed waived or excused by either party unless such waiver or consent is in writing signed by the party granting such waiver or consent. The waiver by or consent of a party to a breach of any provision of this Agreement shall not operate or be construed as a waiver of or consent to any other or subsequent breach by such other party.
- This Agreement may not be assigned (including by operation of law or otherwise) by you without WILEY's prior written consent.

- Any fee required for this permission shall be non-refundable after thirty (30) days from receipt by the CCC.
- These terms and conditions together with CCC's Billing and Payment terms and conditions (which are incorporated herein) form the entire agreement between you and WILEY concerning this licensing transaction and (in the absence of fraud) supersedes all prior agreements and representations of the parties, oral or written. This Agreement may not be amended except in writing signed by both parties. This Agreement shall be binding upon and inure to the benefit of the parties' successors, legal representatives, and authorized assigns.
- In the event of any conflict between your obligations established by these terms and conditions and those established by CCC's Billing and Payment terms and conditions, these terms and conditions shall prevail.
- WILEY expressly reserves all rights not specifically granted in the combination of (i) the license details provided by you and accepted in the course of this licensing transaction, (ii) these terms and conditions and (iii) CCC's Billing and Payment terms and conditions.
- This Agreement will be void if the Type of Use, Format, Circulation, or Requestor Type was misrepresented during the licensing process.
- This Agreement shall be governed by and construed in accordance with the laws of the State of New York, USA, without regards to such state's conflict of law rules. Any legal action, suit or proceeding arising out of or relating to these Terms and Conditions or the breach thereof shall be instituted in a court of competent jurisdiction in New York County in the State of New York in the United States of America and each party hereby consents and submits to the personal jurisdiction of such court, waives any objection to venue in such court and consents to service of process by registered or certified mail, return receipt requested, at the last known address of such party.

WILEY OPEN ACCESS TERMS AND CONDITIONS

Wiley Publishes Open Access Articles in fully Open Access Journals and in Subscription journals offering Online Open. Although most of the fully Open Access journals publish open access articles under the terms of the Creative Commons Attribution (CC BY) License only, the subscription journals and a few of the Open Access Journals offer a choice of Creative Commons Licenses. The license type is clearly identified on the article.

The Creative Commons Attribution License

The [Creative Commons Attribution License \(CC-BY\)](#) allows users to copy, distribute and transmit an article, adapt the article and make commercial use of the article. The CC-BY license permits commercial and non-

Creative Commons Attribution Non-Commercial License

The [Creative Commons Attribution Non-Commercial \(CC-BY-NC\) License](#) permits use, distribution and reproduction in any medium, provided the original work is properly cited and is not used for commercial purposes.(see below) 231

Creative Commons Attribution-Non-Commercial-NoDerivs License

The [Creative Commons Attribution Non-Commercial-NoDerivs License](#) (CC-BY-NC-ND) permits use, distribution and reproduction in any medium, provided the original work is properly cited, is not used for commercial purposes and no modifications or adaptations are made. (see below)

Use by commercial "for-profit" organizations

Use of Wiley Open Access articles for commercial, promotional, or marketing purposes requires further explicit permission from Wiley and will be subject to a fee.

Further details can be found on Wiley Online Library
<http://olabout.wiley.com/WileyCDA/Section/id-410895.html>

Other Terms and Conditions:

v1.10 Last updated September 2015

Questions? customercare@copyright.com or +1-855-239-3415 (toll free in the US) or +1-978-646-2777.



Email Support



Yanxiao Han ▾

Supramolecular Control of Azobenzene Switching on Nanoparticles

**Author:** Zonglin Chu, Yanxiao Han, Tong Bian, et al**Publication:** Journal of the American Chemical Society**Publisher:** American Chemical Society**Date:** Feb 1, 2019*Copyright © 2019, American Chemical Society*

PERMISSION/LICENSE IS GRANTED FOR YOUR ORDER AT NO CHARGE

This type of permission/license, instead of the standard Terms & Conditions, is sent to you because no fee is being charged for your order. Please note the following:

- Permission is granted for your request in both print and electronic formats, and translations.
- If figures and/or tables were requested, they may be adapted or used in part.
- Please print this page for your records and send a copy of it to your publisher/graduate school.
- Appropriate credit for the requested material should be given as follows: "Reprinted (adapted) with permission from (COMPLETE REFERENCE CITATION). Copyright (YEAR) American Chemical Society." Insert appropriate information in place of the capitalized words.
- One-time permission is granted only for the use specified in your request. No additional uses are granted (such as derivative works or other editions). For any other uses, please submit a new request.

[BACK](#)[CLOSE WINDOW](#)